

Conformational Analysis and Absolute Configuration Determination of Some Organic and Coordination Chemistry Compounds Using Chiroptical Spectroscopy and DFT calculations

by

Zahra Dezhahang

A thesis submitted in partial fulfillment of the requirements for the degree of

Doctor of Philosophy

Department of Chemistry  
University of Alberta

© Zahra Dezhahang, 2015

## Abstract

---

My PhD thesis projects revolve around three main parts, namely synthesis, conformational analysis, and absolute configuration determination of a number of chiral Schiff base ligands and axial chiral binaphthyl type ligands or molecules and some of their transition metal complexes in solution. To obtain the structural information of these chiral systems in solution, chiroptical spectroscopic techniques, such as electronic and vibrational circular dichroism (ECD and VCD) spectroscopy, as well as the related linear spectroscopy, i.e., IR and UV-Vis spectroscopy, have been used as the main experimental tools. In addition, density functional theory (DFT) has been employed to perform all calculations for the conformational searches, geometry optimizations, and simulations of VA, VCD, UV-Vis, and ECD spectra. Comparison of the theoretical and experimental spectra has been utilized to provide detailed and rigorous spectral interpretations and therefore to extract essential structural properties of the targeted species in solution. To account for the bulk solvent environment, the implicit solvation approach, i.e. the polarizable continuum model (PCM), has been applied where no strong solvent–solute hydrogen-bonding interactions are expected. Initial conformational analyses of the systems studied have been performed using small basis sets, such as 6-31G(d). For the final calculations, several larger basis sets, namely 6-31++G(d,p), 6-311++G(d,p), and cc-pVTZ have been used for the C, H, N, O atoms and the LanL2DZ basis sets for the metal atoms. We found that flexible ligands, such as the multidentate nitrogen donor ligands, BINAP and related ligands, show a number of minima on their potential energy surfaces. Further coordination to one or more metal centers often introduces dramatically the structural rigidity and consequently results in a smaller number of minima. For example, in the case of Pd(BINAP)Cl<sub>2</sub> and Pd(TOLBINAP)Cl<sub>2</sub>, a single conformation has been identified in solution. Especially for the VCD spectra observed, it has

been demonstrated that the gas phase models failed to capture the experimental optical responses properly, and the inclusion of solvent whether implicitly or explicitly has been shown to be of high importance. In addition, in the study of a triply axial chiral binaphthyl based molecule, it has been demonstrated that the solute concentration may play a crucial role on its conformational landscape as well as its axial chirality in solution. To probe structural properties including induced chirality at the metal centers, the bis(pyrrol-2-ylmethyleneamine)-cyclohexane ( $H_2L$ ) ligand and its five metal complexes (e.g. Ni (II), Cu (II), Pd (II), Pt (II), and Zn (II)) have been synthesized and their VA, VCD, UV-Vis and ECD spectra have been recorded and analyzed. We found that while  $M-Ni-(R,R)-L$ ,  $M-Cu-(R,R)-L$ ,  $M-Pd-(R,R)-L$ , and  $M-Pt-(R,R)-L$  complexes take on the *mono*-nuclear geometries, the  $[M-Zn-(R,R)-L]_2$  complex in solution exists in the *di*-nuclear geometry. Furthermore, these metal complexes take on  $M$ -helicity as dictated by the chirality of the  $(R,R)$ -ligand.

## Preface

---

My PhD journey at the University of Alberta started in January 2009 and finished in December 2013. I have taken a maternity leave in 2014. My thesis is composed of several chiroptical spectroscopic projects. Information regarding the contribution of each author is listed below. Chapter 2 of my thesis has been published as Zahra Dezhahang, Mohammad Reza Poopari, and Yunjie Xu, *Chem. Asian J.*, 8, 6, 2013, 1205-1212 with the title of “vibrational circular dichroism spectroscopy of three multidentate nitrogen donor ligands: conformational flexibility and solvent effects”. This paper was chosen as the inside cover of the issue. I have done the syntheses and characterizations of three compounds, carried out the spectroscopic measurements and most of the spectral simulations as well as writing the first draft of the paper. Dr. Poopari contributed to the theoretical calculations. Professor Y. Xu was the supervisory author and was involved in the concept formation, data analysis, and manuscript composition.

Chapter 3 of my thesis has been published in the Journal of Molecular Structure under the title of “hydrogen bonding interaction with the crystal water in [(R,R)-1,5-diaza-cis-decalin] copper (II) complex and its conformation: a combined experimental VA and ECD spectroscopic and DFT study”, as Zahra Dezhahang, Mohammad Reza Poopari, and Yunjie Xu, *J. Mol. Struct.*, 2012, 1024, 123-131. In this project, I was responsible for all solution measurements, theoretical calculations, data analyses, and preparation of the first draft of the manuscript. Dr. Poopari helped me to prepare the solid sample as well as running the solid measurements. Professor Y. Xu was the supervisory author and was involved in the concept formation, data analysis, and manuscript composition.

Chapter 4 of my thesis has been published in Dalton Transactions with the title of “vibrational circular dichroism spectroscopy of two chiral binaphthyl diphosphine ligands and their palladium

complexes in solution” as Zahra Dezhahang, Christian Merten, Mohammad Reza Poopari, and Yunjie Xu, *Dalton Trans.*, 2012, 41, 10817-10824. In this project, I was fully responsible for the experimental measurements, and partially for the theoretical calculations. Drs. Poopari and Merten helped me to finish the theoretical calculations. The manuscript was originally written by me. Professor Y. Xu was the supervisory author and was involved in the concept formation, data analysis, and manuscript composition.

Chapter 5 of my thesis will be submitted to a journal shortly with the following title: “structural properties and induced helicity of a chiral pyrrol-2-yl Schiff base ligand and its five transition metal complexes in solution: combined vibrational and electronic CD, and DFT studies” by Zahra Dezhahang, Mohammad Reza Poopari, Joseph Cheramy, and Yunjie Xu. The syntheses of the ligands and their corresponding transition metal complexes were carried out by me, Dr. Poopari and Joseph Cheramy. I did part of the spectral simulations and data analysis, and wrote the first draft of the manuscript. Dr. Poopari did the other part of the spectral simulations. Professor Y. Xu was the supervisory author and was involved in the concept formation, data analysis, and manuscript composition.

Chapter 6 of my thesis has been published in *Physical Chemistry Chemical Physics* with the title of “diastereomeric preference of a triply axial chiral binaphthyl based molecule: a concentration dependent study by chiroptical spectroscopies” by Zahra Dezhahang, Mohammad Reza Poopari, Eloy Florencio Hernández, Carlos Diaz, Yunjie Xu, *Phys. Chem. Chem. Phys.*, 2014, 16, 12959-12967. I was responsible for the experimental measurements and theoretical calculations as well as preparing the first draft of the manuscript. Prof. Hernández and Carlos Diaz from the University of Central Florida (UCF) provided the sample and scientific discussion of the project. Dr. Poopari helped me in data analyses and the modification of the manuscripts. This paper was

selected as one of the hot papers of the issue. Professor Y. Xu was the supervisory author and was involved in the concept formation, data analysis, and manuscript composition.

## **Acknowledgements**

---

I would like to express my special appreciation to my PhD advisor Prof. Yunjie Xu for being an incredible mentor, and allowing me to grow as a research scientist. During the past five years of my PhD journey, she has always been giving me priceless advice on both my research and future careers, which I am so grateful to her. I would also like to thank my committee members, Prof. Alex Brown, Prof. Steven Bergens, and Prof. Jon Veinot for serving as my internal committee members, Prof. Hongbo Zeng and Prof. Wouter Herrebout for serving as my external examiners in my PhD defense. Thanks for your brilliant suggestions and comments, and for making my defense an enjoyable moment. I would especially like to thank Prof. Wolfgang Jaeger for his valuable advice and discussion, which helped me to strengthen my knowledge about the world of science. I also would like to thank Prof. Florencio Hernandez from the University of Central Florida (UCF) for giving me a chance to collaborate with him. A special thanks to my colleagues and friends, Steve, Javix, Chrissy, Jen, Fumie, Connie, Christian, Nargess, Olivier, and Joseph for being so helpful, kind, and making me laugh.

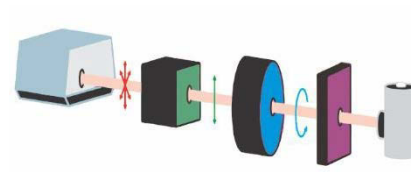
I would love to thank my beloved family members. Without a doubt, words cannot express how grateful I am to my father, Abdolreza Dezhahang, my mother, Mozhgan Shahpar, and my sisters and brother. They have been always so supportive and that's what sustained me thus far and incited me to strive towards my goals both in scientific and personal lives. I would like to express my great appreciation to my beloved husband Dr. Mohammad Reza Poopari, and my new lovely family addition Carmen who will be staying in my heart forever.

# Table of contents

Chapter

Page

**1**

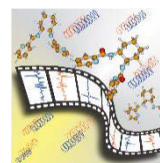


<b>Chapter 1: Introduction.....</b>	<b>1</b>
1.1 Molecular Chirality .....	2
1.2 Experimental.....	6
1.2.1 Chiroptical spectroscopy.....	6
1.2.2 Optical rotatory dispersion experiments.....	6
1.2.3 Electronic and vibrational circular dichroism experiments.....	9
1.3 Theoretical.....	13
1.3.1 Basics of VCD spectroscopy and spectral calculations.....	13
1.3.2 Basics of ECD spectroscopy and spectral calculations.....	17
1.3.3 Solvent effects.....	17
1.4 Objectives and Scope of the thesis.....	19
References .....	25



# 2

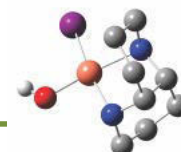
## Chapter 2: Vibrational circular dichroism spectroscopy of three multidentate nitrogen donor ligands: conformational flexibility and solvent effects.....28



2.1 Introduction .....	29
2.2 Results and discussions .....	31
2.2.1 Compound 1 .....	32
2.2.2 Compound 2 .....	37
2.2.3 Compound 3.....	41
2.3 Conclusion .....	44
2.4 Experimental section .....	46
2.4.1 Experimental details .....	46
2.4.2 Computational details.....	46
2.5 Acknowledgements.....	47
References .....	48

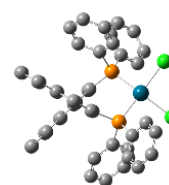
# 3

## Chapter 3: Hydrogen bonding interaction with the crystal water in [(R,R)-1,5-Diaza-cis-decalin] copper (II) complex and its conformation: a combined experimental VA and ECD spectroscopic and DFT study.....50



3.1 Introduction .....	51
------------------------	----

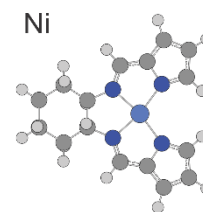
3.2 Experimental and theoretical details .....	52
3.2.1 Spectroscopic measurements .....	52
3.2.2 Theoretical calculations .....	54
3.3 Results and discussions.....	55
3.3.1 Conformational analysis and spectral simulation of the [(R,R)-1,5-diaza-cis-decalin] ligand.....	55
3.3.2 Conformational analysis and spectral simulations of the [(R,R)-1,5-diaza-cis-decalin] copper (II) hydroxide iodine complex.....	61
3.3.3 Hydrogen bonding effects on the VA, VCD, UV–Vis and ECD spectra of the [(R,R)-1,5-diaza-cis-decalin] copper (II) hydroxide iodine complex.....	68
3.4 Conclusions.....	76
3.5 Acknowledgements.....	76
References.....	77



# 4

## Chapter 4: Vibrational circular dichroism spectroscopy of two chiral binaphthyls diphosphine ligands and their palladium complexes in solution.....79

4.1 Introduction .....	80
4.2 Results and discussions.....	82
4.2.1 Experimental spectra .....	82
4.2.2 Conformations of the 1 and 2 ligands and of the Pd(1)Cl <sub>2</sub> and Pd(2)Cl <sub>2</sub> complexes.....	83
4.2.3 Interpretation of the experimental VA and VCD spectra of the 1 and 2 ligands and their palladium complexes.....	87
4.2.4 Experimental and computational details .....	93
4.3 Conclusions.....	95
4.4 Acknowledgements.....	95
References.....	97



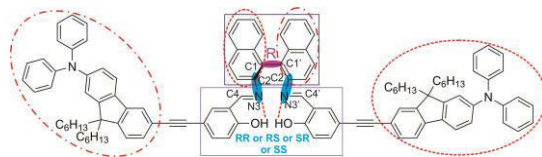
# 5

## Chapter 5: Structural properties and induced helicity of a chiral pyrrol-2-yl Schiff base ligand and its five transition metal complexes in solution: combined vibrational and electronic CD, and DFT studies.....99

5.1 Introduction.....	100
5.2 Results and discussions.....	103
5.2.1 Experimental and theoretical VA, VCD, UV-Vis and ECD spectra of the Ligand.....	103
5.2.2 Experimental and theoretical VA and VCD spectra of Ni (II), Cu (II), Pd (II), and Pt (II) complexes .....	109
5.2.3 Experimental and theoretical VA and VCD spectra of the Zn (II) complexes...	116
5.2.4 M- and P-helicity in the Zn (II) complex and other complexes .....	119
5.3 Experimental .....	124
5.3.1 Synthesis.....	124
5.3.2 IR and VCD spectroscopic measurements.....	124
5.3.3 Theoretical calculations.....	125
5.4 Conclusions.....	126
References.....	127

# 6

## Chapter 6: Diastereomeric preference of a triply axial chiral binaphthyl based molecule: a concentration dependent study by chiroptical spectroscopies...129



6.1 Introduction .....	130
6.2 Experimental and theoretical details.....	132
6.3 Results and discussions.....	134
6.3.1 Possible diastereomers of AXF-155.....	134
6.3.2 Experimental VCD spectra AXF-155.....	135
6.3.3 Comparison of experimental and simulated VCD spectra AXF155.....	136
6.3.4 Concentration dependent diastereomeric preference.....	144
6.4 Conclusions.....	148
6.5 Acknowledgments.....	148
References.....	149

# 7

## Conclusions and Future Work.....152

7.1 Concluding remarks .....	153
7.1.1. Conformational flexibility in solution.....	154

7.1.2. Solvent effects.....	155
7.1.3. Concentration effects.....	157
7.1.4. Helicity in solution and in solid.....	158
7.2 Future work.....	160
References.....	163
Work Cited.....	164
Appendix A. Supporting Information for Chapter 2.....	174
Appendix B. Supporting Information for Chapter 4.....	181
Appendix C. Supporting Information for Chapter 5.....	186
Appendix D. Supporting Information for Chapter 6.....	192
Appendix E. Contributed Journal Papers.....	195

# List of Tables

Table	Page
2.1 Dihedral angle values for the ten most stable conformers of SS-2 at the PCM/B3PW91/cc-pVTZ level.....	39
3.1 Calculated relative energies, Gibbs free energies, and the corresponding percentage Boltzmann population factors at room temperature of the six most stable conformers of the Chair–Chair 1,5-diaza-cis-decalin ligand at the B3LYP/6-31++G(d,p) level.....	56
3.2 Calculated relative energies, relative Gibbs free energies and the corresponding percentage Boltzmann population factors at room temperature of the decalin ring conformers of the N-in H-ea and N-in H-ee 1,5-diaza-cis-decalin ligands at the B3LYP/6-31++G(d,p) level.....	58
3.3 Calculated relative energies, relative Gibbs free energies and the corresponding percentage Boltzmann population factors at room temperature of the four conformers of [(R,R)-1,5-diaza-cis-decalin] copper (II) hydroxide iodine complex at the B3LYP/ LanL2DZ level.....	63
3.4 Calculated relative energies, relative Gibbs free energies and the corresponding percentage Boltzmann population factors at room temperature of the three most stable hydrogen bonded conformers of C-I Chair–Chair N-in H-ee [(R,R)-1,5-diaza-cisdecalin] copper (II) hydroxide iodine complex with the crystal water at the B3LYP/LanL2DZ level.....	69
4.1 Calculated dihedral angle values (in degrees) between the two naphthalene rings for 1 and 2 and their corresponding Pd complexes.....	85
4.2 Predicted relative energies and Gibbs free energies (in kcal mol <sup>-1</sup> ) of the three most stable conformers of the 1 and 2 ligands and their Boltzmann factors at room temperature.....	86
5.1 The helicity-determining angle $\theta$ for the H <sub>2</sub> L ligand and the associated complexes.....	123

## List of Tables [Appendices]

Table	Page
A1. Vibrational motions of the amide I bands and robust modes analyses.....	178
D1. Relative energies (in kcal/mol) of AXF-155 conformers using PCM for CHCl <sub>3</sub> .....	194

# List of Figures

Figure	Page
1.1 Molecular chirality: (I) Stereogenic center where 1, 2, 2, and 4 denote the priority of the substituents, (II) Axial chirality, and (III) Helical chirality.....	4
1.2 The representation of the lambda ( $\Lambda$ ) and the delta ( $\Delta$ ) stereoisomers of tris(ethylenediamine)cobalt(III).....	5
1.3 Optical rotation measurements of a pair of <i>enantiomers</i> and their <i>racemic</i> mixture .....	7
1.4 A schematic diagram of a polarimeter .....	9
1.5 A schematic diagram of the FTIR-VCD instrument used in my thesis research.....	10
1.6 A schematic diagram of a Michelson interferometer. ....	11
1.7 Increasing the structural flexibility due to increasing rotational degree of freedom along single bonds for three ligands, I, II and III reported in Chapter 2, and IV and V studied in Chapter 5.....	21
2.1 2D stereo-chemical structures of compounds SS-1, SS-2, and SS-3 reported herein. * indicates the stereogenic center of the compounds.....	30
2.2 Experimental VA (left) and VCD (right) spectra of 1, 2, and 3 in CDCl <sub>3</sub> from top to bottom, respectively. The VA and VCD spectra of 1 and 2, as well as the inserted spectrum of 3, were recorded with a path length of 0.1 mm. The VA and VCD spectra of 3 were recorded with a shorter path length of 0.025 mm.....	32
2.3 The cis and trans configurations of compound 1 with axial and equatorial substitutions. The rotatable C–Cpyridine and N–C <sub>hexane</sub> bonds are indicated by small arrows.....	33
2.4 Conformations of compound SS-1 at the PCM/B3PW91/ccpVTZ level. The corresponding relative Gibbs free energies in kcal mol <sup>-1</sup> and the percentage Boltzmann factors at room temperature are also listed. Secondary intramolecular hydrogen bonds with bond lengths of <2.8 Å are indicated with dotted lines.....	34
2.5. Comparison of the experimental and calculated VA (left) and VCD (right) spectra and the associated population-weighted spectra of SS-1 at the PCM/B3PW91/cc-pVTZ level. The corresponding spectra of the two main conformers of 1 are also included.....	36
2.6 The rotatable bonds used in the conformational search are indicated with double arrows. The four conformationally important dihedral angles of 2 are also shown.....	37



2.7	The ten most stable conformers of SS-2. The corresponding relative Gibbs free energies in kcal mol <sup>-1</sup> at the PCM/B3PW91/cc-pVTZ level and the corresponding Boltzmann factors at room temperature are also listed. The NH•••N hydrogen bonds are indicated with dotted lines.....	38
2.8	Comparison of the experimental and calculated VA (left) and VCD (right) spectra of the population-weighted spectra of SS-2 calculated at the PCM/B3PW91/cc-pVTZ level.....	43
2.9	Geometries of the dominant conformer of SS-3 (left) at the PCM/B3PW91/cc-pVTZ level and of the 1:2 explicit solvated complex of 3 with two molecules of CDCl <sub>3</sub> (right) at the B3PW91/cc-pVTZ level. The intermolecular hydrogen-bond lengths are given in Å.....	44
2.10	Comparison of the experimental and calculated VA (left) and VCD (right) spectra of implicit solvated 3 at the PCM/B3PW91/cc-pVTZ level and the explicit solvated complex of 3 with two molecules of CDCl <sub>3</sub> at the B3PW91/cc-pVTZ level. The dotted experimental spectra are taken from the insert in Figure 2.2. A number of bands are labeled to aid a visual comparison (see text for details).....	45
3.1	Six most stable conformers of the Chair–Chair 1,5-diaza-cis-decalin ligand at the B3LY/6-31++G(d,p) level of theory.....	55
3.2	Geometries of the decalin ring conformers of (a) N-in H-ea and (b) N-in H-ee 1,5-diaza-cis-decalin ligand at the B3LY/6-31++G(d,p) level. Hydrogen atoms attached to the carbon atoms are not displayed for simplicity.....	57
3.3	Simulated VA and VCD spectra of the six most stable conformers of the Chair–Chair 1,5-diaza-cis-decalin ligand listed in Table 3.1 at the B3LYP/6-31++G(d,p) level.....	59
3.4	Simulated UV–Vis and ECD spectra of the two most stable conformers of Chair–Chair [(R,R)-1,5-diaza-cis-decalin] ligand in the gas phase and with PCM of CH <sub>3</sub> CN solvent at the B3LYP/6-31++G(d,p) level.....	61
3.5	Optimized geometries of the four decalin ring conformers of N-in H-ee [(R,R)-1,5-diaza-cis-decalin] copper (II) hydroxide iodine complex at the B3LYP/ LanL2DZ level. Hydrogen atoms attached to the carbon atoms are not displayed for simplicity.....	63
3.6	Simulated VA and VCD spectra of the four conformers of [(R,R)-1,5-diaza-cisdecalin] copper (II) hydroxide iodine complex listed in Table 3.3 at the B3LYP/ LanL2DZ level. The experimental VA spectrum obtained with a KBr pellet is also included for comparison....	65
3.7	Simulated UV–Vis and ECD spectra of the four conformers of [(R,R)-1,5- diaza-cis-decalin] copper (II) hydroxide iodine complex listed in Table 3.3 at the B3LYP/LanL2DZ level. The experimental UV–Vis and ECD spectra obtained in CH <sub>3</sub> CN solution are also included for comparison. The inserts were measured with a higher concentration (see Section 2.1 for details).....	67

3.8 Geometries of the three most stable conformers of the hydrogen bonded cluster of C-I Chair–Chair N-in H-ee [(R,R)-1,5-diaza-cis-decalin] copper (II) hydroxide iodine complex with a crystal water molecule obtained at the B3LYP/LanL2DZ level. Hydrogen atoms attached to the carbon atoms are not displayed for simplicity. The important hydrogen bond lengths (in Å) are also indicated.....	69
3.9 Comparison of the experimental VA spectrum of the copper complex obtained with a KBr pellet with the simulated VA and VCD spectra of the three most stable hydrogen bonded conformers of C-I Chair–Chair N-in H-ee [(R,R)-1,5-diazacis-decalin] copper (II) hydroxide iodine complex with water, listed in Table 3.4, at the B3LYP/LanL2DZ level.....	71
3.10 Comparison of the experimental UV–Vis and ECD spectra of the copper complex with the corresponding simulated spectra of the three most stable hydrogen bonded conformers of C-I Chair–Chair N-in H-ee [(R,R)-1,5-diaza-cis-decalin] copper (II) hydroxide iodine complex with water, listed in Table 3.4, at the B3LYP/LanL2DZ level.....	73
3.11 Comparison of the simulated UV–Vis and ECD spectra at the B3LYP/ LanL2DZ level of C-I Chair–Chair N-in H-ee [(R,R)-1,5-diaza-cis-decalin] copper (II) hydroxide iodine complex, of its most stable hydrogen bonded cluster W-I, and of the hypothetical molecular system where the structure of W-I was frozen and the crystal water was removed for spectral simulation.....	75
4.1 Structures of the BINAP (1, Ar=C <sub>6</sub> H <sub>5</sub> ) and TOLBINAP (2, Ar=4-CH <sub>3</sub> -C <sub>6</sub> H <sub>4</sub> ) ligands (left) and their corresponding palladium complexes (right) investigated in this report.....	81
4.2 The experimental VA (left) and VCD (right) spectra of R-1, R-Pd(1)Cl <sub>2</sub> , R-2, and R-Pd(2)Cl <sub>2</sub> in CDCl <sub>3</sub> .....	83
4.3 Three most stable conformers of R-1 and R-2 at the B3LYP/ 6-31G(d,p) level viewed along the C1–C1' bond.....	85
4.4 Comparison of the simulated VA and VCD spectra in the gas phase and with the PCM for chloroform with the corresponding experimental spectra of 1 (left) and 2 (right).....	88
4.5 Comparison of the simulated VA and VCD spectra in the gas phase and with the PCM for chloroform with the corresponding experimental spectra of Pd(1)Cl <sub>2</sub> (left) and Pd(2)Cl <sub>2</sub> (right).....	89
4.6 Comparison of the experimental VA and VCD spectra of Pd(2)Cl <sub>2</sub> with the corresponding calculated spectra using several different basis sets.....	93
5.1 <i>M</i> -( <i>R,R</i> )-H <sub>2</sub> L ligand and five transition metal complexes, namely <i>M</i> -Ni-( <i>R,R</i> )-L, <i>M</i> -Cu-( <i>R,R</i> )-L, <i>M</i> -Pd-( <i>R,R</i> )-L, <i>M</i> -Pt-( <i>R,R</i> )-L, and [ <i>M</i> -Zn-( <i>R,R</i> )-L] <sub>2</sub> studied in this paper.....	103

5.2	The <i>cis</i> configuration of ( <i>R,R</i> )-H <sub>2</sub> L ligand with axial and equatorial arrangement at cyclohexane. The rotatable N-Chexane bonds are indicated by small arrows. ....	105
5.3	Relative energies of the four most stable conformers of H <sub>2</sub> L obtained at the B3LYP/cc-pVTZ level of theory. ....	105
5.4	Comparison of the experimental VA (left) and VCD (right) spectra of the ( <i>R,R</i> )-H <sub>2</sub> L ligand in DMSO-d <sub>6</sub> with the corresponding single conformer spectra calculated at the B3LYP/cc-pVTZ level of theory in DMSO-d <sub>6</sub> solution.....	106
5.5	Left: half of the H <sub>2</sub> L ligand molecule is highlighted and some relevant atoms are labeled. Right: the assignments of the major vibrational modes observed. ....	107
5.6	Comparison of the experimental UV-Vis (left) and ECD (right) spectra H <sub>2</sub> L in acetonitrile with the corresponding spectra calculated at the B3LYP/cc-pVTZ level of theory in acetonitrile solution.....	108
5.7	The most stable diastereomeric conformer of the mono-nuclear Cu, Ni, Pd and Pt complexes predicted at the DFT/B3LYP/Gen level of theory. Some bond distances (in Å) and angles (in °) are listed.....	110
5.8	Comparison of the experimental VA spectra of the Ni (II), Cu (II), Pd (II), and Pt (II) complexes in DMSO-d <sub>6</sub> with the corresponding calculated spectra (right) at the DFT/B3LYP/Gen level of theory in DMSO-d <sub>6</sub> solution.....	112
5.9	Comparison of the experimental VCD spectra of the Ni (II), Cu (II), Pd (II), and Pt (II) complexes in DMSO-d <sub>6</sub> with the corresponding calculated spectra (right) at the DFT/B3LYP/Gen level of theory in DMSO-d <sub>6</sub> solution.....	113
5.10	The main vibrational modes of the <i>M</i> -Cu-( <i>R,R</i> )-L complex in the region of 1750 - 1200 cm <sup>-1</sup> .....	114
5.11	The HOMO and LUMO molecular orbital (MO) representations of M-Ni-( <i>R,R</i> )-L and M-Cu-( <i>R,R</i> )-L compounds.....	116
5.12	Comparison of the experimental VA (left) and VCD (right) spectra of the Zn (II) complex in DMSO-d <sub>6</sub> with the corresponding spectra of the mono and di-nuclear Zn (II) complex calculated at the B3LYP/Gen level of theory in DMSO-d <sub>6</sub> solution where the LANL2DZ basis set is assigned for the Zn atom and the cc-pVTZ basis set for the other atoms.....	118
5.13	Illustration of M- and P-helicity for the di-nuclear Zn (II) complex.....	119
5.14	Comparison of the experimental VA (left) and VCD (right) spectra of the Zn (II) complex in DMSO-d <sub>6</sub> with the corresponding spectra of the <i>M</i> - and <i>P</i> -[Zn-( <i>R,R</i> )-L] <sub>2</sub> diastereomers	

calculated at the B3LYP/Gen level of theory in DMSO-d <sub>6</sub> solution where LANL2DZ basis set is assigned for Zn atom and the cc-pVTZ basis set for the other atoms.....	120
5.15 Comparison of the experimental UV-Vis (left) and ECD (right) spectra of the Zn (II) complex in acetonitrile with the corresponding spectra of the <i>M</i> - and <i>P</i> -[Zn-( <i>R,R</i> )-L] <sub>2</sub> diastereomers calculated at the B3LYP/Gen level of theory in acetonitrile solution where LANL2DZ basis set is assigned for Zn atom and the cc-pVTZ basis set for the other atoms.....	122
5.16 Definition of the helicity-determining angle $\theta$ . For tetrahedral, $\theta=90^\circ$ , whereas for square planar, $\theta=0^\circ$ . N1 and N2 are atoms of one arm, and N3 and N4 are atoms of the other arm.....	123
6.1 Chemical structure of AXF-155 studied in this paper. There are three chiral axes: one at the binaphthyl ring and two along the C-N bonds. All of the chiral axes are highlighted with shady boxes. Chirality of the binaphthyl ring is <i>R</i> , while the associated chirality at the C-N bonds can be <i>RR</i> , <i>RS</i> , <i>SR</i> or <i>SS</i> . The two large substitutes about the C=N bond take on the trans-arrangement shown here. The pair of the bulky group and the opposite binaphthyl half marked with dotted circles (or with dotted-dashed circles) can be in either extra or intra orientation (see Figure D1 for further details). In addition, the -OH...N=C intramolecular H-bonding interactions are indicated. See text for further details.....	135
6.2 Raw experimental VA (left) and VCD (right) spectra of AXF-155 in deuterated chloroform and THF solvents. The measurements below 1200 cm <sup>-1</sup> in THF are removed due to strong THF solvent absorption.....	136
6.3 Optimized geometries of the HB conformers of AXF-155 in CDCl <sub>3</sub> obtained at the PCM/B3LYP/6-31G(d) level of theory. The geometries are separated into three groups based on their associated axial chirality at the -C-N bonds, i.e. <i>RR</i> , <i>RS</i> , or <i>SS</i> .....	138
6.4 Calculated VA (left) and VCD (right) spectra of all nine HB conformers of AXF-155 molecule obtained at the PCM/B3LYP/6-31G(d) level compared to the experimental data at the bottom. For easy comparison, these conformers are separated into three groups based on the associated axial chirality at the -C-N bonds, i.e. <i>RR</i> , <i>RS</i> , or <i>SS</i> .....	140
6.5 Calculated VA (left) and VCD (right) spectra of all the <i>R_intra</i> / <i>R_extra</i> HB or NHB conformers (top panel) and <i>S_intra</i> / <i>S_extra</i> HB or NHB conformers (bottom panel) of AXF-155 molecule obtained at the PCM/B3LYP/6-31G(d) level compared with the experimental ones.....	142
6.6 Comparison of the experimental VA and VCD spectra of AXF-155 in CDCl <sub>3</sub> with the corresponding simulated spectra of <i>S_intra_HB_S_extra_HB</i> obtained at the PCM/B3LYP/6-31G(d) level of theory. The theoretical VCD band intensities in a small region between 1450	

$\text{cm}^{-1}$  to  $1330 \text{ cm}^{-1}$  are amplified by a factor of 2 and indicated with dotted line for easier pattern recognition. The Arabic numerals are used to indicate the corresponding features in the experimental and theoretical data in the crowded region below  $1450 \text{ cm}^{-1}$ .....143

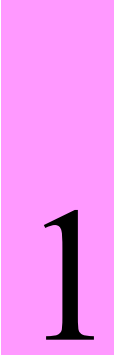
6.7 Comparison of the experimental ECD spectrum in  $\text{CDCl}_3$  (black dotted line) with the theoretical ECD spectra of R\_intra//R\_extra (upper row) and S\_intra//S\_extra (lower row) HB (red dashed-dotted line) and NHB (green solid line) conformers obtained at the PCM/B3LYP/6-31G(d) level of theory.....145

6.8 Comparison of the experimental ORD spectrum in  $\text{CDCl}_3$  with the theoretical ORD spectra of R\_intra//R\_extra HB and NHB conformers as well as S\_intra//S\_extra HB and NHB conformers obtained at the PCM/B3LYP/6-31G(d) level of theory.....146

## List of Figures [Appendices]

Figure	Page
A1. Experimental VCD spectra of the two enantiomers of the three compounds studied, i.e. 1, 2, and 3 from top to bottom. $\text{CDCl}_3$ is the solvent used in all cases. The optimized pathlength is 0.1 mm for all compounds in the $1700\text{-}970\text{ cm}^{-1}$ region, except for the enantiomeric pairs of (SS,3) where the experiment has been done with a shorter pathlength of 0.025 mm. The inserted spectra were recorded with 0.1 mm pathlength.....	175
A2. Comparison of the experimental VA and VCD spectra with the corresponding spectra of the six most stable conformers of (SS, 1) at the PCM/B3PW91/cc-pVTZ level.....	175
A3. Comparison of experimental VA spectrum with the corresponding spectra of the ten most stable conformers of (SS, 2) at the PCM/B3PW91/cc-pVTZ level.....	176
A4. Comparison of the experimental VCD spectrum with the corresponding spectra of the ten most stable conformers of (SS, 2) at the PCM/B3PW91/cc-pVTZ level.....	177
A5. Comparison of the experimental VA and VCD spectra with the corresponding spectra of the [Trans-Cis]equ conformer of (SS, 1) calculated with several different combinations of functional and basis sets. Implicit solvation model was applied using PCM of $\text{CDCl}_3$ as solvent.....	180
B1. The experimental VCD spectra of both R and S enantiomers BINAP, TOLBINAP and $\text{Pd}(\text{TOLBINAP})\text{Cl}_2$ in $\text{CDCl}_3$ solution and their related noise levels. In all the VCD spectra shown, the corresponding $\text{CDCl}_3$ spectrum obtained under identical experimental conditions was subtracted off. As one can see, good mirror images have been obtained for all the VCD spectral features measured except a few broad features at the very low wavenumber region. This is likely due to the strong absorption by the solvent starting at about $970\text{ cm}^{-1}$ .....	182
B2. The calculated gas phase VA and VCD spectra of the three conformers of BINAP (top) and of the three conformers of TOLBINAP (bottom) and their corresponding population weighted spectra based on the relative energies and the relative free energies at the B3LYP/6-31G(d,p) level.....	183
B3. Comparison of the calculated gas phased VA and VCD spectra of 1,1'-binaphthyl, BINAP, and TOLBINAP at B3LYP/6-31G(d,p) level. The VA intensity of 1,1'-binaphthyl was amplified by a factor of two for easy comparison. The intense band in the $1430\text{-}1460\text{ cm}^{-1}$ region in BINAP and TOLBINAP corresponds to the C-C stretching and C-H bending vibrational modes of four phenyl rings bonded to phosphorous, which does not show up for 1,1'-binaphthyl. The bands at $1250\text{ cm}^{-1}$ corresponds to the same vibrational modes in all	

three systems. The related bisignated VCD feature flip going from 1,1'-binaphthyl to BINAP and TOLBINAP. The intense bands at $\sim 1500\text{ cm}^{-1}$ correspond to the C=C stretching vibrational motions of phenyl rings and naphthalene rings.....	184
B4. The calculated VA and VCD spectra with PCM of chloroform of the three conformers of BINAP (top) and of the three conformers of TOLBINAP (bottom) and their corresponding population weighted spectra based on the relative energies and the relative free energies at the B3LYP/6-31G(d,p) level.....	185
C1. The simulated UV (left) and ECD (right) spectra of H <sub>2</sub> L ligand with water, both in crystal and optimized structures, and optimized ligand without water molecule considered.....	177
C2. Electron configuration and orbital overlapping illustrations of Ni (II) and Cu (II) complexes. The hybridized orbital is used for the $\sigma$ bond formation (shown in red) while the unhybridized p-orbital employed for the $\pi$ bond formation (shown in blue).....	188
C3. Illustration of symmetric and anti-symmetric –C=N stretching vibrational modes for [M-Zn-(R,R)-L] <sub>2</sub> complex.....	189
C4. Comparison of the theoretical VA spectra of the <i>mono</i> - and <i>di</i> -nuclear Zn (II) complexes. The main peak assignments are also provided.....	190
C5. Comparison of the experimental and theoretical UV-Vis and ECD spectra of all five metal complexes. The experimental ones are shown in dashed and dotted lines whereas the theoretical spectra are highlighted with solid color.....	191
D1. Illustrations of naming schemes used for R and S for axial chirality around the –C-N bond and for the intra and extra labels for the relative position of the bulky group (in red dashed circle) with respect to the binaphthyl half (in green circle) which is not directly connected to it. Place the binaphthyl ring under consideration closer to the viewer and view the chiral axis –C-N end-on. Align the blue arrow from the bulky group to the –O-H group up. Look at $\theta$ at the right side of the blue line from the blue arrow to the green line. The green arrow is used to aim the identification of intra and extra labels.....	193
D2. Illustration of the different cavity sizes provided by S-intra-HB//S-extra-HB (R-SS), and R-intra-HB//R-extra-HB for solvent molecules. This may influence their stabilities in highly concentrated and highly diluted solutions.....	194



# 1

## Introduction



In this thesis, a number of chiral molecular systems which include some organic ligands and transition metal complexes have been chosen and studied. Their structural properties and conformational distributions in solution have been investigated by using chiroptical spectroscopy, mainly vibrational circular dichroism (VCD) and electronic CD (ECD) spectroscopic techniques, complemented with *ab initio* quantum chemical calculations. In the following, I will first provide some background information on the molecular chirality. Second, a number of common chiroptical experimental techniques will be described with an emphasis on the VCD experimental set-up. Then I will discuss the theoretical basis of both VCD and ECD spectroscopic techniques and the related calculations. Finally, the objectives and scope of the current thesis will be presented.

## 1.1. Molecular Chirality

---

The term *chirality* or handedness comes from the Greek word for hand, *kheir*. Therefore, the straightforward examples of chiral species are human hands or feet. Chiral molecules exist in two mirror-inverted configurations which cannot be superimposed onto each other. Such two possible configurations are called a pair of *enantiomers*. A pair of *enantiomers* share all the same physical properties, as they only differ in spatial configuration of the atoms but not inter-atomic connectivity. It is this difference in spatial ordering that results in the *enantiomer* pairs to interact differently with a chiral species or a chiral environment. For example, a pair of *enantiomers* interact differently with a circularly polarized electromagnetic radiation to generate a pair of mirror-imaged chiroptical spectra. The structural elements directly associated with the molecular chirality are the chiral (or stereogenic) centers, axes, or helices. Therefore, a molecule may have “*handedness*” if one of these structural elements is present. For example, when a carbon atom is bonded to four different substituents, it becomes a stereogenic center. The mirror image of this

molecule is not superposable onto itself. Depending on the spatial arrangements, one *enantiomer* is called right-handed whereas the opposite one is named left-handed.

The absolute configuration of a chiral molecule is labelled using the standard nomenclature. If a chiral species possesses several stereogenic centers, its absolute configurations at each stereogenic center is labeled according to the Cahn-Ingold-Prelog (CIP) priority rules and the precise spatial arrangements of the substituents at the specific stereogenic centers [1]. Based on the CIP rules, an atom with the higher atomic number takes higher priority. Also, if the first atoms of two or more groups attached to the stereogenic center are the same, then the second atom in each group is considered, following the same rules as for the first atom and so on. For example, the  $-\text{OCH}_3$  moiety takes higher priority than the  $-\text{OH}$  group. Depending on the spatial arrangement around the stereogenic centers, the R and S labels are assigned to the right- and left-handed stereogenic centers, respectively. The same R and S labels are used for the axially-chiral species (See Figure 1.1), although the assignment of the axial chirality follows a different strategy. Lastly, the P and M helical chirality labels are given to the clock-wise and counter-clockwise spatial arrangements, respectively. Figure 1.1 illustrates the general principles of naming strategies for the three types of molecular chirality discussed.

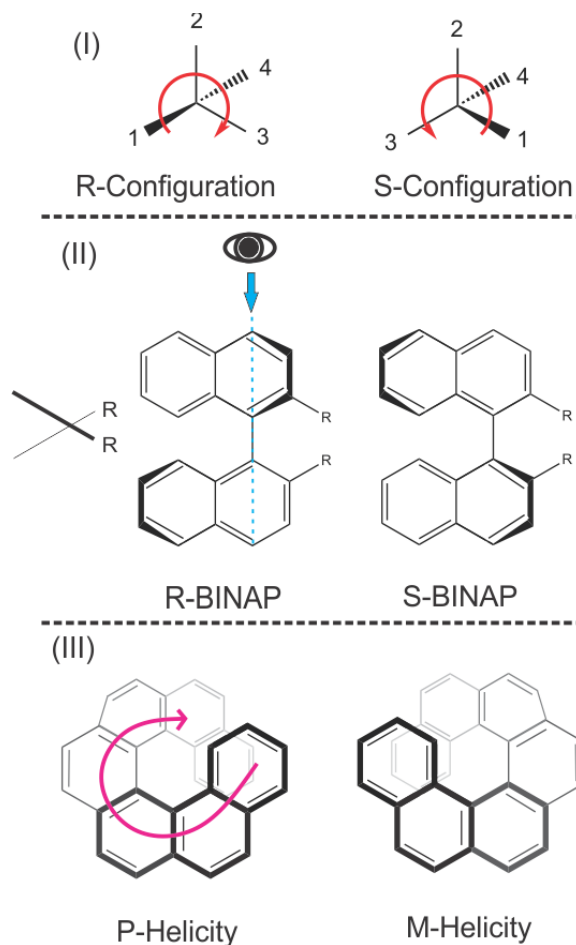


**Figure 1.1.** Molecular chirality: (I) stereogenic center where 1, 2, 3, and 4 denote the priority of the substituents, (II) axial chirality, and (III) helical chirality.

Since my thesis deals mainly with organic ligands and transition metal complexes, some specific terminologies related to their chirality are included below. In the area of coordination chemistry, chirality is further characterized by how the ligands are arranged around one, or several metal centers. For example, Figure 1.2 shows two stereoisomers (optical isomerism) of the tris(ethylenediamine)cobalt(III) molecule. These stereoisomers are obtained as a result of the coordination of the cobalt ion with three bi-dentate ligands, producing a left-handed propeller twist

(Lambda  $\Lambda$ ) and a right-handed propeller twist (Delta  $\Delta$ ). These stereoisomers are optically active, *i.e.*, they can rotate the plane of polarized light with the same magnitude but in the opposite directions, and are not superposable onto their mirror images. Generally, the coordination complexes with the following point groups show optical activity:  $C_1$ ,  $C_n$ ,  $D_n$ , T, O, and I. The geometrical structures belong to these point groups do not possess the symmetry elements of the second kind, *i.e.*, a mirror plane,  $\sigma = S_1$ , a center of inversion,  $i = S_2$ , and a rotation reflection axis,  $S_{2n}$ . [2]

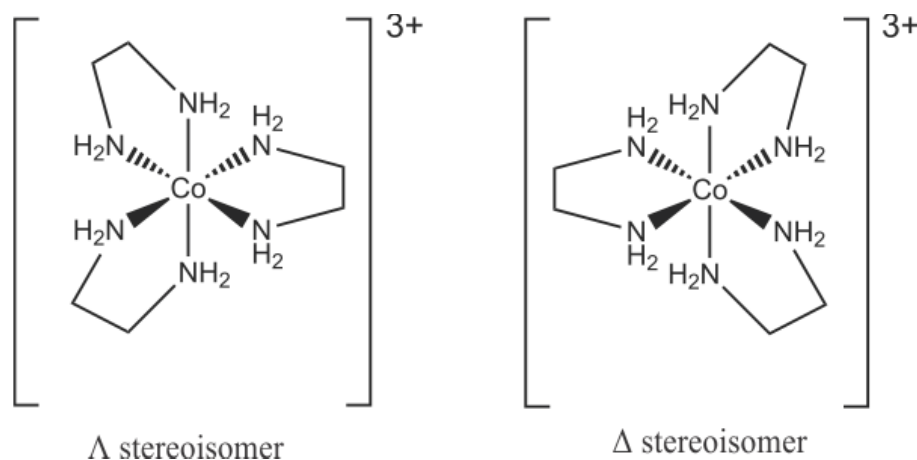


**Figure 1.2.** The representation of the lambda ( $\Lambda$ ) and the delta ( $\Delta$ ) stereoisomers of tris(ethylenediamine)cobalt(III).

Another aspect of my thesis revolves around the conformational landscapes and absolute configuration determinations of several organic and inorganic complexes possessing axial chirality. Axial chirality arises from the presence of the dissymmetric chiral planes that cannot

rotate along each other freely (see Figure 1.1). The two most-known examples in this regard are the allene and binaphthyl derivatives.

Chiroptical spectroscopic techniques, which are in principle based on the interaction of the polarized light with a chiral medium, are well-suited experimental tools to investigate the chirality at the molecular level. These techniques allow one to explore the structural properties of the chiral species by comparing the experimentally observed and theoretically simulated optical responses. Currently, the most frequently-used chiroptical techniques are optical rotatory dispersion (ORD), ECD, VCD, and Raman optical activity (ROA). The following section describes some of these techniques that have been used for my thesis research in more detail.

## **1.2. Experimental**

---

### *1.2.1. Chiroptical spectroscopy*

For my thesis research, I have utilized several chiroptical spectroscopic techniques including VCD, ECD, and ORD techniques. As outlined in Section 1.1., an *enantiomer* interacts differently with the right and left circularly polarized light. The following discussion highlights important experimental details of these measurements and the information they provide.

### *1.2.2. Optical rotatory dispersion experiments*

The main difference between a pair of *enantiomers* is how they rotate plane-polarized light with the same magnitude but in the opposite directions. Therefore, a solution of equally-mixed *enantiomers*, i.e., a *racemic* mixture, will give rise to zero optical rotation. Figure 1.3 illustrates the measurements of the optical rotation for a pair of *enantiomers* and the corresponding *racemic* mixture. The direction and the magnitude of the angle of rotation are characteristics of a specific chiral medium if the dependence of magnitude on the path-length in which the light transverses in

the medium and the sample concentration has been accounted for. This phenomenon was first observed by *Arago* in 1811 using an  $\alpha$ -quartz crystal. A few years later, *Biot* measured the optical rotation of some simple chiral organic liquids [3].

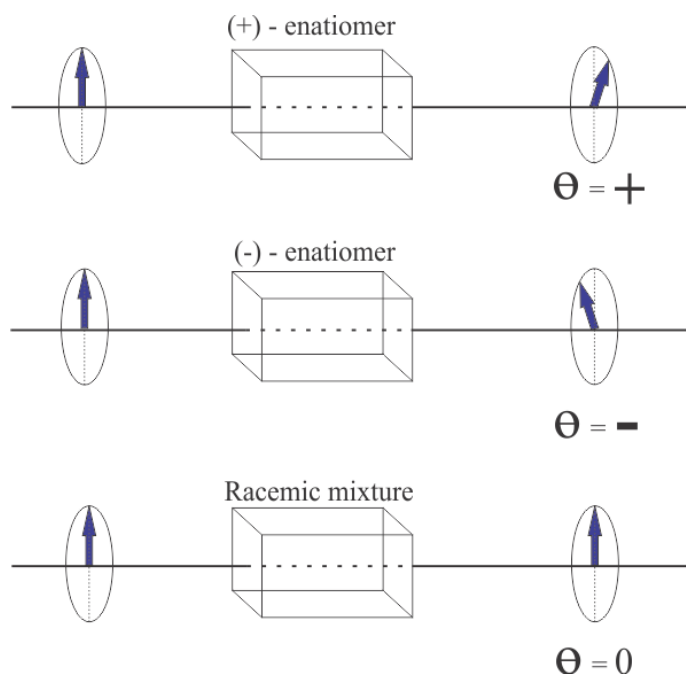


**Figure 1.3.** A general schematic of optical rotation measurements of a pair of *enantiomers* and their *racemic* mixture.

As plane polarized light passes through a chiral medium, the plane of polarization is being rotated. Plane polarized light can be viewed as the superposition of the left and right circularly polarized light, *LCP* and *RCP*, respectively. Since the *LCP* and *RCP* components experience different refractive indices, (*i.e.*,  $n_{LCP} \neq n_{RCP}$ ), in a chiral medium, they acquire a relative phase difference after passing through the medium. The recombination of these two components after leaving the chiral medium, gives rise to a plane polarized light with a relative phase difference with respect to the entering plane polarized light. If the medium also absorbs light, then the transmitted light

becomes elliptically polarized because the *LCP* and *RCP* components have different absorption coefficients and propagation velocities.

Optical rotation is the difference of the refractive indices of *LCP* and *RCP* components of the plane polarized light, i.e.  $\Delta n = n_{LCP} - n_{RCP}$ . Generally, the refractive index depends on the wavelength ( $\lambda$ ) and the variation in optical rotation with the wavelength of the light is called optical rotatory dispersion (ORD) and is characteristic of the chiral medium. Such measurements are typically done with a commercial polarimeter that measures the optical rotation at different wavelengths. Figure 1.4 shows a generic illustration of a polarimeter. During an ORD measurement, unpolarized light (e.g., the sodium D line at 589 nm) passes through a linear polarizer to generate plane polarized light. This plane-polarized light passes through the chiral medium and its polarization direction changes as a result of its interaction with the medium. A polarization analyzer allows comparison with the incoming polarized light source, and the angle of rotation can be determined.

Although this technique is straightforward, currently its application in the determination of the chirality and other structural properties of chiral samples is very limited. One reason is that the experimental ORD values are strongly influenced by the solvent used. More importantly, accurate theoretical modeling for ORD is yet to be achieved.[4] Even for some simple chiral molecules such as propylene oxide, it is still challenging to achieve theoretical predictions with the correct sign and magnitude that agree with the experimental data.

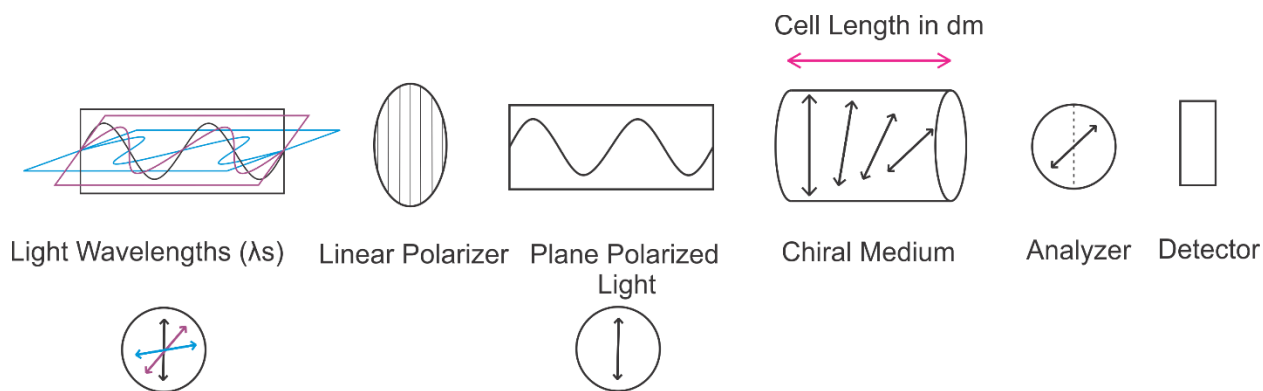


**Figure 1.4.** A schematic diagram of a polarimeter.

### 1.2.3. Electronic and vibrational circular dichroism experiments

Circular dichroism measures the difference between the extinction coefficients of the *LCP* and *RCP* lights, i.e.,  $\Delta\epsilon = \epsilon_{LCP} - \epsilon_{RCP}$ , accompanying an electronic or a vibrational transition. The sign of a CD band can be positive or negative and is determined by the structural properties including the chirality of the targeted compound, thus bringing about more structural information compared to the parent UV-Vis or IR spectroscopy. If a CD band is obtained as a result of electronic transitions in the UV-Vis spectral region, then it is called *electronic CD*; and if it is due to the vibrational absorption in the infrared region, then it is termed *vibrational CD*. While UV-Vis and IR spectra can be generally expected for any molecule, only chiral molecules exhibit mirror-imaged ECD and VCD spectra for a pair of *enantiomers*. In contrast to chiroptical spectroscopy, the standard IR and UV-Vis spectroscopic techniques are insensitive to the chirality information, i.e. IR and UV-Vis spectra for a pair of *enantiomers* are identical. The relative magnitude of an ECD band to that of its parent UV-Vis band is typically about  $10^{-2} \sim 10^{-3}$ , while this ratio is even smaller for the VCD and is in the range of  $10^{-4} \sim 10^{-6}$ .



Solution IR spectra in the finger print region generally provide numerous well-resolved bands, in contrast to the corresponding UV-Vis spectroscopy. VCD spectra, in general, tend to be even better resolved than its parent IR spectra because of the positive and negative signs. As a result, the VCD spectra can provide detailed insights into the chirality and the structures of the systems of interest. Because of the similarities between ECD and VCD techniques, I will only describe the VCD technique in more details.

Historically, VCD phenomenon was first observed by *Holzwarth et al.* in 1974 [5] for the measurement of a vibrational mode of a neat liquid of 2,2,2-trifluoromethyl-1-phenylethanol. This was confirmed by *Nafie et al.* in 1975-1976 for the same sample. The latter authors also expanded the measurement to the other vibrational modes of the sample [6,7]. All these early experiments were carried out with a dispersive infrared spectrometer. The first Fourier transform VCD (FT-VCD) measurement was reported by *Nafie et al.* in 1978 in the mid-IR region for the C-H stretching modes of camphor [8,9].

All vibrational absorption (VA) and VCD measurements in my thesis were carried out with a FTIR-VCD instrument consisting of a FTIR spectrometer (Vertex 70, Bruker) and a VCD module (PMA 50, Bruker). Figure 1.5 shows a schematic diagram of the FTIR-VCD instrument.

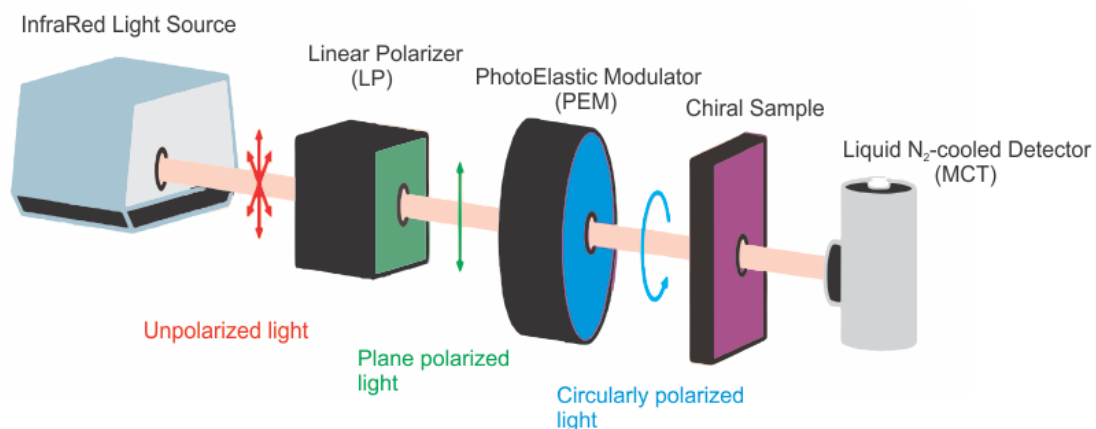


**Figure 1.5.** A schematic diagram of the FTIR-VCD instrument used in my thesis research.

The un-polarized broadband IR light, e.g. Globar (silicon carbide), from the FTIR spectrometer is directed to the VCD compartment by using several steering mirrors. The heart of the FTIR spectrometer is a Michelson interferometer (Figure 1.6). A collimating mirror is positioned right after the light source to produce parallel rays which are transmitted to a beam-splitter at the center of the interferometer. At this stage, some of the light is transmitted to a fixed mirror while the others are reflected to a moving mirror. Thereafter, the light is reflected back from both mirrors and recombined at the beam-splitter. Depending on whether the two beams are in-phase or out-of-phase, the constructive or destructive interferences occur, respectively. The recombined rays then proceed through the sample and finally are collected by a detector that measures the IR spectrum.

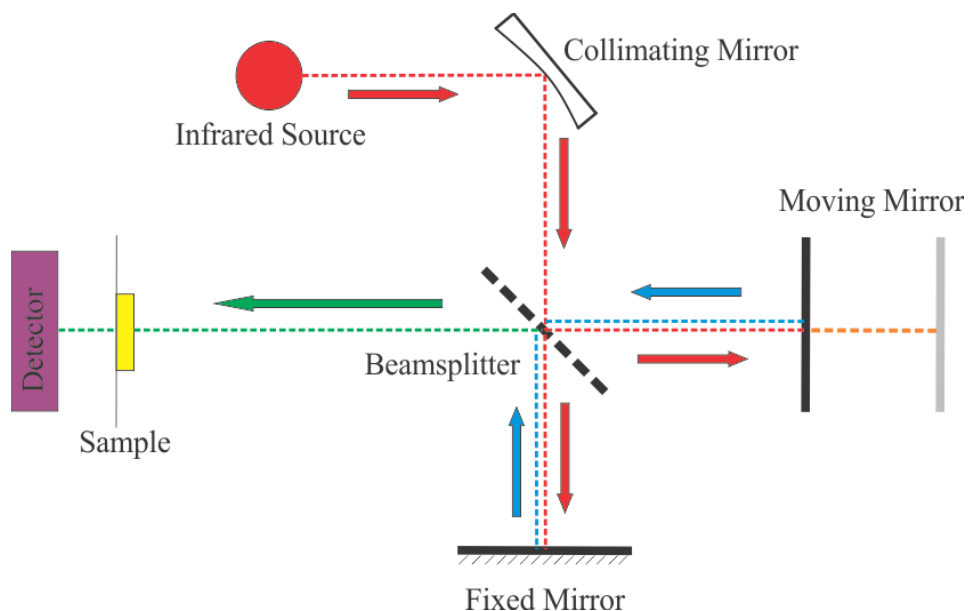


**Figure 1.6.** A schematic diagram of a Michelson interferometer.

For the VCD measurements, the recombined rays are directed to a wire grid linear polarizer to convert the randomly polarized light into the linearly polarized light. The photo-elastic modulator

(PEM), which is commonly made of ZnSe, is placed right after to convert the linearly polarized light to the left and right circularly polarized lights. The PEM consists of a piezoelectric transducer material, which is fused to a transparent bar of silica, and its modulator axis is aligned at 45 degree with respect to the incoming linearly polarized light. This piece of optics is responsible for producing the *LCP* and *RCP* light at a modulation frequency of 50 kHz. The linear polarized light is composed of two orthogonal components; one parallel and the other perpendicular to the axis of the PEM. The transducer material stretches or compresses when the modulated current at 50 kHz is applied, as a result of changing the birefringence of the material. Consequently, the propagation velocities of the parallel and perpendicular components of light are different. On the compress cycle, the perpendicular component of light is being retarded and the parallel component is left unaffected. When the optical device stretches, the parallel component is retarded while the perpendicular one stays unaffected. As a result, a phase difference of 90 degrees between these two components is generated as the light emerges out from the PEM and upon the recombination of two components the right or left circularly polarized lights at a modulation frequency of 50 kHz are produced. The resulting circularly polarized light then hits the chiral sample and the transmitted lights are captured by means of a liquid N<sub>2</sub> cooled detector, in this case a MCT infrared detector. The double-modulation is needed since the VCD signal is inherently small,  $\sim 10^{-4}$  to  $10^{-6}$  of the parent IR signal. Typically, signals from the MCT detector are filtered by using a low pass filter to obtain the dc signal and are converted to the IR signals by means of the electronics and computer software. Similarly, in case of VCD signal acquisition, the signals from the MCT detector are first filtered by using a high pass filter to attenuate the modulation due to the interferometer. These signals are then sent to a Stanford research systems lock-in amplifier (LIA) which is referenced to the PEM modulation frequency of 50 kHz to produce the demodulated ac signal. Eventually, the

VCD spectrum is generated by taking the ratio of the FT spectrum of the ac signal to the associated dc signal.

For the VCD measurements, the concentration and the path-length of the sample should be adjusted so that the absorption intensity of the IR bands of the interest falls in the range of 0.2 – 0.9. The optimization of the concentration and the path-length of the samples are two key factors to obtain the good-quality VCD signals. Typically, to get a reliable VCD spectrum, i.e. with adequate signal-to-noise ratio, the samples typically need to be highly soluble, usually in the range of 20 ~ 100 mg/ml. This requirement is a noticeable disadvantage of VCD spectroscopy.

Although the commercialization of the FT-VCD spectrometers happened gradually, VCD spectroscopy has experienced drastic advances in its applications in the recent years to a wide variety of chiral organic, biological, inorganic, and nano systems. This is due in part to the significant advances made in the theoretical VCD predictions in the recent years. The following section aims at describing the theory of VCD spectroscopy.

### **1.3. Theoretical**

---

#### *1.3.1 Basics of the VCD spectroscopy and spectral calculations*

VCD is the differential absorbance of the left versus right circularly polarized lights by a chiral sample accompanying a vibrational transition:  $\Delta A = A_L - A_R$ . For an infrared transition, the intensity is proportional to the quantity called dipole strength and can be expressed by using the following equation:

$$D_{0a} = | \langle \Psi_0 | \vec{\mu} | \Psi_a \rangle |^2 \quad (1)$$

where  $\Psi_0$  and  $\Psi_a$  are the wavefunctions for the ground and excited states, respectively, and  $\bar{\mu}$  is the electric dipole operator. Here, the term inside  $| \cdot |$  is called the electric dipole transition moment or EDTM.

The intensity and the sign of a VCD band depend on the following quantity called rotational strength. It is defined as the imaginary part of the scalar product of the EDTM and the magnetic dipole transition moment, MDTM, respectively:

$$R_{0a} = Im \{ \langle \Psi_0 | \bar{\mu} | \Psi_a \rangle \cdot \langle \Psi_a | \bar{m} | \Psi_0 \rangle \} \quad (2)$$

where most terms are defined in the same way as in equation (1) and  $\bar{m}$  is the magnetic dipole operator.  $R_{0a}$  can also be rewritten as  $|\mu| \cdot |m| \cdot \cos\theta$ , where  $|\mu|$  and  $|m|$  are the magnitudes of the EDTM and MDTM vectors, respectively, and  $\theta$  is the angle between these two vectors. If  $0^\circ < \theta < 90^\circ$  and  $270^\circ < \theta < 360^\circ$ , then  $\cos\theta$  is positive and therefore the VCD band will have a positive sign, if  $90^\circ < \theta < 270^\circ$ , then  $\cos\theta$  is negative and therefore the corresponding VCD band will have a negative sign. If  $\theta$  is exactly  $90^\circ$  or  $270^\circ$ , then  $\cos\theta = 0$  and therefore the related VCD band will show zero intensity.

For the theoretical VCD intensity and sign calculations, one needs to take into account the contributions from both EDTM and MDTM. While the theoretical treatment of EDTM had long been developed and implemented into many software packages capable of calculating the electronic structure, such as Gaussian, the suitable theoretical treatment of MDTM was only developed more recently. A number of theoretical models were proposed from the early stage of the theoretical VCD developments, such as localized molecular orbital [10] and vibronic coupling models. [11] Unfortunately, their computational implementations were so difficult and these models have not seen wide applications. In these early models, it was found that the electronic

contribution to the vibrational MDTM vanishes upon the application of Born-Oppenheimer (BO) approximation. [12] This issue was overcome by Buckingham [13] and Stephens [14] when they proposed magnetic field perturbation (MFP) theory. In the MFP model, this issue was resolved by considering the first derivatives of the ground state wave-function with respect to the nuclear displacements and the applied magnetic field so that the MDTM can be evaluated precisely. The theoretical VCD calculations based on the MFP model have been implemented in most electronic packages such as Gaussian, Dalton [15], GAMESS [16], and others.

One prerequisite to obtain high quality VCD predictions is to make accurate predictions for the all possible conformations of the targeted molecules. It is now generally well-accepted that the DFT method provides more accurate results than the HF method with similar computational cost. The applications of more accurate approximations such as Moller-Plesset (MP) perturbation theory, coupled-cluster (CC), and configuration interaction (CI) are not feasible for most large chiral systems, such as chiral transition metal complexes, due to the high computational demands and their own restrictions on the size of molecular systems. For DFT calculations, a large number of functionals and basis sets have been developed to date. The development of different functionals has passed through a number of stages, beginning with the “local”, and then “non-local” functionals and culminating with a class of functionals referred to as “hybrid” functionals. [17, 18] At the present time, hybrid functionals are well-known as the most accurate functionals for the calculations of a wide variety of molecular properties. The earliest hybrid functional is B3PW91 and one of the most popular and commonly used hybrid functionals is B3LYP. [19]

The next step is the choice of basis set. Generally, the accuracy of the calculations relies on the size of the basis set chosen. A choice of larger basis set generally means a better agreement with the experimental data, but at the same time it requires considerably more computational effort.

[20] For the chiroptical calculations, the 6-31G(d) basis set is considered as the minimal basis set which offers a reasonable compromise between the accuracy and the computational time. Inclusion of the polarization functions, especially for those systems which are involved in hydrogen-bonding (HB) interactions, is quite essential. Basically, the polarization functions are considered as auxiliary functions with one additional node. For example, in the minimal basis set of the H atom, there is only one basis function which approximates the 1s atomic orbital. Addition of a polarization function, for example a p-type function, to the 1s function, in principle, adds more flexibility to the basis set. This allows an asymmetrical spatial arrangement of the molecular orbital contains the H atom to be involved in non-covalent bonding interactions more effectively. On the other hand, for rigid molecular systems, like the Pd-complex studied in Chapter 4 of this thesis, it was noticed that the addition of polarization and diffuse functions did not significantly improve the spectral appearance except making the calculations unnecessarily demanding.

For the purpose of this thesis, all geometrical searches, optimization, harmonic frequencies, and VA and VCD intensity and sign calculations were performed using the Gaussian 03 [21] and Gaussian 09 [22] suite of programs with the implementation of DFT methods. [23] The well-known B3LYP and B3PW91 hybrid functional were mainly used for the calculations. A number of different basis sets which include both Pople and Dunning types were employed to carry out all the aforementioned calculations. In case of the metal-ligand complexes, different basis sets such as cc-pVTZ [24] were used for the C, N, and H atoms whereas the LanL2DZ basis set was chosen for all transition metals, such as Ni (II), Cu (II), Pd (II), Pt (II), and Zn (II).

In addition, to account for the bulk of solvent environment, the integral equation formalism (IEF) version of the polarization continuum model (PCM) [25] using the universal force field (UFF)

radii was used. For example, the value of  $\epsilon = 46.826$  was used where DMSO was employed as a solvent.

### *1.3.2 Basics of ECD spectroscopy and spectral calculations*

While all geometrical searches and optimization processes are the same as described above, one needs to employ time-dependent DFT (TD-DFT) method to predict the UV-Vis intensity and to simulate the corresponding ECD optical response. At the present time, the accuracy of the excited state calculations is limited and good agreements with the experimental data have only been achieved for relatively small molecular systems. The situation becomes even more challenging when a transition metal complex is the target of the TD-DFT study. Although the applications of ECD spectroscopy to the determination of structural properties such as absolute configuration and conformational distribution have increased noticeably in recent years, [26] ECD predictions still suffer substantially from the considerable dependency on the choice of basis set and functional. [27] Due to the fact that DFT functionals are normally tuned for the molecular systems where light atoms such as carbon, hydrogen, nitrogen, oxygen are involved, the simulations of the ECD spectra of the systems containing d-shell angular momentum and higher are still quite burdensome. Other prominent issues arise from the weak nature of d-d transitions in the coordination metal complexes and the inadequacy of the computational methodologies in describing such transitions.

### *1.3.3. Solvent effects*

Despite the significant progress in the field of VCD spectroscopy, the conformational analysis can be still complicated due to the prominent solvent effects, either through the induction of self-aggregation of solute molecules or the solute-solvent intermolecular hydrogen bonding (HB) interactions. It has also been shown that VCD, ECD and ORD spectra of the same molecule in



different solvents may appear quite different. [28,29,30] The solute-solvent interactions may change the chiral species itself or the dominant conformations of a chiral species in solution, i.e. the Boltzmann factors of different conformers. [31,32,33]

Presently, there are three main computational approaches to account for the effects of solvent: the polarizable continuum model (PCM) [34] or implicit solvation, explicit solvation, and the explicit-implicit combinational approach. In the implicit solvation model, the electrostatic interactions on a solute from a solvent are treated with the use of dielectric continuum models. These models benefit from formulating the dielectric continuum response to represent the response of a statistically averaged solvent system which also require defining a cavity. A cavity can be specified with a size and a shape that excludes solvent and into which the solute can be inserted. This method has been widely used for the relatively non-polar solvents where there are no significant hydrogen bonding interactions expected with the solute molecules. Even though the general geometry of a conformer of a chiral molecule often remains roughly the same with the consideration of the dielectric solvent compared to the isolated system, such a solvent environment may still affect the appearance of chiroptical spectra, especially the VCD spectra. This can either result in changing the relative stability among different conformers or causing some subtle changes in the geometry of the molecular system.

Solvent effects can also be included in the calculation by the explicit approach as well as the combination of the implicit and explicit approaches, mainly when the solvent is polar and has acidic hydrogen atoms. In case of water, the absorption IR bands become very broad and HB interactions between solute and water must be considered explicitly. Our group has proposed the “clusters in a liquid model” where the explicit HB clusters are placed in an implicit bulk of solvent environment to efficiently account for both explicit and implicit solvent effects. [35] Molecular

dynamics simulations have also been employed for this purpose, although in such cases, a huge number of snap shots have to be sampled in order to achieve convergence for chiroptical responses. [36]

#### **1.4. Objectives and Scope of This Thesis**

---

The knowledge of the absolute configuration of a chiral sample is of significant importance in any research area where chirality plays an important role, such as in stereoselective syntheses and in pharmaceutical industry. While X-ray crystallography has been the method for obtaining the absolute configuration of chiral samples for many decades, in many cases, it can be difficult or sometimes even impossible to obtain a single crystal of the targeted substance with sufficient quality for the X-ray structural analyses. Both ECD and VCD measurements contain specific information about chirality of the compound. With the significant advances in both experimental and theoretical aspects of ECD and VCD spectroscopy, these two chiroptical techniques are being used more and more to derive the absolute configuration of the chiral substances in solution directly in the last ten years. [37] Indeed, the absolute configurations of more than 1000 chiral molecules have been determined by chiroptical spectroscopies. [38]

As pointed out in the theoretical section, the general methodology for the determination of the absolute configuration is based on the comparison of the solution experimental VCD and/or ECD spectra of a chiral molecule with the simulated spectra obtained through the application of *ab initio* quantum chemical calculations. Therefore the absolute configuration analyses automatically require the related conformational analyses. While the NMR spectroscopy has been utilized for the conformational analyses in solution, such applications are limited to the populations exchanging slower than the NMR timescale (microseconds). For the optical spectra in the IR and UV-Vis regions, one can simply treat the final spectrum as a linear superposition of the individual

conformers' spectra weighted with their respective abundances, i.e., their Boltzmann factors. With a large number (typically ten or more) of fundamental bands in the finger print region, the sensitivity of IR and especially VCD spectra to the different conformers is sufficiently high to allow clear identifications of the dominant conformational species.

In my PhD research, I have focused on characterizing the structural properties of a particular subset of chiral ligands and their transition metal complexes by using mainly VCD and ECD spectroscopic tools as well as ORD spectroscopy. One group of these ligands includes multidentate nitrogen donor ligands such as (N,N'-bis(pyridine-2-ylmethylene)-(S,S)-1,2-cyclohexanediamine, (N,N'-bis(pyridine-2-ylmethyl)-(S,S)-1,2-cyclohexanediamine, and {(S,S)-2-[(2-pyridinylcarbonyl) amino] cyclohexyl}-2-pyridinecarboxamide depicted in Figure 1.7. Another group of chiral molecules consists of several axially chiral systems, such as BINAP (2,2' -diphenylphosphino-1,1' -binaphthyl) and its derivative TOLBINAP, as well as a recently synthesized triply axial chiral binaphthyl fluorene based salen ligand, named AXF-155, {[2,20-(1E,10E)-(R)-1,10-binaphthyl-2,20-diylbis(azan-1-yl-1-ylidene)bis(methan-1-yl-1-ylidene)bis-(4-((7-(diphenylamino)-9,9-dihexyl-9H-fluoren-2-yl)ethynyl)-phenol)]}. In contrast to the more commonly known stereogenic center where a carbon atom is bonded to four different substituents, the axial chirality arises from the presence of the dissymmetric chiral planes which cannot rotate against each other freely. Finally, the third group of chiral systems studied includes a series of transition metal complexes consist of Ni, Pd, Pt, Cu, and Zn with chiral Pyrrol-2-yl Schiff base ligands and of Pd with BINAP and TOLBINAP ligands.

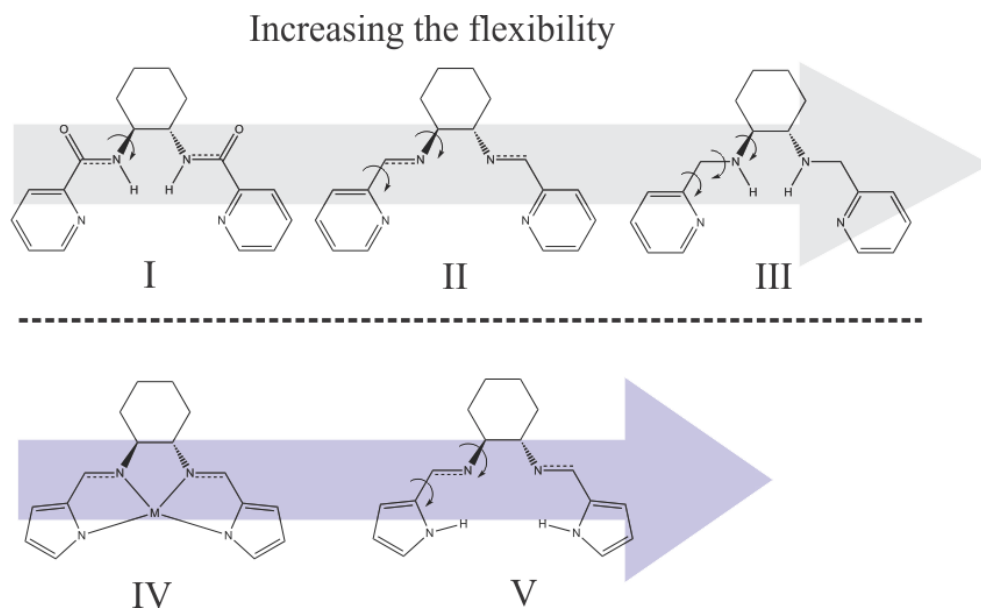


**Figure 1.7.** Increasing the structural flexibility due to increasing rotational degrees of freedom along single bonds for three ligands, I, II and III reported in Chapter 2, and IV and V studied in Chapter 5.

Besides the advantage of using a solution sample directly for the absolute configuration determination, ECD and especially VCD spectroscopic techniques also offer additional advantages of identifying the dominant species in solution, providing solution conformational distributions, monitoring the effects of solvent and concentrations, and capturing chirality transfer phenomena from chiral ligand to the metal center through coordination bonds. These are several primary aspects of my thesis research which will be discussed in detail in this thesis.

Furthermore, in the coordination chemistry and supramolecular chemistry, it is a common practice to assign the absolute configurations and structural properties based on X-ray structure. Then solution ECD spectra are further interpreted based on the X-ray chirality assignment. In the recent years, a few reports surface where this practice may not be valid. For one, a single X-ray structure obtained may not represent a fair sampling of the structure rather a particular crystal chosen.

Second, there may be considerable changes in the structure going from the solid state to solution phase because the solid state structures are strongly influenced by intermolecular contacts and lattice forces. These aspects emphasize the intrinsic differences between the solution and solid state structures. UV-Vis and ECD spectra observed may not be sensitive to all these structural differences including the chirality of the ligand and the helicity of the complexes. For example, in Chapter 5, one can see clearly that the ECD spectra of the *M*- and *P*-helicity Zn (II) complex with the same (*R,R*) ligand are essentially mirror-images to each other. With the typical broad ECD spectral width, one can therefore not tell apart *M*-(*R,R*) from *M*-(*S,S*) or *P*-(*R,R*) from *P*-(*S,S*). Theoretical modeling of UV-Vis and ECD spectra in solution has experienced significant advances in the recent years, although their ability to capture experimental data still leaves much to be desired. There are very few solid state ECD calculations reported due to the significant challenges in capturing all inter- and intra-molecular interactions in the solid state. In this thesis research, we pursue the opportunity to verify the potential structural differences from the solid to solution phases where a clear identification of the dominant species and their structural properties in solution can be achieved by using VCD spectroscopy as well ECD spectroscopy.

The rest of the thesis is organized as follows. In Chapter 2, the VA and VCD studies of three multidentate nitrogen donor ligands, i.e. (N,N'-bis(pyridine-2-ylmethylene)-(S,S)-1,2-cyclohexanediamine (SS-1), (N,N'-bis(pyridine-2-ylmethyl)-(S,S)-1,2-cyclohexanediamine (SS-2), and {(S,S)-2-[(2-pyridinylcarbonyl)amino] cyclohexyl}-2-pyridinecarboxamide (SS-3) have been described. These three ligands demonstrate very different conformational flexibility and different VCD spectra. In Chapter 3, the chiral (*R,R*)-1,5-diaza-cis-decalin ligand and its copper (II) hydroxide iodine hydrate complex have been investigated by using VA, UV-Vis, and ECD experimental spectroscopic measurements, as well as the DFT calculations. Since this complex

has a very low solubility in most common VCD solvents, one cannot obtain a reliable VCD spectrum in solution. Rather, we utilized solid-state VA technique and solution ECD spectroscopy where much lower sample concentrations are required. Chapter 4 presents the study of the palladium complexes of BINAP, (2,2'-diphenylphosphino-1,1'-binaphthyl) which is a unique binaphthyl diphosphine ligand with axial chirality, and of its derivative TOLBINAP. The conformational alterations in the BINAP and TOLBINAP ligands have been investigated before and after coordination with Pd by means of density functional theory and chiroptical spectroscopy in CDCl<sub>3</sub>. In Chapter 5, structural properties and induced helicity of a chiral Pyrrol-2-yl Schiff base ligand and its five transition metal complexes in solution, namely with M = Ni (II), Pd (II), Pt (II), Cu (II), and Zn(II), have been investigated. We have further examined the induced helicity at the metal centers and what factors governed such helicity preferences in solution. The results are compared to those obtained in solid. In Chapter 6, the effects of environmental perturbations, specifically solvent and concentration, on axial chirality of a recently synthesized triple axial chiral binaphthyl fluorene based salen ligand, named AXF-155, {[2,20-(1E,10E)-(R)-1,10-binaphthyl-2,20-diylbis(azan-1-yl-1-ylidene)bis(methan-1-yl-1-ylidene)bis-4-((7-(diphenylamino)-9,9-dihexyl-9H-fluoren-2-yl)ethynyl)-phenol)]} have been examined. The dominant conformations of AXF-155 in CDCl<sub>3</sub> solvent as well as its chirality have been characterized using chiroptical spectroscopy in combination with theoretical calculations. We paid special attention to the effects of concentration. The final chapter of my thesis summarizes some general conclusions and proposes future work to further explore and evaluate the metal-ligand coordination compounds both in terms of structural configurations and also spectral simulations. I have also included a number of appendices at the end of my thesis which deal with the supporting information

associated with each research chapter. Finally, I end my thesis by introducing other joint projects which I have been involved in during my PhD study.

## References

---

[1] (a). R. S. Cahn, C. K. Ingold, V. Prelog, *Angew. Chem. Int. Ed.*, **1966**, *5*, 385. (b). J. March. *Advanced Organic Chemistry* 3Ed. **2007**, John Wiley & Sons. ISBN 0-471-85472-7.

- 
- [2] T. Wu, X. Z. You, P. Bouř, *Coordin. Chem. Rev.*, **2015**, 284, 1–18.
- [3] G. H. Wagnière, *On Chirality and the Universal Asymmetry*, Wiley-VCH, **2007**.
- [4] J. Autschbach, *Comprehensive Chiroptical Spectroscopy*, **2012**, Volume 1, chapter 21, 593-642.
- [5] G. Holzwarth,; Hsu, E. C.; Mosher, H. S; Faulkner, T. R.; Moscovitz, A., *J. Am. Chem. Soc.* **1974**, 96, 251-252.
- [6] L. A. Nafie, J. C. Cheng, P. J. Stephens, *J. Am. Chem. Soc.* **1975**, 97, 3842-3843.
- [7] L. A. Nafie, T. A. Keiderling, P. J. Stephens, *J. Am. Chem. Soc.* **1976**, 98, 2715-2723.
- [8] L. A. Nafie, M. Diem, *Appl. Spectrosc.* **1979**, 33, 130-135.
- [9] L. A. Nafie, M. Diem, D. W. Vidrine, *J. Am. Chem. Soc.* **1979**, 101, 496-498.
- [10] (a) L. A. Nafie, T. H. Walnut, *Chem. Phys. Lett.*, **1977**, 49, 441. (b) T. H. Walnut, L. A. Nafie, *Chem. Phys.*, **1977**, 67, 1501.
- [11] (a) L. A. Nafie, T. B. Freedman, *J. Phys. Chem.*, **1983**, 78, 7108. (b) R. Dutler, A. Rauk, *J. Am. Chem. Soc.*, **1989**, 111, 6957. (c) D. Yang, A. Rauk, *J. Chem. Phys.*, **1992**, 97, 6517.
- [12] P. J. Stephens, *J. Phys. Chem.*, **1985**, 89, 148-752.
- [13] A. D. Buckingham, P. W. Fowler, P.A. Galwas, *Chem. phys.*, **1987**, 112, 1-14.
- [14] P.J. Stephens, *J. Phys. Chem.*, **1987**, 91, 1712-1715.
- [15] K. Aidas, C. Angeli, K. L. Bak, V. Bakken, R. Bast, L. Boman, O. Christiansen, R. Cimiraglia, S. Coriani, P. Dahle, E. K. Dalskov, U. Ekström, T. Enevoldsen, J. J. Eriksen, P. Ettenhuber, B. Fernández, L. Ferrighi, H. Fliegl, L. Frediani, K. Hald, A. Halkier, C. Hättig, H. Heiberg, T. Helgaker, A. C. Hennum, H. Hettema, E. Hjertenæs, S. Høst, I.-M. Høyvik, M. F. Iozzi, B. Jansik, H. J. A. Jensen, D. Jonsson, P. Jørgensen, J. Kauczor, S. Kirpekar, T. Kjærgaard, W. Klopper, S. Knecht, R. Kobayashi, H. Koch, J. Kongsted, A. Krapp, K. Kristensen, A. Ligabue, O. B. Lutnæs, J. I. Melo, K. V. Mikkelsen, R. H. Myhre, C. Neiss, C. B. Nielsen, P. Norman, J. Olsen, J. M. H. Olsen, A. Osted, M. J. Packer, F. Pawłowski, T. B. Pedersen, P. F. Provasi, S. Reine, Z. Rinkevicius, T. A. Ruden, K. Ruud, V. Rybkin, P. Salek, C. C. M. Samson, A. Sánchez de Merás, T. Saue, S. P. A. Sauer, B. Schimmelpfennig, K. Sneskov, A. H. Steindal, K. O. Sylvester-Hvid, P. R. Taylor, A. M. Teale, E. I. Tellgren, D. P. Tew, A. J. Thorvaldsen, L. Thøgersen, O. Vahtras, M. A. Watson, D. J. D. Wilson, M. Ziolkowski, and H. Ågren, "The Dalton quantum chemistry program system", *WIREs Comput. Mol. Sci.* **2013**.
- [16] M. W. Schmidt, K. K. Baldrige, J. A. Boatz, S. T. Elbert, M. S. Gordon, J. H. Jensen, S. Koseki, N. Matsunaga, K. A. Nguyen, S. Su, T. L. Windus, M. Dupuis, J. A. Montgomery, *J. Comput. Chem.*, **1993**, 14, 1347-1363.
- [17] A. D. Becke, *J. Chem. Phys.*, **1993**, 98, 1372-1377.
- [18] A. D. Becke, *J. Chem. Phys.*, **1993**, 98, 5648-5652.
- [19] P. J. Stephens, F. J. Devlin, C. F. Chabalowski, M. J. Frisch, *J. Phys. Chem.* **1994**, 98, 11623-11627.
- [20] P. J. Stephens, F. J. Devlin, J. R. Cheeseman, CRC Press, *VCD Spectroscopy for Organic Chemist*, **2012**.
-



---

[21] Gaussian 03, Revision **E.01**, M. J. Frisch, G. W. Trucks, H. B. Schlegel, G. E. Scuseria, M. A. Robb, J. R. Cheeseman, J. A. Montgomery, Jr., T. Vreven, K. N. Kudin, J. C. Burant, J. M. Millam, S. S. Iyengar, J. Tomasi, V. Barone, B. Mennucci, M. Cossi, G. Scalmani, N. Rega, G. A. Petersson, H. Nakatsuji, M. Hada, M. Ehara, K. Toyota, R. Fukuda, J. Hasegawa, M. Ishida, T. Nakajima, Y. Honda, O. Kitao, H. Nakai, M. Klene, X. Li, J. E. Knox, H. P. Hratchian, J. B. Cross, V. Bakken, C. Adamo, J. Jaramillo, R. Gomperts, R. E. Stratmann, O. Yazyev, A. J. Austin, R. Cammi, C. Pomelli, J. W. Ochterski, P. Y. Ayala, K. Morokuma, G. A. Voth, P. Salvador, J. J. Dannenberg, V. G. Zakrzewski, S. Dapprich, A. D. Daniels, M. C. Strain, O. Farkas, D. K. Malick, A. D. Rabuck, K. Raghavachari, J. B. Foresman, J. V. Ortiz, Q. Cui, A. G. Baboul, S. Clifford, J. Cioslowski, B. B. Stefanov, G. Liu, A. Liashenko, P. Piskorz, I. Komaromi, R. L. Martin, D. J. Fox, T. Keith, M. A. Al-Laham, C. Y. Peng, A. Nanayakkara, M. Challacombe, P. M. W. Gill, B. Johnson, W. Chen, M. W. Wong, C. Gonzalez, J. A. Pople, Gaussian, Inc., Wallingford, CT, **2004**.

[22] (a). Gaussian 09, Revision **B.01**, M. J. Frisch, G. W. Trucks, H. B. Schlegel, G. E. Scuseria, M. A. Robb, J. R. Cheeseman, G. Scalmani, V. Barone, B. Mennucci, G. A. Petersson, H. Nakatsuji, M. Caricato, X. Li, H. P. Hratchian, A. F. Izmaylov, J. Bloino, G. Zheng, J. L. Sonnenberg, M. Hada, M. Ehara, K. Toyota, R. Fukuda, J. Hasegawa, M. Ishida, T. Nakajima, Y. Honda, O. Kitao, H. Nakai, T. Vreven, J. A. Montgomery, Jr., J. E. Peralta, F. Ogliaro, M. Bearpark, J. J. Heyd, E. Brothers, K. N. Kudin, V. N. Staroverov, R. Kobayashi, J. Normand, K. Raghavachari, A. Rendell, J. C. Burant, S. S. Iyengar, J. Tomasi, M. Cossi, N. Rega, J. M. Millam, M. Klene, J. E. Knox, J. B. Cross, V. Bakken, C. Adamo, J. Jaramillo, R. Gomperts, R. E. Stratmann, O. Yazyev, A. J. Austin, R. Cammi, C. Pomelli, J. W. Ochterski, R. L. Martin, K. Morokuma, V. G. Zakrzewski, G. A. Voth, P. Salvador, J. J. Dannenberg, S. Dapprich, A. D. Daniels, Ö. Farkas, J. B. Foresman, J. V. Ortiz, J. Cioslowski, D. J. Fox, Gaussian, Inc., Wallingford CT, **2009**.

(b).Gaussian 09, Revision **D.01**, M. J. Frisch, G. W. Trucks, H. B. Schlegel, G. E. Scuseria, M. A. Robb, J. R. Cheeseman, G. Scalmani, V. Barone, B. Mennucci, G. A. Petersson, H. Nakatsuji, M. Caricato, X. Li, H. P. Hratchian, A. F. Izmaylov, J. Bloino, G. Zheng, J. L. Sonnenberg, M. Hada, M. Ehara, K. Toyota, R. Fukuda, J. Hasegawa, M. Ishida, T. Nakajima, Y. Honda, O. Kitao, H. Nakai, T. Vreven, J. A. Montgomery, Jr., J. E. Peralta, F. Ogliaro, M. Bearpark, J. J. Heyd, E. Brothers, K. N. Kudin, V. N. Staroverov, R. Kobayashi, J. Normand, K. Raghavachari, A. Rendell, J. C. Burant, S. S. Iyengar, J. Tomasi, M. Cossi, N. Rega, J. M. Millam, M. Klene, J. E. Knox, J. B. Cross, V. Bakken, C. Adamo, J. Jaramillo, R. Gomperts, R. E. Stratmann, O. Yazyev, A. J. Austin, R. Cammi, C. Pomelli, J. W. Ochterski, R. L. Martin, K. Morokuma, V. G. Zakrzewski, G. A. Voth, P. Salvador, J. J. Dannenberg, S. Dapprich, A. D. Daniels, Ö. Farkas, J. B. Foresman, J. V. Ortiz, J. Cioslowski, and D. J. Fox, Gaussian, Inc., Wallingford CT, **2009**.

[23] W. Kohn, L. J. Sham, *Phys. Rev.*, **1965**, 140, A1133-A38.

[24] R. A. Kendall, T. H. Dunning Jr., R. J. Harrison, *J. Chem. Phys.*, **1992**, 96, 6796-806.

[25] B. Mennucci; J. Tomasi, R. Cammi, J. R. Cheeseman, M. J. Frisch, F. J. Devlin, S. Gabriel, P. J. Stephens, *J. Phys. Chem. A*, **2002**, 106, 6102–6113.

[26] S. Kaizaki, *Comprehensive Chiroptical Spectroscopy: Applications in Stereochemical Analysis of Synthetic Compounds, Natural Products, and Biomolecules* by N. Berova, P.L. Polavarapu, K. Nakanishi, R.W. Woody (Eds.), vol.2, John Wiley & Sons, Inc., New Jersey, **2012**, pp. 451–471.

[27] B. Le Guennic, W. Hieringer, A. Görling, J. Autschbach, *J. Phys. Chem. A*, **2005**, 109, 4836-4846.

[28] C. Cappelli, S. Monti, A. Rizzo, *Int. J. Quantum Chem.*, **2005**, 104, 744-757.

[29] D. R. Turner, J. Kubelka, *J. Phys. Chem. B*, **2007**, 111, 1834-1845.

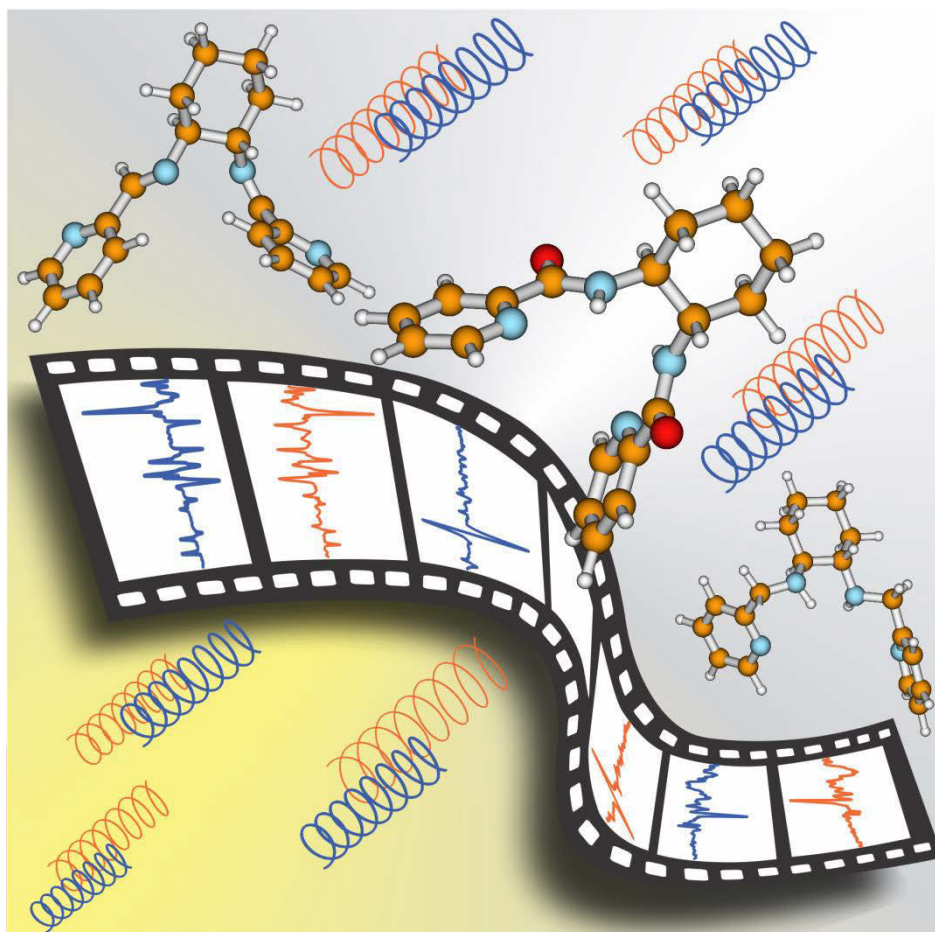
[30] A. Vargas, N. Bonalumi, D. Ferri, A. Baiker, *J. Phys. Chem. A*, **2006**, 110, 1118-1127.

- 
- [31] V. P. Nicu, E. J. Baerends, L. Polavarapu, *J. Phys. Chem. A*, **2012**, 116, 8366-8373.
- [32] E. Debie, P. Bultinck, W. Herrebout, B. van der Veken, *Phys. Chem. Chem. Phys.*, **2008**, 10, 3498-3508.
- [33] A. Giugliarelli, P. Sassi, M. Paolantoni, A. Morresi, R. Dukor, L. Nafie, *J. Phys. Chem. B*, **2013**, 117, 2645- 2652.
- [34] J. Tomasi, B. Mennucci, R. Cammi, *Chem. Rev.*, **2005**, 105, 2999-3093.
- [35] (a). M. R. Poopari, Z. Dezhahang, G. Yang, Y. Xu, *ChemPhysChem*, **2012**, 13, 2310-2321. (b). Z. Dezhahang, C. Merten, M. R. Poopari, Y. Xu, *Dalton Trans.*, **2012**, 41, 10817-10824. (c). M. R. Poopari, Z. Dezhahang, Y. Xu, *Phys. Chem. Chem. Phys.*, **2013**, 15, 1655-1665. (d). Z. Dezhahang, M. R. Poopari, Y. Xu, *Chem, Asian J.*, **2013**, 8, 1205-1212.
- [36] J. R. Cheeseman, M. S. Shaik, P. L. A. Popelier, E. W. Blanch, *J. Am. Chem. Soc.*, **2011**, 133, 4991-4997
- [37] (a). P. L. Polavarapu, *Chirality*, **2012**, 24, 909-920. (b). A. -C. Chamayou, S. Lüdeke, V. Brecht, T. B. Freedman, L. A. Nafie, C. Janiak, *Inorg. Chem.*, **2011**, 50, 11363-11374. (c). F. Gutiérrez-Nicolás, B. Gordillo-Román, J. C. Oberti, A. Estévez-Braun, A. G. Ravelo, P. Joseph-Nathan, *Journal of Nat Prod*, **2012**, 75, 669-676. (d). Y. He, B. Wang, R. K. Dukor, L. A. Nafie, *Appl. Spectros*, **2011**, 65, 699-723.
- [38] N. Berova, P. L. Polavarapu, K. Nakanishi, R. W. Woody, *Comprehensive Chiroptical Spectroscopy*, Volume 1 (Instrumentation, Methodologies, and Theoretical Simulations ) and volume 2 (Applications in Stereochemical Analysis of Synthetic Compounds, Natural Products, and Biomolecules), John Wiley & Sons, Inc., **2012**.

# 2

## Vibrational circular dichroism spectroscopy of three multidentate nitrogen donor ligands: conformational flexibility and solvent effects

Zahra Dezhahang, Mohammad Reza Poopari, Yunjie Xu



## 2.1. Introduction

---

Picolylamine-type ligands, such as N,N'-bis(pyridine-2-yl-methylene)-(S,S)-1,2-cyclohexanediamine (SS-1), N,N'-bis(pyridine-2-ylmethyl)-(S,S)-1,2-cyclohexanediamine (SS-2), and {(S,S)-2-[(2-pyridinylcarbonyl)amino]cyclohexyl}-2-pyridinecarboxamide (SS-3), are multidentate nitrogen-donor ligands with amine and/or pyridine-type nitrogen atoms. These nitrogen lone pairs can form transition-metal complexes with, for example, copper and silver.[1, 2] They are called N3 or N4 donor ligands, depending on the number of nitrogen atoms that are involved in coordination to the metal atoms. Many of these transition-metal complexes show catalytic activities in asymmetric reactions, such as the Ullmann reaction, Henry (nitroaldol) reaction, and allylation reaction.[1–3] In addition, cobalt and zinc complexes with the N3 and N4 ligands have also been used to mimic biological systems, such as coenzyme vitamin B-12,[4] and some of their crystal structures have been reported.[5]

Although some N3 and N4 ligands, such as diiminopyridine, dipicolylamine, tripicolylamine, and pyridinophane, are achiral compounds, we focused on the three chiral multidentate nitrogen-donor ligands shown in Figure 2.1. Chirality is an essential aspect in asymmetric catalysis and in molecular-recognition events in biological systems. Conformational flexibility in these chiral N3 and N4 ligands often plays a crucial role in their catalytic capabilities in asymmetric reactions. It has also been documented that the solvent may influence the catalytic activity of a certain copper complex of SS-1.[2] While X-ray crystallography can provide detailed structural information of a single crystal, it is desirable to have a spectroscopic tool that can probe the chirality and conformations of these important species in solution directly. Vibrational circular dichroism (VCD) spectroscopy measures the preferential absorption of left versus right circularly polarized light that accompanies a vibrational transition. It therefore has

unique specificity to chirality and is also highly sensitive to conformations.[6] In recent years, VCD spectroscopy has emerged as a powerful tool to determine chirality and conformations of chiral inorganic compounds in solution when combined with DFT calculations.[7–16] For example, Sato *et al.* recently applied VCD spectroscopy to probe interesting chiroptical properties of coordinated bis-diketonato ligands[15] and a starburst-type tetranuclear ruthenium(III) complex.[13] Herein, we report extensive conformational searches for the three chiral N<sub>4</sub> inorganic ligands presented in Figure 2.1. Vibrational absorption (VA) and VCD spectra of all three ligands have been measured and compared with simulated spectra. One main objective is to obtain structural information and conformational distributions of these chiral ligands in solution. The second objective is to compare the similarity and dissimilarity of the VA and VCD spectral features of these three related ligands to further the goal of following these ligands in reactions in solution. Finally, we wish to evaluate the effects of solvent on the observed VCD features through theoretical modeling.

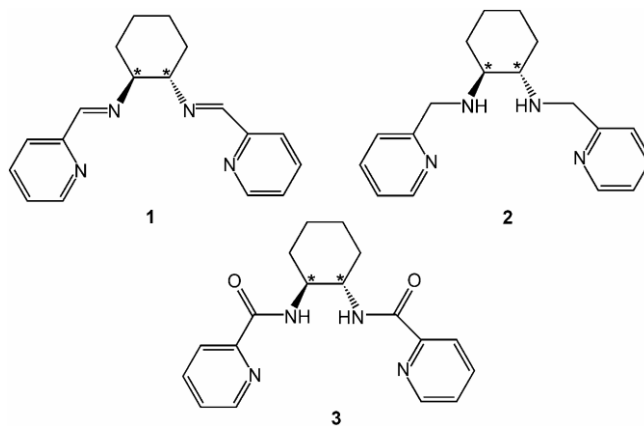


**Figure 2.1.** 2D stereo-chemical structures of compounds SS-1, SS-2, and SS-3 reported herein.

\* indicates the stereogenic center of the compounds.

## 2.2. Results and Discussion

---

Figure 2.2 shows the experimental VA and VCD spectra of 1, 2, and 3 in CDCl<sub>3</sub>. Experimental VCD spectra of both enantiomers, which show good mirror images for the three compounds studied, are provided in Figure A1 in the Appendix A. The S,S enantiomers of 1, 2, and 3 were used throughout, unless otherwise indicated. To highlight the similarities and differences in the VA and VCD spectra, we examined the experimental spectra in five regions marked A to E in Figure 2.2. In region A, there is a strong VA band corresponding to the C=N and C=O stretching vibrational modes of 1 and 3, respectively, whereas 2 shows no band in this region. This amide I band of 3 is somewhat broadened, possibly as a result of hydrogen-bonding like interactions with the solvent. In region B, two bands associated with vibrational modes of the pyridine rings are visible for all three compounds. In region C, only 3 exhibits a strong and somewhat broadened band that corresponds to the amide II vibrational mode. No such bands are detected for 1 and 2 because they do not contain a peptide bond, which is present in 3. In region D, three closely spaced bands are visible for all three compounds; these are associated with vibrational motions of the cyclohexane and pyridine rings. Lastly, region E contains a number of low-intensity vibrational bands related to the vibrational motions of mainly C–C and C–H of the cyclohexane rings. Although one can correlate the VA features in regions A–D straightforwardly among these three compounds, the differences are drastic for the associated VCD features. For example, whereas the VA spectra of compounds 1 and 2 are similar in regions B and D, their corresponding VCD spectra differ greatly. This may be surprising at first glance because 1 and 2 differ only in that the two C=N functional groups of 1 are reduced in 2. On the other hand, this observation highlights the sensitivity of VCD spectroscopy to even small structural and conformational differences.

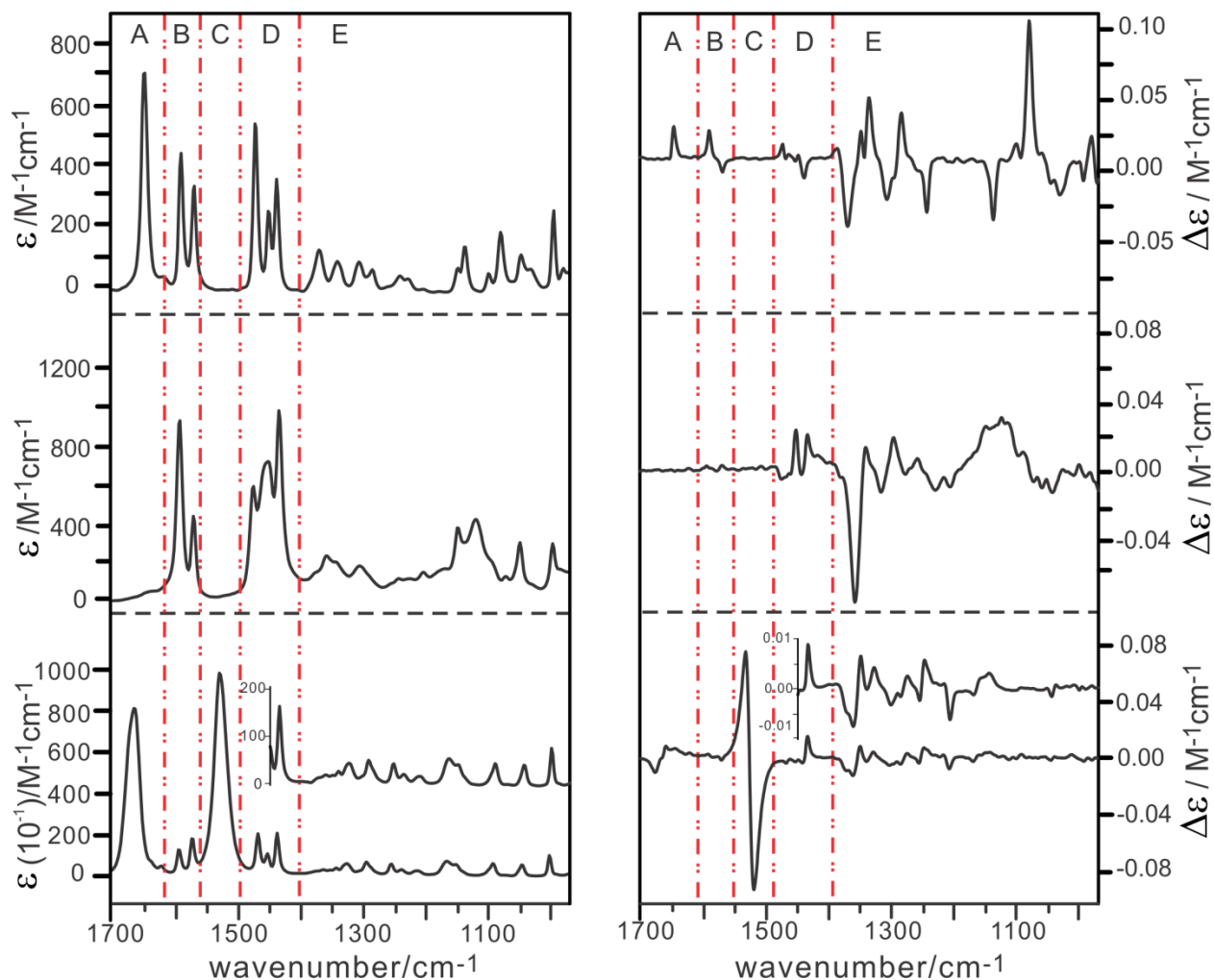


**Figure 2.2.** Experimental VA (left) and VCD (right) spectra of 1, 2, and 3 in  $\text{CDCl}_3$  from top to bottom, respectively. The VA and VCD spectra of 1 and 2, as well as the inserted spectrum of 3, were recorded with a path length of 0.1 mm. The VA and VCD spectra of 3 were recorded with a shorter path length of 0.025 mm.

### 2.2.1. Compound 1

Compound 1 has a number of rotatable bonds that make it a fairly flexible molecule. In this system, the cyclohexane ring is in its chair configuration because the boat configuration is much less stable at room temperature.[17] The two nitrogen atoms may adopt either equatorial or axial

positions at the cyclohexane ring. We use the subscripts “equ” and “ax” to note the equatorial and axial orientations, respectively, of the nitrogen atoms at the cyclohexane rings. In addition, the nitrogen atoms of the pyridine rings may take on a cis or trans orientations with respect to the nitrogen atoms of the C=N groups (see Figure 2.3 for a definition of the cis and trans arrangements).

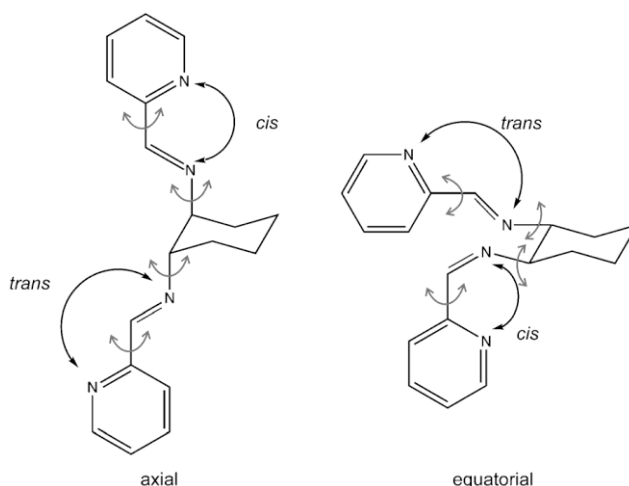


**Figure 2.3.** The cis and trans configurations of compound 1 with axial and equatorial substitutions. The rotatable C–C<sub>pyridine</sub> and N–C<sub>hexane</sub> bonds are indicated by small arrows.

The dihedral angle NCCN does not need to be 0 or 180° in the case of the cis or trans configurations, respectively. Rather, these dihedral angles vary as the pyridine subunits rotate about the C–C bond to achieve stable conformations. Similarly, the whole substituted units can rotate around the N–C<sub>hexane</sub> bond. These motions are indicated with arrows in Figure 2.3. Altogether, a flexible molecule such as this may accommodate numerous conformers, labeled [trans–cis]equ, [trans–cis]ax, and so forth in Figure 2.4.



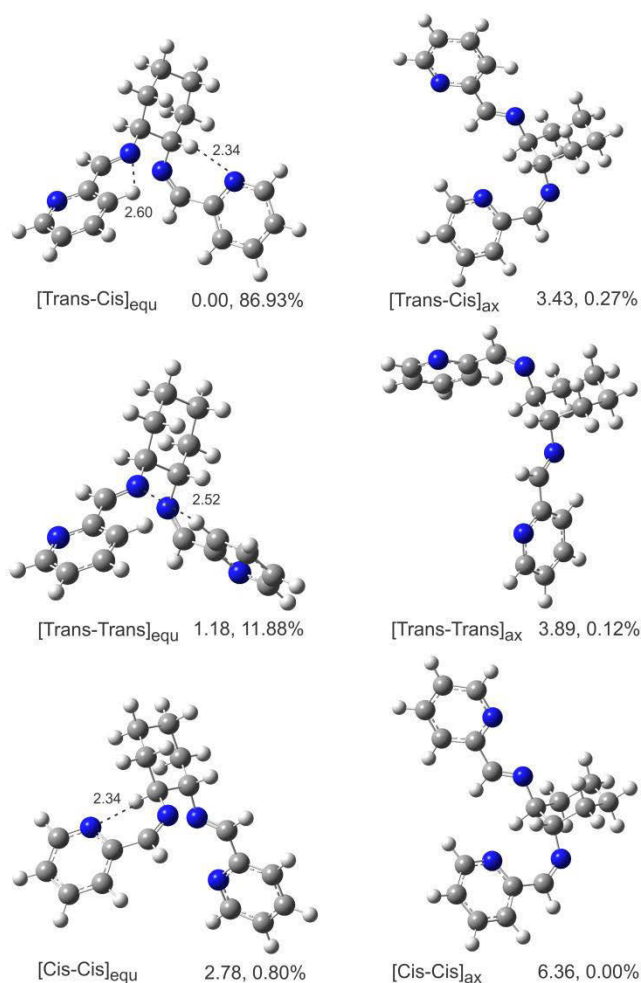


**Figure 2.4.** Conformations of compound SS-1 at the PCM/B3PW91/ccpVTZ level. The corresponding relative Gibbs free energies in kcal mol<sup>-1</sup> and the percentage Boltzmann factors at room temperature are also listed. Secondary intramolecular hydrogen bonds with bond lengths of <2.8 Å are indicated with dotted lines.

To account for the implicit solvent effect, a polarization continuum model (PCM) with CDCl<sub>3</sub> as the solvent was applied. The lowest energy conformers obtained at the PCM/ B3PW91/cc-pVTZ level are summarized in Figure 2.4, along with the relative Gibbs free energies and the corresponding percentage Boltzmann factor at room temperature. Based on the calculations, the

equatorial orientation is favored over the axial orientation in all three possible pyridine orientations that is, trans–cis, trans–trans, and cis–cis. The preference for the equatorial position can be attributed to the opportunity to form secondary hydrogen-bonding interactions between a hydrogen atom of the cyclohexane ring and a nitrogen atom of the pyridine rings or between a hydrogen atom of one pyridine ring with the nitrogen atom of the C=N bond (see Figure 2.4). This also explains why the [trans–cis]equ arrangement is favored over the other two equatorial arrangements.

In the following discussions, we focus on the two dominant conformers of 1 because the other four conformers have a negligible contribution at room temperature. For completion, simulated VA and VCD spectra of all conformers of 1 are depicted in Figure A2 in the Appendix A. In Figure 2.5, VA and VCD spectra of the two most stable conformers of 1 and the population-weighted spectrum based on their relative Gibbs free energies are compared with the corresponding experimental data. All experimental VA bands with visible intensities in the  $\bar{\nu} = 1700\text{--}1400\text{ cm}^{-1}$  region have been predicted accordingly. The two closely spaced bands in the  $\bar{\nu} = 1450\text{--}1400\text{ cm}^{-1}$  region appear as one broader band in the calculation because the very small frequency shift is not accurately captured theoretically. Detailed comparisons between the experimental and calculated VA spectra in the region of  $\bar{\nu} = 1400\text{--}970\text{ cm}^{-1}$  are more challenging partly because the intensity is low and the density of peaks is high and some peaks are not well resolved experimentally. Nevertheless, it is straightforward to correlate most of the experimental VA bands in this region to the calculated ones. Notably, the VCD band intensity is strong in the  $\bar{\nu} = 1400\text{--}970\text{ cm}^{-1}$  region, where the VA intensity is low. One can confidently correlate all major VCD bands in this low-wavenumber region to the calculated ones. In the  $\bar{\nu} = 1700\text{--}1400\text{ cm}^{-1}$  region, on the other hand, the VCD intensity is generally weak, whereas the VA bands are

strong. Although the calculated and experimental VCD patterns agree in general, some discrepancies are noted. For example, the bisignate +/- couplet in the  $\bar{\nu} = 1600\text{--}1550\text{ cm}^{-1}$  region was predicted to have a noticeably weaker positive feature than that observed experimentally. Overall, good agreement between the experimental and predicted VCD spectra for 1 in the entire region of  $\bar{\nu} = 1700\text{--}970\text{ cm}^{-1}$  is achieved, despite the flexibility of the molecule.

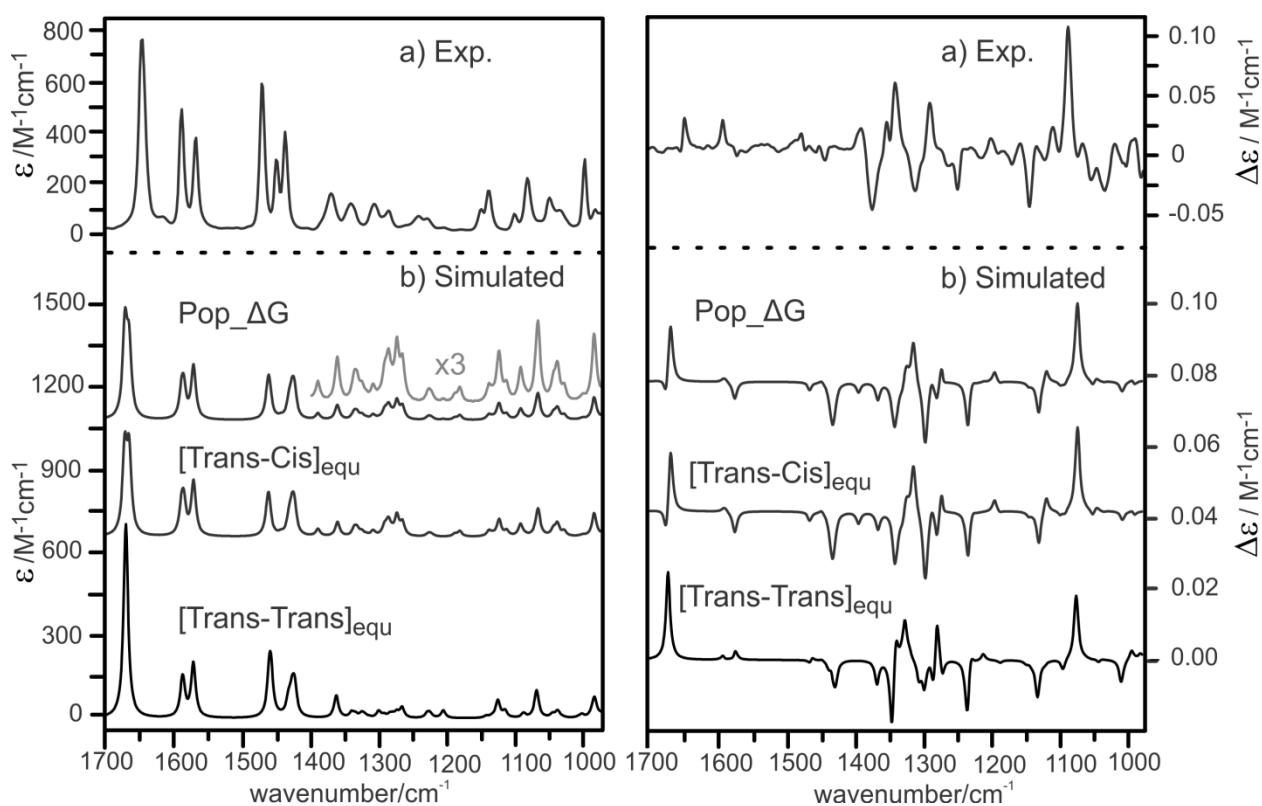


**Figure 2.5.** Comparison of the experimental and calculated VA (left) and VCD (right) spectra and the associated population-weighted spectra of SS-1 at the PCM/B3PW91/cc-pVTZ level. The corresponding spectra of the two main conformers of 1 are also included.

## 2.2.2. Compound 2

In compound 2, the C=N bonds of 1 are reduced by NaBH<sub>4</sub>. Consequently, the degree of flexibility increases considerably from 1 to 2 because of the additional rotatable bonds. The rotatable bonds and four conformationally important dihedral angles are indicated in Figure 2.6. Preliminary searches suggest that conformers with intramolecular hydrogen-bonding interactions between the two NH groups are considerably more stable than those without. Keeping the aforementioned intramolecular hydrogen-bonding interactions intact, we varied the other four dihedral angles shown in Figure 2.6 to search for more conformers.

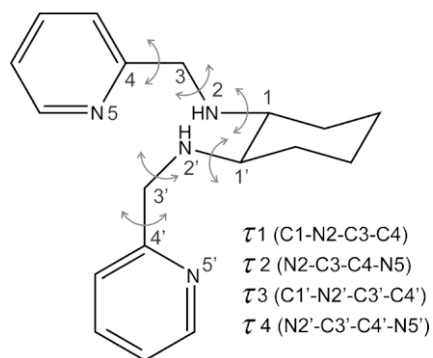


**Figure 2.6.** The rotatable bonds used in the conformational search are indicated with double arrows. The four conformationally important dihedral angles of 2 are also shown.

This search resulted in 32 potential conformers. Although there are only 2 major conformers for compound 1, there are 10 conformers of 2 with a percentage Boltzmann factor larger than 1% and they account for over 96% of the total population at room temperature in the initial search with the 6-311+ +G(d,p) basis set. The final optimized geometries of these ten conformers at the PCM/B3PW91/cc-pVTZ level are shown in Figure 2.7, as well as their relative Gibbs free energies and percentage Boltzmann factors at room temperature. Similar to compound 1, the two pyridine substitutions prefer to adopt the equatorial orientation at the cyclohexane ring to retain

the NH $\cdots$ N hydrogen- bonding interaction indicated in Figure 2.7. This portion of compound 2 remains essentially unchanged in all ten conformers shown in Figure 2.7. The values for the four conformationally important dihedral angles of these ten conformers are provided in Table 2.1.

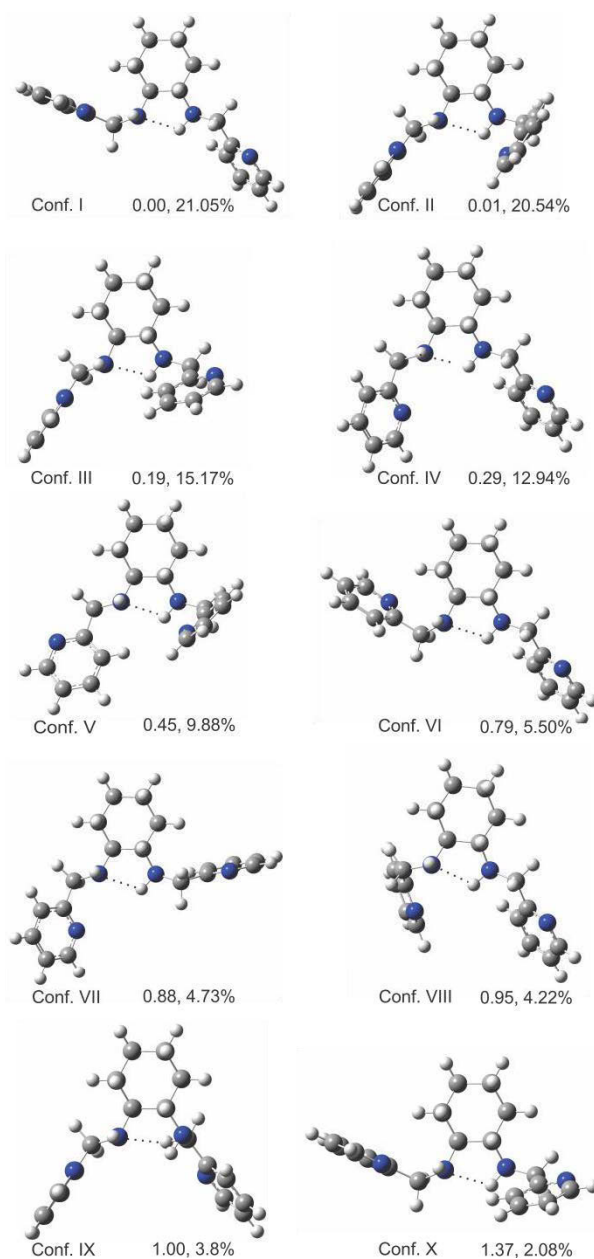


**Figure 2.7.** The ten most stable conformers of SS-2. The corresponding relative Gibbs free energies in kcal mol $^{-1}$  at the PCM/B3PW91/cc-pVTZ level and the corresponding Boltzmann

factors at room temperature are also listed. The NH···N hydrogen bonds are indicated with dotted lines.

**Table 2.1.** Dihedral angle values for the ten most stable conformers of SS-2 at the PCM/B3PW91/cc-pVTZ level.

Conformer	t1[°]	t2[°]	t3[°]	t4[°]
I	84.98	41.08	177.56	164.17
II	164.39	35.76	64.43	60.68
III	165.80	33.25	66.13	158.77
IV	175.03	78.18	178.16	166.83
V	168.86	164.69	62.27	53.83
VI	66.84	103.89	176.33	164.01
VII	173.89	76.61	98.33	156.07
VIII	75.65	66.79	176.31	165.55
IX	167.34	38.68	174.79	163.77
X	80.64	46.08	64.00	156.53

[a] Conformers are shown in Figure 2.7.

Population-weighted VA and VCD spectra of these ten conformers are compared with the associated experimental data given in Figure 2.8. Because all of these conformers are relatively close in energy, the VA and VCD spectra of each individual conformer are also presented in Figures A3 and A4 in the Supporting Information, respectively, and compared with the experimental data. As seen in Figure A3 in the Supporting Information, the VA spectra of all ten conformers are similar. The two intense VA bands observed in panel B, corresponding to the C–C vibrational motions of the pyridine rings, are predicted for all ten conformers. On the other hand, in panel D, a group of fairly strong VA bands, associated with the cyclohexane C–H and pyridine C–H motions, are predicted for all conformers, but with somewhat different relative intensities. Closer examination reveals that the VA bands related to the cyclohexane C–H

motions remain more or less the same among these conformers in panel D; this is consistent with the fact that the cyclohexane ring remains relatively unchanged among the conformers. The VA bands associated with the pyridine C–H motions, on the other hand, experience intensity changes from one conformer to the next, in which the pyridine rings take on different relative orientations. Although there are some small differences in the VA bands of different conformers in panel E, the predicted dominant VA bands are similar for all. Overall, the population-weighted VA spectrum is in good agreement with the experimental one (Figure 2.8).

A number of interesting points can be made for the VCD spectra of different conformers shown in Figure A4 in the Supporting Information. First, the VCD intensities are predicted to be weak for all conformers in the  $\bar{\nu} = 1670\text{--}1560\text{ cm}^{-1}$  region, that is, panel B. Although the VA patterns are similar in panel B, the VCD patterns are different for different conformers. Second, in the  $\bar{\nu} = 1560\text{--}1500\text{ cm}^{-1}$  region (panel D), strong VCD intensities are predicted for all conformers, but with drastically different patterns going from one conformer to the next. In the final population-weighted spectrum, accidental intensity cancelations result in much weaker VCD bands; this is consistent with somewhat weak and congested VCD signals observed experimentally. Agreement between the experimental and predicted VCD patterns is good, except that the negative band at  $\bar{\nu} = 1470\text{ cm}^{-1}$  is predicted to be much stronger than that observed experimentally; this highlights the challenges in dealing with flexible molecules with a large number of relevant conformers. Lastly, in the region below  $\bar{\nu} = 1400\text{ cm}^{-1}$  (panel E), all six most abundant conformers are predicted to show strong to medium negative VCD bands at  $\bar{\nu} = 1360\text{ cm}^{-1}$ ; this is consistent with the most intense VCD band observed in this vicinity experimentally. Considering that 2 is very flexible and has a significant number of relevant conformers with noticeably different VCD patterns, the overall agreement between the experimental VCD

spectrum and the population-weighted spectrum is quite good. This in turn supports the conformers and conformational distributions identified.

### 2.2.3. Compound 3

---

In compound 3, the subunit  $-\text{NH}-\text{CH}_2-$  in 2 is replaced with  $-\text{NH}-\text{C}(=\text{O})-$ . The introduction of the two peptide bonds in 3 brings substantial rigidity to the structure. The lone electron pairs of the nitrogen atoms are involved in the resonance with the p electrons of the carbonyl groups. As a result, rotation around the  $\text{N}-\text{C}_{\text{carbonyl}}$  bond is restricted, in contrast to free rotation around the  $\text{N}-\text{C}$  bond in 2. As with the previous compounds, the equatorial position is much more favored than the axial orientation for 3. In addition, the  $\text{C}=\text{O}$  group and the N atom of pyridine prefers to stay in the trans arrangement around the  $\text{C}_{\text{carbonyl}}-\text{C}_{\text{pyridine}}$  bond, corresponding to the cis arrangement for the two N atoms shown in Figure 2.1. This results in a strong preference for the cis-cis configuration. One ends up with only one major conformer for 3 (Figure 2.9). The experimental VA and VCD data are summarized in Figure 2.10 and compared with spectra calculated at the PCM/B3PW91/cc-pVTZ level. For easier visual comparison, the simulated VA and VCD intensities are amplified by a factor of 5 and 8, respectively, in the region below  $\bar{\nu} = 1450 \text{ cm}^{-1}$ . The majority of experimental features are reasonably reproduced by the simulated ones, despite their low intensity in the  $\bar{\nu} = 1400-970 \text{ cm}^{-1}$  region. The only noticeable exception is the VCD experimental features at  $\bar{\nu} = 1650 \text{ cm}^{-1}$ , corresponding to the amide I vibrational motions, which show a negative-positive doublet, in contrast to the prediction with PCM.

It has been demonstrated before that hydrogen-bonding interactions between a chiral solute and solvent may alter the appearance of the VCD spectral pattern noticeably in solution. [18–24] Such hydrogen-bonding interactions may be the cause for the disagreement between theory and



experiment with regard to the amide I VCD signs. Such phenomena in the amide I region were investigated, for example, for N-acetylproline amide [25] and for the tryptophan zipper (trpzip) model hairpin in water. [26] Compound 3 has two carbonyl oxygen atoms that can serve as proton acceptors to the D atom of  $\text{CDCl}_3$ . We therefore constructed an explicit solvated complex of 3 with two molecules of  $\text{CDCl}_3$ , which is also depicted in Figure 2.9. The simulated VA and VCD spectra of this explicit solvated complex are also presented in Figure 2.10. The assignment for the bands in the  $\bar{\nu} = 1700\text{--}1450\text{ cm}^{-1}$  region is straightforward. In the  $\bar{\nu} = 1450\text{--}1050\text{ cm}^{-1}$  region, to aid a visual comparison, a number of experimental VA and VCD bands are labeled and have also been cross-checked for consistency in their VA and VCD band positions. The corresponding assignments for these bands are also provided in the calculated spectra. There are some minor changes to the VA and VCD features on going from 3 calculated with PCM to the explicitly solvated complex of 3 with two molecules of  $\text{CDCl}_3$ . For example, the calculated VA feature of the solvated complex at  $\bar{\nu} = 1250\text{ cm}^{-1}$  appears to be stronger owing to severe overlap of two VA bands, whereas these two VA bands of 3 calculated with PCM are well separated. The most noticeable change is that the signs for the bisignate VCD couplet at  $\bar{\nu} = 1650\text{ cm}^{-1}$  are reversed with the explicit solvation model and are now in agreement with experimental results. A similar sign-reversed phenomenon was reported for the carbonyl stretching band in the VCD study of pulegone in chloroform, [18, 19] although the VCD carbonyl band was later identified as a non-robust mode.[19, 24] Closer examination of the VCD amide I bands reveals that these modes are robust and the VCD signs associated with the symmetric and anti-symmetric C=O bands have not changed upon hydrogen-bonding interactions with  $\text{CDCl}_3$ . Rather, the reversed VCD signs observed are due to switching of the frequency ordering of the symmetric and antisymmetric C=O bands caused by hydrogen-bonding interactions with  $\text{CDCl}_3$ . Detailed

vibrational motion and robust mode analyses are provided in Table A1 in the Supporting Information. The above observations and discussion highlight the importance of explicit solvent–solute hydrogen-bonding interactions in interpreting VCD spectra.

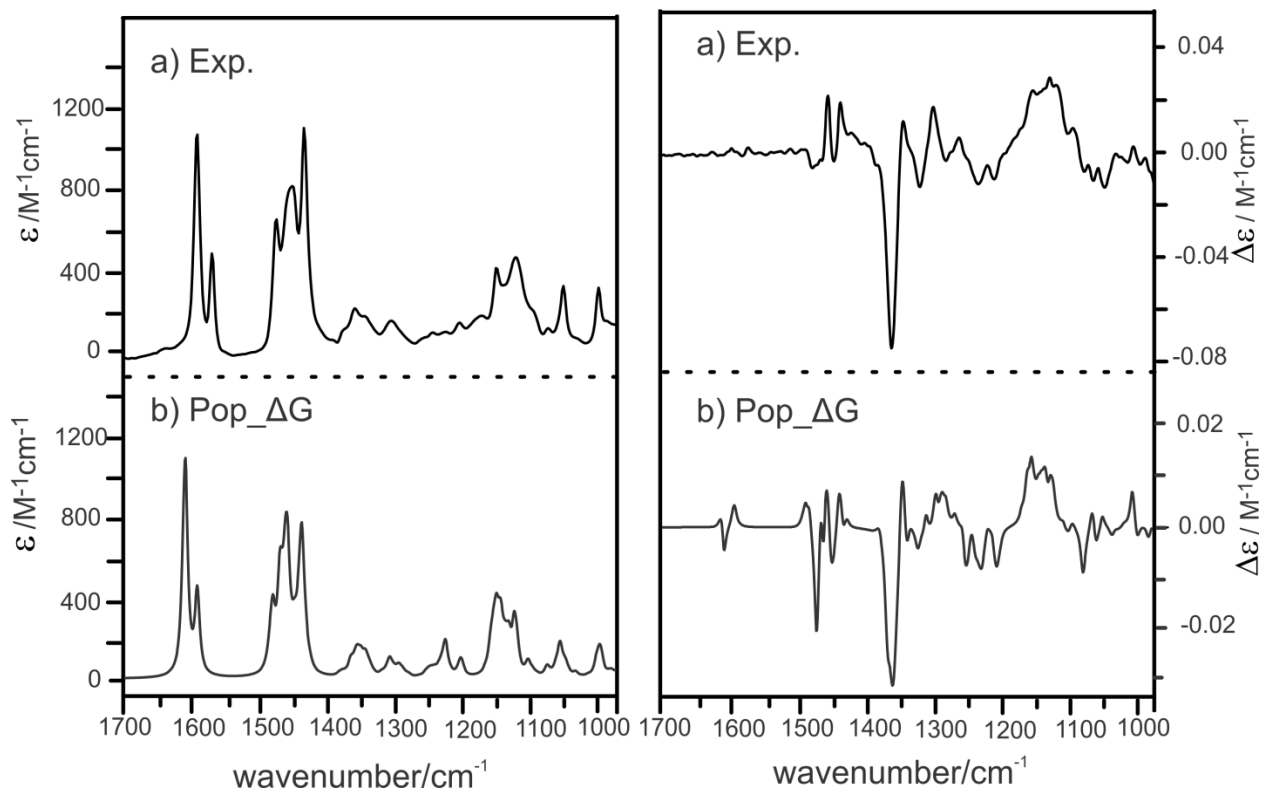


**Figure 2.8.** Comparison of the experimental and calculated VA (left) and VCD (right) spectra of the population-weighted spectra of SS-2 calculated at the PCM/B3PW91/cc-pVTZ level.

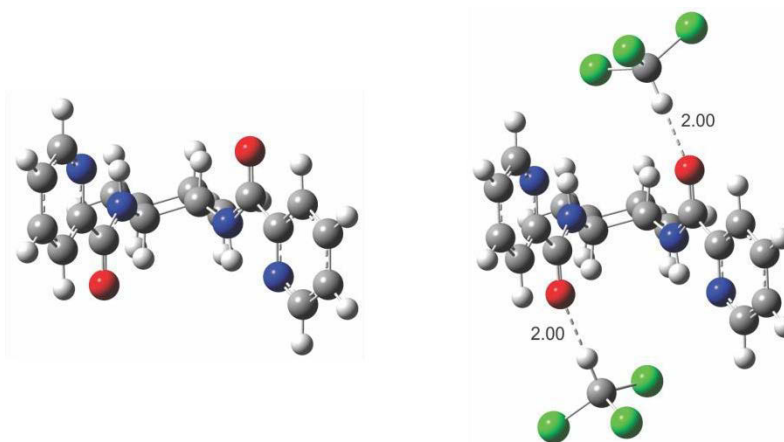


**Figure 2.9.** Geometries of the dominant conformer of SS-3 (left) at the PCM/B3PW91/cc-pVTZ level and of the 1:2 explicit solvated complex of 3 with two molecules of  $\text{CDCl}_3$  (right) at the B3PW91/cc-pVTZ level. The intermolecular hydrogen-bond lengths are given in Å.

### 2.3. Conclusion

---

Three nitrogen-donor ligands, namely, SS-1, SS-2, and SS-3, with different conformational flexibility, have been synthesized and characterized. Their VA and VCD spectra have been measured in the fingerprint region in  $\text{CDCl}_3$ . Systematic searches were carried out to identify the lowest energy conformers in  $\text{CDCl}_3$  by using the implicit solvent model. The explicit hydrogen-bonding solvation model was also evaluated for 3 in  $\text{CDCl}_3$  to adequately explain the observed reverse in sign in the VCD couplet in the amide I region. Good agreement between experimental and theoretical spectra was achieved for all three ligands, leading to the determination of the conformational distributions for all three compounds. This includes the highly flexible compound 2, which has ten most stable conformers with Boltzmann factors ranging from about 2 to 20% at room temperature. Although detailed assignment of VA and VCD spectra becomes tougher with increasing flexibility of molecules, and thus, increasing number of conformers; this work demonstrates that conclusive assignment can nevertheless be achieved. In particular,

although VA spectra of different conformers show only minor differences, the corresponding VCD spectra show exquisite sensitivity to chirality and are, at the same time, highly sensitive to even subtle conformational changes. Such high sensitivity of VCD spectroscopy to chirality and conformations makes it an attractive approach to investigate chirality and structural properties of multidentate nitrogen ligands and their metal complexes in solution.

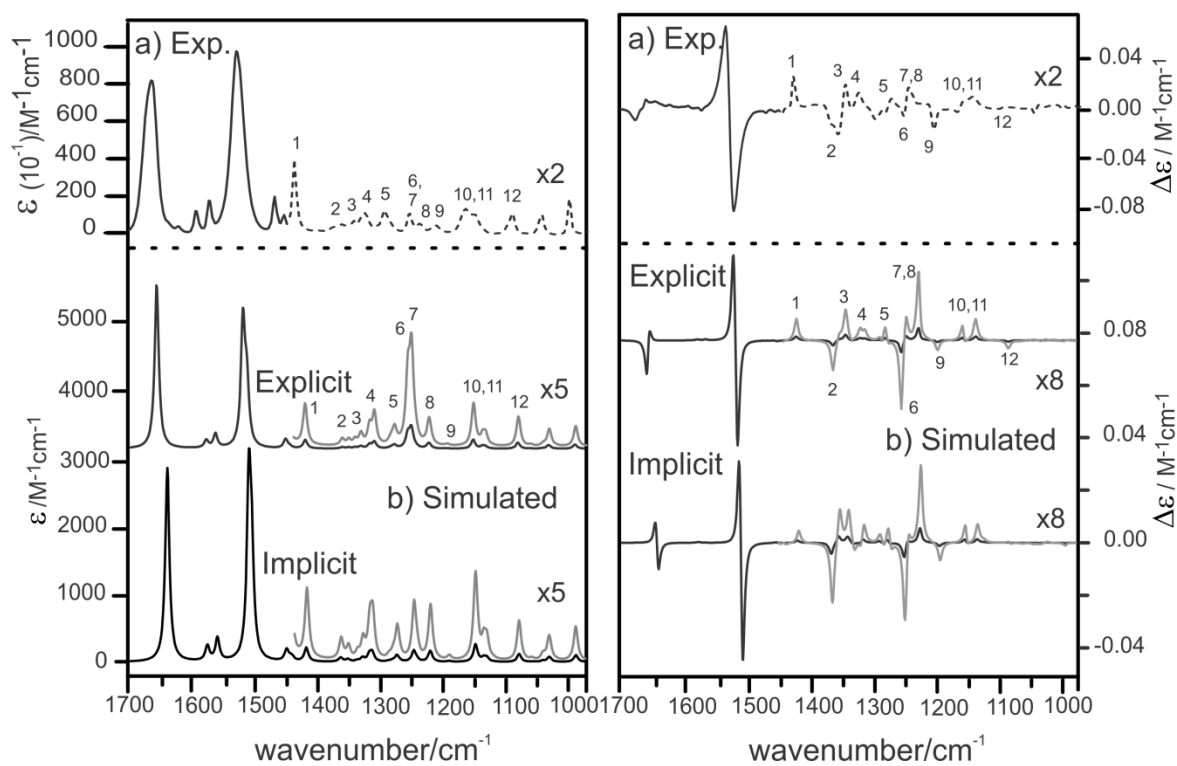


**Figure 2.10.** Comparison of the experimental and calculated VA (left) and VCD (right) spectra of implicit solvated **3** at the PCM/B3PW91/cc-pVTZ level and the explicit solvated complex of **3** with two molecules of CDCl<sub>3</sub> at the B3PW91/cc-pVTZ level. The dotted experimental spectra are taken from the insert in Figure 2.2. A number of bands are labeled to aid a visual comparison (see text for details).

## 2.4. Experimental Section

---

### 2.4.1. Experimental Details

Compounds SS-1 and SS-2 and their opposite enantiomers were synthesized according to a reported experimental procedure. [27] Compound SS-3 compound was purchased from Sigma Aldrich (purity 97%) and used without further purification. All compounds are air stable and unsusceptible to light. Both SS-1 and SS-2 are soluble in dichloromethane, chloroform, toluene, and benzene. These synthesized compounds were fully characterized by several spectroscopic techniques, such as  $^1\text{H}$  and  $^{13}\text{C}$  NMR spectroscopy and mass spectrometry, and shown to be pure. VA and VCD spectra of both enantiomers of these three compounds were recorded with an FTIR spectrometer (Bruker) equipped with a VCD optical bench (PMA 50). Different combinations of concentration and path length were used to optimize the absorbance of each sample to ensure reliable VCD measurements. Solutions with concentrations of about 0.38, 0.37, and 0.30m were prepared for the enantiomeric pairs of SS-1, SS-2, and SS-3 in  $\text{CDCl}_3$  (purity 99.96%, Aldrich), respectively. The optimized path length was 0.1 mm for all compounds in the  $\nu = 1700\text{--}970\text{ cm}^{-1}$  region, except for the enantiomeric pairs of SS-3 for which the experiment was also performed with a shorter path length of 0.025 mm, owing to the strong absorbance in the amide I and amide II regions. All VCD spectra were recorded at  $4\text{ cm}^{-1}$  resolution and with a total data collection time of 3 h (3 x 60 min). The  $\text{BaF}_2$  cell windows were used. Final experimental VCD spectra were baseline corrected by using the difference between the SS and RR enantiomers under the same conditions. [6]

### 2.4.2. Computational Details

Geometry optimizations and harmonic calculations of vibrational frequencies of all conformers, as well as the VA and VCD intensities, were performed by using the Gaussian 09[28] program

package. Lorentzian line shapes with a half width at half height (HWHH) of  $4\text{ cm}^{-1}$  were used to simulate the VA and VCD spectra calculated at the B3PW91/cc-pVTZ level. To evaluate the sensitivity of VA and VCD spectra to functionals and basis sets, calculations of the most stable conformer of SS-1 were performed with several combinations of functionals and basis sets, namely, B3LYP/6-311++(d,p), B3LYP/cc-pVTZ, B3PW91/6-311++(d,p), and B3PW91/cc-pVTZ. The results are summarized in Figure A5 in the Supporting Information. Theoretical VA and VCD spectra obtained were similar to each other, thus demonstrating good theoretical stability with different combinations of functionals and basis sets. The VCD spectra at the B3PW91/cc-pVTZ level showed slightly better agreement with the experimental data. This level of theory was therefore used for all calculations performed herein. The integral equation formalism (IEF) of PCM [29] with application of universal force field (UFF) radii was utilized to account for the implicit solvent effect of  $\text{CDCl}_3$ , for which a dielectric constant of 4.711 was used for chloroform.

## **2.5. Acknowledgements**

---

This research was funded by the University of Alberta and the Natural Sciences and Engineering Research Council of Canada. We thank Nargess Hosseini for her help with the syntheses. We also gratefully acknowledge access to the computing facilities provided by the Academic Information and Communication Technology group at the University of Alberta and by the Western Canada Research Grid (Westgrid). Y.X. holds a Tier I (Senior) Canada Research Chair in Chirality and Chirality Recognition.

## References

- [1] Y. Zhang, L. Xiang, Q. Wang, X. F. Duan, G. Zi, *Inorg. Chim. Acta*, **2008**, 361, 1246–1254.
- [2] A. Ouali, M. Taillefer, J.-F. Spindler, A. Jutand, *Organometallics*, **2007**, 26, 65–74.
- [3] H. Zhang, L. Chen, H. Song, G. Li, *Inorg. Chim. Acta*, **2011**, 366, 320–336.
- [4] a) M. Livieri, F. Mancin, G. Saielli, J. Chin, U. Tonellato, *Chem. Eur. J.* **2007**, 13, 2246–2256; b) Y. Murakami, J. I. Kikuchi, Y. Hisaeda, O. Hayashida, *Chem. Rev.* **1996**, 96, 721–758.
- [5] T. M. Kooistra, K. F. W. Hekking, Q. Knijnenburg, B. de Bruin, P. H. M. Budzelaar, R. De Gelder, J. M. M. Smits, A. W. Gal, *Eur. J. Inorg. Chem.* **2003**, 648–655.
- [6] a) L. A. Nafie, *Vibrational Optical Activity: Principles and Applications*, Wiley, Chichester, **2011**; b) Y. He, B. Wang, R. K. Dukor, L. A. Nafie, *Appl. Spectrosc.* **2011**, 65, 699–723; c) G. Yang, Y. Xu, “Vibrational Circular Dichroism Spectroscopy of Chiral Molecules”, in *Top. Curr. Chem. Volume: Electronic and Magnetic Properties of Chiral Molecules and Supramolecular Architectures* (Eds.: R. Naaman, D. N. Beratan, D. H. Waldeck), Springer, Berlin, **2011**, 298, 189–236.
- [7] a) P. J. Stephens, F. J. Devlin, J. J. Pan, *Chirality*, **2008**, 20, 643–663; b) M. Gbor, T. Gyçrgy, V. Elemr, *Wiley Interdiscip. Rev.: Comput. Mol. Sci.* **2011**, 1, 403–425.
- [8] Y. He, X. Cao, L. A. Nafie, T. B. Freedman, *J. Am. Chem. Soc.* **2001**, 123, 11320–11321.
- [9] C. Johannessen, P. W. Thulstrup, *Dalton Trans.* **2007**, 1028–1033.
- [10] W. Armstrong, F. A. Cotton, A. G. Petrovic, P. L. Polavarapu, M. M. Warnke, *Inorg. Chem.* **2007**, 46, 1535–1537.
- [11] T. Wu, X.-P. Zhang, C.-H. Li, P. Bourç, Y.-Z. Li, X.-Z. You, *Chirality*, **2012**, 24, 451–458.
- [12] Z. Dezhahang, C. Merten, M. R. Poopari, Y. Xu, *Dalton Trans.* **2012**, 41, 10817–10824.
- [13] C. Merten, K. Hiller, Y. Xu, *Phys. Chem. Chem. Phys.* **2012**, 14, 12884–12891.
- [14] H. Sato, F. Sato, M. Taniguchi, A. Yamagishi, *Dalton Trans.* **2012**, 41, 1709–1712.
- [15] H. Sato, Y. Mori, T. Kitazawa, A. Yamagishi, *Dalton Trans.* **2013**, 42, 232–237.
- [16] H. Sato, A. Yamagishi, *Int. J. Mol. Sci.* **2013**, 14, 964–978.
- [17] Z. Dezhahang, M. R. Poopari, Y. Xu, *J. Mol. Struct.* **2012**, 1024, 123–131.
- [18] E. Debie, P. Bultinck, W. Herrebout, B. van der Veken, *Phys. Chem. Chem. Phys.* **2008**, 10, 3498–3508.
- [19] V. P. Nicu, E. Debie, W. Herrebout, B. Van der Veken, P. Bultinck, E. J. Baerends, *Chirality*, **2009**, 21, E287–E297.
- [20] M. R. Poopari, Z. Dezhahang, Y. Xu, *Phys. Chem. Chem. Phys.* **2013**, 15, 1655–1665.
- [21] M. Losada, Y. Xu, *Phys. Chem. Chem. Phys.* **2007**, 9, 3127–3135.
- [22] M. R. Poopari, P. Zhu, Z. Dezhahang, Y. Xu, *J. Chem. Phys.* **2012**, 137, 194308.
- [23] G. Yang, Y. Xu, *J. Chem. Phys.* **2009**, 130, 164506.

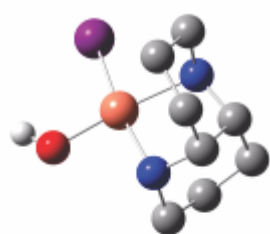
- [24] a) V. P. Nicu, E. J. Baerends, *Phys. Chem. Chem. Phys.* **2009**, *11*, 6107 – 6118; b) V. P. Nicu, E. J. Baerends, *Phys. Chem. Chem. Phys.* **2011**, *13*, 16126 –16129; c) S. Gbi, G. Magyarfalvi, *Phys. Chem. Chem. Phys.* **2011**, *13*, 16130 – 16133; d) V. P. Nicu, J. Neugebauer, E. J. Baerends, *J. Phys. Chem. A* **2008**, *112*, 6978 – 6991.
- [25] K.-K. Lee, S. Hahn, K.-I. Oh, J. S. Choi, C. Joo, H. Lee, H. Han, M. Cho, *J. Phys. Chem. B* **2006**, *110*, 18834 –18843.
- [26] P. Bouř, T. A. Keiderling, *J. Phys. Chem. B* **2005**, *109*, 23687 –23697.
- [27] W. Park, M. H. Shim, J. H. Chung, J. Park, M. S. Lah, D. Lim, *Tetrahedron Lett.* **2006**, *47*, 8841 – 8845.
- [28] Gaussian 09, Revision B.01, M. J. Frisch, G. W. Trucks, H. B. Schlegel, G. E. Scuseria, M. A. Robb, J. R. Cheeseman, G. Scalmani, V. Barone, B. Mennucci, G. A. Petersson, H. Nakatsuji, M. Caricato, X. Li, H. P. Hratchian, A. F. Izmaylov, J. Bloino, G. Zheng, J. L. Sonnenberg, M. Hada, M. Ehara, K. Toyota, R. Fukuda, J. Hasegawa, M. Ishida, T. Nakajima, Y. Honda, O. Kitao, H. Nakai, T. Vreven, J. A. Montgomery, Jr., J. E. Peralta, F. Ogliaro, M. Bearpark, J. J. Heyd, E. Brothers, K. N. Kudin, V. N. Staroverov, R. Kobayashi, J. Normand, K. Raghavachari, A. Rendell, J. C. Burant, S. S. Iyengar, J. Tomasi, M. Cossi, N. Rega, J. M. Millam, M. Klene, J. E. Knox, J. B. Cross, V. Bakken, C. Adamo, J. Jaramillo, R. Gomperts, R. E. Stratmann, O. Yazyev, A. J. Austin, R. Cammi, C. Pomelli, J. W. Ochterski, R. L. Martin, K. Morokuma, V. G. Zakrzewski, G. A. Voth, P. Salvador, J. J. Dannenberg, S. Dapprich, A. D. Daniels, Ö. Farkas, J. B. Foresman, J. V. Ortiz, J. Cioslowski, D. J. Fox, Gaussian, Inc., Wallingford CT, **2009**.
- [29] J. Tomasi, B. Mennucci, R. Cammi, *Chem. Rev.* **2005**, *105*, 2999 – 3093.



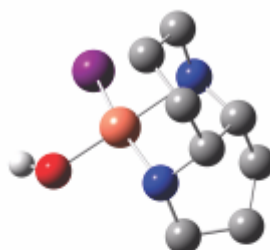
## 3

## Hydrogen bonding interaction with the crystal water in [(R,R)-1,5-Diaza-cis-decalin] copper (II) complex and its conformation: A combined experimental VA and ECD spectroscopic and DFT study

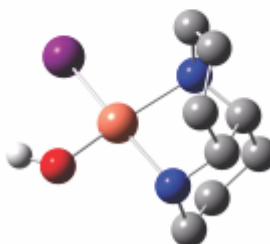
Zahra Dezhahang, Mohammad Reza Poopari, Yunjie Xu



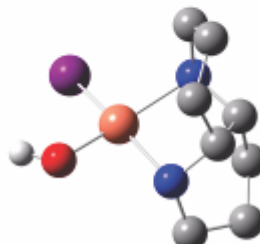
C-I Chair-Chair  
N-in H-ee



C-II Chair-Boat  
N-in H-ee



C-III Boat-Chair  
N-in H-ee



C-IV Boat-Boat  
N-in H-ee

### 3.1. Introduction

---

1,5-Diaza-cis-decalin and its derivatives are important chiral diamine ligands which have found much application in metal-mediated and metal-catalyzed asymmetric organic reactions. For example, it was shown to provide high selectivity with an ee of 90-93% in enantioselective oxidative biaryl coupling reactions [1]. Considerable research efforts have been paid to their syntheses and to the conformational flexibility of the ligand which can have significant impacts on their catalytic ability [2,3,4,5,6,7]. Kozłowski and co-workers investigated the effects of different substitutions at the two amine groups of 1,5-Diaza-cis-decalin and at the decalin ring on the conformational equilibrium position [2,4]. The authors found that these ligands exist in two conformations: N-in and N-out (Scheme 3.1) and that the position of the conformational equilibrium depends mainly on the substitution at the amine groups [2]. Furthermore, the catalytic properties of 1,5-Diaza-cis-decalin, a highly stable bidentate ligand, can vary noticeably with different metal center atoms. For example, the catalytic ability of several complexes formed using 1,5-Diaza-cis-decalin ligand and a few different metals was evaluated for the oxidative asymmetric biaryl coupling of 3-substituted 2-naphthols [7]. In all these studies, it is recognized that the conformations of the chiral metal complexes are an important deciding factor in their catalytic abilities. It is therefore of considerable interest to carry out conformational analysis of the [(R,R)-1,5-Diaza-cis-decalin] and its copper (II) hydroxide Iodine hydrate complex.

Several spectroscopic methods, namely electronic circular dichroism (ECD) and vibrational absorption (VA), and ultraviolet/visible (UV-Vis) spectroscopy have been utilized in this study, in combination with Density Functional Theory (DFT) calculations. Such combinations have been used extensively in the last few years to obtain information about conformations and absolute configurations of many important chiral biological, organic, and inorganic molecules

[1,8,9], thanks to the noticeable theoretical advances. Furthermore, in recent years, the effects of hydrogen bonding have been hypothesized as a possible cause of the discrepancy between calculated and experimental ECD spectra [10], although little has been reported on the subject [11,12]. The copper (II) compound available commercially contains one crystal water molecule. It would therefore be of substantial interest to investigate whether the hydrogen bonding between the copper (II) complex and water has any important effects on the appearance of ECD spectrum. In the present investigation, the VA measurement, and the UV–Vis and ECD measurements of the titled copper complex have been performed using a KBr pellet and in acetonitrile solutions, respectively. Extensive conformational analyses have been carried out for 1,5-diaza-cis-decalin ligand, the corresponding [(R,R)-1,5-diazacis-decalin] copper (II) hydroxide iodine complex, and the associated hydrogen bonded cluster consisting of the copper (II) complex and one additional water molecule using DFT. The experimental VA, UV–Vis and ECD spectra have been compared to the simulated data using DFT and time dependent (TD)-DFT. Important conclusions about the conformations of the complex and the effects of hydrogen bonding interaction on the appearance of these spectra have been obtained.

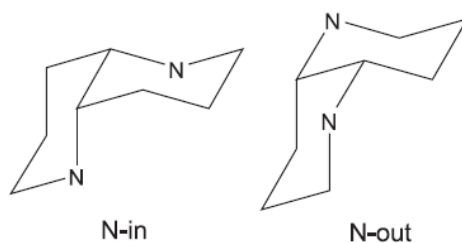
## **3.2. Experimental and theoretical details**

---

### *3.2.1. Spectroscopic measurements*

[(R,R)-1,5-diaza-cis-decalin] copper (II) hydroxide iodine hydrate was purchased from Sigma Aldrich (Canada) and used without any further purification. The UV and ECD measurements were carried out using a HP 8453 UV–Vis instrument and Olis DSM 17 CD spectrophotometer, respectively. A path-length of 0.5 cm was used for the UV–Vis and ECD measurements. Solutions of the copper (II) complex in acetonitrile with a concentration of  $3.4 \times 10^{-5}$  M and  $1.1 \times 10^{-3}$  M were used for the UV and ECD measurements in the 190–300 nm and 300–500 nm

regions, respectively, because of the low absorption intensity in the longer wavelength region. The VA measurements in the finger print region from 700 to 1800  $\text{cm}^{-1}$  were performed using a KBr pellet with a 0.6% concentration using VERTEX 70 FTIR spectrometer (Bruker) module [13]. It is in principle possible to obtain a vibrational CD (VCD) measurement of the KBr pellet. However, we found that the artefacts were too severe and no solid state VCD measurements were further pursued in the present study. The targeted copper complex has very low solubility in all common solvents such as methanol, water, chloroform, and acetonitrile, with the highest solubility in acetonitrile. Even in acetonitrile (both normal and  $\text{CD}_3\text{CN}$ ), we were not able to obtain reliable VA spectral features because the solvent absorption features in the same spectral range completely overwhelm those of the complex. Consequently, we were not able to obtain solution VCD spectra either.



**Scheme 3.1.** Two main conformations of 1,5-diaza-cis-decalin ligand identified in Refs. [2,6].

Both N atoms are in the proximal position in N-in, and both N atoms are in the distal position in N-out.

### 3.2.2. Theoretical calculations

The geometry optimizations, vibrational frequencies, and VA and VCD intensities, as well as frequencies and intensities of UV and ECD spectra have been performed using the Gaussian03 program package [14]. B3LYP exchange correlation functional has been widely used for structural studies of transition metal complexes with reliable results [15–18]. It is also known to provide structural and VA and VCD spectral predictions in good agreement with the experimental data for hydrogen-bonded systems [19–23]. Therefore, geometry optimizations of the ligand and the copper complex without and with the hydrogen bonded water molecule were carried out at this level of theory with 6-31++G(d,p) for the ligand and with LanL2DZ basis set for the copper complex. The corresponding Boltzmann population analyses based on the relative energies and Gibbs free energies were performed. To confirm that the optimized geometries were true minima, their harmonic frequency calculations were checked to be without any imaginary frequencies. The predicted harmonic VA frequencies are not scaled in the current study. The calculations of the corresponding UV–Vis and ECD spectra were completed using TD-DFT. To simulate the VA and VCD spectra, a Lorentzian line shape with a half width at half maximum of  $4\text{ cm}^{-1}$  was used, whereas a half width at half maximum of 0.3 eV was used for the UV–Vis and ECD simulations [24]. To account for the solvent effects in the UV–Vis and ECD solution measurements, the integral equation formalism (IEF) version of implicit polarization continuum model (PCM) [25,26] as implemented in Gaussian 03 was applied. Within this model, the  $\text{CH}_3\text{CN}$  solvent was treated as a continuum dielectric environment and a permittivity value of  $\epsilon_0=36.64$  was used. No scaling factor was applied to the predicted electronic transition wavelengths in this paper.

### **3.3. Results and discussions**

---

### 3.3.1. Conformational analysis and spectral simulation of the [(R,R)-1,5-diaza-cis-decalin] ligand

Two major conformations, associated with the proximal and distal position of the N atoms, of 1,5-diaza-cis-decalin, had been discussed before in literature [2,6]. Since chiroptical measurements can be quite sensitive to even the more subtle conformations resulted from different orientations of the amine hydrogen atoms in the ligand [27], a further conformational search was carried out. For the N-in and N-out conformations, the H atoms of the two amine groups can be either in the equatorial (e) position or axial (a) position, giving rise to three conformations, labeled as H-ee, H-ea and H-aa, in each case. This resulted in a total of six conformers as shown in Figure 3.1.

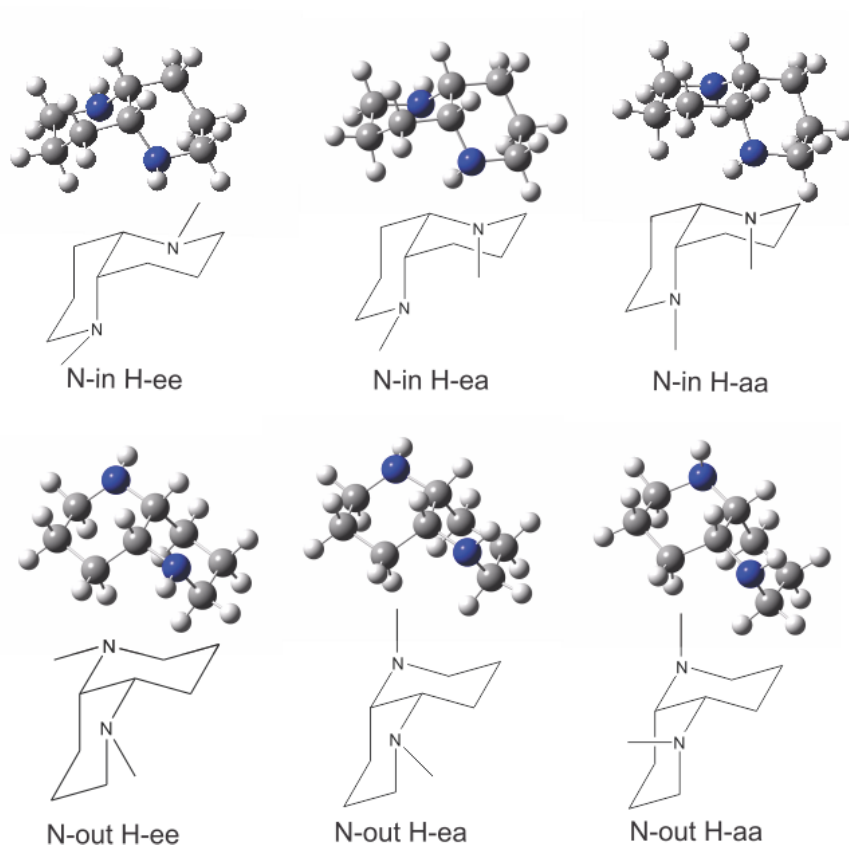


**Figure 3.1.** Six most stable conformers of the Chair–Chair 1,5-diaza-cis-decalin ligand at the B3LY/6-31++G(d,p) level of theory.

It should be pointed out here that in all these six conformations, the decalin rings have been kept in the Chair–Chair conformation which has a close to 100% Boltzmann population factor based on the relative Gibbs free energies, as discussed in the next paragraph. Please note that H-ea and H-ae are the same here since the two decalin rings are identical. The calculated relative energies and Gibbs free energies are listed in Table 3.1, together with the corresponding percentage Boltzmann population factors at room temperature based on the relative energies and Gibbs free energies. From Table 3.1, one can conclude that the N-in conformers are much more stable than the N-out conformers and that the N-in H-ea conformer is the most stable ligand conformer with a dominating Boltzmann factor of 88% at room temperature.

**Table 3.1.** Calculated relative energies, Gibbs free energies, and the corresponding percentage Boltzmann population factors at room temperature of the six most stable conformers of the Chair–Chair 1,5-diaza-cis-decalin ligand at the B3LYP/6-31++G(d,p) level.

Conformers of ligand	$\Delta E^\circ$ (kcal/mol)	$\Delta G^\circ$ (kcal/mol)	Pop% ( $\Delta E^\circ$ )	Pop% ( $\Delta G^\circ$ )
N-in Hee	0.50	1.14	21.12	12.19
N-in Hea	0.00	0.00	48.84	82.98
N-in Haa	0.80	1.86	12.65	3.60
N-out Hee	1.19	3.19	6.58	0.38
N-out Hea	1.23	2.84	6.14	0.68
N-out Haa	1.39	3.66	4.67	0.17

Clearly, the nitrogen atoms favor the proximal position, i.e. N-in, consistent with the finding reported previously [2]. The two amine hydrogen atoms, on the other hand, prefer to occupy two different positions, i.e. one axial and one equatorial. This might be due to an energetically favorable interaction between the axial hydrogen atom with the other nitrogen atom in the H-ea

conformation while none of the other five conformers can enable such an interaction. Indeed, the distance of N(axial) and H(equatorial),  $r_{\text{N(axial)} \cdots \text{H(equatorial)}}$ , is about 2.72 Å, considerably shorter than a regular van der Waals distance [28]. Besides the conformations associated with the amine N and H atoms, the decalin rings can also take on different conformations, such as Chair–Chair, Chair–Boat, Boat–Chair, and Boat–Boat, although only the Chair–Chair conformation had been explicitly considered in the previous literature [2,3,6]. For completion, we used two most stable conformers, i.e. N-in H-ea and N-in H-ee, as starting points for considering the decalin ring conformations. This resulted in four ring conformers of N-in H-ea and three of N-in H-ee, which are depicted in Figure 3.2.

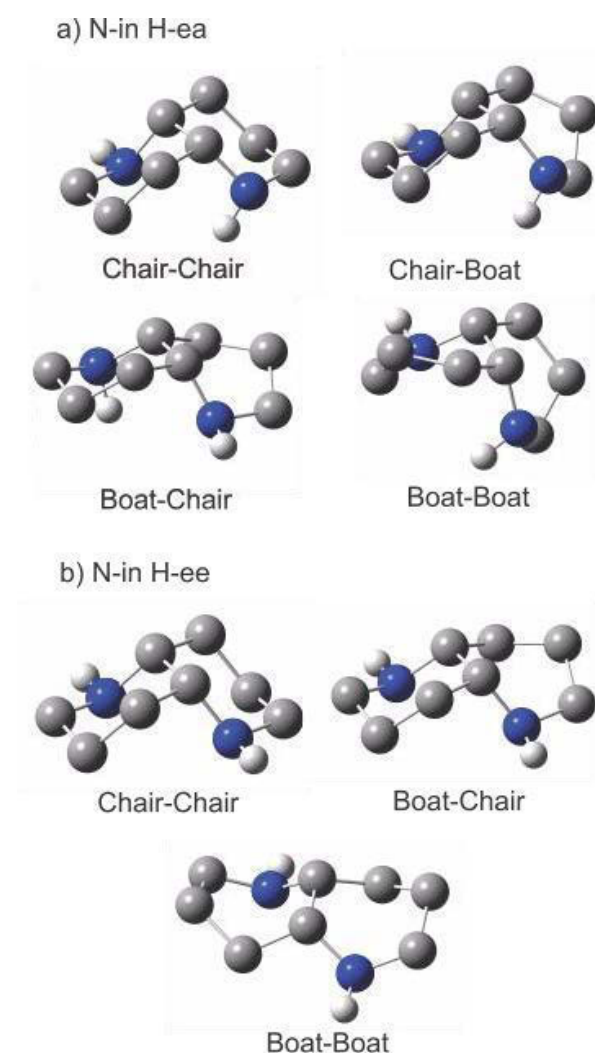




**Figure 3.2.** Geometries of the decalin ring conformers of (a) N-in H-ea and (b) N-in H-ee 1,5-diaza-cis-decalin ligand at the B3LY/6-31++G(d,p) level. Hydrogen atoms attached to the carbon atoms are not displayed for simplicity.

The corresponding relative energies and Gibbs free energies are provided in Table 3.2. Clearly, the Chair–Chair conformers are by far the most stable structures in the gas phase with a close to 100% Boltzmann population factor at room temperature in both cases. We therefore considered only the Chair–Chair conformation in the spectral simulation of the ligand.

**Table 3.2.** Calculated relative energies, relative Gibbs free energies and the corresponding percentage Boltzmann population factors at room temperature of the decalin ring conformers of the N-in H-ea and N-in H-ee 1,5-diaza-cis-decalin ligands at the B3LYP/6-31++G(d,p) level.

Conformers of ligand	$\Delta E^\circ$ (kcal/mol)	$\Delta G^\circ$ (kcal/mol)	Pop% ( $\Delta E^\circ$ )	Pop% ( $\Delta G^\circ$ )
<b>Four decalin ring conformers of N-in H-ea</b>				
Chair-Chair	0.00	0.00	100.00	99.99
Chair-Boat	6.61	5.99	0.00	0.00
Boat-Chair	6.23	5.80	0.00	0.01
Boat-Boat	13.59	12.97	0.00	0.00
<b>Three decalin ring conformers of N-in H-ee</b>				
Chair-Chair	0.00	0.00	100.00	99.98
Chair-Boat	11.37	8.87	0.00	0.01
Boat-Boat	13.59	10.48	0.00	0.00

The VA and VCD spectra of the six most stable Chair–Chair ring conformers are shown in Figure 3.3. While the three N-out conformers have fairly similar VA spectra, the VA spectra of the three N-in conformers are noticeably different among themselves and from those of the N-out conformers, especially in the 600–800  $\text{cm}^{-1}$  region. The bands in the 600–800  $\text{cm}^{-1}$  region correspond mainly to those associated with the N–H bending motion. Clearly, different placements of the nitrogen atoms in the decalin rings are responsible for this. The equatorial and

axial orientations of the amine hydrogen atoms introduce only minor differences in the VA spectra of the N-out conformers. In contrast, such orientations have very noticeable effects on the appearance of VA spectra of the N-in conformers, most likely due to the forming and breaking of the intramolecular hydrogen bond (or at least strong interaction) between the N and H atoms. The VCD spectra of the six conformers are as expected very different from each other because of the high sensitivity of VCD spectra to variations in dihedral angles. Unfortunately, 1,5-diaza-cis-decalin ligand is not available commercially and no experimental VA and VCD data of the ligand have been obtained.

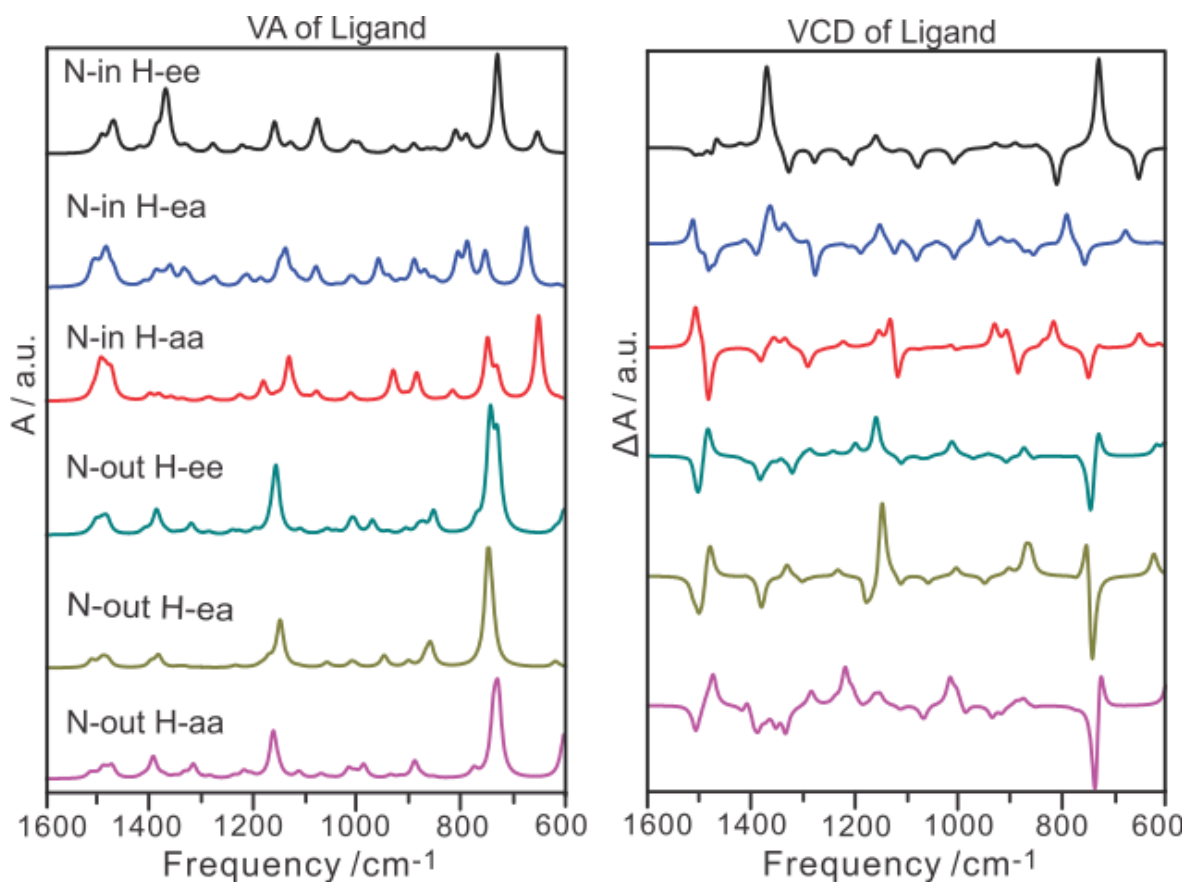


**Figure 3.3.** Simulated VA and VCD spectra of the six most stable conformers of the Chair–Chair 1,5-diaza-cis-decalin ligand listed in Table 3.1 at the B3LYP/6-31++G(d,p) level.

The UV–Vis and ECD spectra of the two most stable Chair–Chair ring conformers, i.e. N-in H-*ea* and N-in H-*ee*, have also been simulated with TDDFT in order to compare to the experimental ECD spectrum reported in Ref. [3]. To account for the effects of CH<sub>3</sub>CN solvent, the geometries of these two conformers have been re-optimized with PCM of CH<sub>3</sub>CN and the related spectra simulated. These simulated UV–Vis and ECD spectra are summarized in Figure 3.4. The effects of a polar solvent on the appearances of the UV–Vis and ECD spectra of a range of chiral molecules [29] have been investigated theoretically using the conductor-like screening model (COSMO) [30, 31] and PCM, both of the continuum solvent model type. For a conformationally rigid system, such as methyloxirane [29] and [Co(en)<sub>3</sub>]<sup>3+</sup> [32], the inclusion of the continuum solvent model seems to only shift some band frequencies and relative band intensities slightly in UV–Vis spectra and introduce minor changes in the shapes of ECD spectra [32]. For a more flexible system, such as 3,3',4,4',7-flavanpental [33], the ECD features of some conformers experience more dramatic intensity alternations, while others remain more or less the same. From Figure 3.4, one can see that the inclusion of PCM produced only minor changes in the appearance of the UV–Vis and ECD spectra. It is interesting to note that the ECD spectra for these two conformers appear quite different. The simulated ECD spectrum of N-in H-*ea* shows a positive broad first Cotton band in the longer wavelength region, in good agreement with the observed spectrum for (R,R)- 1,5-diaza-cis-decalin reported in Ref. [3]. The simulated ECD spectrum of N-in H-*ee*, on the other hand, shows essentially no ECD activity in the same region. The comparison of the simulated and experimental ECD data therefore supports the conclusion that N-in H-*ea* is the dominant ligand conformer at room temperature.

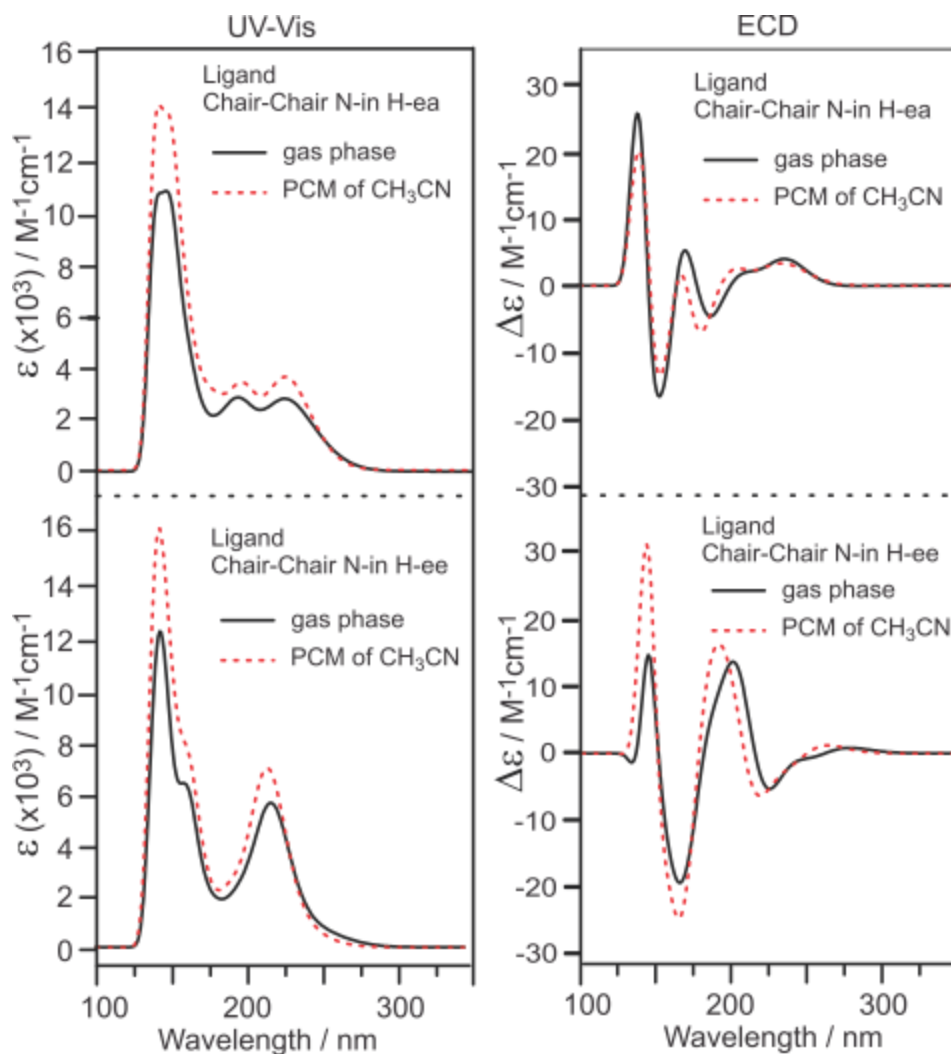


**Figure 3.4.** Simulated UV–Vis and ECD spectra of the two most stable conformers of Chair–Chair [(R,R)-1,5-diaza-cis-decalin] ligand in the gas phase and with PCM of CH<sub>3</sub>CN solvent at the B3LYP/6-31++G(d,p) level.

### 3.3.2. Conformational analysis and spectral simulations of the [(R,R)-1,5-diaza-cis-decalin] copper (II) hydroxide iodine complex

As discussed in the previous section, the 1,5-diaza-cis-decalin ligand strongly prefers the Chair–Chair conformation for the decalin rings, the N-in conformation for the nitrogen atoms, and the ea conformation for the amine hydrogen atoms. On the other hand, based on the geometric

consideration and the results from previous studies [2,3], only the N-in H-ee ligand conformers are capable of forming coordination bonds to the copper atom. Consequentially, the coordination to the copper atom must have moved the equilibrium towards the N-in H-ee ligand conformer from the dominating N-in H-ea ligand conformer. It would also be interesting to investigate if binding to copper can also alter the preferred conformation of the decalin rings. Therefore, four N-in H-ee conformers of the copper complex were constructed where each decalin ring can have either chair or boat conformations. These are Chair–Chair, Chair–Boat where the iodine ligand is adjacent to the Chair ring, Boat–Chair where the iodine ligand is adjacent to the Boat ring, and Boat–Boat. The optimized geometries of these four conformers are presented in Figure 3.5 and the calculated relative energies and relative Gibbs free energies are summarized in Table 3.3, together with the corresponding percentage Boltzmann population factors at room temperature. As one can see, the Chair–Chair conformer is still favoured with a commanding Boltzmann population factor of 99%, while the rest of conformers have only negligible contributions at room temperature. This indicates that while the preferred orientation of the amine H atoms changes from ea to ee to accommodate the coordination binding, the coordination to copper imposes little effect on the preferred geometries taken by either the decalin rings or the N-atoms.

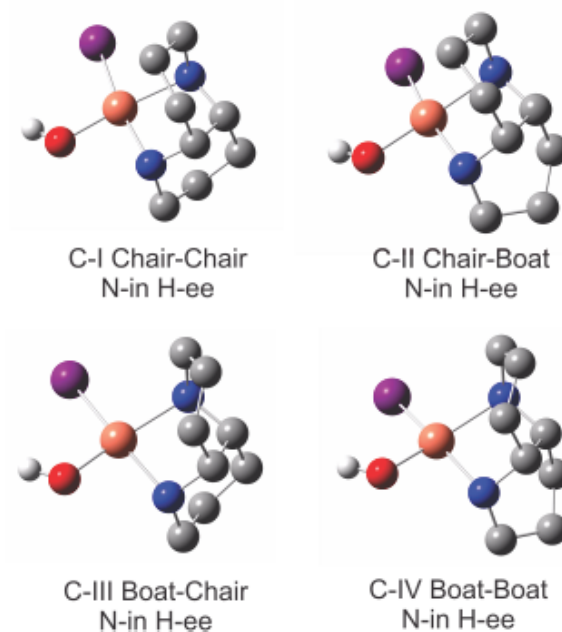


**Figure 3.5.** Optimized geometries of the four decalin ring conformers of N-in H-ee [(R,R)-1,5-diaza-cis-decalin] copper (II) hydroxide iodine complex at the B3LYP/ LanL2DZ level. Hydrogen atoms attached to the carbon atoms are not displayed for simplicity.

**Table 3.3.** Calculated relative energies, relative Gibbs free energies and the corresponding percentage Boltzmann population factors at room temperature of the four conformers of [(R,R)-1,5-diaza-cis-decalin] copper (II) hydroxide iodine complex at the B3LYP/ LanL2DZ level.

Conformers of complex	$\Delta E^\circ$ (kcal/mol)	$\Delta G^\circ$ (kcal/mol)	Pop% ( $\Delta E^\circ$ )	Pop% ( $\Delta G^\circ$ )
C-I Chair-Chair N-in Hee	0.00	0.00	99.96	99.94
C-II Chair-Boat N-in Hee	5.17	4.75	0.02	0.03
C-III Boat-Chair N-in Hee	5.17	4.90	0.02	0.03
C-IV Boat-Boat N-in Hee	9.78	9.33	0.00	0.00

The simulated VA and VCD spectra of the above four conformers of the copper complex are depicted in Figure 3.6. The experimental VA spectrum of [(R,R)-1,5-diaza-cis-decalin] copper (II) hydroxide iodine hydrate measured with a translucent KBr pellet is also shown in Figure 3.6a for comparison. The VA spectra of all four conformers show similar main features although

some minor differences exist. The main VCD features, on the other hand, are more different among these conformers. This is consistent with the general observation that VCD spectra are more sensitive to conformational changes than the related VA spectra. The observed VA spectrum, however, shows little resemblance to that of the most stable conformer, i.e. C-I Chair–Chair N-in H-ee conformer, of [(R,R)-1,5-diaza-cis-decalin] copper (II) hydroxide iodine complex, or to those of any other minor conformers. Since a complete conformational search has been carried out for the complex, the disagreement between the experimental and the simulated spectra suggests that one may need to consider the crystal water molecule in the simulation. This point will be addressed in Section 3.3.3.

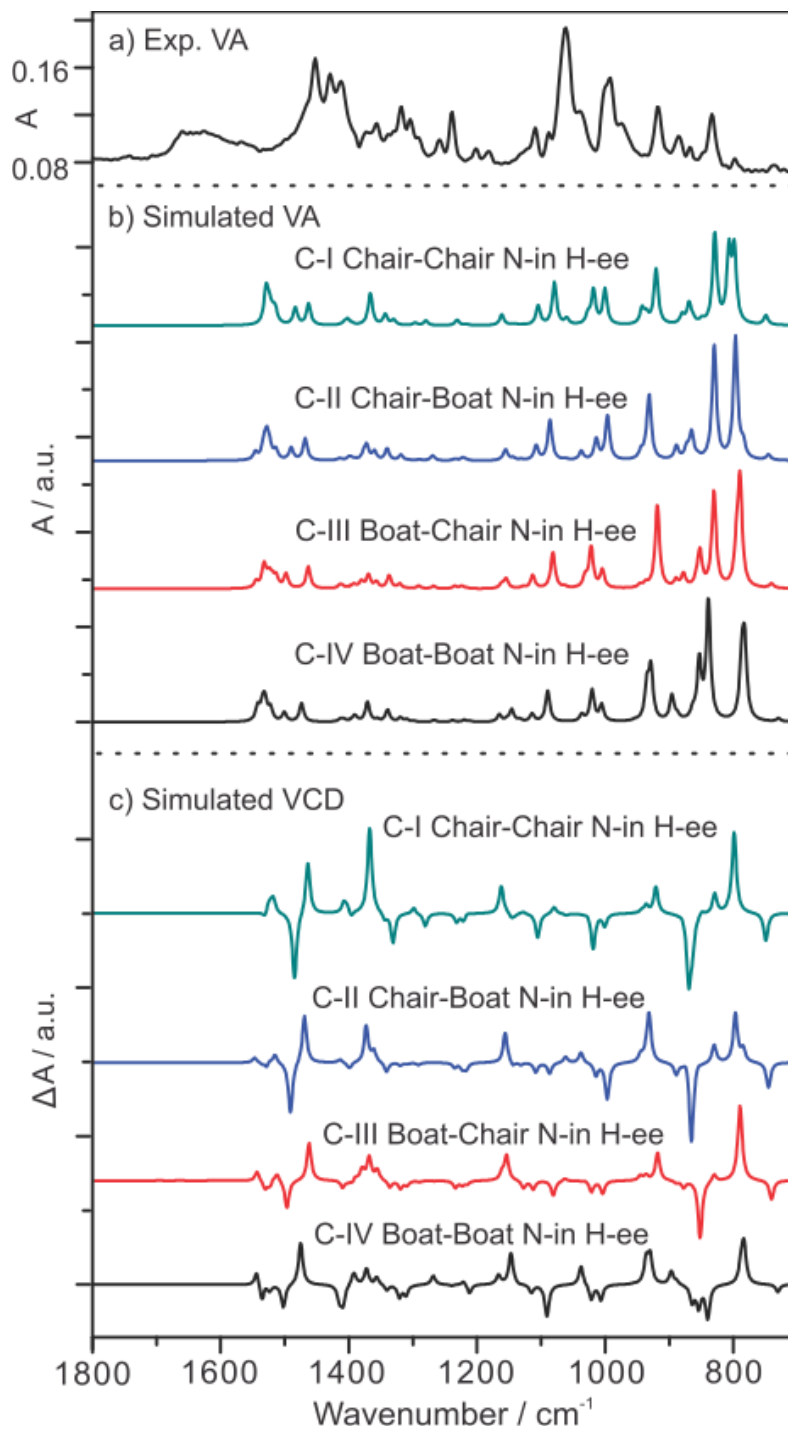


**Figure 3.6.** Simulated VA and VCD spectra of the four conformers of [(R,R)-1,5-diazacisdecalin] copper (II) hydroxide iodine complex listed in Table 3.3 at the B3LYP/ LanL2DZ level. The experimental VA spectrum obtained with a KBr pellet is also included for comparison.



The simulated UV–Vis and ECD spectra of the above four conformers of the copper complex are depicted in Figure 3.7, together with the experimental UV–Vis and ECD spectra of the [(R,R)-1,5-diazacis-decalin] copper (II) hydroxide iodine hydrate measured in CH<sub>3</sub>CN solution. All the conformers show similar simulated UV–Vis spectra, whereas some minor differences can be seen in the related ECD spectra. The experimental UV–Vis spectrum can be correlated to the simulated UV–Vis features reasonably well. The experimental ECD spectrum, however, shows little resemblance to that of any conformer, including the dominant conformer, C-I Chair–Chair N-in H-ee of the complex. We therefore hypothesized that the hydrogen bonding interaction between the complex and the crystal water molecule may be responsible for the disagreement between theory and experiment, just as in the case of the VA comparison discussed above. This issue will be addressed in Section 3.3.3.

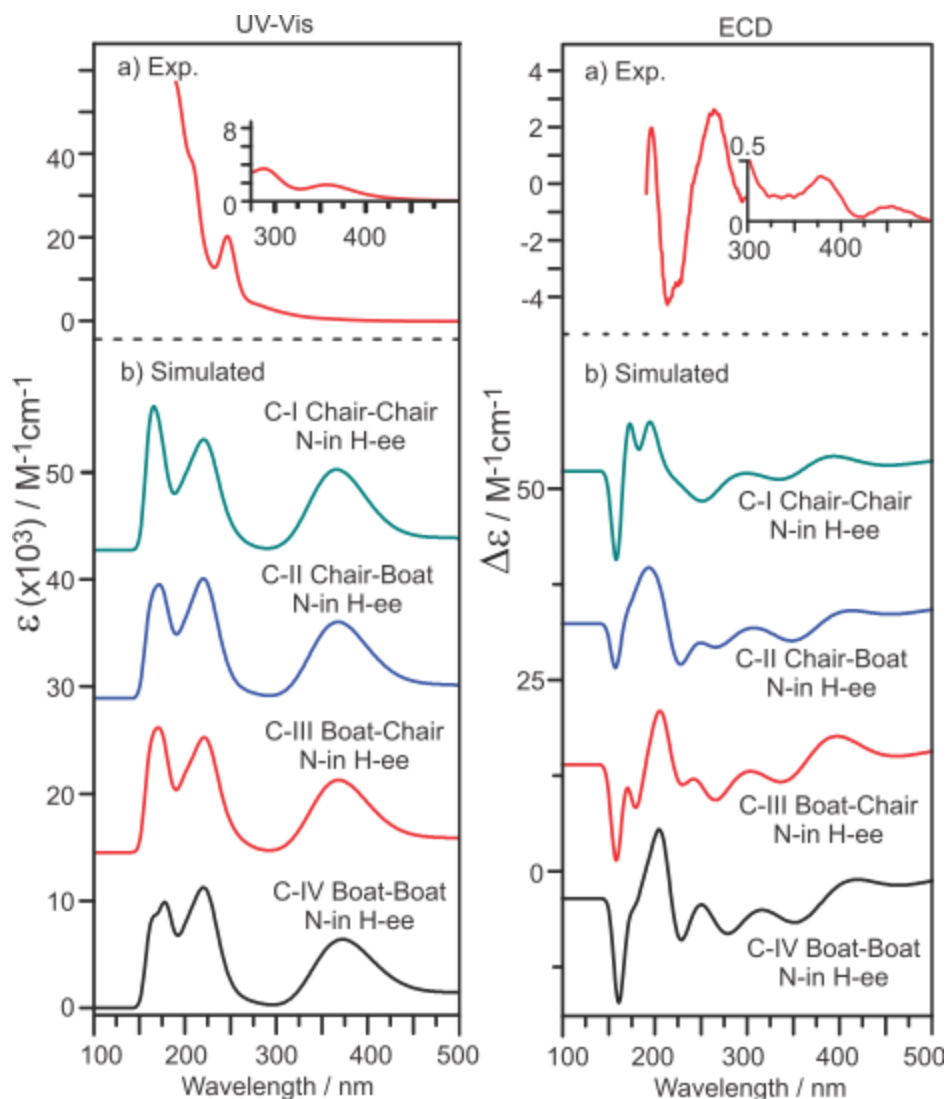


**Figure 3.7.** Simulated UV–Vis and ECD spectra of the four conformers of [(R,R)-1,5- diaza-cis-decalin] copper (II) hydroxide iodine complex listed in Table 3.3 at the B3LYP/LanL2DZ level. The experimental UV–Vis and ECD spectra obtained in CH<sub>3</sub>CN solution are also included for comparison. The inserts were measured with a higher concentration (see Section 3.2.1 for details).

### 3.3.3. Hydrogen bonding effects on the VA, VCD, UV-Vis and ECD spectra of the [(R,R)-1,5-diaza-cis-decalin] copper (II) hydroxide iodine complex

There is one water molecule for each coordination complex in the sample purchased from Sigma Aldrich. It had been demonstrated both theoretically and experimentally that hydrogen bonding interactions with water molecules can have dramatic effects on the VCD spectral signatures [8, 22, 34, 35]. This encouraged us to investigate the effects of the hydrogen bonding interaction of the copper complex with water on the spectra observed. A water molecule can bind to the copper complex with two hydrogen bonds simultaneously. This resulted in three possible geometries using the dominant C-I Chair–Chair N-in H-ee conformer as the starting point. The main conformer, W-I ( $\text{NH}_d\text{--O}_a$ ), refers to the conformer of the hydrogen bonded cluster where the amine H and O atoms of the copper complex serve as the proton donor and acceptor to simultaneously form the  $\text{NH}\dots\text{OwHw}$  and  $\text{OwHw}\dots\text{O}$  hydrogen bonds, respectively. Here Ow and Hw are the oxygen and hydrogen atoms of water, respectively. We use “W” to signify the inclusion of the crystal water molecule. This conformer has a 100% Boltzmann population factor at room temperature. The next most stable conformer, W-II ( $\text{NH}_d\text{--I}_a$ ), designates the hydrogen bonding conformer with the  $\text{NH}\dots\text{OwHw}$  and  $\text{OwHw}\dots\text{I}$  hydrogen bonds. The third most stable conformer, W-III ( $\text{OH}_d\text{--I}_a$ ), refers the conformer containing the  $\text{OH}\dots\text{OwHw}$  and  $\text{OwHw}\dots\text{I}$  hydrogen bonds. The most stable one has two strong hydrogen bonds involving the highly electronegative N and O atoms. The other two, on the other hand, contain one  $\text{OwHw}\dots\text{I}$  hydrogen bond in addition to the  $\text{NH}\dots\text{OwHw}$  or  $\text{OH}\dots\text{OwHw}$  bond. Since the iodine ligand is bigger and less electronegative than the oxygen and nitrogen atoms involved in a hydrogen bond, it is not surprising that  $\text{NH}_d\text{--O}_a$  is the most stable conformer among them. The corresponding theoretical relative energies and relative Gibbs free energies are listed in Table 3.4, while the

optimized geometries are given in Figure 3.8 where the intermolecular hydrogen bond lengths are indicated.

**Table 3.4.** Calculated relative energies, relative Gibbs free energies and the corresponding percentage Boltzmann population factors at room temperature of the three most stable hydrogen bonded conformers of C-I Chair–Chair N-in H-ee [(R,R)-1,5-diaza-cis-decalin] copper (II) hydroxide iodine complex with the crystal water at the B3LYP/LanL2DZ level.

Conformers of complex	$\Delta E^\circ$ (kcal/mol)	$\Delta G^\circ$ (kcal/mol)	Pop% ( $\Delta E^\circ$ )	Pop% ( $\Delta G^\circ$ )
W-I (NH <sub>d</sub> -O <sub>a</sub> )	0.00	0.00	100.00	100.00
W-II (NH <sub>d</sub> -I <sub>a</sub> )	9.98	8.97	0.00	0.00
W-III (OH <sub>d</sub> -I <sub>a</sub> )	15.48	15.48	0.00	0.00

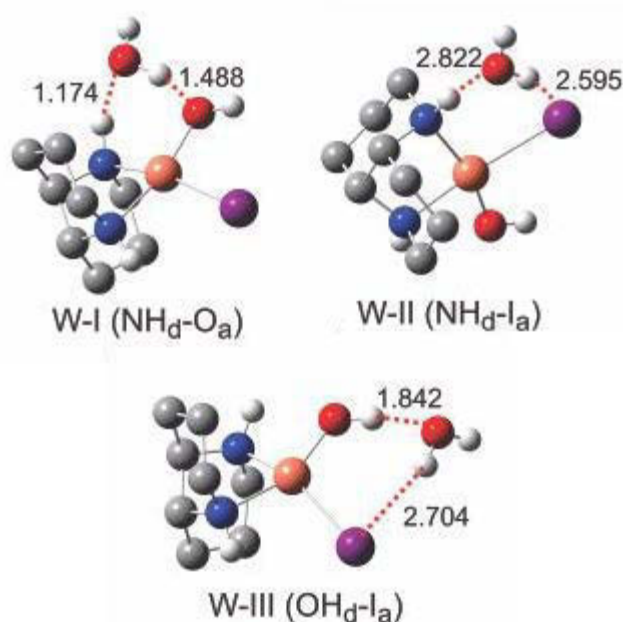


**Figure 3.8.** Geometries of the three most stable conformers of the hydrogen bonded cluster of C-I Chair–Chair N-in H-ee [(R,R)-1,5-diaza-cis-decalin] copper (II) hydroxide iodine complex with a crystal water molecule obtained at the B3LYP/LanL2DZ level. Hydrogen atoms attached to the carbon atoms are not displayed for simplicity. The important hydrogen bond lengths (in Å) are also indicated.

The simulated VA and VCD spectra of these water hydrogen bonded conformers are depicted in Figure 3.9, together with the experimental VA spectrum of the complex. First of all, the hydrogen bonding interaction with water at different binding sites introduces significant differences to both VA and VCD spectra among the three conformers. Second, the hydrogen bonding interaction with water also leads to drastic changes in the VA and VCD spectra, compared to those of the starting conformer, C-I Chair–Chair N-in H-ee (Figure 3.6), where water was not included. There are two strong bands at  $1056\text{ cm}^{-1}$  and  $1684\text{ cm}^{-1}$  in the W-I VA spectrum which correspond mainly to the bending of OH group in the complex and that of water, respectively, and which do not show up as prominently or at all in the VA spectrum of C-I Chair–Chair N-in H-ee. The VA pattern predicted for W-I correlated very well with the observed VA spectrum measured with a KBr pellet, whereas the other two conformers alone show much poorer agreement. This indicates that W-I is the dominant conformational structure favoured at room temperature. It is plausible that W-II and W-III also make some minor contributions to the observed VA spectrum since the water bending band observed is quite broad, suggesting that the local environment to water is not uniform. The comparison discussed above clearly demonstrates the importance of including crystal water in such simulations.

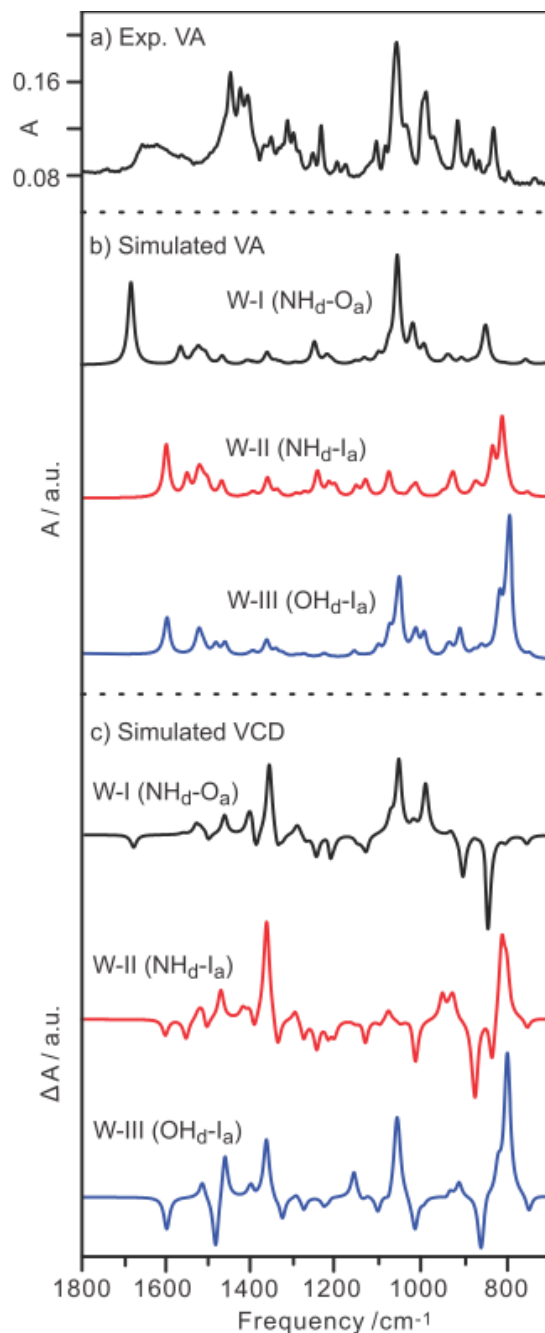


**Figure 3.9.** Comparison of the experimental VA spectrum of the copper complex obtained with a KBr pellet with the simulated VA and VCD spectra of the three most stable hydrogen bonded conformers of C-I Chair–Chair N-in H-ee [(R,R)-1,5-diazacis-decalin] copper (II) hydroxide iodine complex with water, listed in Table 3.4, at the B3LYP/LanL2DZ level.

The corresponding simulated UV–Vis and ECD spectra of the hydrogen bonded clusters of the copper complex with water are given in Figure 3.10, together with the experimental UV–Vis and ECD spectra. The two strong absorption bands observed at the shorter wavelength region were well captured by the simulated UV–Vis spectra of all three conformers since there are no significant differences among them. In general, the TDDFT method seems to underestimate the wavelengths of these strong electronic transitions. In the longer wavelength region, two experimental bands (insert of Figure 3.10) are visible with much lower relative intensities than the two in the shorter wavelength region. This can be compared to the simulated band with a very broad profile, although it was predicted with much higher relative intensity than that observed experimentally. Since the UV–Vis spectra for all three water containing conformers are similar, it is difficult to conclude which one of them dominates in solution. In the 190–300 nm range, the experimental ECD spectrum shows a series of prominent ECD features with sequentially positive–negative–positive (+/-/+) signs. This correlated well with the predicted ECD spectrum of W-I in the short wavelength region. The predicted ECD spectra of W-II and W-III are noticeably different from the experimental one. For example, W-III exhibits a series of ECD features with sequentially negative–positive–negative (-/+/-) signs in the shorter wavelength region, almost exactly the opposite of what was detected experimentally. In the longer wavelength region, the ECD spectrum measured with a higher concentration was again qualitatively captured by the W-I conformer. Overall, the comparison of the experimental and simulated ECD spectra discussed above led to the conclusion that W-I is the dominant species in solution at room temperature. It is gratifying to see that the detailed VA analysis pointed to the same conclusion that W-I is the main species at room temperature. Clearly, the inclusion of the crystal water in modeling is essential for achieving such consistent conclusions.

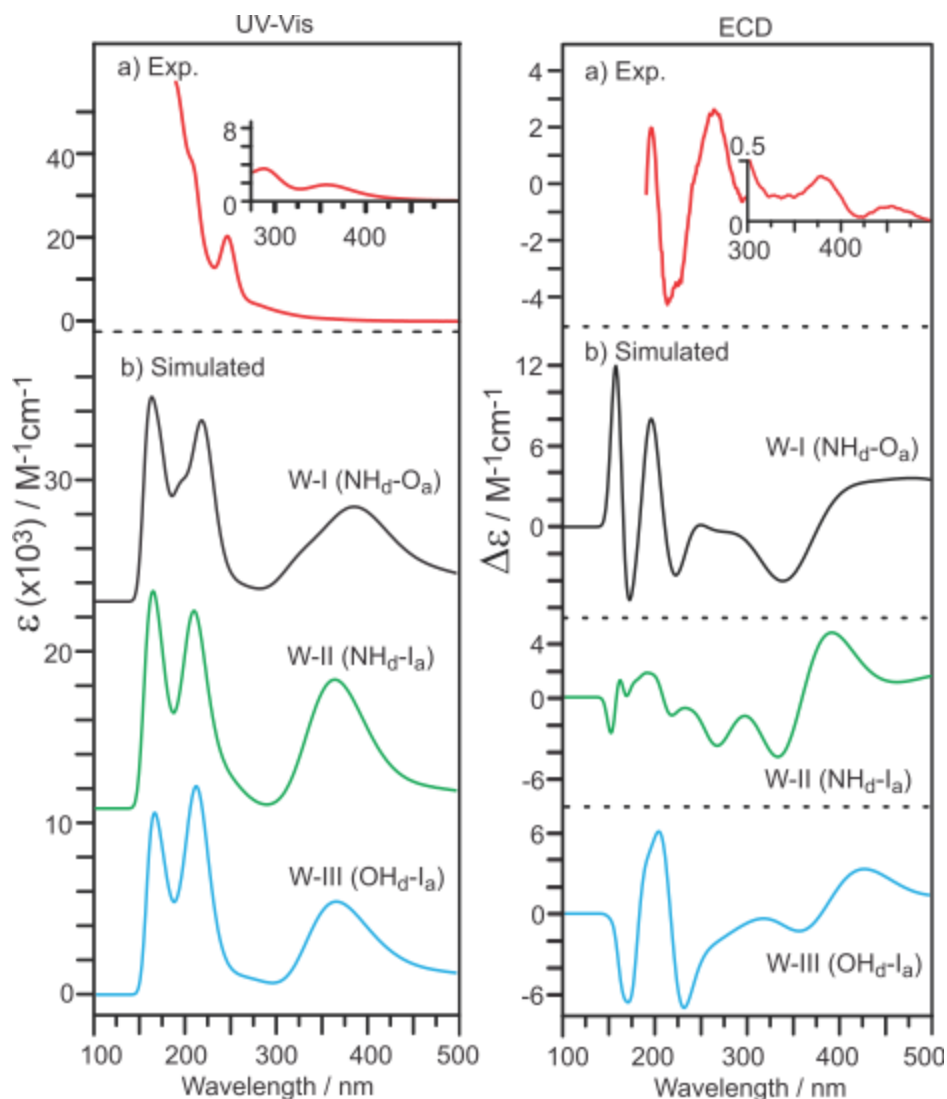


**Figure 3.10.** Comparison of the experimental UV–Vis and ECD spectra of the copper complex with the corresponding simulated spectra of the three most stable hydrogen bonded conformers of C-I Chair–Chair N-in H-ee [(R,R)-1,5-diaza-cisdecalin] copper (II) hydroxide iodine complex with water, listed in Table 3.4, at the B3LYP/LanL2DZ level.

From Figure 3.10, one can see that the main features in the simulated UV–Vis spectra of the three conformers are quite similar, although there are some minor differences in the appearances of the unresolved shoulders. Furthermore, the UV–Vis spectrum of W-I is comparable to that of



C-I Chair–Chair N-in H-ee, (Figure 3.7). Since H<sub>2</sub>O is not directly bonded to the copper atom, one may anticipate that its inclusion has only minor effects on the main electronic transition dipole moments of the metal complex. The predicted ECD spectra, on the other hand, are dramatically different among these three water containing conformers and from that of C-I Chair–Chair N-in H-ee (Figure 3.7). This was somewhat surprising at first glance, especially since the UV–Vis spectra for all conformers remain similar upon inclusion of H<sub>2</sub>O. On the other hand, ECD spectra can sense different hydrogen bonding environments much more sensitively than UV–Vis spectra, in a similar fashion as VCD verses VA in the mid-infrared region [36]. Drastic effects of hydrogen bonding interactions on the ECD spectra had been discussed only in a limited number studies [11], although the degree of effects seems to depend on the specific cases [12].

Why does the inclusion of crystal water have such a strong impact on the appearance of the ECD spectrum here? Since ECD spectra are in general highly sensitive to variations in dihedral angles of conformers, it would be of interest to examine if the changes in ECD are mainly due to the structural modifications of the complex itself upon hydrogen bonding with water. To test this, the geometry of W-I was frozen at its optimized geometry and then water was removed for the subsequent UV–Vis and ECD simulation. The resulting UV–Vis and ECD spectra are summarized in Figure 3.11, together with those of W-I and C-I Chair–Chair N-in H-ee for comparison. Clearly, the UV–Vis spectra remain more or less the same throughout. It is interesting to note that the ECD spectrum of the frozen W-I with the crystal water removed looks very similar to that of C-I. This suggests that the small conformational changes induced by the hydrogen bonding interaction to water are not the main reason for the drastically different ECD appearances of C-I and W-I. Rather the associated magnetic transition dipoles and their

orientations relative to the related electric transition dipoles have been modified to generate the noticeable changes in the ECD spectrum.

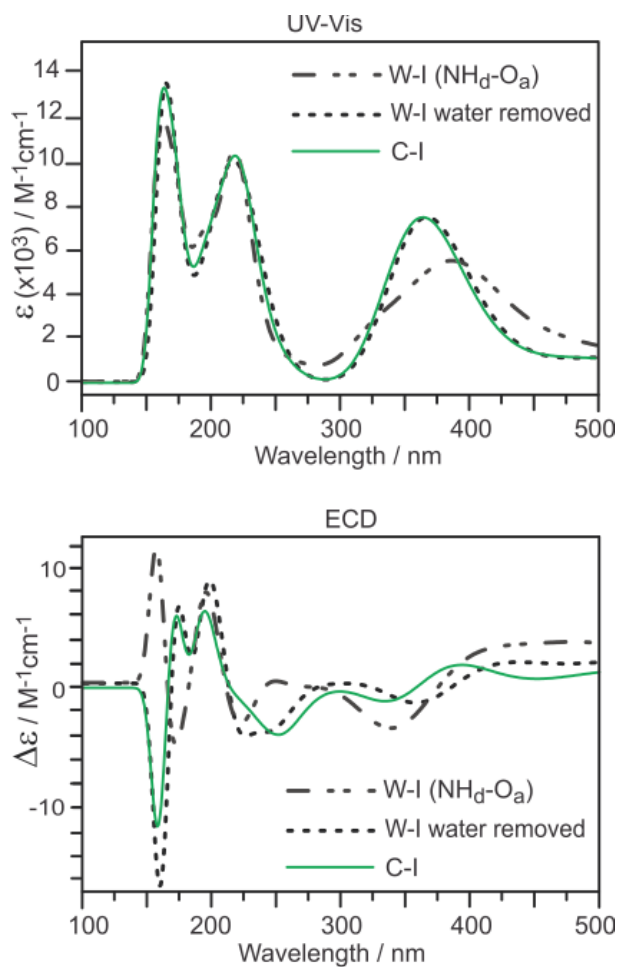


**Figure 3.11.** Comparison of the simulated UV–Vis and ECD spectra at the B3LYP/ LanL2DZ level of C-I Chair–Chair N-in H-ee [(R,R)-1,5-diaza-cis-decalin] copper (II) hydroxide iodine complex, of its most stable hydrogen bonded cluster W-I, and of the hypothetical molecular system where the structure of W-I was frozen and the crystal water was removed for spectral simulation.

### **3.4. Conclusion**

---

In the present report, extensive structural searches of the [(R,R)-1,5-diaza-cis-decalin] ligand and its associated copper(II) hydroxide iodine hydrate show that the ligand favors the Chair–Chair N-in H-ea conformation, whereas the same ligand in the copper complex favors the Chair–Chair N-in H-ee conformation. The comparison of the experimental VA and ECD spectra of the copper complex with the corresponding simulated spectra of [(R,R)-1,5-diazacis-decalin] copper (II) hydroxide iodine hydrate showed poor agreement. The inclusion of the hydrogen bonding interaction of crystal water with the complex resulted in one dominant hydrogen bonded cluster whose VA and ECD exhibit close resemblance to the experimental data. The current study demonstrates the importance of inclusion of the hydrogen bonding interaction with the crystal water in interpreting the experimental VA and ECD spectra. The results show that VA and ECD spectroscopy complemented with DFT calculations is a powerful method for probing not only conformations but also specific hydrogen bonding interactions in transition metal complexes.

### **3.5. Acknowledgments**

---

This research was funded by the University of Alberta, the Natural Sciences and Engineering Research Council of Canada, and the Canada Research Chairs Program. We thank Dr. J. Cooke and W. Moffat for their assistance in preparing KBr pellets and in the electronic circular dichroism measurements and Dr. C. Merten for discussions. We also gratefully acknowledge access to the computing facilities provided by the Academic Information and Communication Technology group at the University of Alberta.

## References

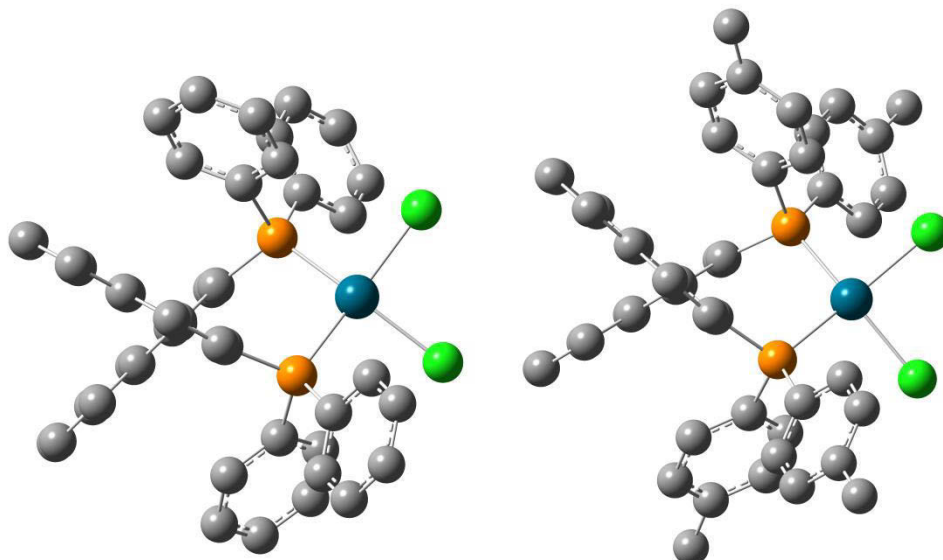
- [1] X. Li, J. Yang, M.C. Kozlowski, *Org. Lett.* 3 (2001) 1137.
- [2] M.C. Kozlowski, Z. Xu, A. Gil Santos, *Tetrahedron* 57 (2001) 4537.
- [3] J. Fleischhauer, G. Raabe, A.G. Santo, J. Schiffer, A. Wollmer, *Z. Naturforsch* 53a (1998) 896.
- [4] B. Ganguly, D.A. Freed, M.C. Kozlowski, *J. Org. Chem.* 66 (2001) 1103.
- [5] Z. Xu, M.C. Kozlowski, *J. Org. Chem.* 67 (2002) 3072.
- [6] A. Santos, W. Klute, J. Torode, V.P.W. Böhm, E. Cabrita, J. Runsink, R.W. Hoffmann, *New J. Chem.* (1998) 993.
- [7] X. Li, L.B. Schenkel, M.C. Kozlowski, *Org. Lett.* 2 (2000) 875.
- [8] G. Yang, Y. Xu, in: R. Naaman, D.N. Beratan, D.H. Waldeck (Eds.), *Top. Curr. Chem.*, Volume: Electronic and Magnetic Properties of Chiral Molecules and Supramolecular Architectures, Springer-Verlag, Berlin Heidelberg, vol. 298, 2011, pp. 189.
- [9] T. Mori, Y. Inoue, in: R. Naaman, D.N. Beratan, D.H. Waldeck (Eds.), *Top. Curr. Chem.*, Volume: Electronic and Magnetic Properties of Chiral Molecules and Supramolecular Architectures, Springer-Verlag, Berlin Heidelberg, vol. 298, 2011, pp. 99.
- [10] N. Berova, L. Di Bari, G. Pescitelli, *Chem. Soc. Rev.* 36 (2007) 914.
- [11] J. Šyebek, B. Gyuresik, J. Šyebestík, Z. Kejík, L. Bednárová, P. Bouř, *J. Phys. Chem. A* 111 (2007) 2750.
- [12] H. Hussain, I. Ahmed, B. Schulz, S. Draeger, U. Flörke, G. Pescitelli, K. Krohn, *Chirality* 23 (2011) 617.
- [13] M. Losada, Y. Xu, *Phys. Chem. Chem. Phys.* 9 (2007) 3127.
- [14] M.J. Frisch, G.W. Trucks, H.B. Schlegel, G.E. Scuseria, M.A. Robb, J.R. Cheeseman, J.A. Montgomery Jr., T. Vreven, K.N. Kudin, J.C. Burant, J.M. Millam, S.S. Iyengar, J. Tomasi, V. Barone, B. Mennucci, M. Cossi, G. Scalmani, N. Rega, G.A. Petersson, H. Nakatsuji, M. Hada, M. Ehara, K. Toyota, R. Fukuda, J. Hasegawa, M. Ishida, T. Nakajima, Y. Honda, O. Kitao, H. Nakai, M. Klene, X. Li, J.E. Knox, H.P. Hratchian, J.B. Cross, C. Adamo, J. Jaramillo, R. Gomperts, R.E. Stratmann, O. Yazyev, A.J. Austin, R. Cammi, C. Pomelli, J.W. Ochterski, P.Y. Ayala, K. Morokuma, G.A. Voth, P. Salvador, J.J. Dannenberg, V.G. Zakrzewski, S. Dapprich, A.D. Daniels, M.C. Strain, O. Farkas, D.K. Malick, A.D. Rabuck, K. Raghavachari, J.B. Foresman, J.V. Ortiz, Q. Cui, A.G. Baboul, S. Clifford, J. Cioslowski, B.B. Stefanov, G. Liu, A. Liashenko, P. Piskorz, I. Komaromi, R.L. Martin, D.J. Fox, T. Keith, M.A. Al-Laham, C.Y. Peng, A. Nanayakkara, M. Challacombe, P.M.W. Gill, B. Johnson, W. Chen, M.W. Wong, C. Gonzalez, J.A. Pople, Gaussian 03, Revision B.01, Gaussian 03, Revision E.01., Gaussian, Inc., Pittsburgh, PA, 2003.
- [15] P.J. Stephens, F.J. Devlin, C. Villani, F. Gasparri, S. Levi Mortera, *Inorg. Chem. Acta* 361 (2008) 987.
- [16] H. Sato, T. Taniguchi, K. Monde, S.-I. Nishimura, A. Yamagashi, *Chem. Lett.* 35 (2006) 364.

- [17] H. Sato, T. Taniguchi, A. Nakahashi, K. Monde, A. Yamagashi, *Inorg. Chem.* 46 (2007) 6755.
- [18] C. Merten, M. Amkreutz, A. Hartwig, *J. Mol. Struct.* 970 (2010) 101.
- [19] W.L. Qian, S. Krimm, *J. Phys. Chem. A* 106 (2002) 6628.
- [20] A. Kovacs, A. Szabo, D. Nemcsok, I. Hargittai, *J. Phys. Chem. A* 106 (2002) 5671.
- [21] B. Kirchner, M. Reiher, *J. Am. Chem. Soc.* 124 (2002) 6206.
- [22] M. Losada, H. Tran, Y. Xu, *J. Chem. Phys.* 128 (2008) 014508.
- [23] G. Yang, Y. Xu, *Phys. Chem. Chem. Phys.* 10 (2008) 6787.
- [24] A. Vlċek Jr., S. Zálíš, *Coord. Chem. Rev.* 251 (2007) 258.
- [25] S. Miertus, E. Scrocco, J. Tomasi, *Chem. Phys.* 55 (1981) 117.
- [26] J. Tomasi, M. Persico, *Chem. Rev.* 94 (1994) 2027.
- [27] G. Yang, Y. Xu, J. Hou, H. Zhang, Y. Zhao, *Chem. Eur. J.* 16 (2010) 2518.
- [28] Z. Su, Q. Wen, Y. Xu, *J. Am. Chem. Soc.* 128 (2006) 6755.
- [29] M. Pecull, D. Marchesan, K. Ruud, S. Coriani, *J. Chem. Phys.* 122 (2005) 024106.
- [30] A. Klamt, G. Schüürmann, *J. Chem. Soc. Perkin. Trans. 2* (1993) 799.
- [31] C.C. Pye, T. Ziegler, *Theo. Chem. Acc.* 101 (1999) 396.
- [32] L. Jensen, M. Swart, P.Th. Van Duijnen, J. Autschbach, *Int. J. Quan. Chem.* 106 (2006) 2479.
- [33] C. Cappelli, S. Bronco, S. Monti, *Chirality*,17 (2005) 577.
- [34] J. Sadlej, J. Cz Dobrowolski, J.E. Rode, M.H. Jamróz, *Phys. Chem. Chem. Phys.* 8 (2006) 101.
- [35] G. Yang, Y. Xu, *J. Chem. Phys.* 130 (2009) 164506.
- [36] See for example G. Yang, Y. Xu, J. Hou, H. Zhang, Y. Zhao, *Dalton Trans.* 39 (2010) 6953.

# 4

## Vibrational circular dichroism spectroscopy of two chiral binaphthyl diphosphine ligands and their palladium complexes in solution

Zahra Dezhahang, Christian Merten, Mohammad Reza Poopari, Yunjie Xu



BINAP

TOL-BINAP

## 4.1. Introduction

---

1,1'-Binaphthyl compounds are a special class of biaryl molecules. Considerable amounts of experimental effort have been concentrated on introducing structural modifications to the biaryl groups in order to improve the enantio-selectivity of the catalysts. It was reported that a smaller dihedral angle between the naphthyl rings may lead to better stereo-discrimination in some reactions.[1] BINAP (2,2'-diphenylphosphino-1,1'-binaphthyl, Figure 4.1), a unique binaphthyl diphosphine chiral ligand devised by Noyori (winner of the Nobel Prize in Chemistry in 2001),[2] signifies an important milestone in the development of binaphthyl chemistry. BINAP exhibits axial chirality since the rotation about the bond linking the two naphthyl rings is strongly hindered. As a result of their highly stable chiral configuration, BINAP and its derivative TOLBINAP (also shown in Figure 4.1) have found extensive applications in the field of asymmetric syntheses, such as hydrogenation of olefins[3] and ketones,[4] and isomerisation of allylamines,[5] and have demonstrated outstanding chirality discrimination abilities. Their complexes with transition metals, such as palladium, rhodium, and ruthenium, are widely used as catalysts in stereoselective organic syntheses, for example, in the commercial production of the enantiopure anti-inflammatory drug naproxen. [6] In particular, BINAP- and TOLBINAP-Pd complexes, the two titled complexes investigated here, have been utilized widely as catalysts for the amination of aryl halides, a practical synthetic route for C-N bond formation,[7,8] and for the Mannich-type C-C bond formation reactions. [9, 10] For their extensive applications as catalysts in stereoselective syntheses, there has been intensive interest in their catalytic mechanism. [11, 12] It is, however, highly challenging to establish a mechanism equivocally. While NMR spectroscopy and kinetic studies have been used widely to verify the existence of certain intermediate species and establish reaction orders, it is desirable to have other complementary

techniques which can be applied directly in solution and which are also exquisitely sensitive to chirality of the species involved, such as reactants, intermediates, and products.

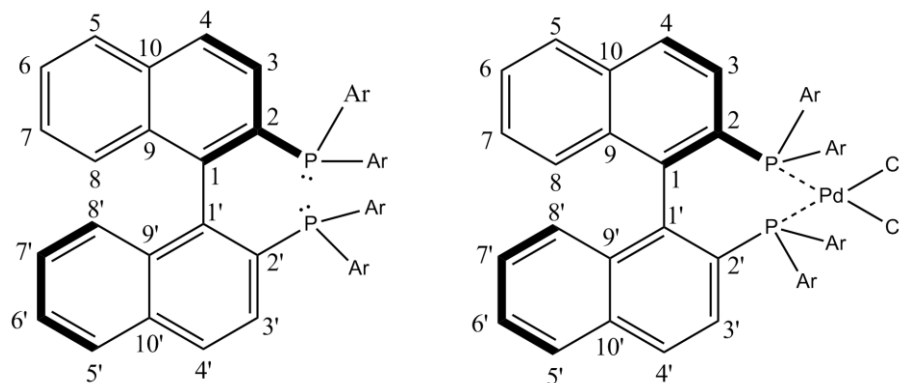


**Figure 4.1.** Structures of the BINAP (**1**, Ar=C<sub>6</sub>H<sub>5</sub>) and TOLBINAP (**2**, Ar=4-CH<sub>3</sub>-C<sub>6</sub>H<sub>4</sub>) ligands (left) and their corresponding palladium complexes (right) investigated in this report.

Vibrational circular dichroism (VCD) spectroscopy [13] has emerged in recent years as a powerful chiroptical spectroscopic tool to examine variation of dihedral angles in these BINAP metallic complexes and to potentially follow their catalytic processes. VCD spectroscopy measures the preferential absorption of the left versus right circularly polarized light accompanying a vibrational transition. VCD spectroscopy in combination with density functional theory (DFT) modeling [14] has been applied successfully to determine the absolute configurations of chiral molecules in solution, thanks to the significant advances in both the experimental technique and the theoretical modelling. In organometallic chemistry, VCD spectroscopy has been applied to probe structures and other properties of metal complexes of different chiral topologies. [15] For example, it has been used to study a star-burst type tetranuclear Ru(III) complex [16] and to evaluate the effects of counter ions in Co(en)<sub>3</sub><sup>2+</sup> complexes [17] and of low-lying electronic transitions in a spin-triplet bis-(biuretato) cobaltate(III) coordination complex. [18] Since neither the ligands nor their metal complexes had



been studied using the VCD approach before, we measured the VCD spectra of the BINAP and TOLBINAP ligands, together with their respective palladium complexes, i.e. Pd(BINAP)Cl<sub>2</sub> and Pd(TOLBINAP)-Cl<sub>2</sub>. One main objective is to examine the conformational changes, in particular the chiral dihedral angles, in the BINAP and TOLBINAP ligands before and after coordination to palladium. The second main objective is to assert how well the observed VCD features in solution can be produced by the theoretical modelling. To be able to evaluate the effects of solvation adequately is important since solvents may even alter a reaction mechanism and influence the enantiomeric excess of an asymmetric synthesis. These studies can be regarded as the first step towards establishing the VCD method as a new spectroscopic tool for monitoring reaction species in asymmetric syntheses involving BINAP and its derivative metallic catalysts.

## 4.2. Results and discussions

---

### 4.2.1. Experimental spectra

The experimental VA and VCD spectra of R-BINAP (**1**) and R-TOLBINAP (**2**) in CDCl<sub>3</sub> solution, obtained in the fingerprint region from 1000–1700 cm<sup>-1</sup>, are given in Figure 4.2. The experimental VA and VCD spectra of the corresponding palladium complexes, i.e. R-Pd(**1**)Cl<sub>2</sub> and R-Pd(**2**)Cl<sub>2</sub> in CDCl<sub>3</sub>, are also summarized in Figure 4.2. The experimental VCD spectra of both R- and S-enantiomers of BINAP, TOLBINAP and Pd(TOLBINAP)Cl<sub>2</sub> in CDCl<sub>3</sub> solution and their related noise levels are provided in Figure B1, Appendix B. As one can see, the VCD spectra of the enantiomeric pairs show good mirror images (see also “Experimental and computational details”). First of all, the VA spectra of the **1** and **2** ligands show easily recognizable resemblance to their respective metal complexes. This is not surprising since the VA bands in this region correspond largely to the ligand vibrational modes, whereas the metal related VA modes, such as the Pd–Cl stretching bands, are at ~290–310 cm<sup>-1</sup>, [19] outside the

range of the instrument. Despite their similarity, there are noticeable changes in the relative band intensities, especially for **2** and its complex. Secondly, although the most intense VCD features at  $\sim 1400\text{ cm}^{-1}$  remain similar for **1** and its Pd complex, there are obvious changes in the 1100–1300  $\text{cm}^{-1}$  regions going from the ligand to its Pd complex. For **2** and its Pd complex, the associated VCD spectra are drastically different from each other. These observations demonstrate the sensitivity of VCD features to the binding with Pd. Thirdly, the VA and VCD spectra of the **1** and **2** ligands are visibly different, although there are only four extra methyl groups at the para positions of the phenyl rings for **2** compared to **1**. For example, the strongest VA and VCD features in **1** are noticeably weak or non-existing in **2**.

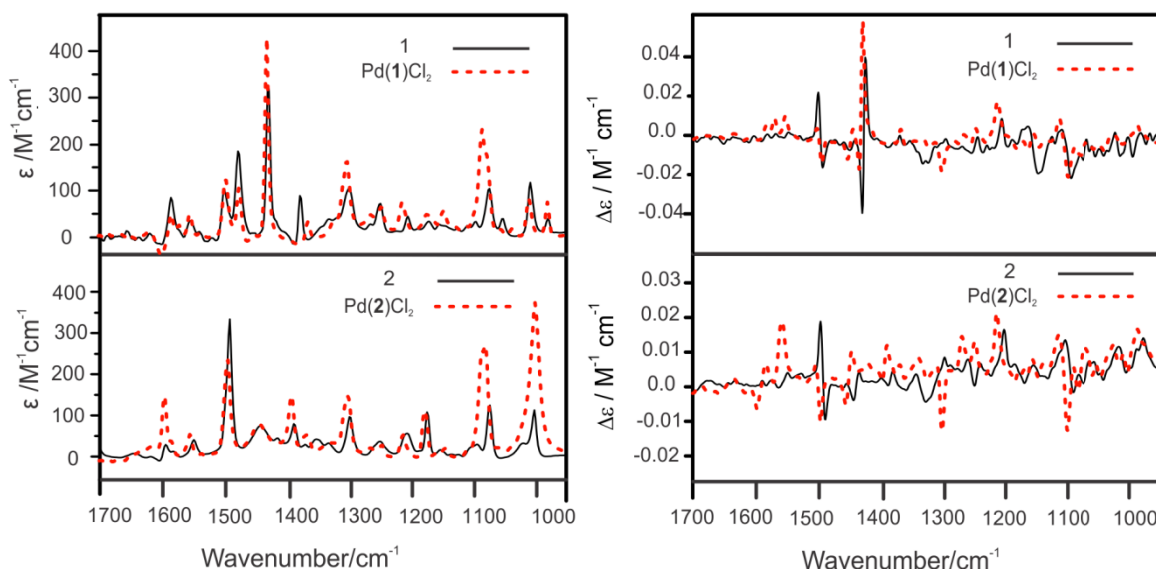


**Figure 4.2.** The experimental VA (left) and VCD (right) spectra of R-**1**, R-Pd(**1**)Cl<sub>2</sub>, R-**2**, and R-Pd(**2**)Cl<sub>2</sub> in CDCl<sub>3</sub>.

#### 4.2.2. Conformations of the **1** and **2** ligands and of the Pd(**1**)Cl<sub>2</sub> and Pd(**2**)Cl<sub>2</sub> complexes

1,1'-Binaphthyl has a rotation barrier of 23.5 kcal mol<sup>-1</sup> [20] around the 1–1' C–C bond, thus allowing the isolation of the related enantiomers at room temperature. It was discovered in 1971

that the racemic solution of 1,1'-binaphthyl underwent spontaneous resolution to form either R or S enantiomeric crystals. [21] The substitution at the 2 and 2' positions, on the other hand, is likely to introduce strong steric repulsion, thus preventing rotation about the bridge C–C bond and generating very stable enantiomers and transoid or cisoid conformers where the dihedral angle between the two naphthalene rings is larger or smaller than 90 degrees, respectively. This dihedral angle was reported to be as high as 108 degrees with the large OSO<sub>2</sub>CF<sub>3</sub> substituents and as low as 52 degrees with a bridge substituent PO<sub>4</sub>H at the 2 and 2' positions of 1,1'-binaphthyl, respectively, in a previous VCD study.[22] Because of the bulky substituents at the 2 and 2' positions in the case of **1** and **2**, one may expect that the two naphthalene rings adopt a roughly perpendicular position with each other due to the steric hindrance and spatial repulsion. At the same time, the phenyl groups may adopt different spatial orientations with respect to each other, and this conformational freedom may be coupled to the dihedral angle mentioned before. Our searches for possible conformers by using the DFT method ended up with three conformers whose geometries are depicted in Figure 4.3. The dihedral angle values predicted for these conformers are listed in Table 1. Several interesting points warrant attention with regard to the conformational geometries obtained. First, the dihedral angles between two naphthalene rings are very close to 90 degrees, i.e. the two rings are perpendicular to each other. The 2–1–1'–2' dihedral angle (see Figure 4.1 for atom numbering), i.e., the dihedral angle between two naphthalene rings, varies slightly from ~87 degrees to ~95 degrees for the three conformers of the **1** and **2** ligands. This implies that there is not much flexibility coming from the naphthalene part of such molecules. Next we consider the possible conformers resulting from relative orientations of the phenyl rings. The two phenyl rings, which are connected to two different P atoms and are closest to each other, were arranged in three possible starting orientations, i.e. face

to face, displaced face to face, and edge to face, analogous to the benzene dimer.[23] It was found that the other two phenyl rings adjusted themselves in the geometry optimization processes accordingly, even if one put them in different starting orientations. Overall, this resulted in the three possible conformers.

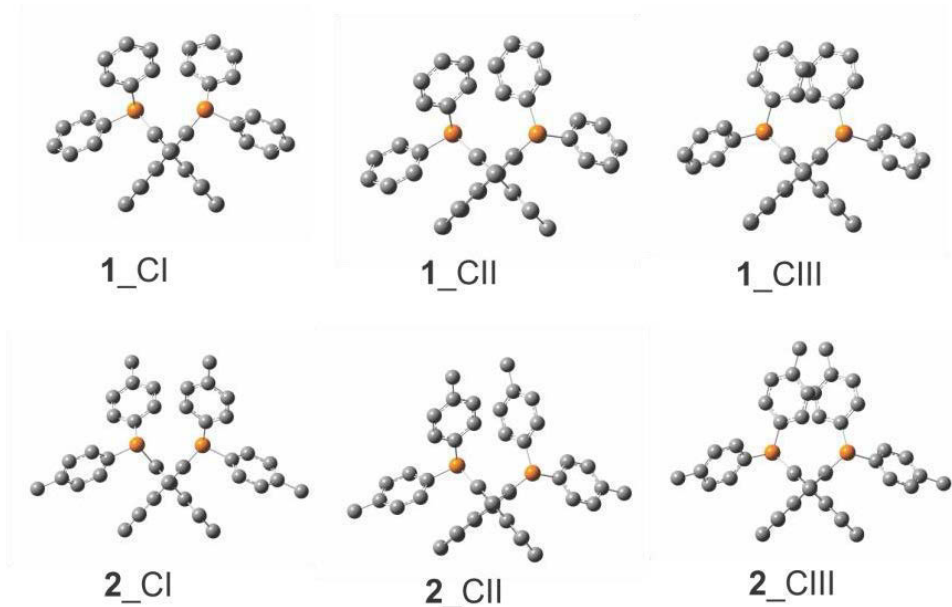


**Figure 4.3** Three most stable conformers of R-1 and R-2 at the B3LYP/ 6-31G(d,p) level viewed along the C1–C1' bond.

**Table 4.1** Calculated dihedral angle values (in degrees) between the two naphthalene rings for **1** and **2** and their corresponding Pd complexes

Ligands	1_CI	1_CII	1_CIII	2_CI	2_CII	2_CIII
Angle <sup>a</sup> 2-1-1'-2'	86.64 (88.31)	94.17 (90.05)	94.82 (95.04)	86.35 (88.34)	94.47 (94.10)	95.05 (95.06)
<b>Complexes</b>		Pd( <b>1</b> )Cl <sub>2</sub>			Pd( <b>2</b> )Cl <sub>2</sub>	
Angle <sup>a</sup> 2-1-1'-2'		75.24 (74.58)			75.08 (74.45)	

<sup>a</sup> The values were calculated at the B3LYP/6-31G(d,p) level for the **1** and **2** ligands and all atoms of the complexes except Pd where the LanL2DZ basis set was used for the Pd atom in both complexes. The gas phase values are listed first and the values with the polarizable continuum model (PCM) of the chloroform solvent are in brackets. Please see the “Inclusion of solvent effects with PCM” section for a description of PCM.

In Table 4.2, the relative energies, the relative Gibbs free energies, and the corresponding Boltzmann population factors of the three stable conformers of **1** and **2** in the gas phase are given. The relative stabilities of the **1** conformers in the gas phase can be understood in terms of the  $\pi$ - $\pi$  stacking interactions of the phenyl groups. Three possible conformations previously proposed for the benzene dimers by Burley and Petsko [23] are based on the electrostatic interactions: [24] face to face (or parallel), displaced face to face, and edge to face. According to this model, the face to face interaction destabilizes the dimer because of the repulsive nature of the interaction, whereas the face to edge orientation is a true ground state due to  $\pi$ - $\sigma$  attraction. The stabilities of the first and second conformers of each ligand (**1** and **2**) have their adjacent phenyl groups forming the edge to face and the displaced face to face orientations which are more favourable. The third conformer which has the face to face spatial arrangement is the least populated one in the gas phase.

**Table 4.2** Predicted relative energies and Gibbs free energies (in kcal mol<sup>-1</sup>) of the three most stable conformers of the **1** and **2** ligands and their Boltzmann factors at room temperature

Conf.	$\Delta E^a$	$\Delta G^a$	pop% ( $\Delta E$ )	pop% ( $\Delta G$ )
<b>1_CI</b>	0.00 (0.17)	1.52 (1.12)	49.98 (35.92)	45.70 (8.64)
<b>1_CII</b>	0.13 (0.00)	0.00 (0.31)	40.13 (47.82)	50.81 (34.01)
<b>1_CIII</b>	0.96 (0.64)	1.59 (0.00)	9.90 (16.24)	3.49 (57.35)
<b>2_CI</b>	0.00 (3.67)	0.31 (4.36)	50.33 (0.15)	36.48 (0.06)
<b>2_CII</b>	0.11 (0.00)	0.00 (0.00)	41.72 (73.13)	61.91 (97.88)
<b>2_CIII</b>	1.09 (0.60)	2.16 (2.29)	7.96 (26.52)	1.61 (2.06)

<sup>a</sup>  $\Delta E$  and  $\Delta G$  values were calculated at the B3LYP/6-31G(d,p) level. The gas phase values are listed first and the values with the PCM of the chloroform solvent are in brackets.

Coordination to palladium introduces further constraints to the spatial orientation of the **1** and **2** ligands (Figure 4.1) in Pd(**1**)Cl<sub>2</sub> and Pd(**2**)Cl<sub>2</sub>. Despite extensive searches, only one conformer was located for the Pd(**1**)Cl<sub>2</sub> and Pd(**2**)Cl<sub>2</sub> complexes where the diphenyl rings take on the edge-

face arrangement. Clearly, coordination increases the rigidity of the di-phenyl ligand parts. As a result, the rigidity of the entire structure is significantly enhanced. The values of the associated dihedral angle between the two naphthalene rings are given in Table 4.1 for comparison with those of ligand conformers. As one can see, the dihedral angles are essentially the same for both Pd complexes and are considerably smaller than those of the related ligand conformers.

#### *4.2.3. Interpretation of the experimental VA and VCD spectra of the 1 and 2 ligands and their palladium complexes*

**The gas phase simulation.** The calculated population weighted VA and VCD spectra of the three conformers of **1** are compared with the related experimental data in Figure 4.4, left panel. The corresponding comparison of **2** is given in Figure 4.4, right panel. The simulated VA and VCD spectra for each conformer of **1** and **2** are provided in Figure B2, Appendix B. While the VA spectra of the three conformers of **1** are essentially the same, noticeable differences are present in the VCD spectra. A similar observation can be made for the conformers of **2**. In particular, the differences in the VCD features among the conformers of **2** are quite prominent. To get a rough understanding of the large number of VA bands encountered here, related calculations have been performed for 1,1'-binaphthyl which shares the same core structure as **1** and **2**. It is tedious and not so informative to provide detailed VA band assignments. Rather, the comparison with the simpler 1,1'-binaphthyl system is provided in Figure B3, Appendix B. Most of the prominent bands present are from the C–C stretching and C–H bending vibrational modes of the binaphthyl rings which are the common parts among **1**, **2** and 1,1'-binaphthyl. More detailed discussions are given in Figure B3, Appendix B. In Figure 4.4, the experimental VA and VCD spectra are also compared with the corresponding calculated spectra in the gas phase. Overall, for the **1** and **2** ligands, the calculated and experimental VA spectra are in reasonable

agreement. The same cannot be said for the VCD comparison, especially for that of **2**. For example, the strong VCD signature predicted at the  $\sim 1550\text{ cm}^{-1}$  region was not observed experimentally for **2**.

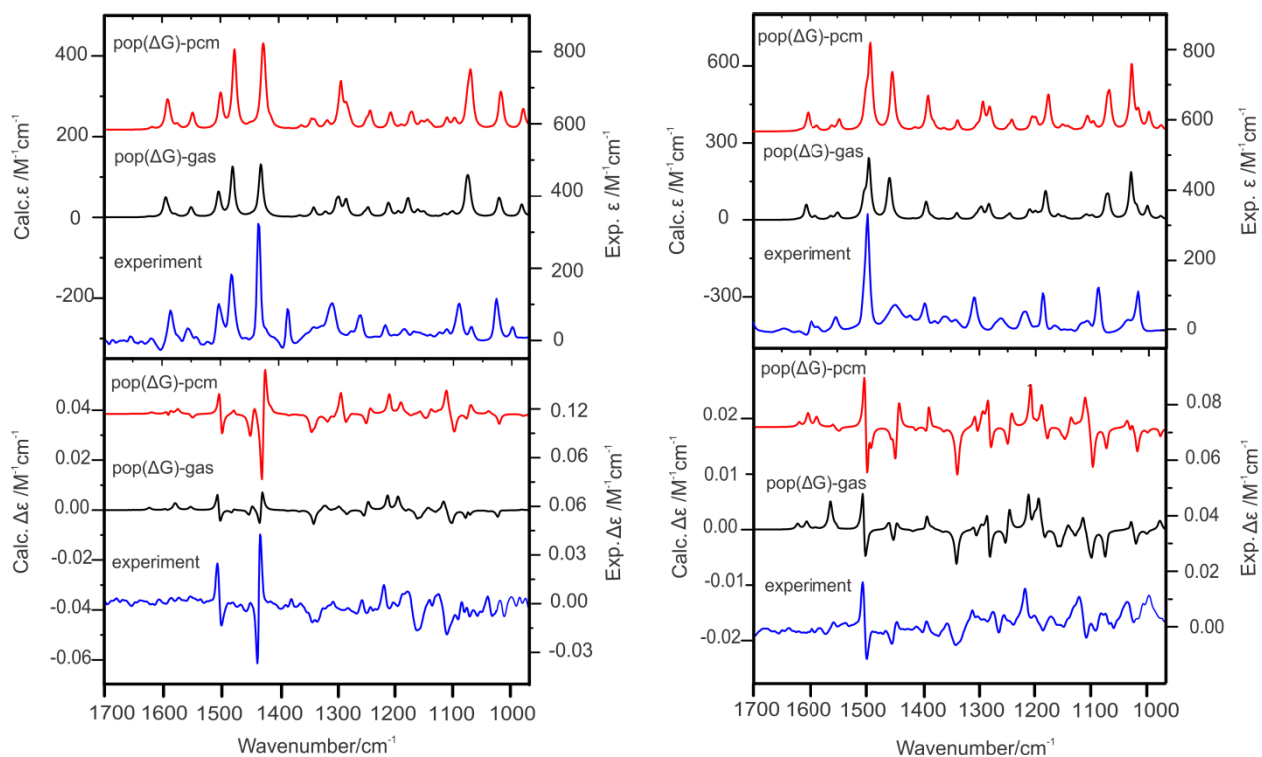


**Figure 4.4.** Comparison of the simulated VA and VCD spectra in the gas phase and with the PCM for chloroform with the corresponding experimental spectra of **1** (left) and **2** (right).

The experimental and calculated VA and VCD spectra of Pd(**1**)Cl<sub>2</sub> and Pd(**2**)Cl<sub>2</sub> are compared in Figure 4.5. Again, the VA spectra show reasonable agreement between experiment and theory for both complexes, while the same cannot be said about the VCD spectral comparison. Since these two complexes are more rigid than their corresponding ligands and have only one dominant conformer, one would expect better agreement between the simulated and experimental spectra because any deviations due to conformational degrees of freedom are no longer a concern. The

above observation indicates that other factors must be responsible for this. Larger basis sets with more sophisticated polarization and diffuse functions were considered in order to better describe the interaction with a transition metal center. Another possible source of discrepancy is the effect of solvent. Although the effects of DMSO were found to be negligible in the previous VCD study of the small 1,1'-binaphthyl derivatives, [22] their effects on the transition metal complexes may be much more severe. These considerations are described in the next two sections.

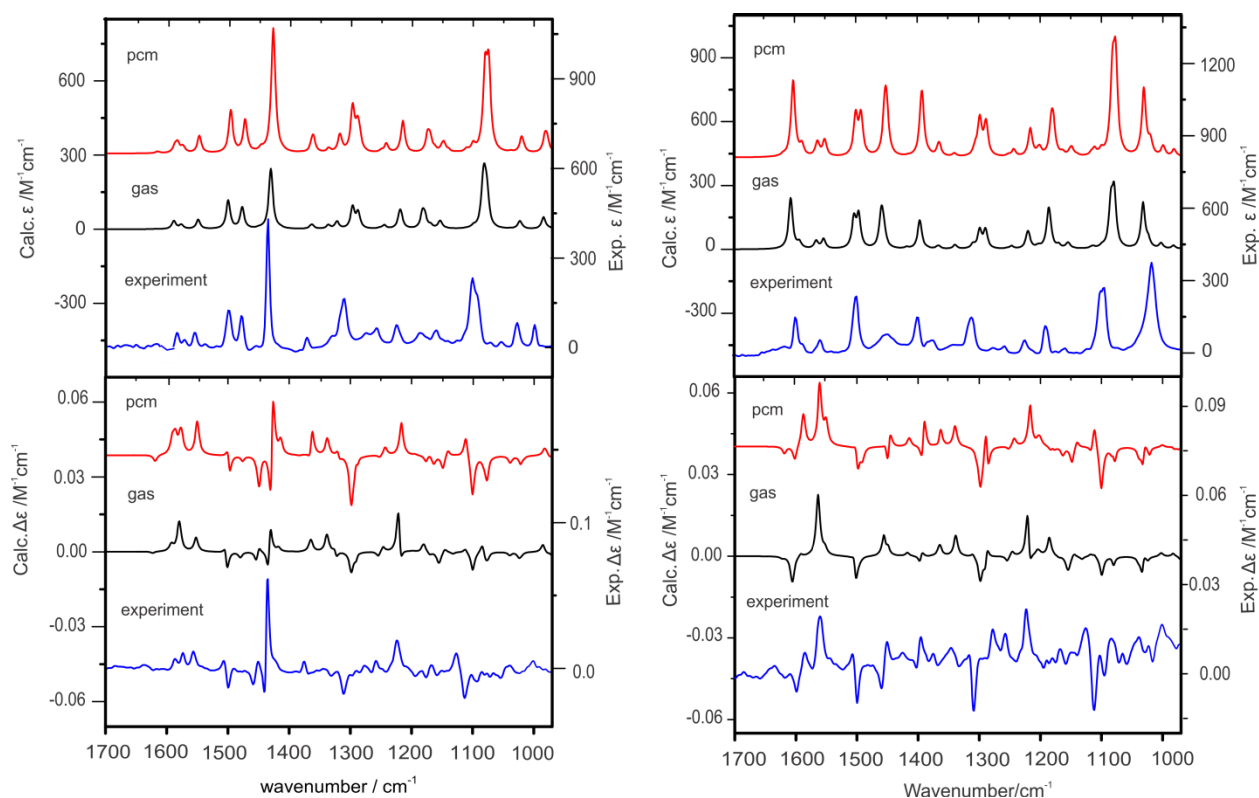


**Figure 4.5.** Comparison of the simulated VA and VCD spectra in the gas phase and with the PCM for chloroform with the corresponding experimental spectra of Pd(1)Cl<sub>2</sub> (left) and Pd(2)Cl<sub>2</sub> (right).



**Basis set consideration.** The previously used basis set 6-31G-(d,p) is comparatively small and may in general influence the results of spectral calculations since weak intramolecular interactions, such as those between the phenyl rings, might not be accurately described. To test if the basis set selection is the reason for the discrepancies observed between the simulated and experimental data, several basis sets with various polarizations and diffuse functions, i.e. 6-31+G(d), 6-31+G(d,p), 6-31G-(2d,2p), 6-31++G(d,p), were also used for the C, H, Cl, and P atoms with the LanL2DZ basis set for the Pd atom. The geometry of the Pd(2)Cl<sub>2</sub> complex was re-optimized and the VA and VCD spectra of the complex re-simulated with the B3LYP functional and the new basis sets chosen. The results are summarized in Figure 4.6. We chose to do such a testing on one representative complex because the targeted system is quite large with 93 atoms and 438 electrons and its geometry optimization and frequency calculation took a significant amount of time. As clearly demonstrated in Figure 4.6, the simulated spectra obtained with all these basis sets are comparable to each other and no significant improvement was achieved by increasing the size of the basis set. It thus appears that for a rigid metal complex with one main conformer, adding polarization and diffuse functions does not alter the appearance of the VA or VCD features noticeably.

**Inclusion of solvent effects with PCM.** A solvent may have a significant effect on stability of solute conformers since it can establish strong explicit solute–solvent hydrogen-bonding interactions [25] and/or provide an implicit dielectric environment. Since CDCl<sub>3</sub> is unlikely to form any strong hydrogen bonding interaction with the bulky ligands and their complexes investigated here, we treated the solvent by applying the integral equation formalism (IEF) version of the PCM solvation model. [26] In this model, the solvent is treated as a continuum

dielectric environment and no explicit intermolecular interactions are taken into account. In this continuum dielectric environment, the solute is hosted inside a molecularly shaped cavity defined through interlocking van der Waals spheres centered at the atomic positions. The electrostatic, dispersion, repulsion, and cavity contributions are included for the energy calculations. Geometries of the predicted conformers were re-optimized and harmonic frequency calculations and intensities of VA and VCD bands were re-calculated. The calculated dihedral angles, the relative energies and the Gibbs free energies of all conformers of the **1** and **2** ligands and their palladium complexes obtained with the PCM of chloroform are listed in Tables 4.1 and 4.2, respectively. Indeed, the solvent has noticeable effects on the relative stability of conformers for the chiral ligands. Although the geometries of individual conformers appear more or less the same with the PCM of chloroform solvent as in the gas phase, such a solvent environment may affect the relative stability of the conformers and optical responses to the chiral polarized light. Indeed, the relative stability of the three conformers of **1** and **2** changes. Their relative energies, the relative Gibbs free energies, and the corresponding Boltzmann population factors with PCM are given in Table 4.2, while the corresponding values for the dihedral angle between the two naphthalene rings are summarized in Table 4.1. The calculated VA and VCD spectra of **1** and **2** with PCM are also included in Figure 4.4 for comparison with the experimental data. The corresponding simulated spectra of the individual conformers of the **1** and **2** ligands are provided in Figure B4, Appendix B.

The simulated VA and VCD spectra of the two palladium complexes with **1** and **2** with PCM are provided in Figure 4.5 for comparison with the gas phase calculation and the associated experimental data. The values for the dihedral angle between the two naphthalene rings for these two complexes with PCM are also summarized in Table 4.1. There are a number of bands which

are not visible in the gas phase simulation but become much more prominent in the PCM spectra. For instance, for both Pd complexes, the positive–negative bands at  $1100\text{ cm}^{-1}$ , which correspond to a mixture of the C=C vibrational modes and the C–H bending of naphthalene rings, appear only in the PCM spectra. For Pd(**2**)Cl<sub>2</sub>, the VCD signatures predicted with PCM in the  $1600\text{--}1400\text{ cm}^{-1}$  region show very good agreement with the experimental data. The corresponding gas phase features, on the other hand, are very different from the experimental ones, making it not possible to draw any definite conclusion. Overall, the calculated VA and VCD spectra with PCM are in much better agreement with the experimental data than the gas phase ones, allowing one to identify the species and possible conformers in solution confidently.

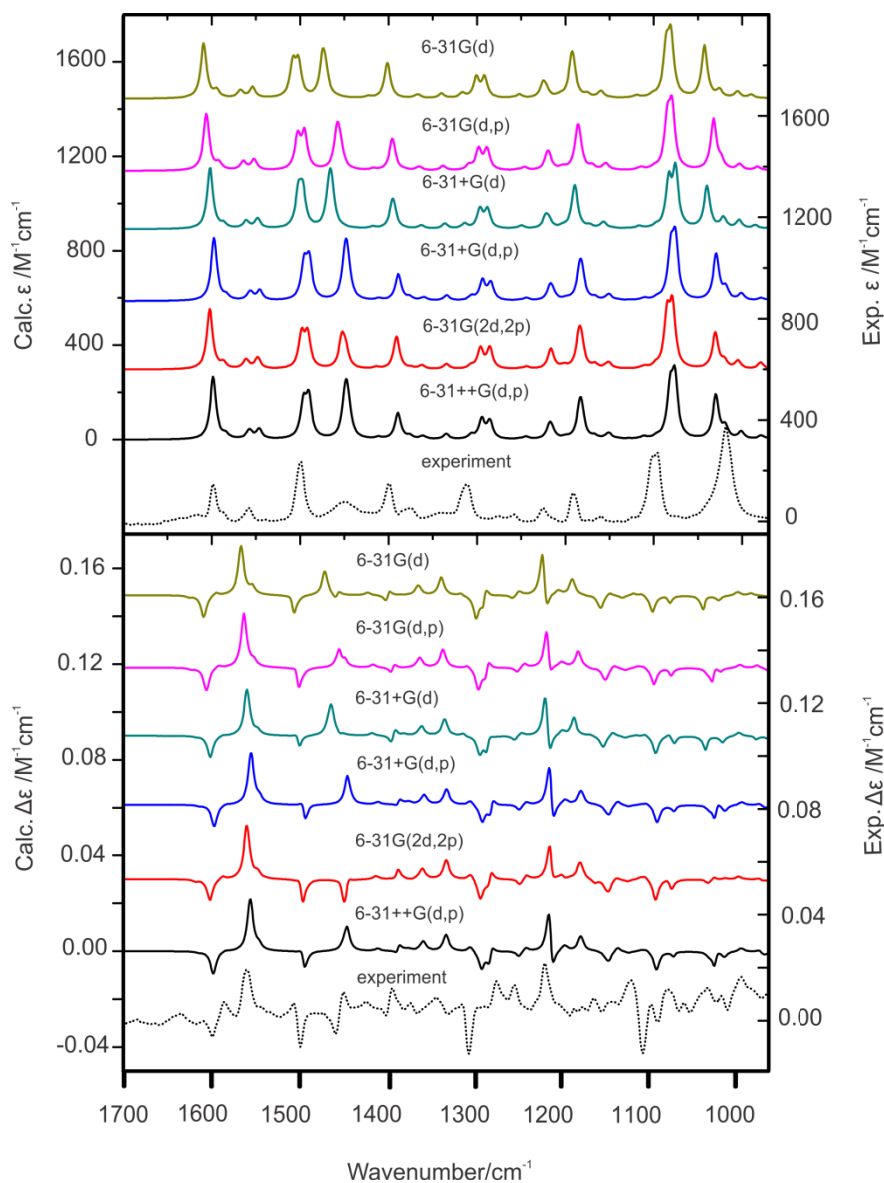


**Figure 4.6.** Comparison of the experimental VA and VCD spectra of Pd(2)Cl<sub>2</sub> with the corresponding calculated spectra using several different basis sets.

#### 4.2.4. Experimental and computational details

R-1, R-2, R-Pd(1)Cl<sub>2</sub> (purity 97%) and R-Pd(2)Cl<sub>2</sub> (purity 97%) samples were purchased from Sigma Aldrich and used without further purification. Sample solutions were prepared using

deuterated chloroform, CDCl<sub>3</sub> (Sigma Aldrich, purity 99.9%). The VA absorbance coefficients were optimized to be in the range of 0.2 to 0.8 for the main vibrational bands in the 1000–1800 cm<sup>-1</sup> region for the subsequent VCD measurements by varying sample concentrations and path lengths. The optimum concentration and path length used are 0.1 M and 100 μm, respectively. The VA and VCD spectra were collected using a Fourier transform IR spectrometer (Vertex 70, Bruker) which is equipped with a PMA 50 VCD module (Bruker). [27] Each VCD spectrum was averaged over 25000 recorded in four blocks of 1 h accumulation time and the related solvent spectrum under identical condition was subtracted off for base line correction. Because CDCl<sub>3</sub> exhibits a strong absorption band at ~920 cm<sup>-1</sup>, the usable region of the measured spectra is from ~970 to 1700 cm<sup>-1</sup>. For BINAP, TOLBINAP and Pd(TOLBINAP)Cl<sub>2</sub> whose S-enantiomers were available to us commercially, comparisons of the VCD spectra of the R- and S-enantiomers of these molecular systems in CDCl<sub>3</sub> solution are provided in Figure B1, Appendix B, together with their related noise levels. The noise levels were obtained as described on page 240 of ref. 13a. Each enantiomeric pair shows good mirror image spectral features, except a few broad features at the very low wavenumber region. This is likely due to the strong absorption by the solvent starting at about 970 cm<sup>-1</sup>. The VCD spectrum of Pd(BINAP)Cl<sub>2</sub> is expected to have similar good quality as the other three systems studied.

Geometry optimization, harmonic vibrational frequencies, and intensities of vibrational and vibrational circular bands of all conformers of the **1** and **2** ligands and their related palladium complexes were performed using the Gaussian 03 program packages. [28] Density functional theory with the B3LYP functional and the 6-31G(d,p) basis set was used for all the results reported. Several basis sets, i.e. 6-31+G(d), 6-31+G(d,p), 6-31G-(2d,2p), 6-31++G(d,p), were also used for the C, H, P, Cl atoms and LanL2DZ for the Pd atom for the calculations of

Pd(2)Cl<sub>2</sub>. Lorentzian band shape with a half width at half height of 4 cm<sup>-1</sup> is used to simulate all the VA and VCD spectra. To properly account for the solvent effects of CDCl<sub>3</sub>, the integral equation formalism (IEF) version of the PCM solvation model [26] was utilized where the solvent is treated as a continuum dielectric environment with a dielectric constant of 4.71.

### **4.3. Conclusions**

---

In this report, conformational analyses for the **1** and **2** ligands show that the naphthalene rings are nearly rigid, while the flexibility of the ligands originates from the orientations of the phenyl rings with respect to each other. The flexibility of both ligands decreases upon coordination to the palladium metal ion. The VA and VCD measurements of both ligands and the complexes show noticeable differences from the calculated ones in the gas phase. In particular, the differences between experiment and theory are so large for the two palladium complexes studied here that it would be extremely difficult to identify them based on the VA and VCD data. Inclusion of the solvent effects with PCM in the calculations results in much better agreement for both VA and VCD spectra of all the ligands and complexes studied, allowing the species and their conformations to be identified. With proper care for locating the possible conformers and accounting for solvent effects, one can potentially use VA and especially VCD spectroscopy, because of its high sensitivity to chirality and conformation, to follow these important species in reactions.

### **4.4. Acknowledgements**

---

This research was funded by the University of Alberta, the Natural Sciences and Engineering Research Council of Canada, and the Canada Research Chairs Program. CM thanks the

Alexander von Humboldt foundation for a Feodor-Lynen postdoctoral fellowship. We gratefully acknowledge access to the computing facilities provided by the Academic Information and Communication Technology group at the University of Alberta.

## References

- [1] I. G. Rios, A. Rosas-Hernandez and E. Martin, *Molecules*, **2011**, 16, 970–1010.
- [2] R. Noyori and T. Ohkuma, *Angew. Chem., Int. Ed.*, **2001**, 40(1), 40–73.
- [3] T. Ohkuma, M. Kitamura and R. Noyori, *Catalytic Asymmetric Synthesis*, John Wiley & Sons, 2nd edn, **2000**, pp. 1–110.
- [4] R. Noyori, T. Ohkuma, M. Kitamura, H. Takaya, N. Sayo, H. Kumobayashi and S. Akutagawa, *J. Am. Chem. Soc.*, **1987**, 109, 5856–5858.
- [5] S. Akutagawa and K. Tani, *Catalytic Asymmetric Synthesis*, John Wiley & Sons, 2nd edn, **2000**, pp. 145–161.
- [6] R. Noyori, *Asymmetric Catalysis in Organic Synthesis*, John Wiley & Sons, **1994**.
- [7] J. F. Hartwig, in *Handbook of Organopalladium Chemistry for Organic Synthesis*, ed. E. I. Negishi, Wiley-Interscience, New York, **2002**, vol. 1, p. 1051.
- [8] A. R. Muci and S. L. Buchwald, *Top. Curr. Chem.*, **2002**, 219, 131–209.
- [9] E. F. Kleinman, in *Comprehensive Organic Synthesis*, ed. B. M. Trost and I. Fleming, Pergamon, Oxford, **1991**, ch. 4.1, vol. 2.
- [10] Y. Hamashima, N. Sasamoto, D. Hotta, H. Somei, N. Umebayashi and M. Sodeoka, *Angew. Chem., Int. Ed.*, **2005**, 44, 1525–1529.
- [11] J. Hao, M. Hatano and K. Mikami, *Org. Lett.*, **2000**, 2, 4059–4062.
- [12] S. Shekhar, P. Ryberg, J. F. Hartwig, J. S. Mathew, D. G. Blackmond, E. R. Strieter and S. L. Buchwald, *J. Am. Chem. Soc.*, **2006**, 128(11), 3584–3591.
- [13] (a) L. A. Nafie, *Vibrational Optical Activity: Principles and Applications*, John Wiley & Sons, Ltd, Chichester, 2011; (b) Y. He, B. Wang, R. K. Dukor and L. A. Nafie, *Appl. Spectrosc.*, **2011**, 65(7), 699–723; (c) G. Yang and Y. Xu, *Vibrational circular dichroism spectroscopy of chiral molecules*, in *Top. Curr. Chem.*, Volume: Electronic and Magnetic Properties of Chiral Molecules and Supramolecular Architectures, ed. R. Naaman, D. N. Beratan and D. H. Waldeck, Springer-Verlag, Berlin, Heidelberg, **2011**, vol. 298, pp. 189–236.
- [14] (a) P. J. Stephens, F. J. Devlin and J. J. Pan, *Chirality*, 2008, 20(5), 643–663; (b) M. Gábor, T. György and V. Elemér, *Vibrational circular dichroism*, *WIREs Comput. Mol. Sci.*, **2011**, 1, 403–425, DOI: 10.1002/wcms.39.
- [15] (a) F. D. Montigny, L. Guy, G. Pilet, N. Vanthuyne, C. Roussel, R. Lombardi, T. B. Freedman, L. A. Nafie and J. Crassous, *Chem. Commun.*, **2009**, 4841–4843; (b) V. A. Soloshonok, T. Ono, H. Ueki, N. Vanthuyne, T. S. Balaban, J. Brück, H. Fliegl, W. Klopfer, J.-V. Naubron, T. T. T. Bui, A. F. Drake and C. Roussel, *J. Am. Chem. Soc.*, **2010**, 132(30), 10477–10483; (c) C. Merten, M. Amkreutz and A. Hartwig, *J. Mol. Struct.*, **2010**, 970, 101–105.
- [16] (a) H. Sato, F. Sato, M. Taniguchi and A. Yamagishi, *Dalton Trans.*, **2012**, 41, 1709–1712; (b) H. Sato, T. Taniguchi, A. Nakahashi, K. Monde and A. Yamagishi, *Inorg. Chem.*, **2007**, 46, 6755–6766.

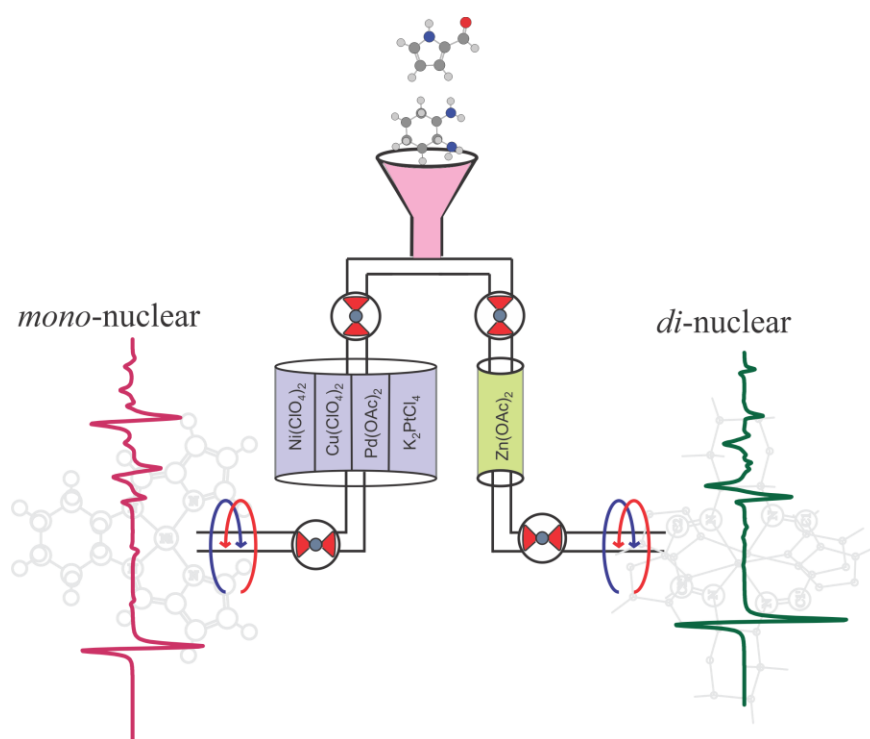


- [17] V. P. Nicu, M. Heshmat and E. J. Baerends, *Phys. Chem. Chem. Phys.*, **2011**, 13, 8811–8825.
- [18] C. Johannessen and P. W. Thulstrup, *Dalton Trans.*, **2007**, 1028–1033.
- [19] (a) B. J. V. Verkuijl, B. Schuur, A. J. Minnaard, J. G. de Vries and B. L. Feringa, *Org. Biomol. Chem.*, **2010**, 8, 3045–3054; (b) C. H. Perry, D. P. Athans, E. F. Young, J. R. Durig and B. R. Mitchell, *Spectrochim. Acta*, **1967**, 23A, 1137–1147.
- [20] A. S. Cooke and M. M. Harris, *J. Chem. Soc.*, **1963**, 2365–2373.
- [21] R. E. Pincock, R. R. Perkins, A. S. Ma and K. R. Wilson, *Science*, **1971**, 174, 1018–1020.
- [22] V. Setnička, M. Urbanová, P. Bouř, V. Král and K. Volka, *J. Phys. Chem. A*, **2001**, 105(39), 8931–8938.
- [23] S. K. Burley and G. A. Petsko, *Science*, **1985**, 229, 23–28.
- [24] C. A. Hunter and J. K. M. Sanders, *J. Am. Chem. Soc.*, **1990**, 112(14), 5525–5534.
- [25] (a) M. R. Poopari, Z. Dezhahang, G. Yang and Y. Xu, *ChemPhysChem*, **2012**, 13, 2310–2321; (b) P. Zhu, G. Yang, M. R. Poopari, Z. Bie and Y. Xu, *ChemPhysChem*, **2012**, 13, 1272–1281.
- [26] J. Tomasi, B. Mennucci and R. Cammi, *Chem. Rev.*, **2005**, 105, 2999–3093.
- [27] M. Losada and Y. Xu, *Phys. Chem. Chem. Phys.*, **2007**, 9, 3127–3135.
- [28] Gaussian 03, Revision B.01, M. J. Frisch, G. W. Trucks, H. B. Schlegel, G. E. Scuseria, M. A. Robb, J. R. Cheeseman, J. A. Montgomery Jr., T. Vreven, K. N. Kudin, J. C. Burant, J. M. Millam, S. S. Iyengar, J. Tomasi, V. Barone, B. Mennucci, M. Cossi, G. Scalmani, N. Rega, G. A. Petersson, H. Nakatsuji, M. Hada, M. Ehara, K. Toyota, R. Fukuda, J. Hasegawa, M. Ishida, T. Nakajima, Y. Honda, O. Kitao, H. Nakai, M. Klene, X. Li, J. E. Knox, H. P. Hratchian, J. B. Cross, C. Adamo, J. Jaramillo, R. Gomperts, R. E. Stratmann, O. Yazyev, A. J. Austin, R. Cammi, C. Pomelli, J. W. Ochterski, P. Y. Ayala, K. Morokuma, G. A. Voth, P. Salvador, J. J. Dannenberg, V. G. Zakrzewski, S. Dapprich, A. D. Daniels, M. C. Strain, O. Farkas, D. K. Malick, A. D. Rabuck, K. Raghavachari, J. B. Foresman, J. V. Ortiz, Q. Cui, A. G. Baboul, S. Clifford, J. Cioslowski, B. B. Stefanov, G. Liu, A. Liashenko, P. Piskorz, I. Komaromi, R. L. Martin, D. J. Fox, T. Keith, M. A. Al-Laham, C. Y. Peng, A. Nanayakkara, M. Challacombe, P. M. W. Gill, B. Johnson, W. Chen, M. W. Wong, C. Gonzalez and J. A. Pople, GAUSSIAN 03 (Revision C.02), Gaussian, Inc., Pittsburgh, PA, **2003**.

# 5

## Structural properties and induced helicity of a chiral Pyrrol-2-yl Schiff base ligand and its five transition metal complexes in solution: combined vibrational and electronic CD, and DFT studies

Zahra Dezhahang, Mohammad Reza Poopari, Joseph Cheramy, and Yunjie Xu



## 5.1. Introduction

---

Many pure optically active organic and inorganic molecules can be synthesized by using only a small amount of stereoselective transition metal catalysts. Because of their potential important applications in asymmetric catalysis, the chiral transient metal coordination complexes have attracted a substantial research attention. In the recent years, with the significant advances of both experimental and theoretical vibrational circular dichroism (VCD) spectroscopy and also theoretical electronic CD (ECD) spectroscopy, these two chiroptical techniques have seen increasing applications in the field of transition metal complexes. In particular, one can apply these two chiroptical techniques complemented with the DFT calculations to extract the structural information such as the conformational distributions and the induced chirality of the transition metal complexes in solution. While the early studies had mainly relied on the X-ray crystallography to provide detailed structural information of the transition metal complexes which includes chirality information, researchers have increasingly recognized the dynamic nature of molecular structures. Indeed, these complexes may adopt very different structures in solution compared to in solid.

The VCD technique measures the differential absorbance of the left versus right circularly polarized infrared radiation by a chiral sample accompanying a vibrational transition. A VCD spectrum often provides ten or more well resolved bands in the finger-print region. Furthermore, the VCD spectral simulations are based on the ground electronic state structural calculations which have proven to be quite reliable. Both these factors make the VCD technique a powerful tool for the coordination chemistry. One key subject of the recent interest is the induced-metal-centered chirality and how factors, such as solvent, [1,2] substitution on ligands, [3,4,5,6] and the properties of metal centers influence its formation. [7,8] For example, Sato and co-workers [2]

applied the VCD spectroscopy to study the conformational changes of a chiral Schiff base Ni(II) complex with a binaphthyl moiety. They found that the complex transformed reversibly between the square-planar, tetrahedral and octahedral configurations, depending on the solvents and the applied temperature. In addition, the other recent topics in this area of research include the effects of the electronic properties of central metal ions on the vibrational energy states of the ligands [9,10,11] and on the geometrical isomers, i.e. cis/trans and fac/mer, of a series of mixed-ligand diamagnetic Co(III) octahedral complexes, i.e.  $[\text{Co}(\text{tfac})_n(\text{acac})_{3-n}]$  where  $n=0$  to 3, [12] and how the conformations of chiral binaphthyl diphosphine ligands change upon the complexation with Pd(II) ion. [13].

Very recently, a number of publications on the structures and diastereoselectivity of four-coordinated transition metal complexes with *N,O*-chelate Schiff base ligands in solution by the VCD and sometimes ECD spectroscopy have emerged. [4,14,15] These publications show that a pair of enantiopure *R*- or *S-N,O* chelate ligands can lead to four diastereomers:  $\Lambda$ -*M-R-N,O* and  $\Delta$ -*M-R-N,O*, and  $\Lambda$ -*M-S-N,O* and  $\Delta$ -*M-S-N,O*, respectively and the ratio of the  $\Delta$  and  $\Lambda$  forms can differ drastically in solution and in solid states. In fact, the preference for the  $\Delta$  or  $\Lambda$  forms can be exactly the opposite in solution and in solid states and furthermore such a preference can be switched upon changing of solvents. [1] Clearly, it may not be sufficient to determine the induced metal chirality using X-ray crystallography alone. This is especially important considering that such transition metal catalysts are often used in stereoselective syntheses in solution. Furthermore, these studies highlight the importance of applying theoretical modelings to interpret the experimental VCD and ECD spectra in order to extract the solution phase structural information reliably and also the deficiency in the empirical spectral assignment procedures.

In the present paper, we focus on applying VCD and ECD spectroscopic tools to probe structural properties of a series of chiral transition metal (M= Ni (II), Cu (II), Pd (II), Pt (II) and Zn(II)) complexes with the bis(pyrrol-2-ylmethyleneamine)-cyclohexane ligand (H<sub>2</sub>L) in solution, complemented with DFT calculations. The H<sub>2</sub>L ligand is of particular interest as there are several examples of similar metal-ligand complexes being used effectively in the asymmetrical catalysis. [16,17,18,19] A more unconventional use of this type of metal complexes is in self-assembly and building of supramolecules, in particular, supramolecular hetero- and homo-nuclear helices. [20,21,22,23] Figure 5.1 summarizes the five complexes and the ligand investigated in this study. We synthesized both the ligand and the complexes following the previous literatures. [21,24,25] While ECD spectra of these complexes were reported, no theoretical calculations were performed for spectral interpretations and the discussion of the solution structures was based on the crystal structures. [10,12,14] In this study, the sensitivity of IR and especially the VCD spectroscopy to the ligand-to-metal coordination topology, i.e. *mono*-nuclear versus *di*-nuclear arrangement, the latter to the chirality of ligand and to the induced chirality at the metal centers have been examined. In particular, we have investigated how the initial helicity of the ligand is modified by coordination to these five transition metals in different ways. The effects of the electron configurations of the central metal ions on the IR and VCD spectra of the complexes have also been probed. The theoretical ECD spectra have been generated for all six systems to interpret the experimental spectra and the key factors which influences the appearance of the ECD spectra, have been discussed.

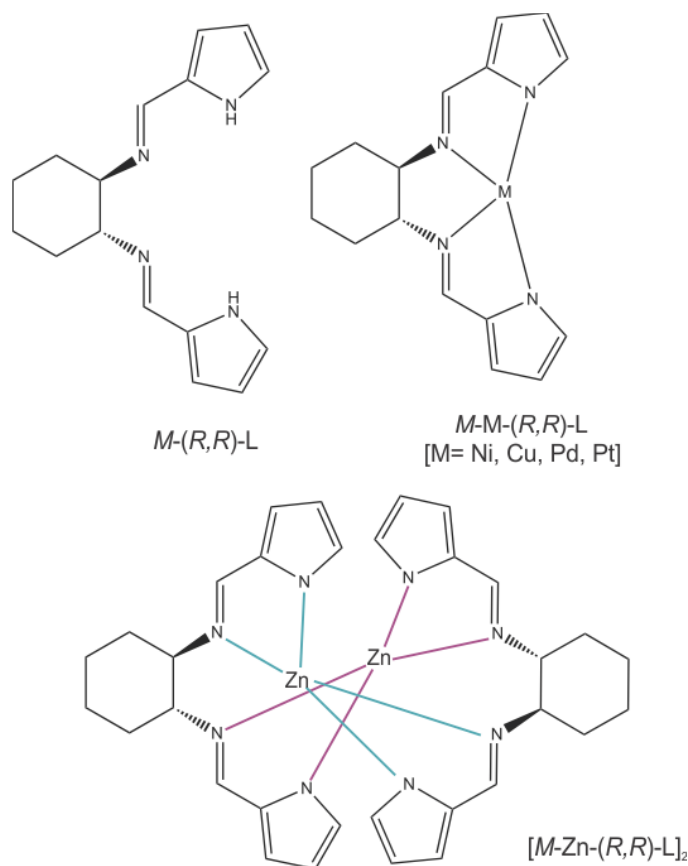


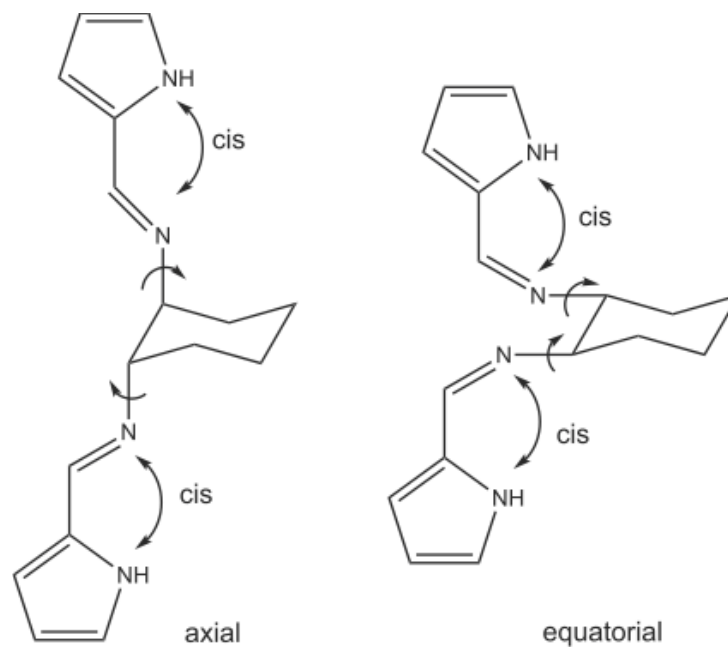
**Figure 5.1.**  $M-(R,R)-H_2L$  ligand and five transition metal complexes, namely  $M-Ni-(R,R)-L$ ,  $M-Cu-(R,R)-L$ ,  $M-Pd-(R,R)-L$ ,  $M-Pt-(R,R)-L$ , and  $[M-Zn-(R,R)-L]_2$  studied in this paper.

## 5.2. Results and discussion

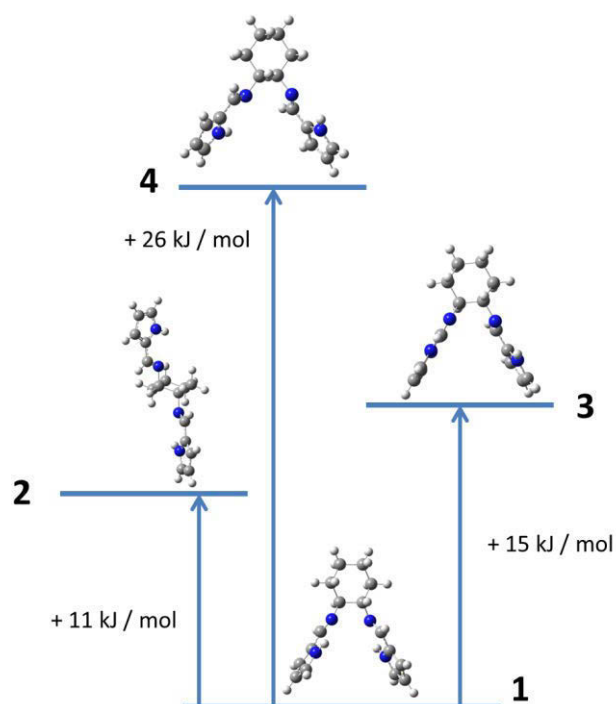
### 5.2.1. Experimental and theoretical VA, VCD, UV-Vis and ECD spectra of the Ligand

The  $(R,R)-H_2L$  ligand is similar to another picolylamine-type ligand, i.e.  $N,N'$ -bis(pyridine-2-ylmethylene)- $(S,S)$ -1,2-cyclohexanediamine which was studied by using the VCD technique recently [26], except that the pyridine is replaced by a pyrrole functional group in the current ligand. The replacement of pyridine with pyrrole brings a substantial rigidity to the structure. The lone pair electrons of the nitrogen atoms are involved in the resonance with the p electrons of the pyrrole ring and the  $H_{py}$  atom is intramolecular hydrogen (H)-bonded with the nitrogen atom of

the  $-N=C$  group. In  $H_2L$ , the cyclohexane ring takes on the chair configuration as this is by far the dominant arrangement versus the boat configuration at room temperature. [27] The nitrogen atoms at the cyclohexane ring may adopt either both equatorial (equ) or both axial (ax) positions dictated by its (*R,R*) chirality (See Figure 5.2). Furthermore, these nitrogen atoms may take on either cis or trans orientations with respect to the nitrogen atoms of the pyrrole rings. A definition of the cis arrangement and the rotatable bonds motions indicated with arrows are provided in Figure 5.2. The initial conformational searches using the HF/STO-3G method implemented in the Spartan package [28] produced 7 candidates. These preliminary conformers were re-optimized at the DFT/B3LYP/cc-pVTZ level of theory and the four most stable conformers are given in Figure 5.3. The relative energies of these conformers indicate that only one conformer with the equatorial cis–cis configuration, i.e. [cis-cis]<sub>equ</sub> (Figure 5.2), is the dominant species at room temperature. Contributions from other conformers are negligible. It is noted that the  $H_2L$  and other related ligands studied before all favor the equatorial arrangement. It is also no surprise that the cis-cis configuration is preferred since this arrangement allows the intramolecular H-bonding between  $-NH$  of pyrrole group and the nitrogen atom of  $-C=N$  group to happen. The creation of the resonance structure between the two aforementioned groups bestows the structural rigidity to the ligand.

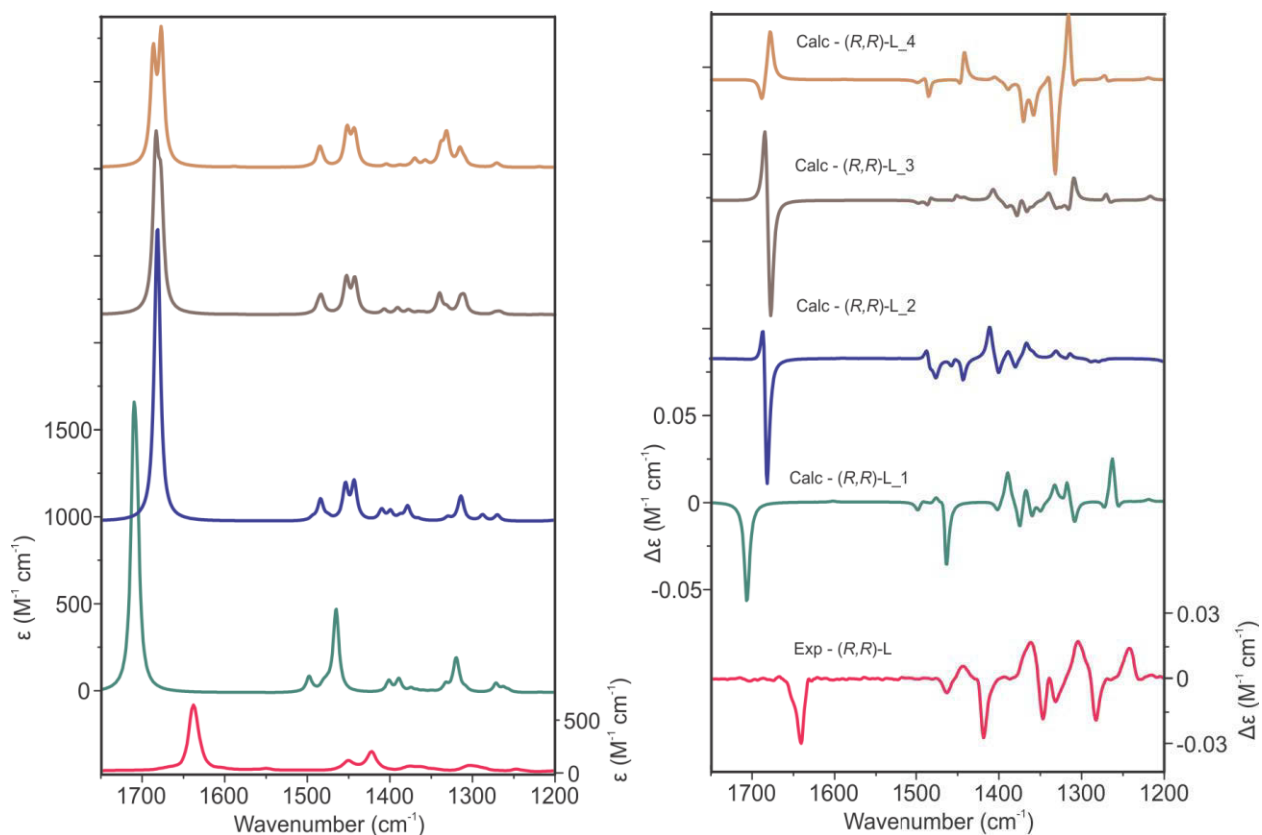


**Figure 5.2.** The *cis* configuration of  $(R,R)$ - $H_2L$  ligand with axial and equatorial arrangements at cyclohexane. The rotatable  $N-C_{hexane}$  bonds are indicated by small arrows.



**Figure 5.3.** Relative energies of the four most stable conformers of  $H_2L$  obtained at the B3LYP/cc-pVTZ level of theory.

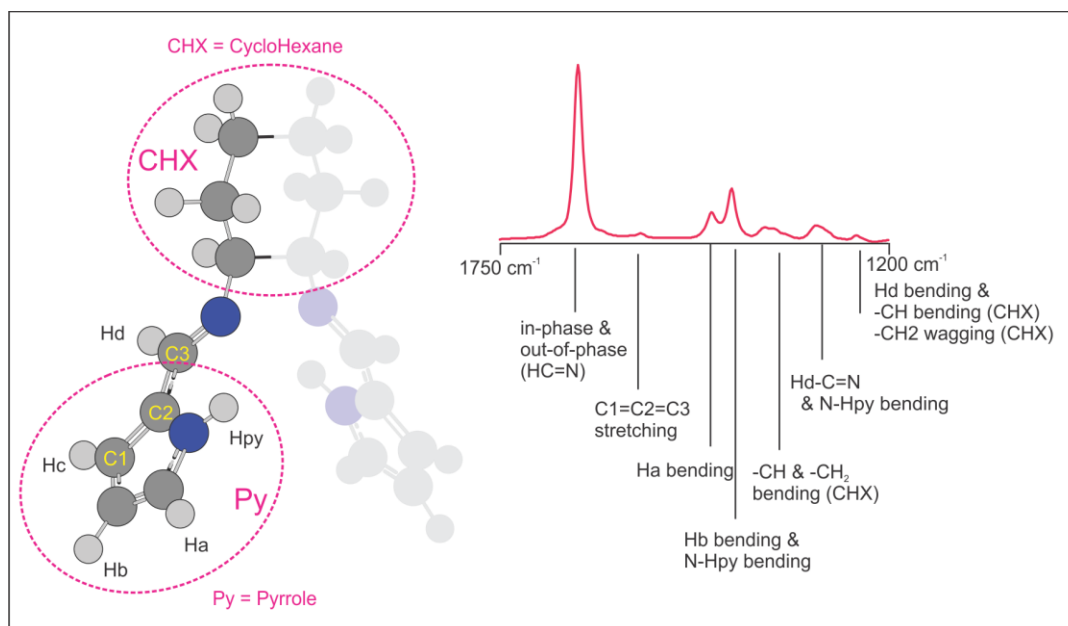




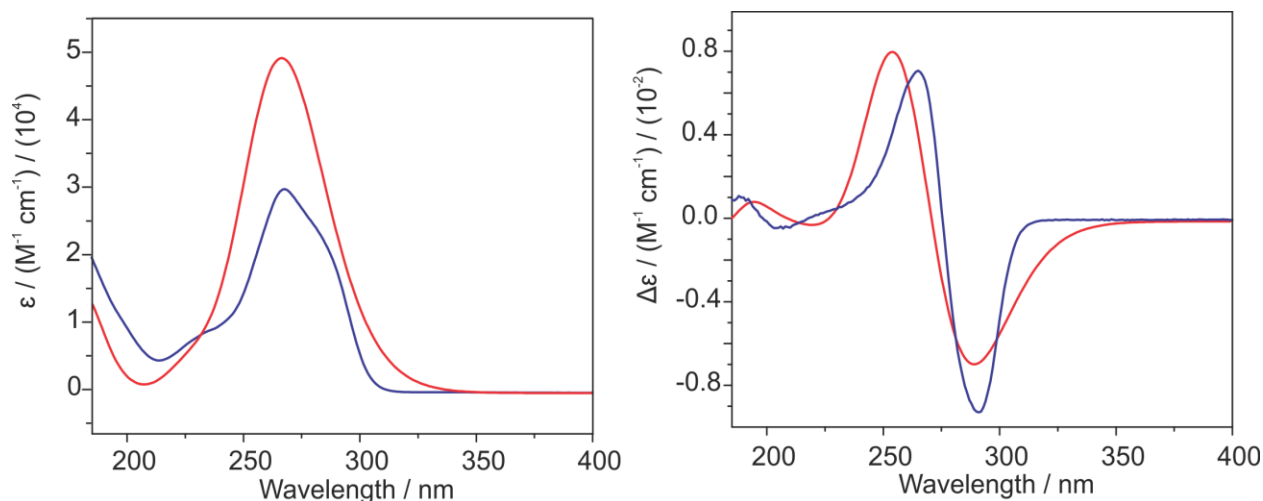
**Figure 5.4.** Comparison of the experimental VA (left) and VCD (right) spectra of the  $(R,R)$ -H<sub>2</sub>L ligand in DMSO-d<sub>6</sub> with the corresponding single conformer spectra calculated at the B3LYP/cc-pVTZ level of theory in DMSO-d<sub>6</sub> solution.

Figure 5.4 shows the experimental and calculated VA and VCD spectra obtained for the  $(R,R)$ -H<sub>2</sub>L ligand in DMSO-d<sub>6</sub>. Comparing the experimental and the calculated spectra reveals that conformer 1 is by far the dominant species in solution. In ref. 20, a second conformer was suggested as the possible main conformation in solid state. This suggestion corresponds to the conformer 4 in Figure 5.3. This particular conformer clearly has a negligible contribution in solution based on both the relative energy calculated and the comparison of the experimental and theoretical VCD spectra shown in Figure 5.4. Note that we chose not to scale the frequency axis

for an easier discussion later on for the vibrational frequency shift upon complexation. As one can see, the calculated VCD spectrum reproduces the experimental spectrum quite well and all major features observed have been captured theoretically. The bands in the 1650 ~ 1600  $\text{cm}^{-1}$  region correspond to the  $\text{-C=N}$  stretching vibrational modes, both in-phase and out-of-phase  $\text{-C=N}$  stretching modes. In the range below 1600  $\text{cm}^{-1}$ , the vibrational modes can be assigned mainly to  $\text{-C-H}$  and  $\text{-N-H}$  bending motions of the pyrrole rings and different  $\text{-CH}$  and  $\text{-CH}_2$  vibrational modes of the cyclohexane ring. See Figure 5.5 for more detailed on the vibrational modes analysis of the ligand molecule.



**Figure 5.5.** Left: half of the H<sub>2</sub>L ligand molecule is highlighted and some relevant atoms are labeled. Right: the assignments of the major vibrational modes observed.



**Figure 5.6.** Comparison of the experimental (blue) UV-Vis (left) and ECD (right) spectra (*R,R*)-H<sub>2</sub>L in acetonitrile with the corresponding spectra calculated (red) at the B3LYP/cc-pVTZ level of theory in acetonitrile solution.

Figure 5.6 shows the experimental and calculated UV-Vis and ECD spectra obtained for conformer 1 of the (*R,R*)-H<sub>2</sub>L ligand in acetonitrile. Here, very good agreements between the experimental spectra and calculated ones have been achieved, supporting the conclusion drawn from the VA and VCD spectral studies of the ligand. Furthermore, we examined the effects of coordination with a water molecule to this ligand on the UV-Vis and ECD spectra. The theoretical UV-Vis and ECD spectra have been generated by using directly the X-ray structural parameters of H<sub>2</sub>L with water and by optimizing the H<sub>2</sub>L-water complex using the solid state structure as the starting point. The resulting spectra are summarized in Figure C1, Appendix C, comparing to the simulation without water. Overall, the UV-Vis and ECD spectra look quite similar for the two systems with and without water coordination, except some minor changes in the short wavelength region below 200 nm. We note that the dihedral angle  $\theta$  between the plane N-C3-C2-N (See Figure 5.5 for atom labels) and the other corresponding plane in H<sub>2</sub>L is the

helicity-determining angle. The  $\theta$  value for the H<sub>2</sub>L ligand by itself is 63.4° and with water is 64.4°, in comparison to 70.5° obtained from the solid state structure which contains crystal water. [21] Clearly, we have a severe deviation from square-planar geometry even without coordination to water molecule or the lattice forces and other environmental perturbation in solid state. It would be quite interesting to see this helicity-determining angle  $\theta$  changes upon coordination to different metals. A closer examination of the dominant ligand species, i.e. conformer 1, indicates that (*R,R*)-H<sub>2</sub>L actually adopts *M*-helicity. This will be further discussed in Section 5.2.4 in comparison with helicity of the other metal complexes.

#### *5.2.2. Experimental and theoretical VA and VCD spectra of Ni (II), Cu (II), Pd (II), and Pt (II) complexes*

The coordination of H<sub>2</sub>L ligand to these four metal centers results in near square planar coordination structures, based on the previous X-ray crystal structures. [20,23,24] Theoretical conformational and configurational searches have been carried out for these four complexes with (*R,R*)-H<sub>2</sub>L. One hypothesis to test here is if the  $\Delta$ - or  $\Lambda$ -configurations at the metal center can be possibly interconverted by a ligand rearrangement through a planar geometry. Since these four complexes are only slightly distorted from the square-planar geometry, such an interconversion may be feasible. Considerable efforts have been spent to generate both *M*-(*R,R*) and *P*-(*R,R*) diastereomers. It became clear that relative rigidity of the cyclohexane ring in chair configuration and its (*R,R*) chirality dictate the pyrrole substitutes to adopt *M*-helicity. *P*-(*R,R*) diastereomer could only be generated with the cyclohexane ring in a boat configuration which is well known to be of negligible contribution. [29] Therefore for all these four ligands, only one dominant

diastereomeric structure is identified for each in Figure 5.7, as well as some related structural parameters.

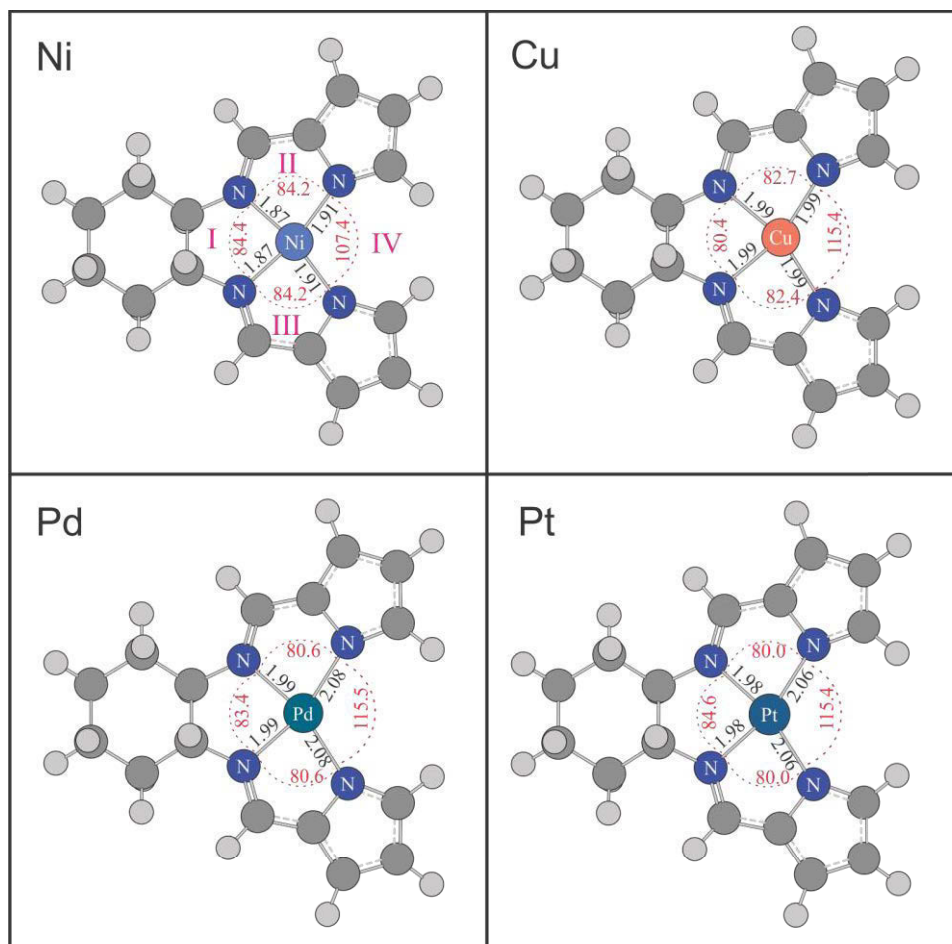


**Figure 5.7.** The most stable diastereomeric conformer of the *mono*-nuclear Cu(II) , Ni(II) , Pd(II) and Pt(II) complexes predicted at the DFT/B3LYP/Gen level of theory. Some bond distances (in Å) and angles (in °) are listed.

The experimental and calculated VA and VCD spectra for the Ni (II), Cu (II), Pd (II), and Pt (II) complexes are shown in Figures 5.8 and 5.9, respectively. For the experimental VA spectra, one can see the correlation among these four complexes. The same vibrational assignment for the

ligand holds for the metal complexes, with two exceptions. First, the spectrum for the Cu (II) complex shows an additional shoulder for the  $\text{-C=N}$  stretching vibrational mode, indicating the larger separation of the in-phase and out-of-phase  $\text{-C=N}$  stretching modes. Second, each metal VA spectrum displays an overlapped peak between  $1525$  and  $1500\text{ cm}^{-1}$ . This peak is due to the overlap of the in-phase and out-of-phase asymmetric  $\text{C=C=C}$  stretching modes. These modes have essentially no intensity for the corresponding ligand. Detailed assignments of these vibrational modes are illustrated in Figure 5.10, using the spectrum of the Cu (II) complex as an example.

The simulated VA spectra provide good agreements with the experiment. For the peaks below  $1500\text{ cm}^{-1}$ , there are only very minor differences among these metal complexes, indicating that the metal center has little effect on the vibrational modes of the pyrrole and cyclohexane rings. However, some small shifts exist for the  $\text{-C=N}$  stretching vibrational modes. The relative vibrational frequency shifts among these four metal complexes are well reproduced by the theoretical calculations. Such shifts can be understood by examining the electronic properties of the metal centers. The electronegativity of the metal centers which act as *Lewis* acids has the following ordering:  $\text{Cu (II)} < \text{Ni (II)} < \text{Pd (II)} < \text{Pt (II)}$ . Since the metal center pulls away the electron density around the  $\text{-C=N}$  group (*Lewis* base), these  $\text{-C=N}$  bond become weaker. One may therefore expect that the resulting red shift of the related  $\text{-C=N}$  stretching mode is larger for the larger electronegativity. The trend observed follows the prediction: ligand ( $1640\text{ cm}^{-1}$ )  $>$  Cu ( $1610\text{ cm}^{-1}$  &  $1593\text{ cm}^{-1}$ )  $>$  Ni ( $1580\text{ cm}^{-1}$ )  $>$  Pd ( $1578\text{ cm}^{-1}$ )  $>$  Pt ( $1572\text{ cm}^{-1}$ ). Similarly, the VCD spectral features also resemble each other in the region below  $1500\text{ cm}^{-1}$ . The most prominent difference among them for the VCD features is that the Ni (II) and Cu (II) complexes

produce a bisignate  $-/+$  signal from low to high frequencies around  $1600\text{ cm}^{-1}$ , whereas a negative band is observed for the Pd (II) and Pt (II) complexes instead.

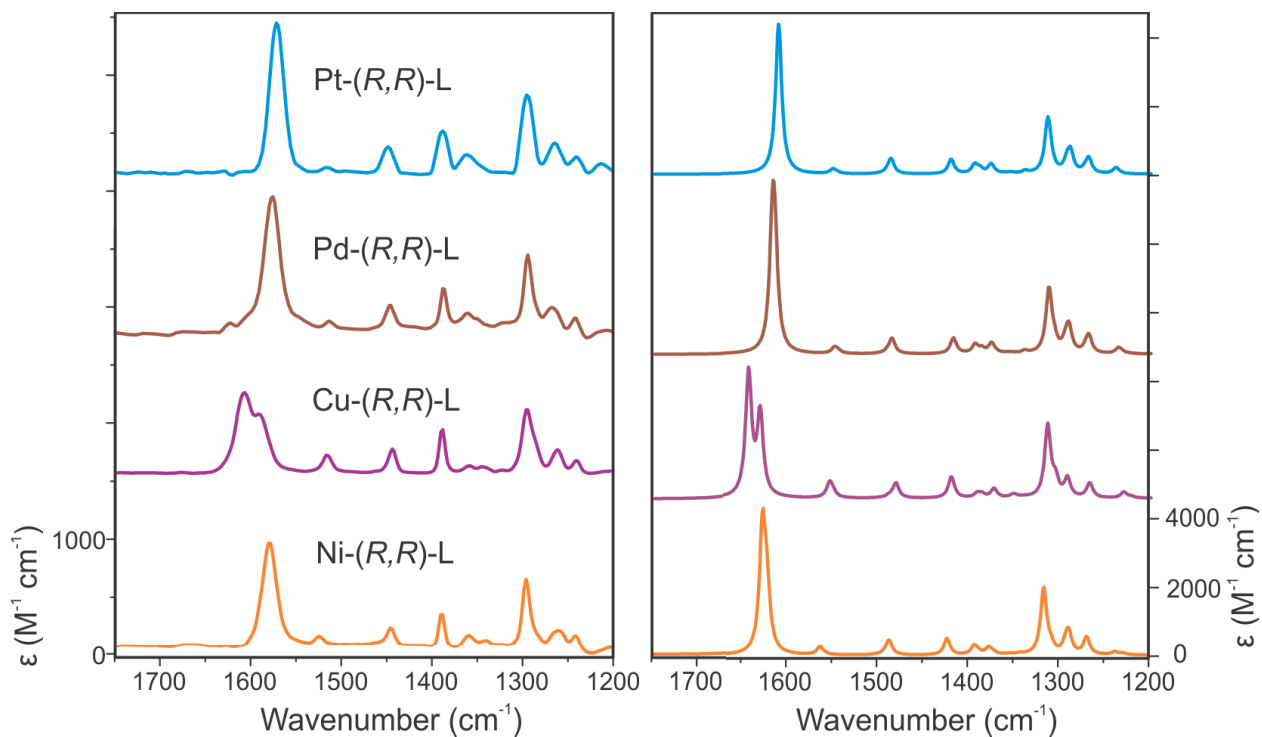


**Figure 5.8.** Comparison of the experimental VA spectra of the Ni (II), Cu (II), Pd (II), and Pt (II) complexes in DMSO-d<sub>6</sub> with the corresponding calculated spectra (right) at the DFT/B3LYP/Gen level of theory in DMSO-d<sub>6</sub> solution.

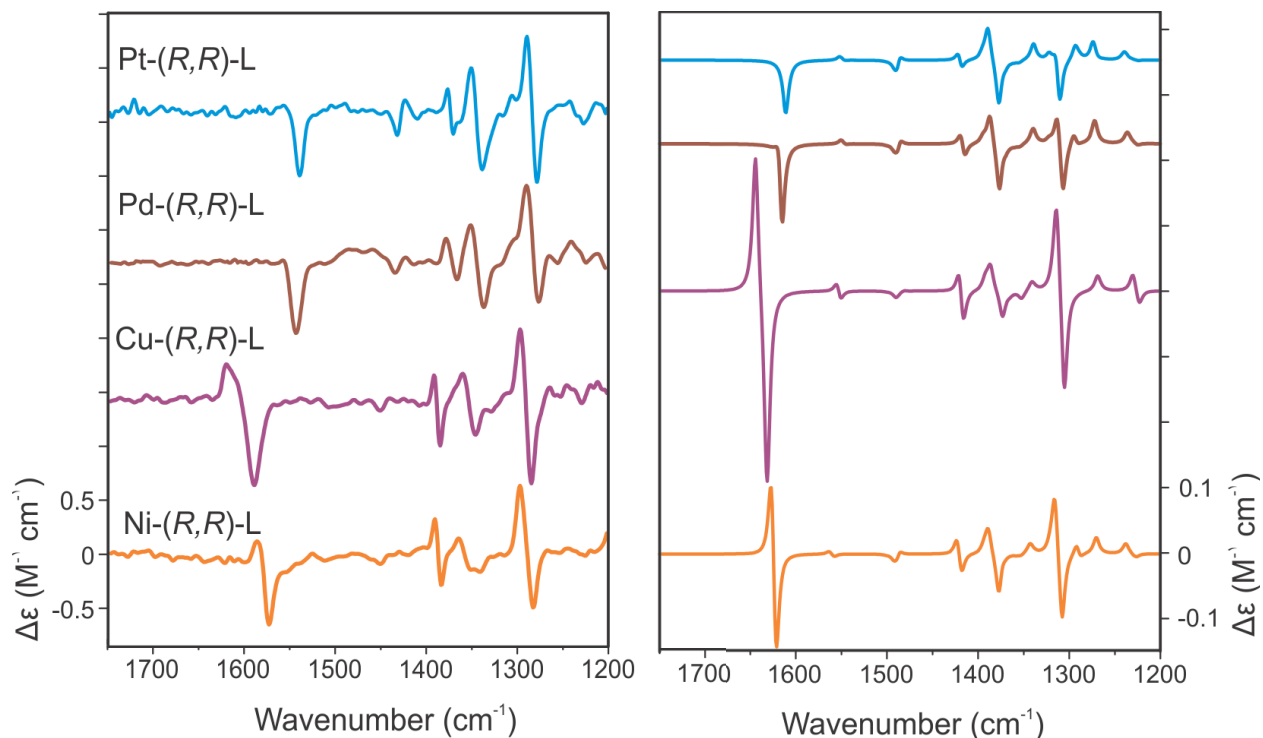


**Figure 5.9.** Comparison of the experimental VCD spectra of the Ni (II), Cu (II), Pd (II), and Pt (II) complexes in DMSO-d<sub>6</sub> with the corresponding calculated spectra (right) at the DFT/B3LYP/Gen level of theory in DMSO-d<sub>6</sub> solution.



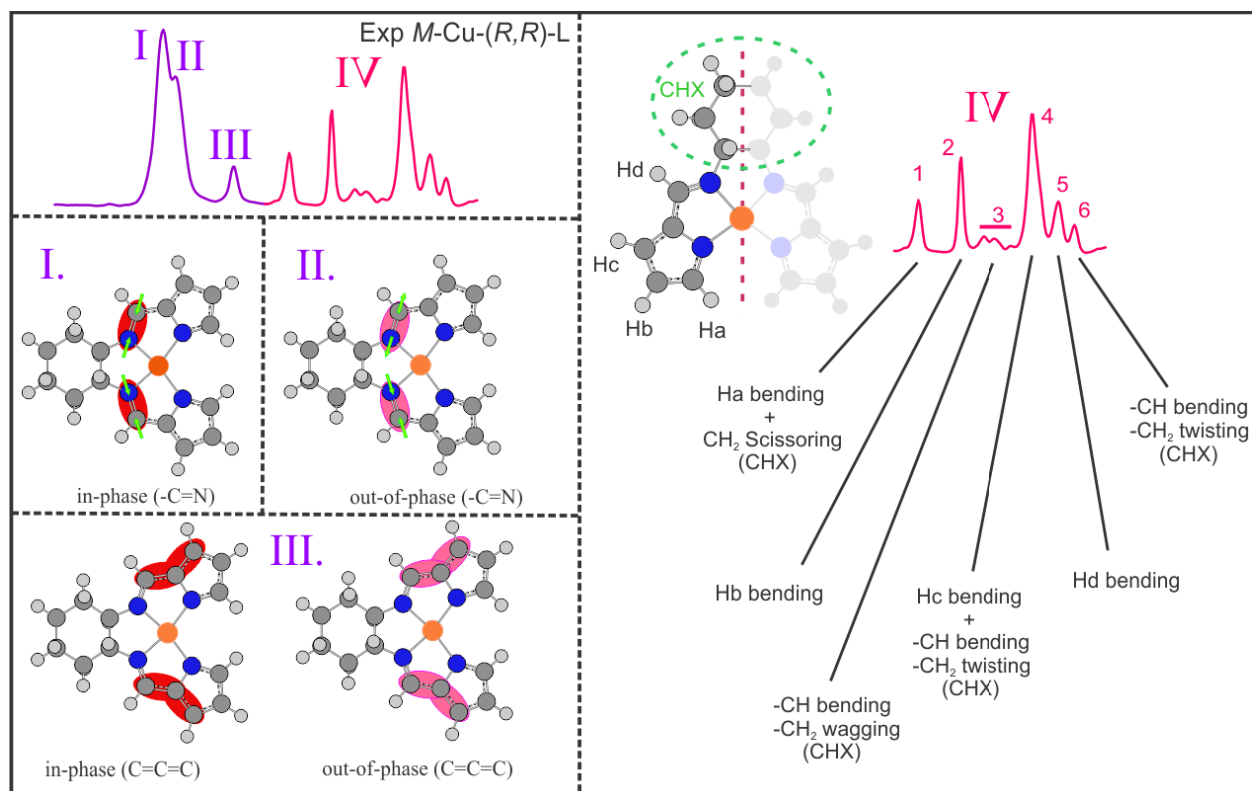


**Figure 5.10.** The main vibrational modes of the  $M\text{-Cu-(}R,R\text{)-L}$  complex in the region of  $1750 - 1200 \text{ cm}^{-1}$ .

In the *mono*-nuclear complexes, the diamagnetic Ni (II), Pd (II), and Pt (II) ions take  $d^8$  electron configuration with a  $d_{z^2}$  orbital as *HOMO*, while the paramagnetic Cu complex take  $d^9$  electron configuration with a  $d_{x^2-y^2}$  orbital as *HOMO*. Therefore, for the Ni, Pd, and Pt metal centers,  $3d_{x^2-y^2}$  orbital is the *LUMO*, whereas for Cu,  $4d_{yz}$  is the *LUMO* since all its  $3d$  orbitals are either full or half-full and  $d_{yz}$  is the next lowest energy  $d$  orbital available. For the metal-N bonds, the N of the  $-\text{C}=\text{N}$  group shares its lone pair electrons through a dative-covalent bond using a  $sp^2$ -hybridized orbital in the  $xy$  plane, while the metal center utilizes a  $sp^2d$  hybrid orbital. As shown in Figure C2, Appendix C, the metal-N  $\sigma$  bond can achieve a better head-to-head overlapping

with a  $sp^2d_{x^2-y^2}$  hybrid orbital of Ni, Pd, and Pt than with a  $sp^2d_{yz}$  hybrid orbital of Cu. The weaker Cu-N bond results in a higher  $-C=N$  stretching frequency for Cu than Zn.

The above argument can also be visualized by the molecular orbital (MO) representations of the Cu and Ni complexes (Figure 5.11). As one can see, there is more overlap expected between the  $d_{x^2-y^2}$  orbital of Ni (II) ( $sp^2d$  hybridization) and the  $p$  orbital ( $sp^2$  hybridization) of the nitrogen atoms of the  $-C=N$  groups than there is between the *LUMO* orbital of Cu (II) and the same  $p$  orbital of the nitrogen atoms of the  $-C=N$  groups. From the MO analysis, it was found that the *LUMO* orbital of Cu (II) complex has retained its  $d_{yz}$  orbital characteristics from  $4d$  shell. Therefore, the overall hybridized orbital is more spanned along the  $z$  axis, perpendicular to the plane of the molecule. As a result, the binding strength between the Cu (II) center and the nitrogen atoms is weakened compared to the Ni-N bond, thus resulting in a blue shift for the  $-C=N$  stretching modes of the Cu (II) complex relative to the other metals. The above bonding analysis also allows one to see why these four complexes have the near square-planar coordination geometries.

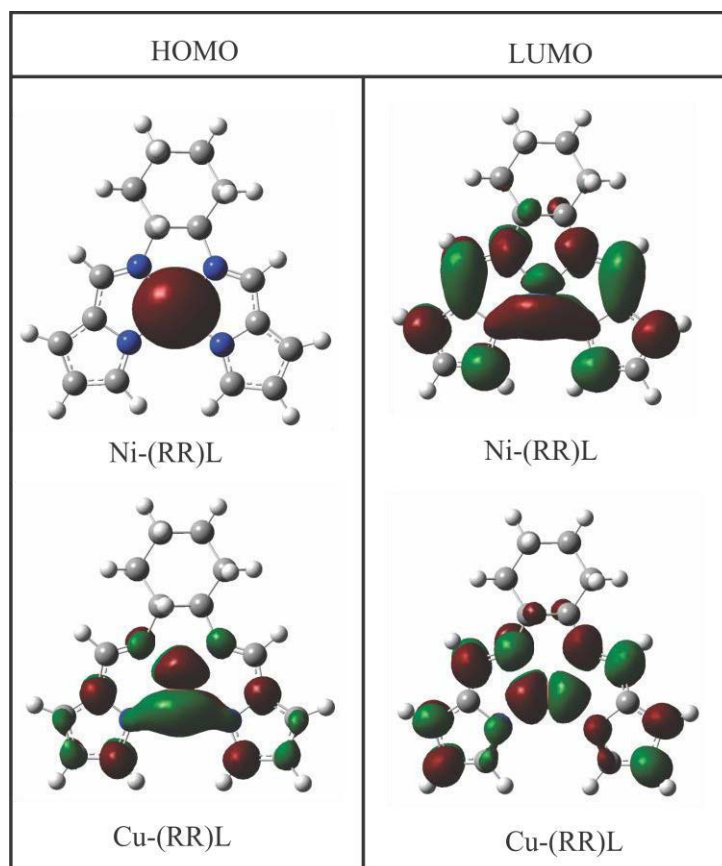


**Figure 5.11.** The *HOMO* and *LUMO* molecular orbital (MO) representations of *M*-Ni-(*R,R*)-L and *M*-Cu-(*R,R*)-L compounds.

### 5.2.3. Experimental and theoretical VA and VCD spectra of the Zn (II) complexes

Since all *d*-orbitals are fully occupied, the Zn (II) ion takes on  $sp^3$  hybridization to make covalent bonds with the *p* orbital ( $sp^2$  hybridization) of the nitrogen atoms of the -C=N groups, favoring the tetrahedral configuration around the metal center. Indeed, the optimized geometry of the *mono*-nuclear Zn (II) complex deviates considerably from a perfect square planar arrangement, in comparison with the four metal complexes discussed above. Furthermore, while the VA and VCD spectra of each of the four metal complexes discussed in the previous section show considerable similarities, those of the Zn (II) complex are noticeably different (see Figure 5.12).

We further note that the simulated VA and especially VCD spectra of the *mono*-nuclear Zn(II) complex show the poor agreement with the experimental data, in contrast to the situation with the other four *mono*-nuclear complexes discussed above.

The X-Ray crystallography structure of the Zn (II) complex indicates a double stranded *di*-nuclear helix where the Zn (II) metal centers adopt a close to tetrahedral geometry rather than a square planar geometry.[21] This is consistent with the fact that the Zn (II) metal has a  $d^{10}$  configuration which generally favors a tetrahedral complexation geometry. We therefore further optimized the *di*-nuclear Zn (II) complex and simulated its VA and VCD spectra. The calculated VA and VCD spectra of both models are compared with the experimental data in Figure 5.12, while the detailed vibrational assignment for the 1700 to 1550  $\text{cm}^{-1}$  region which contains four distinctive  $-\text{C}=\text{N}$  stretching modes is given in Figure C3, Appendix C. All in-phase stretching motions appear at higher frequencies, and those corresponding to out-of-phase vibrations appear at lower frequencies.

As can be seen in Figure 5.12, the calculated VCD spectra in the 1700-1550  $\text{cm}^{-1}$  region show similar bisignate signals for the *mono* and *di*-nuclear structures. Both show reasonable agreement with the experimental results, leaving the assignment ambiguous. By considering the 1550-1200  $\text{cm}^{-1}$  region, the experimental VA spectrum composes of four strong peaks, 1, 2, 2', and 3. Further detailed comparisons of the calculated VA spectra of the *mono*- and *di*-nuclear Zn (II) complexes are summarized in Figure C4, Appendix C. The signal associated with the  $\text{C}=\text{C}=\text{C}$  stretching mode shows up noticeably for the *mono*-nuclear complex but a weak band for the *di*-nuclear complex. The latter is consistent with the experimental observation. Furthermore, the spacing for the peaks between 1500-1350  $\text{cm}^{-1}$  is also quite different for the two complexes, with the *di*-nuclear one has a much better agreement with the experiment. Overall, the observed

experimental VA features are much better reproduced by the predicted VA spectrum of the *di*-nuclear geometry. At the same time, the predicted VCD spectral patterns of the *mono*- and *di*-nuclear complexes are quite different, especially for the region around 1400  $\text{cm}^{-1}$ . The strong +/- +/- features observed from lower to higher frequencies in this region match with those of the *di*-nuclear complex only. Therefore, the comparison of the experimental and theoretical VA and VCD spectra allows one to clearly identify the *di*-nuclear Zn (II) complex as the species in solution.

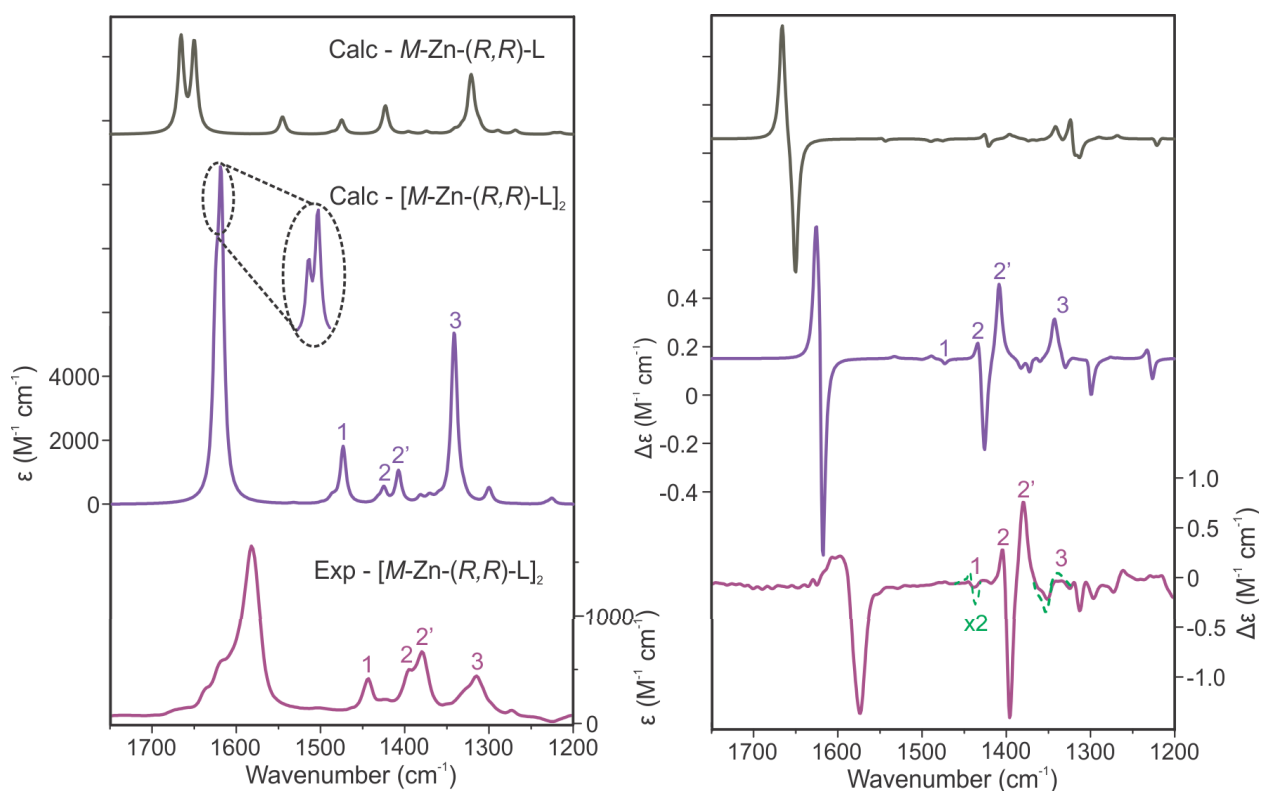


**Figure 5.12.** Comparison of the experimental VA (left) and VCD (right) spectra of the Zn (II) complex in DMSO- $d_6$  with the corresponding spectra of the *mono* and *di*-nuclear Zn (II) complex calculated at the B3LYP/Gen level of theory in DMSO- $d_6$  solution where the LANL2DZ basis set is assigned for the Zn atom and the cc-pVTZ basis set for the other atoms.

#### 5.2.4. *M*- and *P*-helicity in the Zn (II) complex and other complexes

We note in the ligand and in all the transition metal complexes studied here, the metal center takes on the *M*-helicity with the (*R,R*)-H<sub>2</sub>L ligand. Here, we examine the reason for such a specific induced helicity preference and how such a helicity reflects in the corresponding VCD and ECD spectra using the Zn (II) complex as an example. In principle, the *di*-nuclear Zn (II) complex can adopt two different helical configurations with respect to the two capping ligands. If the metal-ligand coordination takes on a right-handed clockwise helical arrangement, it's called *P*-configuration, whereas the opposite helicity is considered *M*-configuration. We have optimized two diastereomeric geometries provided in Figure 5.13.

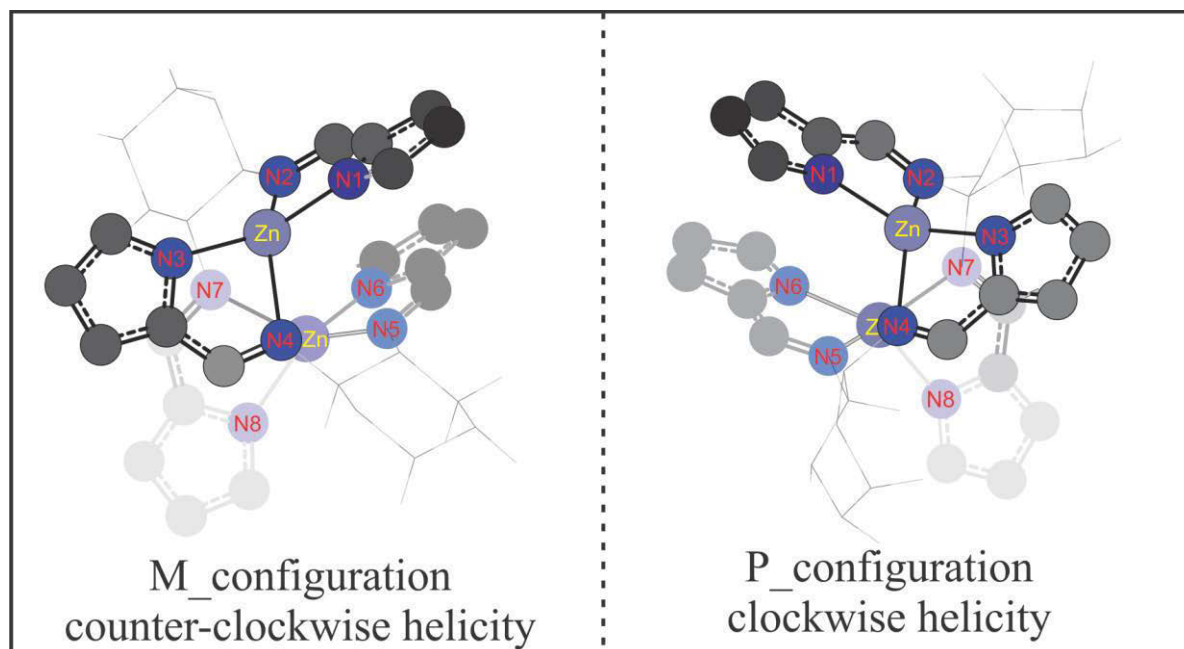


**Figure 5.13.** Illustration of *M*- and *P*-helicity for the *di*-nuclear Zn (II) complex.

Figure 5.14 shows the comparison of the experimental and theoretical VA and VCD spectra of the *M*- and *P*-[Zn-(*R,R*)-L]<sub>2</sub> structures. There are a number of significant differences between the VA and VCD spectra of the *P*-helical configuration with the experiment ones and with those of

the *M*-helical structure. For example, the VA spectrum below 1500  $\text{cm}^{-1}$  comprised of four distinctive intense signals experimentally. These features are only captured by the *M*-helical structure. Furthermore, the +/- bisignate VCD features in the 1650-1550  $\text{cm}^{-1}$  region were only captured properly with the *M*-configuration and not at all by the *P*-configuration. Lastly, for the region between 1450-1350  $\text{cm}^{-1}$ , there exists an obvious +/-/+ couplet which can be only observed for the *M*-configuration while it is missing for the other one. Therefore, one can conclude confidently that *M*-[Zn-(*R,R*)-L]<sub>2</sub> is the dominant species in solution.

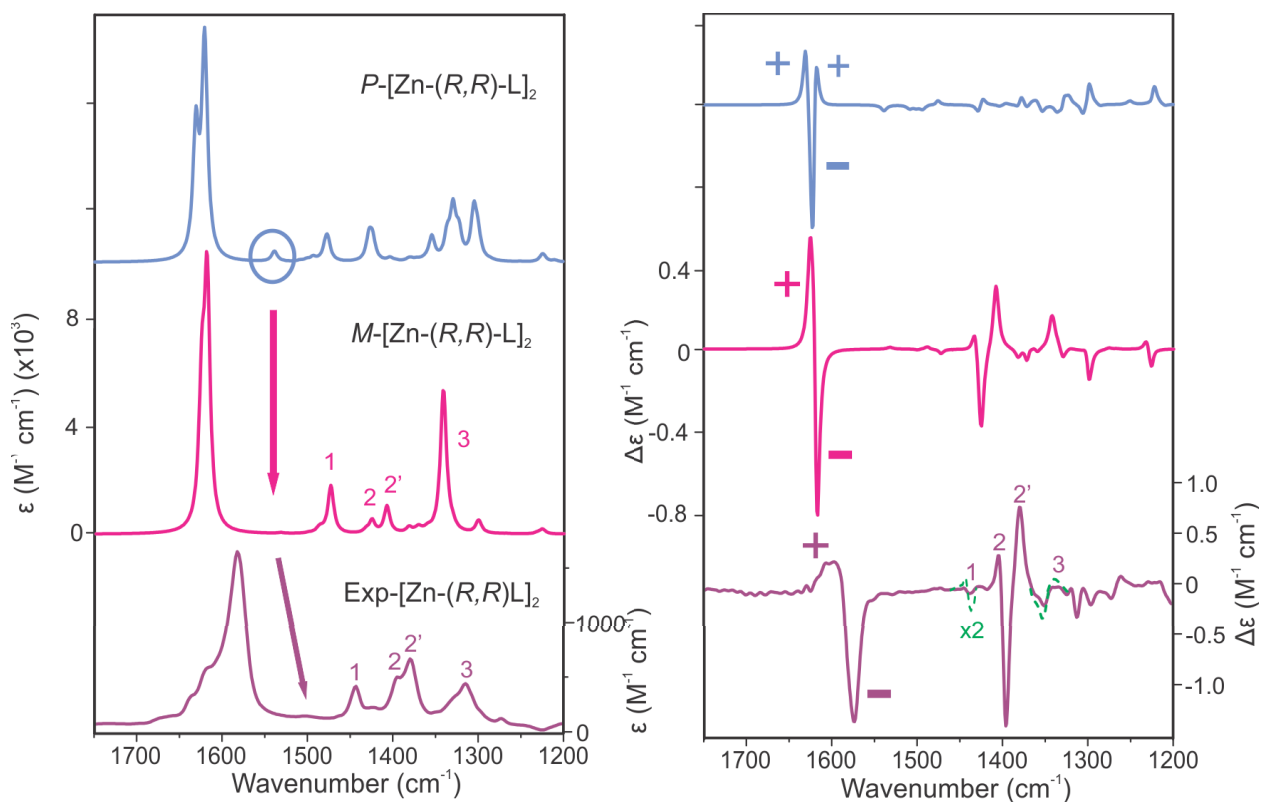


**Figure 5.14.** Comparison of the experimental VA (left) and VCD (right) spectra of the Zn (II) complex in DMSO-d<sub>6</sub> with the corresponding spectra of the *M*- and *P*-[Zn-(*R,R*)-L]<sub>2</sub> diastereomers calculated at the B3LYP/Gen level of theory in DMSO-d<sub>6</sub> solution where LANL2DZ basis set is assigned for Zn atom and the cc-pVTZ basis set for the other atoms.

We further investigate the differences in the UV-Vis and especially ECD spectra of the *M*- and *P*-helicity. In Figure 5.15, we show the comparison of the experimental and theoretical UV and ECD spectra of the *M*- and *P*-[Zn-(*R,R*)-L]<sub>2</sub> diastereomers. As one can see, the predicted UV-Vis spectra for the *M*- and *P*-helicity of the Zn(II) diastereomers are very similar. The corresponding ECD spectra, on the other hand, show essentially the mirror-imaged spectral features in most parts, except in the 275 nm region where negative features were predicted for both. It appears that the ECD features are dominated by the induced helicity at the metal center, while the feature at the 275 nm reflects the ligand chirality. This point will be explored further when we examine the helicity determining-angle  $\theta$  for the ligand and all the metal complexes studied here. As one can see clearly from Figure 5.16, the experimental ECD spectrum observed is consistent with *M*-[Zn-(*R,R*)-L]<sub>2</sub> diastereomer, supporting the conclusion drawn from the VA and VCD study. It is important to emphasize that VCD spectra of *M*-[Zn-(*R,R*)-L]<sub>2</sub> and *P*-[Zn-(*R,R*)-L]<sub>2</sub> do not show nearly mirror-image quality to each other as in the case of ECD. Rather, they show the sensitivity to both chirality and the helicity of the ligand. In addition, the VA spectra for these two diastereomers are also quite different, whereas the UV-Vis spectra of *M*-[Zn-(*R,R*)-L]<sub>2</sub> and *P*-[Zn-(*R,R*)-L]<sub>2</sub> discussed above are very much alike. Therefore, one cannot tell *M*-[Zn-(*R,R*)-L]<sub>2</sub> apart from *M*-[Zn-(*S,S*)-L]<sub>2</sub> based on the UV-Vis and ECD spectra of the sample, whereas VA and VCD spectra allow us to identify them unambiguously.



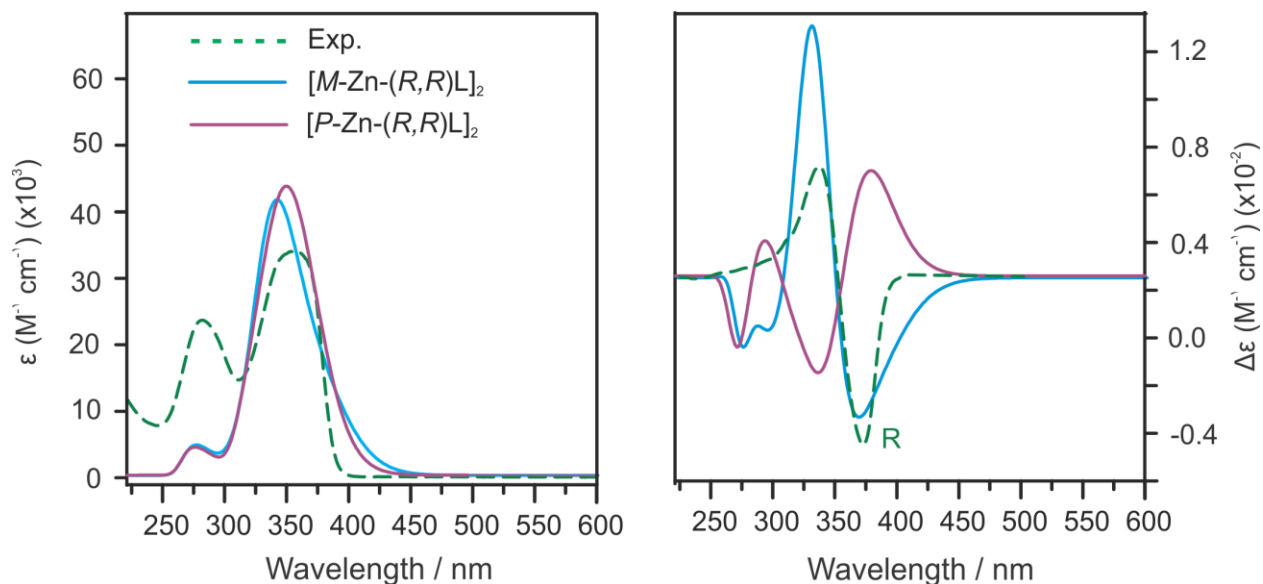


**Figure 5.15.** Comparison of the experimental UV-Vis (left) and ECD (right) spectra of the Zn (II) complex in acetonitrile with the corresponding spectra of the *M*- and *P*-[Zn-(*R,R*)-L]<sub>2</sub> diastereomers calculated at the B3LYP/Gen level of theory in acetonitrile solution where LANL2DZ basis set is assigned for Zn atom and the cc-pVTZ basis set for the other atoms.

In Table 5.1, we compare the values of the helicity-determining angle  $\theta$  defined in Figure 5.16 for all the transition metal complexes, as well as the  $\theta$  values of the ligand which is similarly defined for the ligand as the dihedral angle  $\theta$  between the plane N-C3-C2-N (Figure 5.5) and the other corresponding plane in H<sub>2</sub>L. First of all, the  $\theta$  values for the ligand and for the *di*-nuclear Zn (II) complexes are quite similar to each other and very different from the rest of the metal complexes. Indeed, the overall geometrical arrangements for the ligand part in these two systems are also quite similar. A closer examination shows that the rigidity of the cyclohexane ring in chair configuration and the (*R,R*) chirality of the ligand, dictates that the ligand takes on *M*-helicity. To produce a *P*-helicity, the cyclohexane ring would be distorted into a boat configuration, as demonstrated for the Zn (II) complex in Figure 5.13. This is strongly

energetically unfavorable. Since Pt (II), Pd (II), Ni (II), and Cu (II) favor a square-planar coordination geometry, the coordination of the ligand with these metal centers serve to reduce this helicity angle closer to zero. Formation of the *di*-nuclear Zn (II) complex, on the other hand, offers an efficient way to allow the Zn(II) center to follow its tetrahedral coordination tendency, without putting additional strain on the cyclohexane part. Since ECD spectral features are dominated by the helicity of the system, it is no surprise that the ECD spectra of H<sub>2</sub>L and the *di*-nuclear Zn (II) complex are so similar and that all other metal complexes all exhibit a negative cotton couplet in their ECD spectra (Figure C5, Appendix C).

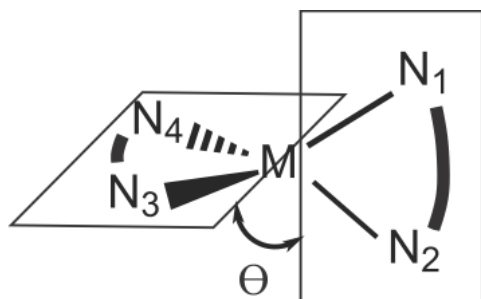


**Figure 5.16.** Definition of the helicity-determining angle  $\theta$ . For tetrahedral,  $\theta=90^\circ$ , whereas for square planar,  $\theta=0^\circ$ . N<sub>1</sub> and N<sub>2</sub> are atoms of one arm, and N<sub>3</sub> and N<sub>4</sub> are atoms of the other arm.

**Table 5.1.** The helicity-determining angle  $\theta$  for the H<sub>2</sub>L ligand and the associated complexes

Compound	$\theta$ (°) Solution <sup>a</sup>	$\theta$ (°) Solid <sup>b</sup>
$\Lambda$ -Pt-( <i>R,R</i> )-L	3.3	N/A
$\Lambda$ -Pd-( <i>R,R</i> )-L	3.7	N/A
$\Lambda$ -Ni-( <i>R,R</i> )-L	5.2	6.5
$\Lambda$ -Cu-( <i>R,R</i> )-L	8.5	18.5
( $\Lambda$ -Zn-( <i>R,R</i> )-L) <sub>2</sub>	75.9	80.9
$\Lambda$ -( <i>R,R</i> )-H <sub>2</sub> L	63.4 <sup>c</sup>	70.5 <sup>c,d</sup>
( $\Delta$ -Zn-( <i>R,R</i> )-L) <sub>2</sub>	74.4 <sup>e</sup>	78.3 <sup>e</sup>

<sup>a</sup> These are based on the optimized geometries in the respective solvents.

<sup>b</sup> These are based on the X-ray structural parameters reported in Refs. 23, 25.

<sup>c</sup> This is the dihedral angle between the N-C3-C2-N plane (Figure 5.5) and the other corresponding plane in the same H<sub>2</sub>L ligand.

<sup>d</sup> Note the crystal structure of the ligand contains water. See Ref. 20 for details.

<sup>e</sup> This is the dihedral angle between the two N-Zn-N planes where the two N atoms are in the same ligand.

## 5.3. Experimental

---

### 5.3.1. Synthesis

The yellow crystalline (*S,S*)-L and (*R,R*)-L molecules, and both enantiomers of all five transition metal complexes, Ni (II), Cu (II), Pd (II), Pt (II), and Zn (II), are synthesized and purified according to the reported synthesis procedures [20,24,25] using Ni(ClO<sub>4</sub>)<sub>2</sub>•6H<sub>2</sub>O, Cu(ClO<sub>4</sub>)<sub>2</sub>•6H<sub>2</sub>O, Pd(OAc)<sub>2</sub>, K<sub>2</sub>PtCl<sub>4</sub>, and Zn(OAc)<sub>2</sub>•2H<sub>2</sub>O salts, respectively. They were purchased from Sigma Aldrich. In brief, two enantiomers of the ligand molecule were synthesized from Pyrrole-2-carbaldehyde and either (*S,S*)- or (*R,R*)-diaminocyclohexane in ethanol, and were crystallized in hot ethanol. Solutions of the initial Ni (II), Cu (II), Pd (II) and Zn (II) complexes in methanol were added to a solution of (*S,S*)-H<sub>2</sub>L and (*R,R*)-H<sub>2</sub>L with an equivalent of potassium hydroxide. The products were further purified by crystallization in CH<sub>2</sub>Cl<sub>2</sub>/CH<sub>3</sub>OH. The starting Pt (II) complex was dissolved in dimethyl sulfoxide and added to a solution of the ligand in dimethyl furan, which was heated to 80 °C. This product was also crystallized using CH<sub>2</sub>Cl<sub>2</sub>/CH<sub>3</sub>OH. Both the ligand and complexes are air stable compounds.

### 5.3.2. IR and VCD Spectroscopic measurements

VA and VCD spectra are measured using the Bruker Vertex 70 and PMA 50 spectrometers, respectively. This is a single photo elastic modulator (PEM) spectrometer in which the PEM

central wavenumber was set at  $1400\text{ cm}^{-1}$  for all measurements. The signals are collected using a liquid nitrogen cooled MCT detector for a period of 4 hours ( $\sim 4300$  scans) with  $4\text{ cm}^{-1}$  resolution in the region of  $1750 - 1200\text{ cm}^{-1}$ . DMSO- $d_6$  solutions of both enantiomers of the ligand and nickel, copper, palladium, platinum, and zinc complexes with concentrations of 0.305M, 0.015M, 0.017M, 0.011M, 0.027M, and 0.026M, respectively, are prepared. These solutions are injected into the space between two BaF<sub>2</sub> windows that is created by a Teflon spacer. The path-length is dictated by the thickness of the spacer — 0.1 mm for the ligand and 0.2 mm for the metal complexes. Under these conditions, the measurement of the parent IR spectrum is optimized first, and then the correct VCD measurement is carried out. IR spectra are background corrected by subtraction of the solvent spectrum, which is measured under identical conditions including cell path-length and cell window orientation, from each sample spectrum. For spectral base-line correction and artifact elimination, VCD spectra are obtained by subtraction of the VCD spectra of (*R,R*) enantiomers from the (*S,S*) enantiomers and dividing by two.

### 5.3.3. Theoretical calculations

All geometrical searches and optimizations, spectral simulations, harmonic frequencies calculations, and VA and VCD intensity predictions were calculated by the Gaussian 09 [30] suite program using density functional theory (DFT) [31]. The well-known B3LYP [32,33] hybrid functional was mainly used for the calculations. The cc-pVTZ [34] basis set was used for C, N, and H atoms and LanL2DZ basis set for all transition metals, namely Ni (II), Cu (II), Pd (II), Pt (II), and Zn (II). To account for the bulk solvent environment, the integral equation formalism (IEF) version of polarization continuum model (PCM) [35,36] using the universal force field (UFF) radii was used. For this purpose, a dielectric constant of  $\epsilon = 46.826$  was used,

corresponding to DMSO. A Lorentzian line shape with a half-width at half-height of  $4\text{ cm}^{-1}$  was used for the simulations of VA and VCD spectra.

## 5.4. Conclusions

Five transition metal (M = Ni (II), Cu (II), Pd (II), Pt (II), and Zn (II)) complexes with the bis(pyrrol-2-ylmethyleneamine)-cyclohexane ligand have been synthesized. Their structural properties and induced helicity have been studied using VA and VCD spectroscopy, as well as UV-Vis and ECD spectroscopic techniques. Comparison of the experimental and theoretical VA and VCD spectra allow us to clearly identify both the *mono*-nuclear geometries of Ni (II), Cu (II), Pd (II), and Pt (II) complexes and the *di*-nuclear geometry of Zn (II) complex in solution. The preferred coordination topology of these metal complexes and the binding strength have been analyzed using molecular orbital calculations. The frequency trend observed for the  $\text{-C=N}$  stretching vibrational mode has been satisfactorily explained. More importantly, this study demonstrates that the VCD spectroscopy offers the possibility to determine both the chirality and the helicity of the ligands and the associated transition metal complexes. The ECD spectra, on the other hand, are dominated by spectral features related to helicity in this case based on the theoretical simulation. Furthermore, the study shows that the extreme diastereoselectivity of the (*R,R*) ligand itself dictates the *M*-helicity in all the systems studied. This specific helicity preference has little to do with interactions with the transition metals. More generally, the conformational preference of the ligands in addition to its chirality will likely have strong influence on the final helicity of the transition metal complexes in solution.

## References

---

- [1] C. Merten, R. McDonald, Y. Xu, *Inorg. Chem.*, **2014**, 53, 3177-3182.
- [2] H. Sato, Y. Mori, A. Yamagishi., *Dalton Trans.*, **2013**, 42, 6873–6878.
- [3] T. Wu, X.-P. Zhang, X.-Z. You, Y.-Z. Li, P. Bouř, *ChemPlusChem.*, **2014**, 79, 698-707.
- [4] M. Enamullah, A.K.M.R. Uddin, G. Pescitelli, R. Berardozi, G. Makhloufi, V. Vasylyeva, A.-C. Chamayou, C. Janiak., *Dalton. Trans.*, **2014**, 43, 3313-3329.
- [5] A.-C. Chamayou, S. Lüdeke, V. Brecht, T. B. Freedman, L.A. Nafie, C. Janiak, *Inorg. Chem.*, **2011**, 50, 11363-11374.
- [6] A.-C Chamayou, S. Lüdeke, V. Brecht, T. B. Freedman, L. A. Nafie, C. Janiak, *Inorg. Chem.*, **2011**, 50, 11363–11374.
- [7] C. Merten, Y. Xu. *Dalton Trans.*, **2013**, 42, 10572-10578.
- [8] H. Sato, H., A. Yamagishi, *Int. J. Mol. Sci.*, **2013**, 14, 964-978.
- [9] H. Sato, T. Taniguchi, K. Monde, S.-I. Nishimura, A. Yamagishi. *Chem. Lett.*, **2006**, 35, 364–365.
- [10] H. Sato, T. Taniguchi, A. Nakahashi, K. Monde, A. Yamagishi., *Inorg. Chem.*, **2007**, 46, 6755–6766.
- [11] H. Mori, A. Yamagishi, H. Sato. *J. Chem. Phys.*, **2011**, 135, 84506.
- [12] H. Sato, H. Uno, H. Nakano. *Dalton Trans.*, **2011**, 40, 1332–1337.
- [13] Z. Dezhahang, C. Merten, M. R. Poopari, Y. Xu. *Dalton Trans.*, **2012**, 41, 10817 – 1082.
- [14] H. Sato, F. Sato, M. Taniguchic, A. Yamagishi. *Dalton Trans.*, **2012**, 41, 1709–1712.
- [15] A-C. Chamayou, S. Lüdeke, V. Brecht, T.B. Freedman, L.A. Nafie, C. Janiak. *Inorg. Chem.*, **2011**, 50, 11363-11374.
- [16] A. Bacchi, M. Carcelli, L. Gabba, S. Ianelli, P. Pelagatti, G. Pelizzi, D. Rogolino. *Inorg. Chem. Acta.*, **2003**, 342, 229-235.
- [17] S. Kano, H. Nakano, M. Kojima, N. Baba, K. Nakajima. *Inorg. Chem. Acta.*, **2003**, 349, 6-16.
- [18] Q. T. Nguyen, J. H. Jeong. *Polyhedron.*, **2006**, 25, 1787-1890
- [19] H-J. Cristau, A. Ouali, J-F. Spindler, M. Taillefer. *Chem. Eur. J.*, **2005**, 11, 2483-2492.
- [20] X. F. Shan, L. Z. Wu, X.Y. Liu, L. P. Zhang, C.H. Tung. *Eur. J. Inorg. Chem.*, **2007**, 3315–3319.
- [21] Y. Wang, H. Fu, F. Shen, X. Sheng, A. Peng, Z. Gu, H. Ma, J. S. Ma, J. Yao. *Inorg. Chem.*, **2007**, 46, 3548-3556.

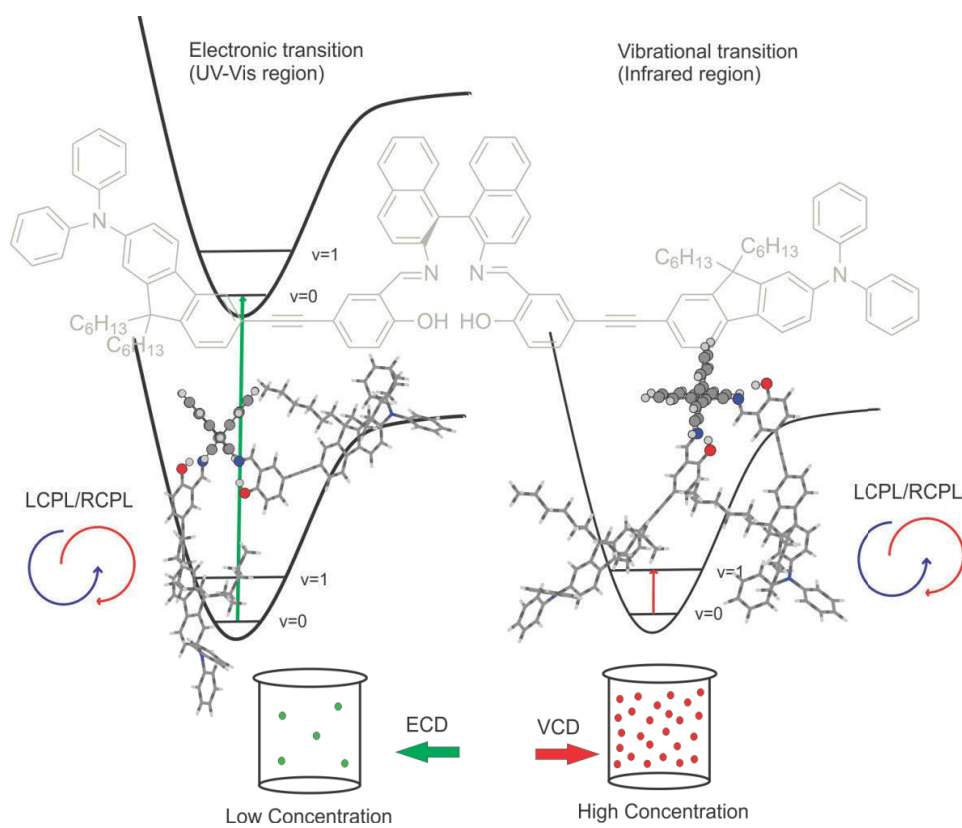
- 
- [22] X-F. Shan, D-H. Wang, C-H. Tung, L-Z. Wu. *Tetrahedron.*, **2008**, 65, 5577-5582.
- [23] X-F. Shan, D-H. Wang, C-H. Tung, L-Z. Wu. *Chinese Sci. Bulletin.*, **2007**, 52, 1581-1584.
- [24] X. Shan, D. Wang, C. Tung, L. Wu, *Tetrahedron.*, **2008**, 64, 5577-5582.
- [25] X. Shan, L. Wu, L. Zhang, C. Tung, *Chinese Science Bulletin*, **2007**, 52, 1581-1584.
- [26] Z. Dezhahang, M. R. Poopari, Y. Xu, *Chem. Asian J.* **2013**, 8, 1205 – 1212.
- [27] S. M. Bachrach, Computational Organic Chemistry, John Wiley & Sons, Inc. publication, **2007**.
- [28] SPARTAN '08; Wavefunction, Inc.: Irvine, CA; [www.wavefun.com/products/spartan.html](http://www.wavefun.com/products/spartan.html).
- [29] G. Yang, H. Tran, E. Fan, W. Shi, T. L. Lowary, Y. Xu, *Chirality*, **2010**, 22, 734-743
- [30] Gaussian 09, Revision **D.01**, M. J. Frisch, G. W. Trucks, H. B. Schlegel, G. E. Scuseria, M. A. Robb, J. R. Cheeseman, G. Scalmani, V. Barone, B. Mennucci, G. A. Petersson, H. Nakatsuji, M. Caricato, X. Li, H. P. Hratchian, A. F. Izmaylov, J. Bloino, G. Zheng, J. L. Sonnenberg, M. Hada, M. Ehara, K. Toyota, R. Fukuda, J. Hasegawa, M. Ishida, T. Nakajima, Y. Honda, O. Kitao, H. Nakai, T. Vreven, J. A. Montgomery, Jr., J. E. Peralta, F. Ogliaro, M. Bearpark, J. J. Heyd, E. Brothers, K. N. Kudin, V. N. Staroverov, R. Kobayashi, J. Normand, K. Raghavachari, A. Rendell, J. C. Burant, S. S. Iyengar, J. Tomasi, M. Cossi, N. Rega, J. M. Millam, M. Klene, J. E. Knox, J. B. Cross, V. Bakken, C. Adamo, J. Jaramillo, R. Gomperts, R. E. Stratmann, O. Yazyev, A. J. Austin, R. Cammi, C. Pomelli, J. W. Ochterski, R. L. Martin, K. Morokuma, V. G. Zakrzewski, G. A. Voth, P. Salvador, J. J. Dannenberg, S. Dapprich, A. D. Daniels, Ö. Farkas, J. B. Foresman, J. V. Ortiz, J. Cioslowski, and D. J. Fox, Gaussian, Inc., Wallingford CT, 2009.
- [31] W. Kohn and L. J. Sham, *Phys. Rev.*, **1965**, 140, A1133-A38.
- [32] A. D. Becke, *J. Chem. Phys.*, **1993**, 98, 5648
- [33] C. T. Lee, W. T. Yang, R. G. Parr, *Phys. Rev. B*, **1988**, 37, 785-789.
- [34] R. A. Kendall, T. H. Dunning Jr., R. J. Harrison, *J. Chem. Phys.*, **1992**, 96, 6796-806.
- [35] J. Tomasi, B. Mennucci, R. Cammi, *Chem. Rev.*, **2005**, 105, 2999-3093.
- [36] B. Mennucci; J. Tomasi, R. Cammi, J. R. Cheeseman, M. J. Frisch, F. J. Devlin, S. Gabriel, P. J. Stephens, *J. Phys. Chem. A*, **2002**, 106, 6102-6113.

## 6

# Diastereomeric preference of a triply axial chiral binaphthyl based molecule: a concentration dependent study by chiroptical spectroscopies

Zahra Dezhahang, Mohammad Reza Poopari, Florencio Eloy Hernández, Carlos

Diaz, Yunjie Xu





## 6.1. Introduction

---

It is well known that solvent can exert deciding influence on the preferred conformation and even chirality of a chiral solute in solution.[1, 2] Such effects are often manifested in severe and sometime non-intuitive effects on chiroptical spectral signatures. Both polarity of a solvent and hydrogen (H)-bonding formation between solute and solvent molecules can influence the optical response.[3] For example, the experimental vibrational circular dichroism (VCD) spectra of methyl mandelate look quite different in chloroform, methanol, and dimethyl sulfoxide (DMSO). While the spectrum in chloroform can be well reproduced by the gas phase simulation, it is necessary to apply the explicit solvation model to account for the spectra in the other two solvents.[3] In another example, chiral poly (ureidophthalimide) foldamers were reported to adopt two opposite helical handedness in water and in tetrahydrofuran (THF) where mirror imaged electronic CD (ECD) bands were detected.[4] Such solvent effects allow one control over the helical architecture and thus direct the supramolecular synthesis. Similarly, solvent-mediated chirality switching was reported for dendrimer folding in aqueous solution.[5] Generally speaking, polar protic solvents, such as water can disrupt intra- and inter-molecular electrostatic and hydrogen (H)-bonding interactions of the example systems discussed above and thereby change the relative stabilities of various conformational assemblies.[6]

Much less reported is the concentration induced conformational change in common organic solvents used for chiroptical spectroscopic studies, such as DMSO, deuterated chloroform ( $\text{CDCl}_3$ ) or THF. This is an interesting and important topic since several commonly used chiroptical spectroscopic tools for absolute configuration and conformational determination

of chiral compounds, such as VCD and ECD, Raman optical activity (ROA), and optical rotary dispersion (ORD) spectroscopy, operate under very different concentration regimes and each has its own advantages and disadvantages. For example, VCD spectroscopy generally provides very rich band structures which often contain detailed structural information. Furthermore, VCD simulations are considerably more reliable than ECD and ORD since only ground electronic state calculations are needed.[7] On the other hand, an ECD or ORD experiment requires much less sample than VCD. While a typical concentration used for an ECD or ORD is in range of  $10^{-5}$  to  $10^{-3}$  M, the concentration needed for VCD experiments are typically  $10^{-1}$  to a few M and often saturated solution is used. In addition, each of these spectroscopy techniques probes only a certain molecular property. Consequently, a number of researchers have advocated using more than one of the spectroscopic monitoring tools to reach a reliable absolute configuration determination, providing there are no major structural changes with concentration.[8, 9, 10, 11]

The susceptibility of axial chirality to the environmental perturbations such as the choice of different solvents and concentrations of the sample is a subject of significant practical and fundamental importance in supramolecular assembly.[12] In the current study, we focus our attention on such the effects of environmental perturbations, i.e. solvent and concentrations, on axial chirality, using AXF-155, a triply axial chiral binaphthyl fluorene based salen ligand, i.e. [2,2'-(1E,1'E)-(R)-1,1'-binaphthyl-2,2'-diyl]bis(azan-1-yl-1-ylidene)bis(methan-1-yl-1-ylidene)bis(4-((7(diphenylamino)-9,9-dihexyl-9H-fluoren-2-yl)ethynyl)-phenol)]. AXF-155 is a model axial chiral system, with a good number of possible diastereomers and a few potential H-bonding sites. This molecule was recently synthesized for its potential applications in homogeneous catalysis, biophotonics, and biosensing.[13,14] It was also

characterized using ECD and two-photon CD (TPCD) spectroscopy by Hernández and co-workers. [13,14] One of our goals is to utilize VCD spectroscopy and DFT calculations to clearly establish the axial chirality of AXF-155 in solution. A second goal of our study is to examine the influence of solvent and concentrations on axial chirality of AXF-155. To achieve that, we carried out VA and VCD experiments in THF and CDCl<sub>3</sub>, as well as ORD and ECD measurements in CDCl<sub>3</sub> under much diluted conditions. From the combined experimental and theoretical results, we reached a surprising and interesting conclusion that the preferred axial chirality at the –C-N bonds is switched under concentrated and much diluted concentrations. Further theoretical modeling was also performed to help to rationalize the observed phenomena.

## **6.2. Experimental and theoretical details**

---

AXF-155 was synthesized using the reported scheme 1 according to refs. 13 and 14. VA and VCD spectra were measured using a Bruker FTIR (Vertex 70) spectrometer equipped with a PMA 50 module for VCD measurements.[15] The data were collected at 4 cm<sup>-1</sup> resolution in the wavenumber region of 1700-1100 cm<sup>-1</sup> using a liquid nitrogen cooled MCT detector for a period of 4 hours (~4300 scans per an hour). 0.046 M solutions of AXF-155 in CDCl<sub>3</sub> and THF-d<sub>8</sub> were used for the VA and VCD measurements. The solution samples were placed between a pair of BaF<sub>2</sub> windows with a path-length of 0.125 mm.

For ORD measurements, a solution of 6.5 x 10<sup>-4</sup> M AXF-155 in CDCl<sub>3</sub> was prepared using a 10 cm cell. The ORD data were collected at a series of wavelengths, namely at 589 nm of sodium D line, and 578 and 546 nm of a mercury lamp by means of a Perkin-Elmer 240

polarimeter. The solution with the same concentration is used to carry out the ECD data acquisitions. To meet spectroscopic criteria for CD measurements, the magnitude of the absorption is adjusted using a UV spectrometer and a 1 mm cell was used. An Olis DSM 17 circular dichroism spectrometer and a Hewlett Packard 8453 UV-VIS Spectrophotometer were used for ECD and UV measurements, respectively.

The Gaussian 09 [16] program was used for all geometrical searches and optimizations, harmonic frequencies calculation, and VA and VCD intensities predictions using density functional theory (DFT). [17] The well-known Becke three parameters, Lee-Yang-Parr, functional (B3LYP) [18] was mainly used for the calculations. Since the AXF-155 molecule contains 224 atoms which makes the usage of high level of quantum chemical calculations prohibitively expensive, the 6-31G(d) basis set [19] was chosen since it offers a good combination of accuracy and computational efficiency. To better capture the relative stability of the potential conformers, single point energy calculations were also performed with cc-pVTZ basis set. [20] In addition, we also carried out geometry optimizations for the targeted conformers with the D3 version of Grimme's dispersion method [21] using B3LYP/6-31G(d). To account for the bulk solvent environment, the integral equation formalism (IEF) version of polarizable continuum model (PCM) using the universal force field radii, implicit solvent model [22,23] was used. In a few previous studies, it was shown that the strength of H-bonding interaction between the chiral solute and  $\text{CDCl}_3$  is not strong enough to demand an explicit treatment.[24,25] For this purpose, the dielectric constant of chloroform,  $\epsilon=4.7113$ , was used. A Lorentzian line shape with a half-width at half-height of  $4 \text{ cm}^{-1}$  was used for the simulations of VA and VCD spectra.

Time dependent density functional theory (TD-DFT) method is employed for all excited state

energies, oscillator strength and optical rotation dispersion calculations. For this purpose, the PCM/DFT/6-31G(d) is used. The first 80 electronic states have been taken into account for theoretical ECD spectral simulations. To account for bulk of solvent environment, the PCM model of chloroform is applied, as it's used for VA and VCD spectral simulations. For a clearer spectral comparison, the half-width at half height (HWHH) of 0.2 eV with a Gaussian line-shaped function is used since the simulated ECD spectra are quite broad compared to the experimental measurements. We note that in the previous work by Hernández et al., a broader Gaussian line-shaped function with 0.35eV HWHH was used on the truncated systems where four  $-C_6H_{13}$  groups were replaced by four methyl groups.[13]

### **6.3. Result and Discussions**

---

#### *6.3.1. Possible diastereomers of AXF-155*

Figure 6.1 shows the chemical structure of this relatively large and flexible triply axial chiral molecule. AXF-155 possesses three chiral axes: one chiral axis for the binaphthyl ring and two others along the  $-C-N$  bonds where the carbon atoms are part of the binaphthyl group. The three chiral axes are highlighted in Figure 6.1. In addition to the chirality labels, there are cis- and trans-conformations about the  $C=N$  bond, intra and extra relative orientations of the salicaldehyde moiety with respect to the other binaphthyl half, finally HB and NHB labels to indicate the existence or non-existence of the  $-OH...N=C-$  intramolecular HB interaction, respectively. Based on the synthesis procedure of AXF-155 molecule, the chirality of binaphthyl ring is determined to be R. For easy comparison with the previous publications on AXF-155, we have adopted the same axial chirality labels along the  $-C-N$  bonds as used in Ref. 13. The details about the axial chirality and intra/extra labels are provided in Figure D1,

## Appendix D.

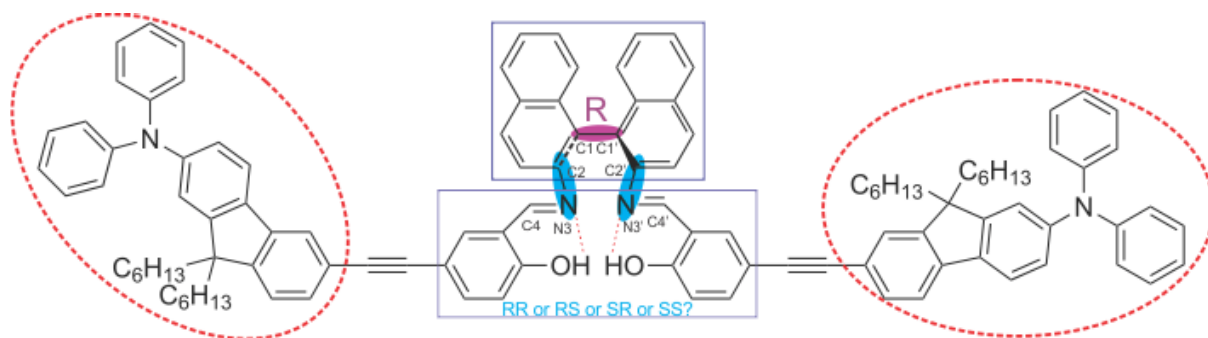


**Figure 6.1.** Chemical structure of AXF-155 studied in this paper. There are three chiral axes: one at the binaphthyl ring and two along the C-N bonds. All of the chiral axes are highlighted with shady boxes. Chirality of the binaphthyl ring is R, while the associated chirality at the C-N bonds can be RR, RS, SR or SS. The two large substituents about the C=N bond take on the trans-arrangement shown here. The pair of the bulky group and the opposite binaphthyl half marked with dotted circles (or with dotted-dashed circles) can be in either extra or intra orientation (see Figure D1 for further details). In addition, the  $\text{-OH}\dots\text{N}=\text{C}$  intramolecular H-bonding interactions are indicated. See text for further details.

### 6.3.2. Experimental VCD spectra AXF-155

VA and VCD spectra of AXF-155 molecule in weakly polar deuterated chloroform, i.e.  $\text{CDCl}_3$ , are presented in Figure 6.2.  $\text{CDCl}_3$  was chosen as it offers sufficient solubility and does not interfere in the IR window from  $1700\text{-}1100\text{ cm}^{-1}$ . Since the previous ECD study [13,14] was carried out in deuterated THF solvent, i.e. THF- $\text{d}_8$ , we also perform further VA and VCD measurements in THF- $\text{d}_8$  for comparison. The resulting VA and VCD spectra in

THF- $d_8$  are also included in Figure 6.2 for comparison. Generally, the raw VA spectra of AXF-155 in these two solvents, i.e. without solvent subtraction, look somewhat different because of different solvent bands in the 1700-1100  $\text{cm}^{-1}$  region. In the 1700-1250  $\text{cm}^{-1}$  region, the VCD band features, on the other hand, look very much the same in both solvent, suggesting that the conformational landscape and the associated axial chirality of AXF-155 remain unchanged in these two solvents. Since  $\text{CDCl}_3$  provides a wider VCD spectral window in the current study, for simplicity, we will use VA and VCD spectra in  $\text{CDCl}_3$  for the spectral analyses in the remainder of this paper, unless indicated otherwise.

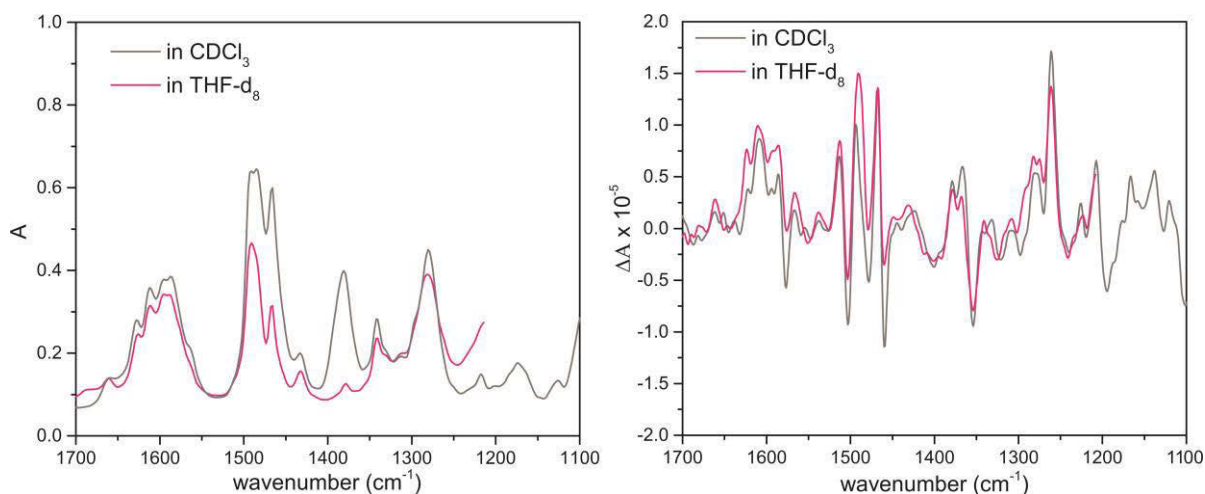


**Figure 6.2.** Raw experimental VA (left) and VCD (right) spectra of AXF-155 in deuterated chloroform and THF solvents. The measurements below 1200  $\text{cm}^{-1}$  in THF are removed due to strong THF solvent absorption.

### 6.3.3. Comparison of experimental and simulated VCD spectra AXF-155

A systematic conformational search for AXF-155 was reported in Ref. 13. All cis-conformers were found to be substantially less stable than the trans-conformers due to severe steric

effects in the former case. Therefore only trans-conformers are considered here. For simplicity, we drop the prefix trans for all conformers in the current study. We would also like to point out that in the previous study, the four alky chains ( $-C_6H_{13}$ ) were replaced by four  $-CH_3$  subunits to reduce computational cost because it was rationalized that these chains do not have any significant contributions on the electronic transitions. Since VCD spectral features are much more sensitive to subtle conformational changes, we decide to include these alkyl chains in our geometry optimizations and VA and VCD spectral simulations. One noticeable outcome with the inclusion of the four alkyl chains is that the number of possible conformers is reduced because of the additional steric hindrance introduced by these bulky subunits. In total nine HB conformers are re-optimized and are confirmed to be real minima. Their geometries are presented in Figure 6.3 where we separate these structures obtained into three groups, based on their associated axial chirality at the  $-C-N$  bonds, i.e. RR, RS, or SS. It's interesting to note that the long bulky side chains form cavities of different sizes in different conformers. As a result, one may anticipate that accessibility to solvent molecules can vary quite differently among various conformers. For example, the R\_intra\_HB//S\_extra\_HB conformer is structurally fully-extended whereas the R\_extra\_HB//R\_extra\_HB is considerably more compact, with a much smaller cavity size. The relative energies and free energies of these three groups of conformers using B3LYP/6-31G(d), single point energy at B3LYP/cc-pVTZ//6-31G(d) and using B3LYP/6-31G(d) with the D3 Grimme's dispersion correction are summarized in Table D1, Appendix D.

In addition to the HB conformers, the relevant HB\_NHB and NHB conformers are also considered and their geometries re-optimized. We note that those conformers with two intramolecular HB bonds are considerably more stable than those with one and even more so



than those without in each of the three groups indicated above. This is consistent with other previous studies that suggest that species with the intramolecular H-bonding interactions become dominant over those without in the presence of non-polar or weakly polar solvent such  $\text{CH}_2\text{Cl}_2$  and  $\text{CHCl}_3$ . [26]

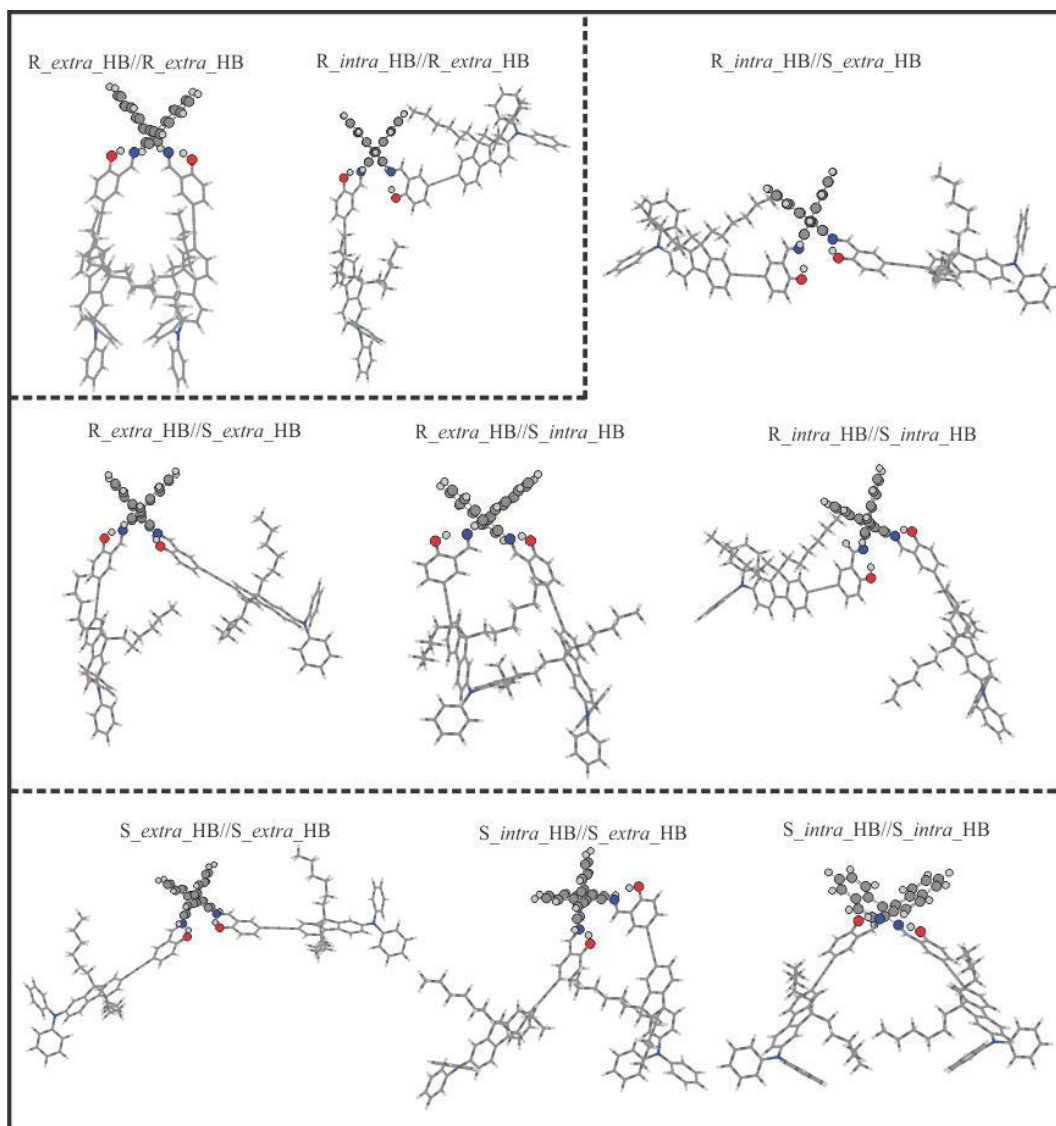


**Figure 6.3.** Optimized geometries of the HB conformers of AXF-155 in CDCl<sub>3</sub> obtained at the PCM/B3LYP/6-31G(d) level of theory. The geometries are separated into three groups based on their associated axial chirality at the –C-N bonds, i.e. RR, RS, or SS.

In Figure 6.4, we compare the calculated VA and VCD spectra of all HB conformers of AXF-155. Since AXF-155 is fairly large and has a significant number of vibrational modes in the finger print region, many of these VA bands overlap with each other. This often makes direct and detailed comparison between experimental and theoretical VA spectra ambiguous and prevents one to draw decisive structural information. On the other hand, VCD spectra tend to show considerable amount of unique spectral signatures related to stereogenic and conformational structural information. For comparison between theory and experiment, we divide the finger print region into three sections from high to low wavenumbers and refer to Figure 6.1 for the functional groups indicated below. Region I from 1700 to 1550 cm<sup>-1</sup> is composed of several strong vibrational bands due to the C=N stretching, O-H bending, and C=C stretching of the binaphthyl rings. Region II from 1550 to 1400 cm<sup>-1</sup> contains mostly vibrational motions associated with the C-H and O-H bending of the two phenyl groups which are in close proximity to the binaphthyl rings, the C-H bending of the aromatic rings of the two bulky end substitutes, and CH<sub>2</sub> scissoring of the four C<sub>6</sub>H<sub>13</sub> alkyl chains. Region III from 1400-1100 cm<sup>-1</sup> contains mainly C-N stretching at the two bulky terminal groups and CH<sub>2</sub> bending of the long alkyl chain. Overall, the simulated IR spectra of all nine HB conformers presented in Figure 6.4 look all alike. Furthermore, they all agree well with the experimental VA data. Therefore, one cannot differentiate these conformers on the basis of their VA spectral signatures.

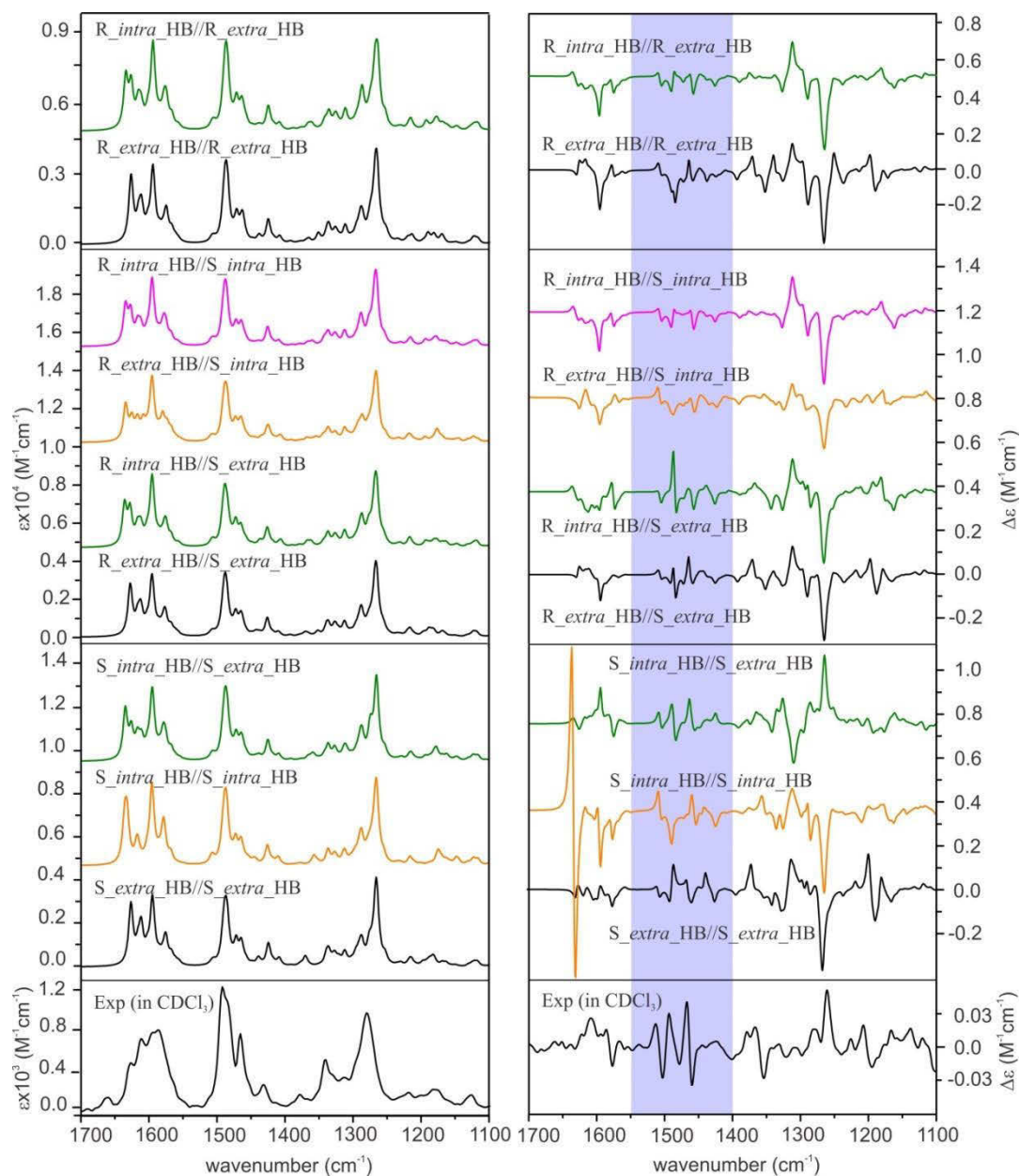


**Figure 6.4.** Calculated VA (left) and VCD (right) spectra of all nine HB conformers of AXF-155 molecule obtained at the PCM/B3LYP/6-31G(d) level compared to the experimental data at the bottom. For easy comparison, these conformers are separated into three groups based on the associated axial chirality at the  $-C-N$  bonds, i.e. RR, RS, or SS.

The theoretical VCD spectral features, on the other hand, look substantially different from one conformer to the next, enabling potentially clear identification of the dominant conformational species in solution. This highlights the significant advantages of VCD spectroscopy in providing structural information of chiral systems in solution. Below, we compare the simulated VCD features of each HB conformers among themselves and with the major experimental VCD spectral features in all three finger print regions. In region I, the prominent experimental positive and negative VCD band at  $1610\text{ cm}^{-1}$  and  $1577\text{ cm}^{-1}$ , respectively, can only be matched by conformers R\_extra\_HB//S\_extra\_HB and S\_intra\_HB//S\_extra\_HB while all the other conformers exhibit major discrepancy. Although the smaller experimental VCD features in this region are somewhat noisy, the consistency they show in both  $\text{CDCl}_3$  and THF solvents gives one confidence in their reliability. In region II, the experimental VCD spectrum shows a beautiful sequence of +/-+/-+/- VCD signatures. This sequence is best matched with S\_intra\_HB//S\_extra\_HB, while all the other conformers exhibit markedly different patterns with the exception of perhaps R\_intra\_HB//S\_extra\_HB. The latter one demonstrates a somewhat similar pattern but with an additional negative band at the high wavenumber end. In region III, the most prominent experimental VCD feature at  $\sim 1270\text{ cm}^{-1}$  is positive, while a negative band is predicted for all HB conformers except S\_intra\_HB//S\_extra\_HB who exhibits a positive VCD band feature. From the above detailed comparison, it is clear that S\_intra\_HB//S\_extra\_HB is the only HB conformer who demonstrates consistent agreement with the experimental data in all three regions.

Since the previous ECD study indicated that R\_intra\_NHB//R\_extra\_NHB conformer provide the best agreement between simulated and experimental ECD spectra, we also

compare simulated VA and VCD spectra of all the R\_intra//R\_extra HB and NHB conformers and S\_intra//S\_extra HB and NHB conformers in Figure 6.5 for completion.

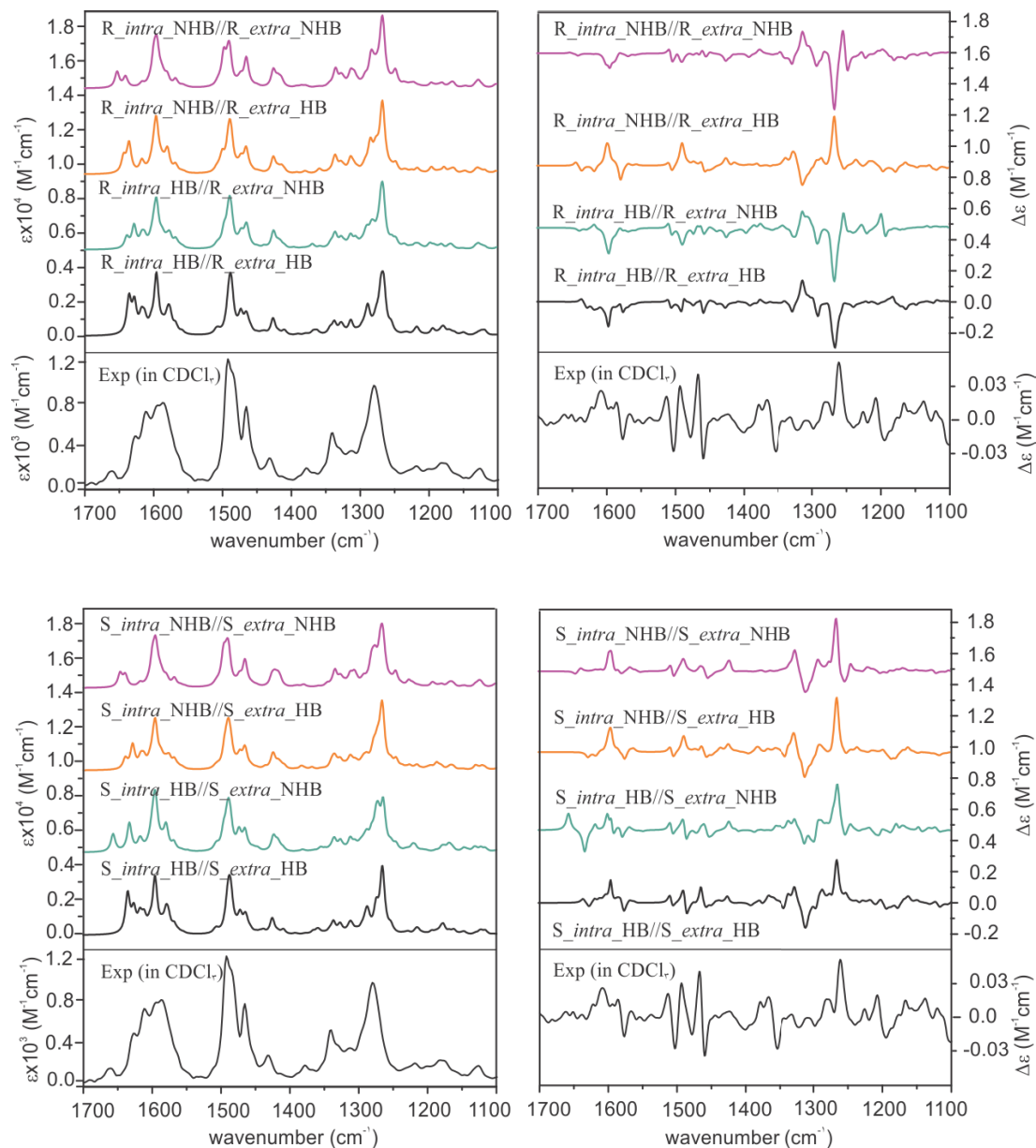


**Figure 6.5.** Calculated VA (left) and VCD (right) spectra of all the R\_intra//R\_extra HB or NHB conformers (top panel) and S\_intra//S\_extra HB or NHB conformers (bottom panel) of AXF-155 molecule obtained at the PCM/B3LYP/6-31G(d) level compared with the experimental ones.

From Figure 6.5, it is immediately obvious that all R\_intra//R\_extra HB or NHB conformers show major discrepancies in the VCD features in the 1300-1200 cm<sup>-1</sup> region. For the S\_intra//S\_extra conformers, the agreements between experiment and theory seem generally better than R\_intra//R\_extra at the first glance. Detailed comparison of VA and VCD spectra of S\_intra\_HB//S\_extra\_HB with the experimental data is summarized in Figure 6.6. While the existence of other S\_intra//S\_extra NHB conformers in small amounts cannot be ruled out completely, S\_intra\_HB//S\_extra\_HB is evidently by far the dominant species. This preference for the HB species observed here is also consistent with the discussion on the relative energies above.

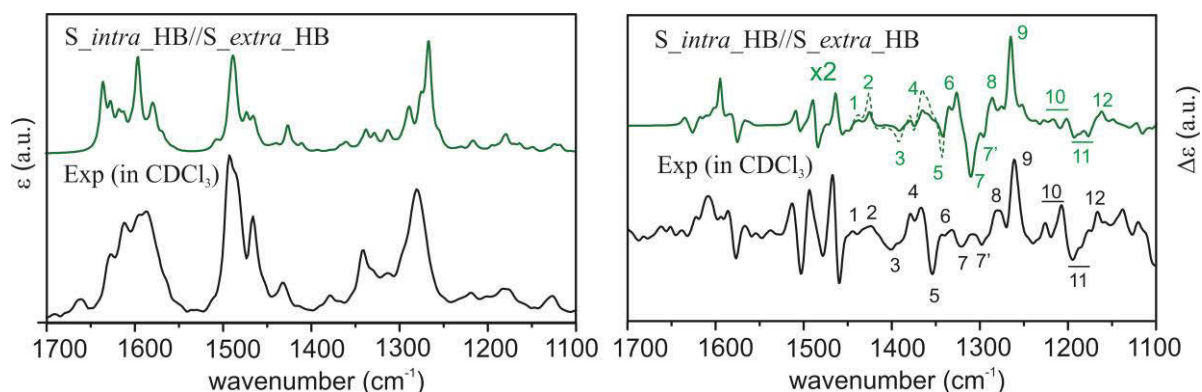


**Figure 6.6.** Comparison of the experimental VA and VCD spectra of AXF155 in CDCl<sub>3</sub> with the corresponding simulated spectra of S\_intra\_HB/S\_extra\_HB obtained at the PCM/B3LYP/6-31G(d) level of theory. The theoretical VCD band intensities in a small region between 1450 cm<sup>-1</sup> to 1330 cm<sup>-1</sup> are amplified by a factor of 2 and indicated with dotted line for easier pattern recognition. The Arabic numerals are used to indicate the corresponding features in the experimental and theoretical data in the crowded region below 1450 cm<sup>-1</sup>.

#### 6.3.4 Concentration Dependent Diastereomeric Preference

Based on the distinctive VCD spectral features described above, we can conclusively identify S<sub>intra</sub>\_HB//S<sub>extra</sub>\_HB as the dominant species in CDCl<sub>3</sub>. This conclusion, however, is at odds with the previous ECD and TPCD investigations of AXF-155 where R<sub>intra</sub>//R<sub>extra</sub> diastereomers were identified as the main species. This prompts us to ask a few interesting and important questions. Why do the previous ECD and the present VCD studies come to such different conclusions? Are there really different dominant species in CDCl<sub>3</sub> in the present study and in THF in the previous studies? If yes, what are the plausible explanations for such strong preference of different diastereomers in solution.

First, we examine if two different solvents, i.e. CDCl<sub>3</sub> and THF, are the cause for such noticeably different conclusions. For that, we already did the VA and VCD measurements in both solvents (see discussion before) and found no obvious difference in the VA and VCD spectral features of AXF-155 excluding absorption due to solvents themselves. Furthermore, both solvents have similar dielectric constants, 4.7113 and 7.4257, respectively. For completion, we also measured UV-Vis and ECD spectra in CDCl<sub>3</sub> (Figure 6.7). As one can see, these spectra are very much the same as those obtained in the previous study using THF. Clearly, solvents themselves are not the issue here.

Another noticeable difference is the concentrations used in ECD and VCD experiments. While ECD experiments typically use highly diluted sample ( $\leq 1 \times 10^{-3}$  M), a highly concentrated sample is needed for VCD measurements because VCD intensity is usually only  $10^{-4}$  to  $10^{-5}$  of VA bands. In the current experiment, a 70 fold higher concentration is used for VCD than ECD. For a more systematic comparison, we included also ORD measurements in CDCl<sub>3</sub>. Furthermore, we performed both ECD and ORD simulations for all conformers of

interest using their full geometries, in contrast to the previous ECD study where some bulky groups  $-C_6H_{13}$  were simplified with  $-CH_3$  groups. The results are summarized in Figure 6.7 and 6.8 for ECD and ORD spectra, respectively. Generally, the simulated ECD spectra are similar to those reported before, suggesting the truncation used before is justified. While the agreement between ECD experimental and simulated spectra is not as decisive as the corresponding VCD counterparts, it is nevertheless quite clear here that the ECD features of R\_intra//R\_extra conformers are in accord with the observed data while S\_intra//S\_extra conformers show severe discrepancies. The experimental ORD spectrum shows an upward trend going from short to long wavelengths. While R\_intra\_HB//R\_extra\_HB exhibits the same upward trend in agreement with the experimental observation, S\_intra\_HB//S\_extra\_HB shows a downward trend. It is noted that although the absolute ORD values are still challenging to be reproduced theoretically, the general variation trend with wavelength is typically better reproduced.[27,28,29] Therefore the ORD study performed here also qualitatively supports the conclusion derived from both the current and previously reported ECD studies [13,14] that R\_intra//R\_extra is the dominant species in the much diluted solution, rather than S\_intra//S\_extra.

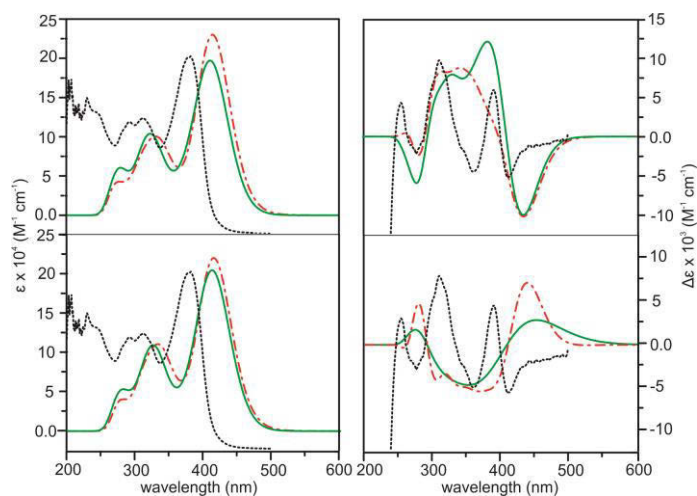




**Figure 6.7.** Comparison of the experimental ECD spectrum in  $\text{CDCl}_3$  (black dotted line) with the theoretical ECD spectra of R\_intra//R\_extra (upper row) and S\_intra//S\_extra (lower row) HB (red dashed-dotted line) and NHB (green solid line) conformers obtained at the PCM/B3LYP/6-31G(d) level of theory.

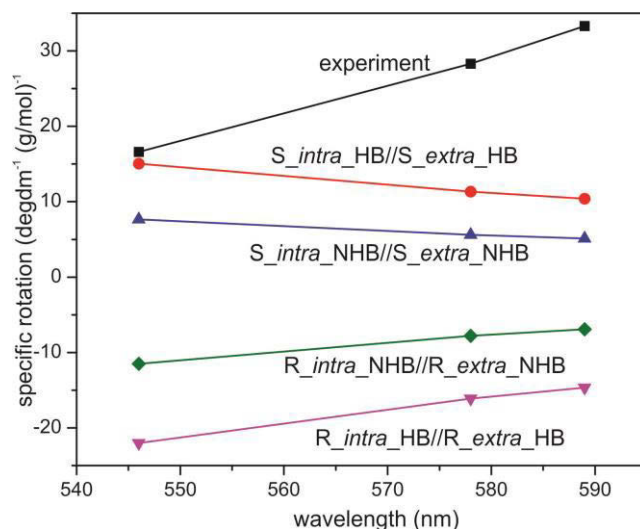


**Figure 6.8.** Comparison of the experimental ORD spectrum in  $\text{CDCl}_3$  with the theoretical ORD spectra of R\_intra//R\_extra HB and NHB conformers as well as S\_intra//S\_extra HB and NHB conformers obtained at the PCM/B3LYP/6-31G(d) level of theory.

It therefore appears that concentration plays a crucial role in which diastereomer is preferred in solution. Although such observations appear not to have been extensively studied, there are a number of theoretical and experimental publications when similar concentration dependent conformational preferences were reported.[30,31,32] For example, inversion of population distribution of felodipine conformations at increased concentration in dimethyl sulfoxide was observed by Khodov and co-workers in 2013. Using NMR spectroscopy, these authors concluded that conformational preference of felodipine in dimethyl sulfoxide is concentration

dependent: conformers that dominate in a dilute solution become the least abundant in the saturated one. Furthermore, they pointed out that conformers that dominate in the saturated solution are of the same type as revealed in crystalline state by X-ray. The authors contribute the inversion of conformer distribution in the saturated solution to both increases in intermolecular felodipine–felodipine and felodipine–DMSO interactions. Ghorai applied molecular dynamics simulations to predict the concentration dependence of trans and gauche conformations of n-butane inside a confined medium such as zeolite NaY. He found that the percentage of gauche conformations inside zeolite increases with concentration and identified guest-guest interaction as the key factor for the enhancement of the gauche conformation.

To understand the observation, we performed an one-dimensional potential energy surface scan for the inter-conversion between R\_intra\_HB//R\_extra\_HB and S\_intra\_HB//S\_extra\_HB and found that the inter-conversion can occur through a planar TS with a barrier energy of 1.8 kcal/mol obtained at the B3LYP/3-21G level of theory. The interconversion between R\_intra//R\_extra and S\_intra//S\_extra conformers of AXF-155 is likely facilitated by solvent molecules. While R\_intra//R\_extra conformers exhibit a larger cavity, allowing easy access by solvent molecules, S\_intra//S\_extra conformers show a much smaller cavity. One may expect that such differences in solvent-solute interactions may lead to preferentially stabilization of certain conformers, as recently reported in the case of a tris(diamine)nickel(II) complex. [33] This is depicted in Figure D2, Appendix D. Further detailed theoretical modeling will be required to understand this interesting and important phenomenon in greater details, but that is out-of-scope of the current study.

## 6.4. Conclusions

---

Axial chirality and conformations of a flexible multiple axial chiral molecule, AXF-155, have

been extensively investigated using three chiroptical spectroscopies, i.e. VCD, ECD, and ORD, in conjugation with DFT calculations. Experimentally, both VCD and ECD spectra of AXF-155 in THF- $d_8$  and  $CDCl_3$  look essentially the same, indicating that the polarity of solvent does not influence the axial chirality and conformational distribution of AXF-155 significantly. The combined VCD and DFT study clearly shows that the dominant species is R-binaphthyl, S-intra-HB//S-extra-HB (R-SS) in the concentrated solution. In the much dilute solution, the dominant species is determined to be R-binaphthyl, R-intra-HB//R-extra-HB (R-RR) based on the ECD and ORD investigations. The latter conclusion is consistent with the previously reported ECD study. This is an area of research which has not yet been fully explored, although a small number of theoretical and experimental publications had reported similar concentration dependent behaviors. Further theoretical modeling will be highly desirable to explain the interesting observations reported here in detail.

## **6.5. Acknowledgement**

---

This research was funded by the University of Alberta and the Natural Sciences and Engineering Research Council of Canada. We gratefully acknowledge access to the computing facilities provided by the Shared Hierarchical Academic Research Computing Network (Sharcnet) and by the Western Canada Research Grid (Westgrid). YX holds a senior Canada Research Chair in Chirality and Chirality Recognition.

## References

- [1] (a). P. Mukhopadhyay, G. Zuber, M. Goldsmith, P. Wipf, and D. N. Beratan, *ChemPhysChem*, **2006**, *7*, 2483 – 2486. (b). B. Mennucci, C. Cappelli, R. Cammi, J. Tomasi, *Chirality*, **2011**, *23*, 717–729. (c). S. Coriani, A. Baranowska, L. Ferrighi, C. Forzato, D. Marchesan, P. Nitti, G. Pitacco, A. Rizzo, K. Ruud, *Chirality*, **2006**, *18*, 357–369.
- [2] G. Yang and Y. Xu, *Top. Curr. Chem.*, Eds R. Naaman, D.N.Beratan, D.H.Waldeck, Springer-Verlag Berlin Heidelberg, **2011**, *298*, 189-236.
- [3] (a). M. R. Poopari, Z. Dezhahang, G. Yang, Y. Xu, *ChemPhysChem* **2012**, *13*, 2310 – 2321. (b). M. R. Poopari, P. Zhu, Z. Dezhahang, . Y. Xu, *J. Chem. Phys.*, **2012**, *137*, 194308. (c). P. Zhu, G. Yang, M. R. Poopari, Z. Bie, Y. Xu, *ChemPhysChem*, **2012**, *13*, 1272 – 1281. (d). P. L. Polavarapu, *Chirality*, **2012**, *24*,909–920.
- [4] R.W. Sinkeldam, M. H. C. J. van Houtem, K. Pieterse, J. A. J. M. Vekemans, E. W. Meijer *Chem. Eur. J.*, **2006**, *12*, 6129 – 6137.
- [5] A. L. Hofacker, J. R. Parquette, *Angew. Chem.* **2005**, *117*, 1077 –1081. *Angew. Chem. - Int Ed.*, **2005**, *44*, Issue 7, 1053-1057.
- [6] M. Losada, P. Nguyen, Yunjie Xu, *J. Phys. Chem. A*, **2008**, *112*, 5621–5627. (b). M. Losada, H. Tran, Y. Xu, *J. Chem. Phys.*, **2008**, *128*, 014508/1-11.
- [7] (a). T. Taniguchi, K. Monde, *J. Am. Chem. Soc.* **2012**, *134*, 3695–3698. (b). V. Andrushchenko, D. Tsankov, M. Krasteva, H. Wieser, P. Bour, *J. Am. Chem. Soc.* **2011**, *133*, 15055–15064. (c). T. Brotin, D. Cavagnat, J.Dutasta, T. Buffeteau, *J. Am. Chem. Soc.* **2006**, *128*, 5533-5540.
- [8] S. Abbate, F. Lebon, G. Longhi, C. F. Morelli, D. Ubiali, and G. Speranza, *RSC Adv.*, **2012**, *2*, 10200-10208.
- [9] P. Scafato, F. Caprioli, L. Pisani, D. Padula, F. Santoro, G. Mazzeo, S. Abbate, F. Lebon, G. Longhi, *Tetrahedron*, **2013**, *69*, ,10752–10762.
- [10] S. Qiu, Ewoud, D. Gussem, K. Abbaspour Tehran, S. Sergeyev, P. Bultinck, W. Herrebout, *J. Med. Chem.*, **2013**, *56* (21), 8903–8914.
- [11] L. Andernach, L. P. Sandjo, J. C. Liermann, I. Buckel, E. Thines, T. Opatz, *Eur. J. Org. Chem.*, **2013**, *26*, , 5946-5951.
- [12] P. L. Polavarapu, N. Jeirath, T. Kurtan, G. Pescitelli, K. Krohn, *Chirality*, **2009**, *21*:E202–E207.
- [13] C. Diaz, A. Fraser, A. Morales, K. D. Belfield, S.Ray, F. E. Hernandez, *J. Phys. Chem. A*, **2012**, *116*, 2453-2465.
- [14] C. Díaz, L. Echevarria, F. E. Hernández, *J. Phys. Chem. A*, **2013**, *117*, 8416–8426.

- [15] M. Losada, Y. Xu, *Phys. Chem. Chem. Phys.*, **2007**, 9, 3127-3135.
- [16] Gaussian 09, Revision D.01, M. J. Frisch, G. W. Trucks, H. B. Schlegel, G. E. Scuseria, M. A. Robb, J. R. Cheeseman, G. Scalmani, V. Barone, B. Mennucci, G. A. Petersson, H. Nakatsuji, M. Caricato, X. Li, H. P. Hratchian, A. F. Izmaylov, J. Bloino, G. Zheng, J. L. Sonnenberg, M. Hada, M. Ehara, K. Toyota, R. Fukuda, J. Hasegawa, M. Ishida, T. Nakajima, Y. Honda, O. Kitao, H. Nakai, T. Vreven, J. A. Montgomery, Jr., J. E. Peralta, F. Ogliaro, M. Bearpark, J. J. Heyd, E. Brothers, K. N. Kudin, V. N. Staroverov, R. Kobayashi, J. Normand, K. Raghavachari, A. Rendell, J. C. Burant, S. S. Iyengar, J. Tomasi, M. Cossi, N. Rega, J. M. Millam, M. Klene, J. E. Knox, J. B. Cross, V. Bakken, C. Adamo, J. Jaramillo, R. Gomperts, R. E. Stratmann, O. Yazyev, A. J. Austin, R. Cammi, C. Pomelli, J. W. Ochterski, R. L. Martin, K. Morokuma, V. G. Zakrzewski, G. A. Voth, P. Salvador, J. J. Dannenberg, S. Dapprich, A. D. Daniels, Ö. Farkas, J. B. Foresman, J. V. Ortiz, J. Cioslowski, and D. J. Fox, Gaussian, Inc., Wallingford CT, **2009**.
- [17] (a) P. Hohenberg, W. Kohn, *Phys. Rev.*, **1964**, 136, B864-B71; (b) W. Kohn, L. J. Sham, *Phys. Rev.*, **1965**, 140, A1133-A38; (c) J. K. Labanowski, J. W. Andzelm, *Density functional Methods in Chemistry*, Springer-Verlag: New York, **1991**.
- [18] (a) A. D. Becke, *J. Chem. Phys.*, **1993**, 98, 5648; (b) A. D. Becke, *Phys. Rev. A*, **1988**, 38, 3098-310; (c) T. Lee, W. T. Yang, R. G. Parr, *Phys. Rev. B*, **1988**, 37, 785-789.
- [19] P. C. Hariharan, J. A. Pople, *Theor. Chem. Acc.*, **1973**, 28, 213-222.
- [20] R. A. Kendall, T. H. Dunning Jr., R. J. Harrison, *J. Chem. Phys.*, **1992**, 96, 6796-806.
- [21] S. Grimme, J. Antony, S. Ehrlich, H. Krieg, *J. Chem. Phys.*, **2010**, 132, 154104.
- [22] J. Tomasi, B. Mennucci, R. Cammi, *Chem. Rev.*, **2005**, 105, 2999-3093.
- [23] B. Mennucci; J. Tomasi, R. Cammi, J. R. Cheeseman, M. J. Frisch, F. J. Devlin, S. Gabriel, P. J. Stephens, *J. Phys. Chem. A* **2002**, 106, 6102-6113.
- [24] M. R. Poopari, Z. Dezhahang, Y. Xu., *Phys. Chem. Chem. Phys.*, **2013**, 15, 1655 - 1665.
- [25] Z. Dezhahang, C. Merten, M. R. Poopari, Y. Xu, *Dalton Trans.*, **2012**, 41 (35), 10817 - 10824.
- [26] V. P. Nicu, E. J. Baerends, P. L. Polavarapu, *J. Phys. Chem. A*, **2012**, 116, 8366-8373.
- [27] P. Lahiri, K. B. Wiberg, P. H. Vaccaro, M. Caricato, T. D. Crawford, *Angew. Chem. Int. Ed.* **2014**, 53, 1386-1389.
- [28] P. Mukhopadhyay, G. Zuber, M. Goldsmith, P. Wipf, D. N. Beratan, *ChemPhysChem*, **2006**, 7, 2483 - 2486.
- [29] K. Ruud, R. Zanasi, *Angew. Chem. Int. Ed.* **2005**, 44, 3594-3596.

- [30] R. Begum, T. Sagawa, S. Masatoki, H. Matsuura, *J. Mol. Struct.*, **1988**, 442, 243-250.
- [31] I. A. Khodov, S. V. Efimov, M. Y. Nikiforov, V. V. Klochkov, N. Georgi, *J. Pharm. Sci.*, **2014**, 103, 392-394.
- [32] P. Kr. Ghorai, *J. Phys. Chem. B*, **2010**, 114, 6492–6499.
- [33] C. Merten, R. McDonald, Y. Xu, *Inorg. Chem.* **2014**, 53, 3177–3182.

A vertical yellow bar is positioned on the left side of the page, containing the number 7.

# 7

## **Conclusions and Future Work**

## 7.1. Concluding remarks

---

My PhD thesis projects include the synthesis, conformational analysis, and absolute configuration determination of a number of chiral Schiff base ligands and axially chiral binaphthyl type ligands or molecules and some of their transition metal complexes in solution. To provide direct structural insight into these groups of diverse chiral molecules in solution, several chiroptical spectroscopic techniques, namely VCD, ECD and occasionally ORD spectroscopy, as well as the corresponding linear spectroscopy, i.e. VA and UV-Vis spectroscopy, have been utilized. In all these studies, the experimental results have been complemented with the DFT calculations to provide detailed and rigorous interpretation of the experimental data, and therefore to extract the essential structural properties of the targeted species in solution.

Through these systematic studies, we have gained considerable knowledge about the structural properties of these targeted molecular systems in solution. Equally importantly, we have gained considerable further insight into the procedures used for assigning the absolute configuration and for identifying the dominant species and their conformations in solution using VCD and ECD chiroptical spectroscopic tools. Such insights will be valuable for designing better approaches to probe the absolute configuration and conformation of other novel organic and inorganic chiral compounds in future. In particular, we have developed deeper understanding about the effects of solvent on the chiroptical measurements and how to account for them properly and adequately to achieve reliable interpretations of the experimental VCD spectra. Furthermore, we have reported the effects of concentration on the experimental chiroptical spectra and pointed out that extreme care must be taken when we are comparing the results obtained using ECD and VCD spectroscopic techniques. It is noted that these two chiroptical techniques typically employ



samples with concentrations which differ by several orders of magnitude. Finally, the subjects of the induced chirality at metal centers by coordinating to chiral ligands and also helicity in a series of Schiff base transition metal complexes with Ni (II), Cu (II), Pd (II), Pt (II), and Zn (II) metal ions have been investigated. In this study, we stressed the potential possibility for different structures to be adopted in solid stated and in solution. We further emphasized the importance of ligand conformational preference besides its chirality on the helicity of these compounds in solution. These findings are highlighted below in the current conclusion chapter.

#### *7.1.1. Conformational flexibility in solution*

Currently, it is still quite acceptable in many research areas to assign the absolute configurations and derived structural properties by comparing chiroptical spectra obtained with other similar compounds. However, it has become increasingly clear that this practice often leads to a misinterpretation of the experimental data. For example, in Chapter 2 of the thesis, the VA and VCD spectra of three closely related multidentate nitrogen donor ligands, i.e. (N,N'-bis(pyridine-2-ylmethylene)-(S,S)-1,2-cyclohexanediamine (SS-1), (N,N'-bis(pyridine-2-ylmethyl)-(S,S)-1,2-cyclohexanediamine (SS-2), and {(S,S)-2-[(2-pyridinylcarbonyl)amino] cyclohexyl}-2-pyridinecarboxamide (SS-3) have been measured. While it is possible to make some correlation of the observed IR bands among these three similar compounds, their VCD spectra are so different so that one can hardly make any connection among these compounds by visual comparisons. Our study shows that these three ligands demonstrate very different conformational flexibilities where the pyridine subunits and the amine groups may adopt a number of different conformations. As the rotational degree of freedom along single bonds increases, in the other words, the system becomes more flexible, many more conformations contribute to the total population. Furthermore, it has been recognized in this thesis research and other studies by our

research group and other groups that the VCD spectral signatures are highly sensitive to structural changes, especially dihedral angle changes, besides chirality. For a flexible molecule, its final VCD spectrum contains the contribution of many conformers whose VCD spectra are often greatly different. Therefore an empirical correlation is difficult if not impossible and should not be encouraged to use on flexible molecular systems.

Another commonly used empirical assignment approach for ECD spectroscopy is to compare the ECD spectrum obtained for solid (crystals) with the corresponding one obtained in solution. If they are similar, one then concludes that the solution structure remain the same as in solid which is determined by using X-ray crystallography. This practice has been utilized in many recent papers on the transition metal complexes and supramolecular assemblies, including some references cited in the thesis. From the above discussion, one can appreciate that the conclusions extracted from such a comparison may not be valid. Indeed, the solid state structure does not necessarily represent the thermodynamically most favorable geometry in solution at all. The ECD spectral features may be sensitive to one specific chirality element while not sensitive to the others at all. This coupled with the much broad ECD bandwidth compared to that of VCD and the potential solvent effects, making such empirical assignments doubtful. This point is further illustrated in the “helicity in solid and in solution” section based on Chapter 5.

### *7.1.2. Solvent effects*

For fair rigid systems, for example, ligand **3**, i.e. {(S,S)-2-[(2-pyridinylcarbonyl)amino]cyclohexyl}-2-pyridinecarboxamide (SS-3) studied in Chapter 2, and the Pd complexes of with BINAP and TOLBINAP studied in Chapter 4, the interpretation of VCD spectra is more straightforward. These molecules actually exist just as a single conformer in solution. In ligand

**3**, the resonance structure of the two peptide bonds locks the molecule into one conformation, whereas the metal-ligand interactions restrict both Pd(BINAP)Cl<sub>2</sub> and Pd(TOLBINAP)Cl<sub>2</sub> complexes into a single conformation in solution. Surprisingly, the agreements of the experimental and theoretical VCD spectra of these fairly rigid systems in the gas phase were not great. This led to the recognition of the solvent effects, both implicit bulk of solvent effect and explicit solvent effect through HB interactions. For example, in Figure 5 in Chapter 4, one can clearly recognize the effect of bulk solvent environment on the VCD spectrum of Pd(TOLBINAP)Cl<sub>2</sub> by comparing the gas phase and solution phase simulations, while the same solvent effect hardly changes the appearance of the related IR spectrum at all.

In case of three ligands studied in Chapter 2, the implicit solvent model was employed to identify the lowest energy conformers in CDCl<sub>3</sub> systematically. Such a bulk solvent effect, however, was not enough to explain the VCD couplet observed in the amide I region which was predicted with the opposite signs for ligand **3**. Rather, the explicit solvent model which includes the HB interaction between the CDCl<sub>3</sub> solvent and the –O=C group for ligand **3** explained the sign reversal correctly. Indeed such an unique sensitivity of VCD technique to the explicit HB interactions in solution has enable the observation of dihydrogen-bonded chiral amine–borane complexes in solution and the detection of chirality transfer from a chiral solute to water molecules. [1,2,3 ]

These studies clearly demonstrate unique sensitivity of VCD spectroscopy to the solvent effects. To correctly account for solvent effects is not only a prominent challenge in chiroptical spectroscopic research but also in many other areas of chemistry such as the stereoselective synthesis. These studies further suggest that using relative rigid molecular systems has the

noticeable advantage of allowing one to untangle many factors which contribute to the final appearance of VCD or ECD spectra and focus on both implicit and explicit solvent effects.

### 7.1.3. Concentration effects

Besides solvent effects, another environmental perturbation which can influence the VCD spectral signatures is concentration. For chiral molecular systems which are prone to HB interactions, one can logically anticipate the formation of dimer or even larger clusters at higher concentrations and therefore the changes of the dominant species in solution, for example in the case of lactic acid.[2] There are, however, very few prior reports on the effects of concentration on the molecular systems in which the formation of dimers or larger clusters are clearly unfavoured. In Chapter 6, I explored this interesting topic with a recently synthesized axially chiral binaphthyl fluorene based salen ligand, namely AXF-155, {[2,20-(1E,10E)-(R)-1,10-binaphthyl-2,20-diylbis(azan-1-yl-1-ylidene)bis(methan-1-yl-1-ylidene)bis-(4-((7-(diphenylamino)-9,9-dihexyl-9H-fluoren-2-yl)ethynyl)-phenol)]}. Possible conformations of this flexible multiple axial chiral molecule have been extensively investigated using VCD, ECD, and ORD spectroscopic tools, in combination with DFT calculations. Although, both experimental VCD and ECD spectra of AXF-155 in THF- $d_8$  and  $CDCl_3$  look essentially the same, indicating that the polarity of solvents does not influence the axial chirality and conformational distribution of AXF-155 significantly, the combined VCD and DFT study clearly shows that the dominant species is R-binaphthyl, S-intra-HB//S-extra-HB (R-SS) in the concentrated solution. However, in the much diluted solution, the dominant species was determined to be R-binaphthyl, R-intra-HB//R-extra-HB (R-RR) based on the ECD and ORD investigations. This means that the concentration of the solution definitely plays a determinant role on the stability of the species. This is an area of research which has not yet been fully explored and much further theoretical

modelling will be highly desirable to explain the interesting observations reported here in detail.

One noticeable drawback of VCD spectroscopy is that VCD measurements typically required considerable high concentrations than necessary for ECD, thus preventing VCD application to systems with low solubility. That was the case for the [(R,R)-1,5-diazacis-decalin] copper (II) hydroxide iodine hydrate complex studied in Chapter 3. In that study, I used a combined VA and ECD study to overcome this limitation. We utilized the VA measurements using a KBr pellet with a 0.6% concentration and the ECD measurement in acetonitrile where a much lower concentration of samples is required. The effects of HB interaction with the crystal water on the VA, VCD, UV-Vis, and ECD spectra have been detected and discussed. In fact, such an interaction with the water molecule has been found to have significant impacts on the appearance of VA, VCD and ECD spectra and inclusion of water in the modeling is essential to obtain satisfactory interpretations of the experimental VA and ECD spectra.

#### *7.1.4. Helicity in solution and in solid*

In Chapter 5, I reported VA and VCD as well as UV-Vis and ECD spectroscopic studies of the bis(pyrrol-2-ylmethyleneamine)-cyclohexane ligand and its five transition metal (Ni (II), Cu (II), Pd (II), Pt (II), and Zn (II)) complexes. One strong motivation for this study is to probe structural properties including the induced chirality at the metal centers of the aforementioned systems directly in solution. The metal centers studied can be divided into three groups: Ni, Pd, Pt (with  $d^8$  valance orbitals), Cu (with  $d^9$  valance orbitals), and Zn (with closed d-shell). With the aid of DFT calculations, I examined the effects of the electronic configurations of the metal ions on the optical responses. It was found that the first two groups favor the formation of pseudo-square planar-based configuration around the metal centers, while the last prefers distorted  $-T_d$  structure. While VA and VCD spectra of the Ni (II), Cu (II), Pd (II), and Pt (II) complexes are all quite

similar with some interesting small differences in their peak frequencies and intensities due to the presence of different metals, the VCD spectrum of Zn (II) complex looks considerably different. Our detailed DFT-VCD simulations show that the first four metal complexes exist only in *mono*-nuclear complex form and the metal chirality is  $\Lambda$  or *M*-helicity, dictated by the chirality of the (*R,R*)-ligand. In case of the Zn (II) complex, the comparison of the simulated and experimental VCD spectra shows conclusively that the geometry of this complex is not a *mono*-nuclear but a *di*-nuclear form. Furthermore, geometries of both *P*- and *M*-helicity Zn (II) complex with the (*R,R*)-ligands have been optimized in solution and their VA and VCD spectra simulated. The comparison of the simulated and experimental VCD spectra again shows conclusively that the observed experimental VCD spectrum can only be explained by the *M*-(*R,R*) chirality of the Zn (II) complex. This study demonstrates that it is possible to determine the chirality information including both chirality of the stereogenic centers on the ligand(s) and the helicity of the complexes for all these systems in solution using VCD spectroscopy. This allows us to compare the structural similarities and differences of the complexes in solution and in solid states.

The study shows that ECD spectral features are dominated by the helicity of the complexes. Furthermore, *M*-(*R,R*) and *M*-(*S,S*) give very much the same UV-Vis and ECD spectra. So one cannot tell these two species apart based on their ECD spectra. Very interesting, we also found that the helicity of the transition metal complexes has little to do with the interactions between the metals and ligand. Rather, it depends strongly on the chirality of the ligand and also its preferred conformation. While the helicity of the systems in solution and in solid is the same in this study, the detailed examination reveals that for a more flexible ligand which can adopt other conformations more freely, the associated helicity may alter easily with some environmental

perturbations. Generally, one may expect that some factors including lattice forces and intermolecular contacts may become crucial during crystallizations. On the other hand, losing these influential parameters and taking into account the effect of solvent may lead to the inversion of the absolute configuration at the metal center or the helicity of the species in solution. Furthermore, it is necessary to simulate the ECD spectrum theoretically to figure out if the spectral signatures are dominated by the chirality of ligands or the helicity of the sample before drawing any conclusions related to the chirality and structure.

## 7.2. Future Work

---

My thesis projects are composed of several structural investigations on the chiral ligands (molecules) and transition metal complexes in solution using mainly VCD and ECD spectroscopic tools. The research results show that a detailed analysis of chiral species including the possible absolute configurations, conformational landscapes of the system, effects of solvent and concentration can be evaluated through the comparison of the experimental and theoretical VCD and ECD spectra, as well as the related linear spectra.

In Chapter 5 of my thesis, I have synthesized a number of N<sub>4</sub>-donor Schiff base metal complexes with metal = Ni, Pd, Pt, and Cu which strongly prefer *mono*-nuclear pseudo-square-planar coordination configuration around the metal centers. These complexes, however, are not perfectly square-planar. Rather the angles between the two relevant planes are in the range of 3 to 8 degrees in solution. Furthermore the current study shows that all of these four complexes take on the *M*-helicity with the (*R,R*)-ligand. This prompts one to ask some interesting questions such as what is the barrier to go from *M* to *P*, especially since they are so close to planar? How will such preference change if different substitutions are used? How about different solvents?

Recently, Merten et al. investigated strong solvent-dependency of  $\Delta$  and  $\Lambda$  stereoisomers preference of a nickel complex in DMSO and acetonitrile solvents using VCD spectroscopy. [4] Despite the fact that both  $\Delta$  and  $\Lambda$  stereoisomers exist in 1:1 ratio in solid state for a tris-nickel (II) complex with chiral diamine dipen as ligands, it has been demonstrated that the  $\Lambda$  form is strongly preferred in DMSO whereas an equal-mixture of both chiral isomers exist in acetonitrile. [4] Other fascinating solvent effects were reported by Sato et al. [5] where both square-planar and tetrahedral structures of chiral Schiff base nickel complex with a binaphthyl moiety coexist in  $\text{CDCl}_3$  solvent. In the presence of strongly donating solvent like DMSO, the spatial configuration around the metal center alters from square-planar to octahedral with a  $C_1$  symmetry with two solvent molecules also coordinating to the nickel center. Related studies can be carried out to rich our understanding of the chirality transfer from chiral ligands to the metal centers. More specifically, in the study in Chapter 5, we recognized the rigidity of the cyclohexane chair configuration has very much to do with the final helicity of the complexes and ligands. It may be of great interest to replace cyclohexane ring with another link which is more flexible. This may allow us to tune the preferred helicity in solution.

Depending on the ligand and the metal centers, a larger deviation from a perfect square-planar structure can be generated. While this deviation for the  $N_4$ -donor type ligands studied where N atoms are of  $sp^2$  hybridization might be quite small, other hetero-type ligands such as  $N_2O_2$ -donor with the  $sp^2$  and  $sp^3$  hybridizations for N and O atoms and with different capping group may results in more prominent deviations from the square-planar coordination configuration. As an example, the distorted square-planar structures of some copper complexes contain Schiff base ligands, i.e. N-1-(Ar) ethyl-2-oxo-1-naphthaldiminato- $\kappa^2N,O$ , were studied and it was found that the deviation from the perfect square planar can be ranging from 4 degrees when  $\text{Ar} = p\text{-C}_6\text{H}_4\text{Br}$



to almost 46 degrees when  $Ar=m\text{-C}_6\text{H}_4\text{OMe}$ . [6] Such a change may cause further structural modification and induction of helicity around the metal centers. This could be another interesting research project to explore.

As a chiroptical spectroscopy chemist, one longer term goal I would like to pursue is to apply my current knowledge of chiral spectroscopy, especially VCD spectroscopy, to better understand the mechanism of a particular reaction. One interesting extension of the current work is to apply this approach to study the reaction intermediates and reaction products in situ.

Chapter 6 of my thesis contains a comprehensive investigation on a relatively large axially chiral molecule, AXF-155. Our study centered on using VCD and ORD spectroscopic techniques and is compared to the original work which was accomplished by using ECD spectroscopy only. Since the required concentrations for the measurements with these techniques are quite different, the un-expected concentration-induced axial-chirality-inversion of AXF-155 was discovered. It was also clear from the work reported in Chapter 6, such structural change is not due to the specific formation of dimer or larger clusters as it was seen previously for the lactic acid molecule.[2] Rather, this seems to do with how the solvent environment is being modified by increasing the concentration. So far this phenomena has not been explained satisfactorily using the usual methodology employed. Further research in this direction with other theoretical groups will be desirable.

## References

---

- [1] C. Merten, C. J. Berger, R. McDonald, Y. Xu, *Angew. Chem – Int. Ed.*, **2014**, 53, 9940-9943.
- [2] M. Losada, H. Tran, Y. Xu, *J. Chem. Phys.*, 128, **2008**, 014508.
- [3] G. Yang, Y. Xu, “Vibrational Circular Dichroism Spectroscopy of Chiral Molecules”, in *Top. Curr. Chem., Volume: Electronic and Magnetic Properties of Chiral Molecules and Supramolecular Architectures*, Eds R. Naaman, D. N. Beratan, D. H. Waldeck, Springer-Verlag, Berlin, Heidelberg, **2011**, 298, 189-236.
- [4] C. Merten, R. McDonald, and Y. Xu, *Inorg. Chem.* **2014**, 53, 3177–3182.
- [5] H Sato, Y. Mori, A. Yamagishi, *Dalton Trans.*, **2013**, 42, 6873.
- [6] M. Enamullah, A. K. M. R. Uddin, G. Pescitelli, R. Berardozi, G. Makhloufi, V. Vasylyeva, A. Chamayoud, C. Janiak, *Dalton Trans.*, **2014**, 43, 3313.

## Work Cited

---

- [1] R. S. Cahn, C. K. Ingold, V. Prelog, *Angew. Chem. Int. Ed.*, **1966**, 5, 385.
- [2] J. March. *Advanced Organic Chemistry* 3Ed. **2007**, John Wiley & Sons. ISBN 0-471-85472-7.
- [3] T. Wu, X. Z. You, P. Bouř, *Coordin. Chem. Rev.*, **2015**, 284, 1.
- [4] G. H. Wagnière, *On Chirality and the Universal Asymmetry*, Wiley-VCH, **2007**.
- [5] J. Autschbach, *Comprehensive Chiroptical Spectroscopy*, **2012**, Volume 1, chapter 21, 593.
- [6] G. Holzwarth, Hsu, E. C., Mosher, H. S, Faulkner, T. R, Moscowitz, A. *J. Am. Chem. Soc.*, **1974**, 96, 251.
- [7] L. A. Nafie, J. C. Cheng, P. J. Stephens, *J. Am. Chem. Soc.*, **1975**, 97, 3842.
- [8] L. A. Nafie, T. A. Keiderling, P. J. Stephens, *J. Am. Chem. Soc.*, **1976**, 98, 2715.
- [9] L. A. Nafie, M. Diem, *Appl. Spectrosc.*, **1979**, 33, 130.
- [10] L. A. Nafie, M. Diem, D. W. Vidrine, *J. Am. Chem. Soc.*, **1979**, 101, 496.
- [11] L. A. Nafie, T. H. Walnut, *Chem. Phys., Lett.*, **1977**, 49, 441.
- [12] T. H. Walnut, L. A. Nafie, *Chem. Phys.*, **1977**, 67, 1501.
- [13] L. A. Nafie, T. B. Freedman, *J. Phys. Chem.*, **1983**, 78, 7108.
- [14] R. Dutler, A. Rauk, *J. Am. Chem. Soc.*, **1989**, 111, 6957.
- [15] D. Yang, A. Rauk, *J. Chem. Phys.*, **1992**, 97, 6517.
- [16] P. J. Stephens, *J. Phys. Chem.*, **1985**, 89, 148-752.
- [17] A. D. Buckingham, P. W. Fowler, P.A. Galwas, *Chem. phys.*, **1987**, 112, 1.
- [18] P.J. Stephens, *J. Phys. Chem.*, **1987**, 91, 1712.
- [19] M. W. Schmidt, K. K. Baldrige, J. A. Boatz, S. T. Elbert, M. S. Gordon, J. H. Jensen, S. Koseki, N. Matsunaga, K. A. Nguyen, S. Su, T. L. Windus, M. Dupuis, J. A. Montgomery J. *Comput. Chem.*, **1993**, 14, 1347.
- [20] A. D. Becke, *J. Chem. Phys.*, **1993**, 98, 1372.

- [21] A. D. Becke, *J. Chem. Phys.*, **1993**, 98, 5648.
- [22] P. J. Stephens, F. J. Devlin, C. F. Chabalowski, M. J. Frisch, *J. Phys. Chem.*, **1994**, 98, 11623.
- [23] P. J. Stephens, F. J. Devlin, J. R. Cheeseman, CRC Press, VCD Spectroscopy for Organic Chemist, **2012**.
- [24] W. Kohn, L. J. Sham, *Phys. Rev.*, **1965**, 140, A1133.
- [25] R. A. Kendall, T. H. Dunning Jr., R. J. Harrison, *J. Chem. Phys.*, 1992, 96, 6796.
- [26] B. Mennucci, J. Tomasi, R. Cammi, J. R. Cheeseman, M. J. Frisch, F. J. Devlin, S. Gabriel, P. J. Stephens, *J. Phys. Chem. A*, **2002**, 106, 6102.
- [27] S. Kaizaki, Comprehensive Chiroptical Spectroscopy: Applications in Stereochemical Analysis of Synthetic Compounds, Natural Products, and Biomolecules by N. Berova, P.L. Polavarapu, K. Nakanishi, R.W. Woody (Eds.), vol.1 and 2, John Wiley & Sons, Inc., New Jersey, **2012**, pp. 451.
- [28] B. Le Guennic, W. Hieringer, A. Görling, J. Autschbach, *J. Phys. Chem. A*, **2005**, 109, 4836.
- [29] C. Cappelli, S. Monti, A. Rizzo, *Int. J. Quantum Chem.*, **2005**, 104, 744.
- [30] D. R. Turner, J. Kubelka, *J. Phys. Chem. B*, **2007**, 111, 1834.
- [31] A. Vargas, N. Bonalumi, D. Ferri, A. Baiker, *J. Phys. Chem. A*, **2006**, 110, 1118.
- [32] V. P. Nicu, E. J. Baerends, L. Polavarapu, *J. Phys. Chem. A*, **2012**, 116, 8366.
- [33] E. Debie, P. Bultinck, W. Herrebout, B. van der Veken, *Phys. Chem. Chem. Phys.*, **2008**, 10, 3498.
- [34] A. Giugliarelli, P. Sassi, M. Paolantoni, A. Morresi, R. Dukor, L. Nafie, *J. Phys. Chem. B*, **2013**, 117, 2645.
- [35] J. Tomasi, B. Mennucci, R. Cammi, *Chem. Rev.*, **2005**, 105, 2999.
- [36] Poopari, M.R, Dezhahang, Z., Yang, G., Xu, Y., *ChemPhysChem.*, **2012**, 13, 2310.
- [37] Dezhahang, Z., Merten, C., Poopari, M.R., Xu, Y., *Dalton Trans*, **2012**, 41, 10817.
- [38] Poopari, M.R., Dezhahang, Z., Xu, Y., *Phys. Chem. Chem. Phys.*, **2013**, 15, 1655.
- [39] Dezhahang, Z., Poopari, M.R., Xu, Y., *Chem. Asian. J.*, **2013**, 8, 1205.

- [40] Cheeseman, J.R., Shaik, M.S., Popelier, P.L.A., Blanch, E.W., *J. Am. Chem. Soc.*, **2011**, 133, 4991.
- [41] Polavarapu, P.L., *Chirality*, **2012**, 24, 909.
- [42] Chamayou, A.-C., Lüdeke, S., Brecht, V., Freedman, T.B., Nafie, L.A., Janiak, C., *Inorganic Chemistry*, **2011**, 50, 11363.
- [43] Gutiérrez-Nicolás, F., Gordillo-Román, B., Oberti, J.C., Estévez-Braun, A. Ravelo, A.G., Joseph-Nathan, P., *J. Nat. Prod.*, **2012**, 75, 669.
- [44] Y. Zhang, L. Xiang, Q. Wang, X. F. Duan, G. Zi, *Inorg. Chim. Acta.*, **2008**, 361, 1246.
- [45] A. Ouali, M. Taillefer, J.-F. Spindler, A. Jutand, *Organometallics.*, **2007**, 26, 65.
- [46] H. Zhang, L. Chen, H. Song, G. Li, *Inorg. Chim. Acta*, **2011**, 366, 320.
- [47] M. Livieri, F. Mancin, G. Saielli, J. Chin, U. Tonellato, *Chem. Eur. J.*, **2007**, 13, 2246.
- [48] Y. Murakami, J. I. Kikuchi, Y. Hisaeda, O. Hayashida, *Chem. Rev.* **1996**, 96, 721.
- [49] T. M. Kooistra, K. F. W. Hekking, Q. Knijnenburg, B. de Bruin, P. H. M. Budzelaar, R. De Gelder, J. M. M. Smits, A. W. Gal, *Eur. J. Inorg. Chem.*, **2003**, 648.
- [50] L. A. Nafie, *Vibrational Optical Activity: Principles and Applications*, Wiley, Chichester, **2011**.
- [51] Y. He, B. Wang, R. K. Dukor, L. A. Nafie, *Appl. Spectrosc.*, **2011**, 65, 699 .
- [52] G. Yang, Y. Xu, "Vibrational Circular Dichroism Spectroscopy of Chiral Molecules", in *Top. Curr. Chem.* Volume: Electronic and Magnetic Properties of Chiral Molecules and Supramolecular Architectures (Eds.: R. Naaman, D. N. Beratan, D. H. Waldeck), Springer, Berlin, **2011**, 298, 189.
- [53] P. J. Stephens, F. J. Devlin, J. J. Pan, *Chirality.*, **2008**, 20, 643.
- [54] M. Gabor, T. Gyçrgy, V. Elemr, *Wiley Interdiscip. Rev.: Comput. Mol. Sci.*, **2011**, 1, 403.
- [55] Y. He, X. Cao, L. A. Nafie, T. B. Freedman, *J. Am. Chem. Soc.*, **2001**, 123, 11320.
- [56] C. Johannessen, P. W. Thulstrup, *Dalton Trans.*, **2007**, 10, 1028.
- [57] W. Armstrong, F. A. Cotton, A. G. Petrovic, P. L. Polavarapu, M. M. Warnke, *Inorg. Chem.*, **2007**, 46, 1535.

- [58] T. Wu, X.-P. Zhang, C.-H. Li, P. Bourč, Y.-Z. Li, X.-Z. You, *Chirality*, **2012**, 24, 451.
- [59] C. Merten, K. Hiller, Y. Xu, *Phys. Chem. Chem. Phys.*, **2012**, 14, 12884.
- [60] H. Sato, Y. Mori, T. Kitazawa, A. Yamagishi, *Dalton Trans.*, **2013**, 42, 232.
- [61] H. Sato, A. Yamagishi, *Int. J. Mol. Sci.*, **2013**, 14, 964.
- [62] Z. Dezhahang, M. R. Poopari, Y. Xu, *J. Mol. Struct.*, **2012**, 1024, 123.
- [63] V. P. Nicu, E. Debie, W. Herrebout, B. Van der Veken, P. Bultinck, E. J. Baerends, *Chirality*, **2009**, 21, E287.
- [64] M. Losada, Y. Xu, *Phys. Chem. Chem. Phys.*, **2007**, 9, 3127.
- [65] M. R. Poopari, P. Zhu, Z. Dezhahang, Y. Xu, *J. Chem. Phys.*, **2012**, 137, 194308.
- [66] G. Yang, Y. Xu, *J. Chem. Phys.*, **2009**, 130, 164506.
- [67] V. P. Nicu, E. J. Baerends, *Phys. Chem. Chem. Phys.*, **2009**, 11, 6107 .
- [68] V. P. Nicu, E. J. Baerends, *Phys. Chem. Chem. Phys.* **2011**, 13, 16126.
- [69] V. P. Nicu, J. Neugebauer, E. J. Baerends, *J. Phys. Chem. A*, **2008**, 112, 6978.
- [70] K.-K. Lee, S. Hahn, K.-I. Oh, J. S. Choi, C. Joo, H. Lee, H. Han, M. Cho, *J. Phys. Chem. B*, **2006**, 110, 18834.
- [71] P. Bouř, T. A. Keiderling, *J. Phys. Chem. B*, **2005**, 109, 23687.
- [72] W. Park, M. H. Shim, J. H. Chung, J. Park, M. S. Lah, D. Lim, *Tetrahedron Lett.*, **2006**, 47, 8841.
- [73] X. Li, J. Yang, M.C. Kozlowski, *Org. Lett.*, **2001**, 3, 1137.
- [74] M.C. Kozlowski, Z. Xu, A. Gil Santos, *Tetrahedron*, **2001**, 57, 4537.
- [75] J. Fleischhauer, G. Raabe, A.G. Santo, J. Schiffer, A. Wollmer, *Z. Naturforsch*, **1998**, 53a 896.
- [76] B. Ganguly, D.A. Freed, M.C. Kozlowski, *J. Org. Chem.* 66, **2001**, 1103.
- [77] Z. Xu, M.C. Kozlowski, *J. Org. Chem.*, **2002**, 67, 3072.
- [78] A. Santos, W. Klute, J. Torode, V.P.W. Böhm, E. Cabrita, J. Runsink, R.W. Hoffmann, *New J. Chem.*, **1998**, 993.

- [79] X. Li, L.B. Schenkel, M.C. Kozlowski, *Org. Lett.*, **2000**, 2, 875.
- [80] T. Mori, Y. Inoue, in: R. Naaman, D.N. Beratan, D.H. Waldeck (Eds.), *Top. Curr. Chem.*, Volume: Electronic and Magnetic Properties of Chiral Molecules and Supramolecular Architectures, Springer-Verlag, Berlin Heidelberg, **2011**, vol. 298, pp. 99.
- [81] N. Berova, L. Di Bari, G. Pescitelli, *Chem. Soc. Rev.*, **2007**, 36, 914.
- [82] J. Šýbek, B. Gyurcsik, J. Šýbestík, Z. Kejík, L. Bednárová, P. Bouř, *J. Phys. Chem. A* **111** (2007) 2750.
- [83] H. Hussain, I. Ahmed, B. Schulz, S. Draeger, U. Flörke, G. Pescitelli, K. Krohn, *Chirality*, **2011**, 23, 617.
- [84] M.J. Frisch, G.W. Trucks, H.B. Schlegel, G.E. Scuseria, M.A. Robb, J.R. Cheeseman, J.A. Montgomery Jr., T. Vreven, K.N. Kudin, J.C. Burant, J.M. Millam, S.S. Iyengar, J. Tomasi, V. Barone, B. Mennucci, M. Cossi, G. Scalmani, N. Rega, G.A. Petersson, H. Nakatsuji, M. Hada, M. Ehara, K. Toyota, R. Fukuda, J. Hasegawa, M. Ishida, T. Nakajima, Y. Honda, O. Kitao, H. Nakai, M. Klene, X. Li, J.E. Knox, H.P. Hratchian, J.B. Cross, C. Adamo, J. Jaramillo, R. Gomperts, R.E. Stratmann, O. Yazyev, A.J. Austin, R. Cammi, C. Pomelli, J.W. Ochterski, P.Y. Ayala, K. Morokuma, G.A. Voth, P. Salvador, J.J. Dannenberg, V.G. Zakrzewski, S. Dapprich, A.D. Daniels, M.C. Strain, O. Farkas, D.K. Malick, A.D. Rabuck, K. Raghavachari, J.B. Foresman, J.V. Ortiz, Q. Cui, A.G. Baboul, S. Clifford, J. Cioslowski, B.B. Stefanov, G. Liu, A. Liashenko, P. Piskorz, I. Komaromi, R.L. Martin, D.J. Fox, T. Keith, M.A. Al-Laham, C.Y. Peng, A. Nanayakkara, M. Challacombe, P.M.W. Gill, B. Johnson, W. Chen, M.W. Wong, C. Gonzalez, J.A. Pople, Gaussian 03, Revision B.01, Gaussian 03, Revision E.01., Gaussian, Inc., Pittsburgh, PA, **2003**.
- [85] P.J. Stephens, F.J. Devlin, C. Villani, F. Gasparrini, S. Levi Mortera, *Inorg. Chem. Acta.*, **2008**, 361, 987.
- [86] H. Sato, T. Taniguchi, K. Monde, S.-I. Nishimura, A. Yamagashi, *Chem. Lett.*, **2006**, 35, 364.
- [87] H. Sato, T. Taniguchi, A. Nakahashi, K. Monde, A. Yamagashi, *Inorg. Chem.*, **2007**, 46, 6755.
- [88] C. Merten, M. Amkreutz, A. Hartwig, *J. Mol. Struct.*, **2010**, 970, 101.
- [89] W.L. Qian, S. Krimm, *J. Phys. Chem. A*, **2002**, 106, 6628.
- [90] A. Kovacs, A. Szabo, D. Nemcsok, I. Hargittai, *J. Phys. Chem. A*, **2002**, 106, 5671.
- [91] B. Kirchner, M. Reiher, *J. Am. Chem. Soc.*, **2002**, 124, 6206.

- [92] M. Losada, H. Tran, Y. Xu, *J. Chem. Phys.*, **2008**, 128, 014508.
- [93] G. Yang, Y. Xu, *Phys. Chem. Chem. Phys.*, **2008**, 10, 6787.
- [94] A. Vlċek Jr., S. Záliṡ, *Coord. Chem. Rev.*, **2007**, 251, 258.
- [95] S. Miertus, E. Scrocco, J. Tomasi, *Chem. Phys.*, **1981**, 55, 117.
- [96] J. Tomasi, M. Persico, *Chem. Rev.*, **1994**, 94, 2027.
- [97] G. Yang, Y. Xu, J. Hou, H. Zhang, Y. Zhao, *Chem. Eur. J.*, **2010**, 16, 2518.
- [98] Z. Su, Q. Wen, Y. Xu, *J. Am. Chem. Soc.*, **2006**, 128, 6755.
- [99] M. Peculli, D. Marchesan, K. Ruud, S. Coriani, *J. Chem. Phys.*, **2005**, 122, 024106.
- [100] A. Klamt, G. Schüürmann, *J. Chem. Soc. Perkin. Trans.*, **1993**, 2, 799.
- [101] C.C. Pye, T. Ziegler, *Theo. Chem. Acc.*, **1999**, 101, 396.
- [102] C. Cappelli, S. Bronco, S. Monti, *Chirality*, **2005**, 17, 577.
- [103] J. Sadlej, J. Cz Dobrowolski, J.E. Rode, M.H. Jamróz, *Phys. Chem. Chem. Phys.*, **2006**, 8, 101.
- [104] G. Yang, Y. Xu, *J. Chem. Phys.*, **2009**, 130, 164506.
- [105] G. Yang, Y. Xu, J. Hou, H. Zhang, Y. Zhao, *Dalton Trans.*, **2010**, 39, 6953.
- [105] I. G. Rios, A. Rosas-Hernandez and E. Martin, *Molecules*, **2011**, 16, 970.
- [106] R. Noyori and T. Ohkuma, *Angew. Chem., Int. Ed.*, **2001**, 40(1), 40.
- [107] T. Ohkuma, M. Kitamura and R. Noyori, *Catalytic Asymmetric Synthesis*, John Wiley & Sons, 2nd edn, **2000**, 1.
- [108] R. Noyori, T. Ohkuma, M. Kitamura, H. Takaya, N. Sayo, H. Kumobayashi and S. Akutagawa, *J. Am. Chem. Soc.*, **1987**, 109, 5856.
- [109] S. Akutagawa and K. Tani, *Catalytic Asymmetric Synthesis*, John Wiley & Sons, 2nd edn, **2000**, 145.
- [110] R. Noyori, *Asymmetric Catalysis in Organic Synthesis*, John Wiley & Sons, **1994**.
- [111] J. F. Hartwig, in *Handbook of Organopalladium Chemistry for Organic Synthesis*, ed. E. I. Negishi, Wiley-Interscience, New York, **2002**, 1, 1051.



- [112] A. R. Muci and S. L. Buchwald, *Top. Curr. Chem.*, **2002**, 219, 131.
- [113] E. F. Kleinman, in *Comprehensive Organic Synthesis*, ed. B. M. Trost and I. Fleming, Pergamon, Oxford, **1991**, ch. 4.1, vol. 2.
- [114] Y. Hamashima, N. Sasamoto, D. Hotta, H. Somei, N. Umabayashi and M. Sodeoka, *Angew. Chem., Int. Ed.*, **2005**, 44, 1525.
- [115] J. Hao, M. Hatano and K. Mikami, *Org. Lett.*, **2000**, 2, 4059.
- [116] S. Shekhar, P. Ryberg, J. F. Hartwig, J. S. Mathew, D. G. Blackmond, E. R. Strieter and S. L. Buchwald, *J. Am. Chem. Soc.*, **2006**, 128, 3584.
- [117] (a) P. J. Stephens, F. J. Devlin and J. J. Pan, *Chirality*, 2008, 20, 643.
- [118] F. D. Montigny, L. Guy, G. Pilet, N. Vanthuyne, C. Roussel, R. Lombardi, T. B. Freedman, L. A. Nafie and J. Crassous, *Chem. Commun.*, **2009**, 4841.
- [119] V. A. Soloshonok, T. Ono, H. Ueki, N. Vanthuyne, T. S. Balaban, J. Brück, H. Fliegl, W. Klopper, J.-V. Naubron, T. T. T. Bui, A. F. Drake and C. Roussel, *J. Am. Chem. Soc.*, **2010**, 132, 10477.
- [120] V. P. Nicu, M. Heshmat and E. J. Baerends, *Phys. Chem. Chem. Phys.*, **2011**, 13, 8811.
- [121] C. Johannessen and P. W. Thulstrup, *Dalton Trans.*, **2007**, 1028.
- [122] (a) B. J. V. Verkuijl, B. Schuur, A. J. Minnaard, J. G. de Vries and B. L. Feringa, *Org. Biomol. Chem.*, **2010**, 8, 3045.
- [123] C. H. Perry, D. P. Athans, E. F. Young, J. R. Durig and B. R. Mitchell, *Spectrochim. Acta*, **1967**, 23A, 1137.
- [124] A. S. Cooke and M. M. Harris, *J. Chem. Soc.*, **1963**, 2365.
- [125] R. E. Pincock, R. R. Perkins, A. S. Ma and K. R. Wilson, *Science*, **1971**, 174, 1018.
- [126] V. Setnička, M. Urbanová, P. Bouř, V. Král and K. Volka, *J. Phys. Chem. A*, **2001**, 105, 8931.
- [127] S. K. Burley and G. A. Petsko, *Science*, **1985**, 229, 23.
- [128] C. A. Hunter and J. K. M. Sanders, *J. Am. Chem. Soc.*, **1990**, 112, 5525.
- [129] P. Zhu, G. Yang, M. R. Poopari, Z. Bie and Y. Xu, *ChemPhysChem*, **2012**, 13, 1272.

- [130] C. Merten, R. McDonald, Y. Xu, *Inorg. Chem.*, **2014**, 53, 3177.
- [131] H. Sato, Y. Mori, A. Yamagishi., *Dalton Trans.*, **2013**, 42, 6873.
- [132] T. Wu, X.-P. Zhang, X.-Z. You, Y.-Z. Li, P. Bouř, *ChemPlusChem*, **2014**, 79, 698.
- [133] M. Enamullah, A. K. M. R. Uddin, G. Pescitelli, R. Berardozzi, G. Makhloufi, V. Vasylyeva, A.-C. Chamayou, C. Janiak., *Dalton. Trans.*, **2014**, 43, 3313.
- [134] C. Merten, Y. Xu. *Dalton Trans.* **2013**, 42, 10572.
- [135] H. Sato, H. Uno, H. Nakano. *Dalton Trans.* **2011**, 40, 1332.
- [136] A. Bacchi, M. Carcelli, L. Gabba, S. Ianelli, P. Pelagatti, G. Pelizzi, D. Rogolino. *Inorg. Chem. Acta.*, **2003**, 342, 229-235.
- [137] S. Kano, H. Nakano, M. Kojima, N. Baba, K. Nakajima. *Inorg. Chem. Acta.*, **2003**, 349, 6.
- [138] Q. T. Nguyen, J. H. Jeong. *Polyhedron.*, **2006**, 25, 1787.
- [139] H-J. Cristau, A. Ouali, J-F. Spindler, M. Taillefer. *Chem. Eur. J.*, **2005**, 11, 2483.
- [140] X. F. Shan, L. Z. Wu, X. Y. Liu, L. P. Zhang, C.H. Tung. *Eur. J. Inorg. Chem.*, **2007**, 3315.
- [141] Y. Wang, H. Fu, F. Shen, X. Sheng, A. Peng, Z. Gu, H. Ma, J. S. Ma, J. Yao. *Inorg. Chem.*, **2007**, 46, 3548.
- [142] X-F. Shan, D-H. Wang, C-H. Tung, L-Z. Wu. *Tetrahedron.*, **2008**, 65, 5577.
- [143] X-F. Shan, D-H. Wang, C-H. Tung, L-Z. Wu. *Chinese Sci. Bulletin.*, **2007**, 52, 1581.
- [144] X. Shan, D. Wang, C. Tung, L. Wu, *Tetrahedron.*, **2008**, 64, 5577.
- [145] X. Shan, L. Wu, L. Zhang, C. Tung, *Chinese Science Bulletin*, **2007**, 52, 1581.
- [146] S. M. Bachrach, Computational Organic Chemistry, John Wiley & Sons, Inc. publication, **2007**.
- [147] SPARTAN '08; Wavefunction, Inc.: Irvine, CA;  
[www.wavefun.com/products/spartan.html](http://www.wavefun.com/products/spartan.html).
- [148] G. Yang, H. Tran, E. Fan, W. Shi, T. L. Lowary, Y. Xu, *Chirality*, **2010**, 22, 734.
- [149] Gaussian 09, Revision **D.01**, M. J. Frisch, G. W. Trucks, H. B. Schlegel, G. E. Scuseria, M. A. Robb, J. R. Cheeseman, G. Scalmani, V. Barone, B. Mennucci, G. A. Petersson, H.

Nakatsuji, M. Caricato, X. Li, H. P. Hratchian, A. F. Izmaylov, J. Bloino, G. Zheng, J. L. Sonnenberg, M. Hada, M. Ehara, K. Toyota, R. Fukuda, J. Hasegawa, M. Ishida, T. Nakajima, Y. Honda, O. Kitao, H. Nakai, T. Vreven, J. A. Montgomery, Jr., J. E. Peralta, F. Ogliaro, M. Bearpark, J. J. Heyd, E. Brothers, K. N. Kudin, V. N. Staroverov, R. Kobayashi, J. Normand, K. Raghavachari, A. Rendell, J. C. Burant, S. S. Iyengar, J. Tomasi, M. Cossi, N. Rega, J. M. Millam, M. Klene, J. E. Knox, J. B. Cross, V. Bakken, C. Adamo, J. Jaramillo, R. Gomperts, R. E. Stratmann, O. Yazyev, A. J. Austin, R. Cammi, C. Pomelli, J. W. Ochterski, R. L. Martin, K. Morokuma, V. G. Zakrzewski, G. A. Voth, P. Salvador, J. J. Dannenberg, S. Dapprich, A. D. Daniels, Ö. Farkas, J. B. Foresman, J. V. Ortiz, J. Cioslowski, and D. J. Fox, Gaussian, Inc., Wallingford CT, **2009**.

[150] W. Kohn and L. J. Sham, *Phys. Rev.*, **1965**, 140, A1133.

[151] C. T. Lee, W. T. Yang, R. G. Parr, *Phys. Rev. B*, **37**, **1988**, 785.

[152] P. Mukhopadhyay, G. Zuber, M. Goldsmith, P. Wipf, and D. N. Beratan, *ChemPhysChem*, **2006**, 7, 2483.

[153] B. Mennucci, C. Cappelli, R. Cammi, J. Tomasi, *Chirality*, **2011**, 23, 717.

[154] S. Coriani, A. Baranowska, L. Ferrighi, C. Forzato, D. Marchesan, P. Nitti, G. Pitacco, A. Rizzo, K. Ruud, *Chirality*, **2006**, 18, 357.

[155] R.W. Sinkeldam, M. H. C. J. van Houtem, K. Pieterse, J. A. J. M. Vekemans, E. W. Meijer *Chem. Eur. J.*, **2006**, 12, 6129.

[156] A. L. Hofacker, J. R. Parquette, *Angew. Chem.* 2005, 117, 1077–1081. *Angew. Chem. - Int Ed.*, **2005**, 44, Issue 7, 1053.

[157] M. Losada, P. Nguyen, Yunjie Xu, *J. Phys. Chem. A*, 2008, 112, 5621.

[158] T. Taniguchi, K. Monde, *J. Am. Chem. Soc.*, **2012**, 134, 3695.

[159] V. Andrushchenko, D. Tsankov, M. Krasteva, H. Wieser, P. Bour, *J. Am. Chem. Soc.*, **2011**, 133, 15055.

[160] T. Brotin, D. Cavagnat, J. Dutasta, T. Buffeteau, *J. Am. Chem. Soc.*, **2006**, 128, 5533.

[161] S. Abbate, F. Lebon, G. Longhi, C. F. Morelli, D. Ubiali, and G. Speranza, *RSC Adv.*, **2012**, 2, 10200.

[162] P. Scafato, F. Caprioli, L. Pisani, D. Padula, F. Santoro, G. Mazzeo, S. Abbate, F. Lebon, G. Longhi, *Tetrahedron*, **2013**, 69, 10752.

[163] S. Qiu, Ewoud, D. Gussem, K. Abbaspour Tehran, S. Sergeev, P. Bultinck, W. Herrebout, *J. Med. Chem.*, **2013**, 56 (21), 8903.

- [164] L. Andernach, L. P. Sandjo, J. C. Liermann, I. Buckel, E. Thines, T. Opatz, *Eur. J. Org. Chem.*, **2013**, 26, , 5946.
- [165] P. L. Polavarapu, N. Jeirath, T. Kurtan, G. Pescitelli, K. Krohn, *Chirality*, **2009**, 21, E202.
- [166] C. Diaz, A. Fraser, A. Morales, K. D. Belfield, S. Ray, F. E. Hernandez, *J. Phys. Chem. A*, **2012**, 116, 2453.
- [167] C. Díaz, L. Echevarria, F. E. Hernández, *J. Phys. Chem. A* **2013**, 117, 8416.
- [168] P. Hohenberg, W. Kohn, *Phys. Rev.*, **1964**, 136, B864.
- [169] W. Kohn, L. J. Sham, *Phys. Rev.*, **1965**, 140, A1133.
- [170] J. K. Labanowski, J. W. Andzelm, *Density functional Methods in Chemistry*, Springer-Verlag: New York, **1991**.
- [171] A. D. Becke, *Phys. Rev. A*, **1988**, 38, 3098.
- [172] T. Lee, W. T. Yang, R. G. Parr, *Phys. Rev. B*, **1988**, 37, 785.
- [173] P. C. Hariharan, J. A. Pople, *Theor. Chem. Acc.*, **1973**, 28, 213.
- [174] S. Grimme, J. Antony, S. Ehrlich, H. Krieg, *J. Chem. Phys.*, **2010**, 132, 154104.
- [175] P. Lahiri, K. B. Wiberg, P. H. Vaccaro, M. Caricato, T. D. Crawford, *Angew. Chem. Int. Ed.* **2014**, 53, 1386.
- [176] P. Mukhopadhyay, G. Zuber, M. Goldsmith, P. Wipf, D. N. Beratan, *ChemPhysChem*, **2006**, 7, 2483.
- [177] K. Ruud, R. Zanasì, *Angew. Chem. Int. Ed.* **2005**, 44, 3594.
- [178] R. Begum, T. Sagawa, S. Masatoki, H. Matsuura, *J. Mol. Struct.*, **1988**, 442, 243.
- [179] I. A. Khodov, S. V. Efimov, M. Y. Nikiforov, V. V. Klochkov, N. Georgi, *J. Pharm. Sci.*, **2014**, 103, 1582.
- [180] P. K. Ghorai, *J. Phys. Chem. B*, **2010**, 114, 6492.
- [181] C. Merten, C. J. Berger, R. McDonald, Y. Xu, *Angew. Chem. Int. Ed.*, **2014**, 53, 9940.



## Supporting Information

### Vibrational circular dichroism spectroscopy of three multidentate nitrogen donor ligands: conformational flexibility and solvent effects

Zahra Dezhahang, Mohammad Reza Poopari, Yunjie Xu

1. Raw VCD spectra of the two enantiomers of **1**, **2** and **3**.
2. Calculated VA and VCD spectra of the six conformers of **1**.
3. Comparison of the experimental VA and VCD spectra with the corresponding spectra of the ten conformers of **2**.
4. Vibrational motion and robust mode analyses for the amide I bands.
5. Test of different combinations of functional and basis sets with the most stable conformer of **1**.

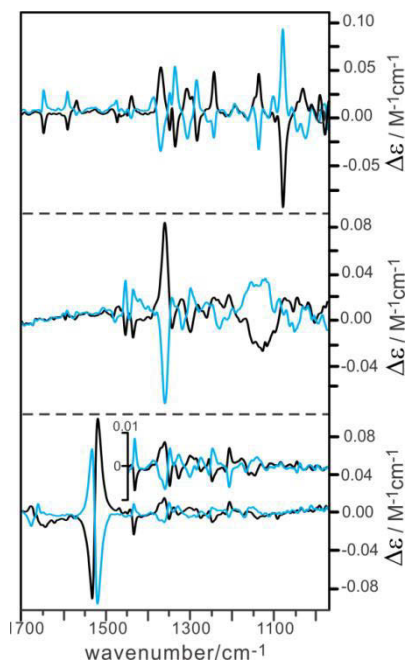


**Figure A1.** Experimental VCD spectra of the two enantiomers of the three compounds studied, i.e. **1**, **2**, and **3** from top to bottom.  $\text{CDCl}_3$  is the solvent used in all cases. The optimized pathlength is 0.1 mm for all compounds in the 1700-970  $\text{cm}^{-1}$  region, except for the enantiomeric pairs of (SS,**3**) where the experiment has been done with a shorter pathlength of 0.025 mm. The inserted spectra were recorded with 0.1 mm pathlength.

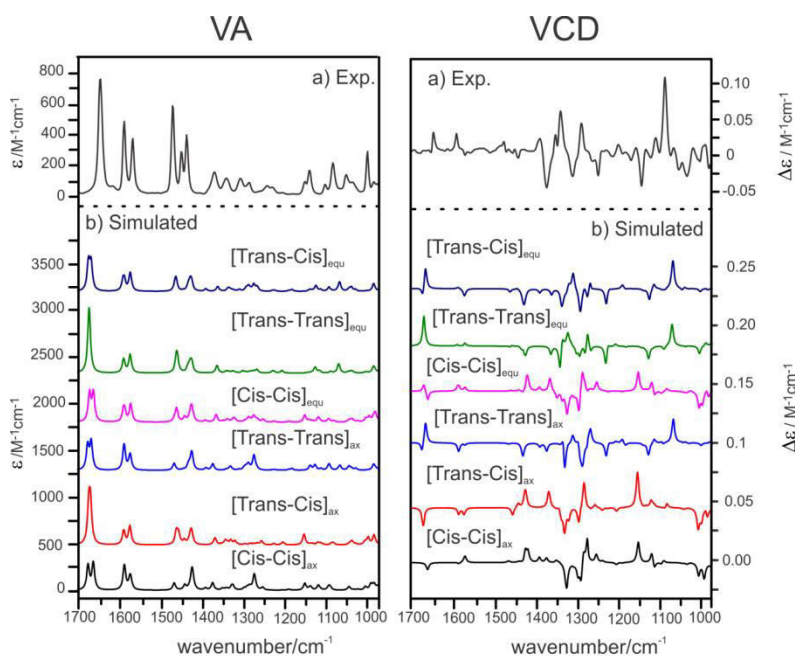


**Figure A2.** Comparison of the experimental VA and VCD spectra with the corresponding spectra of the six most stable conformers of (SS, **1**) at the PCM/B3PW91/cc-pVTZ level.

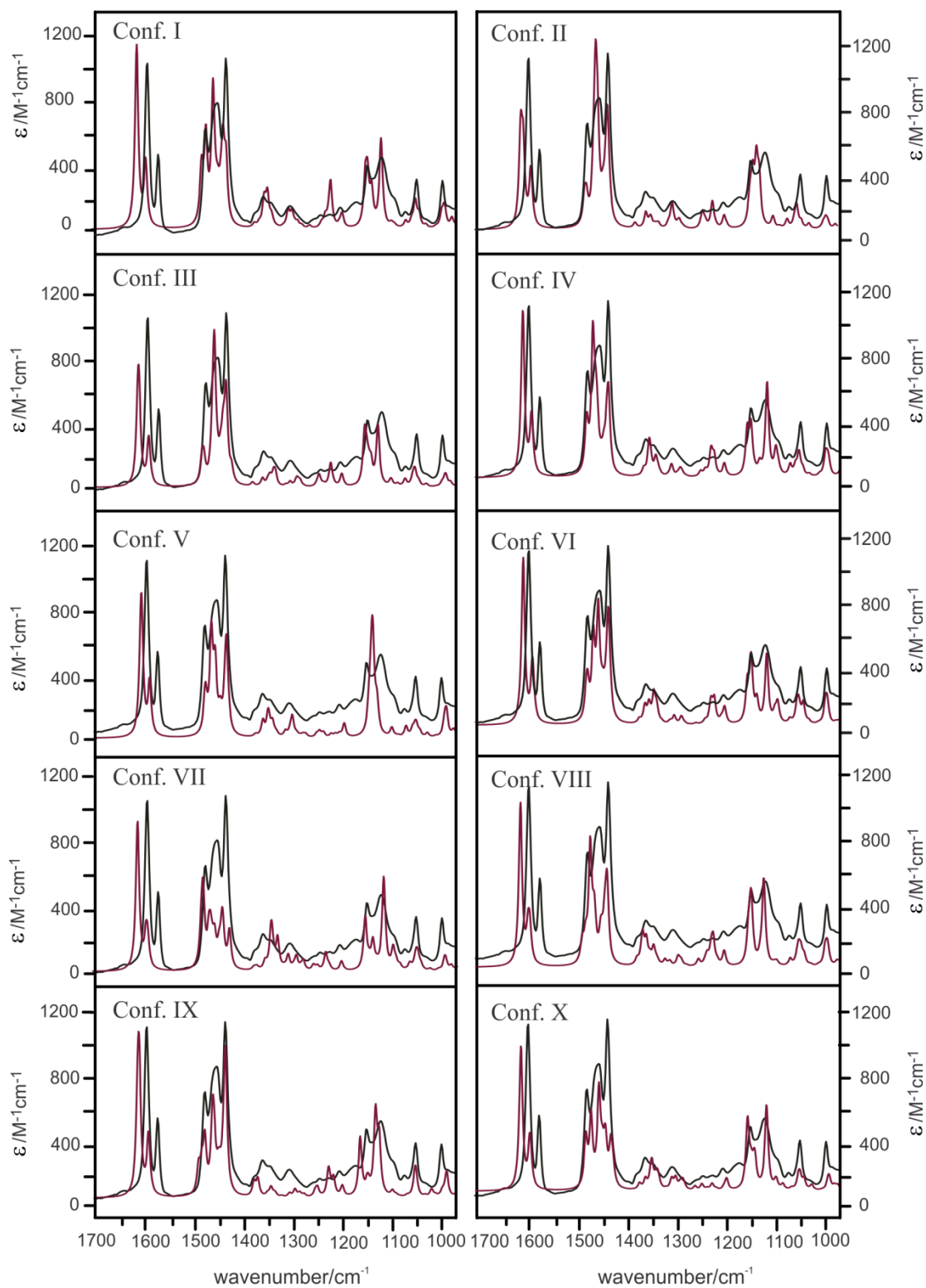


**Figure A3.** Comparison of experimental VA spectrum with the corresponding spectra of the ten most stable conformers of (SS, **2**) at the PCM/B3PW91/cc-pVTZ level.

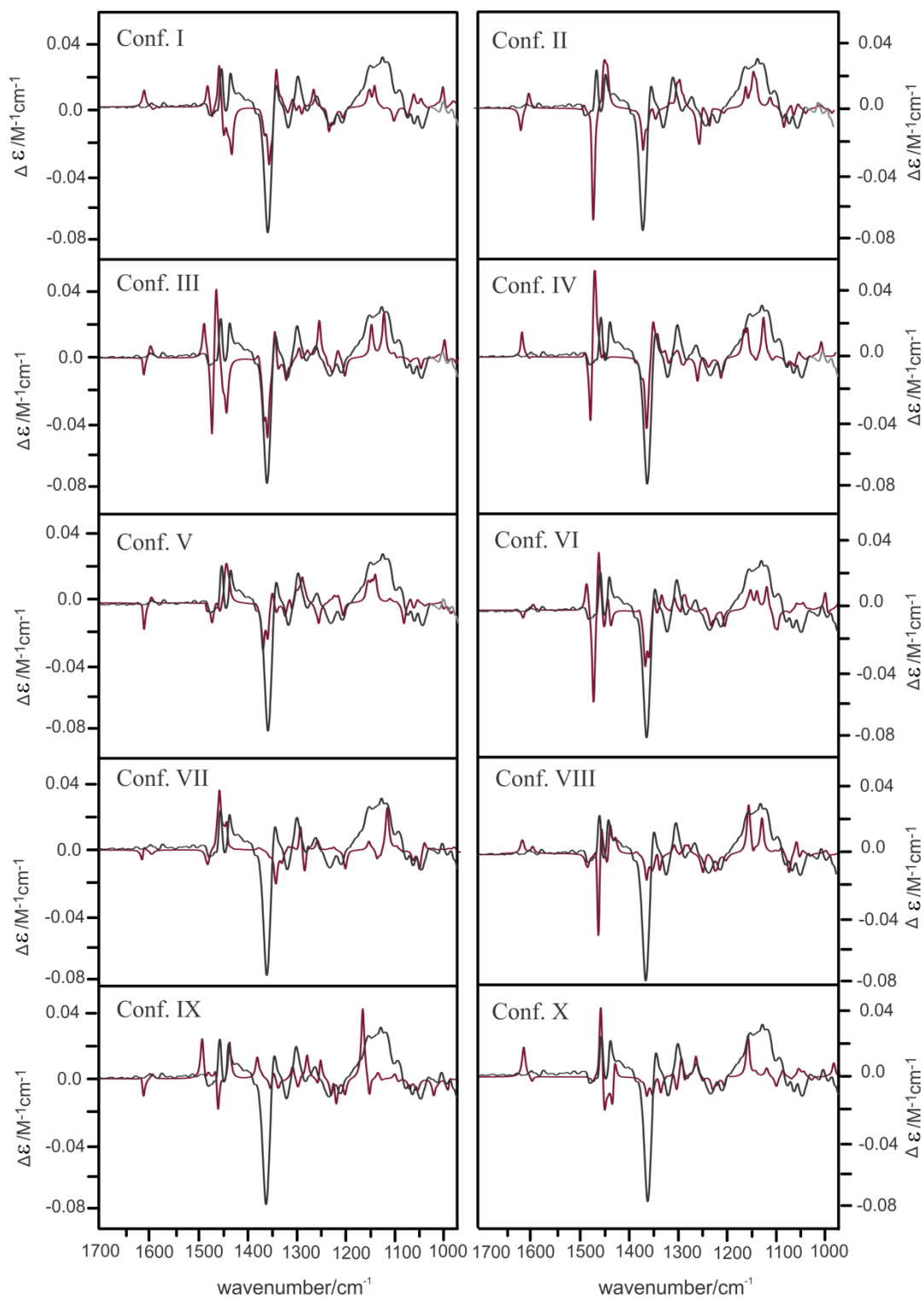


**Figure A4.** Comparison of the experimental VCD spectrum with the corresponding spectra of the ten most stable conformers of (SS, **2**) at the PCM/B3PW91/cc-pVTZ level.

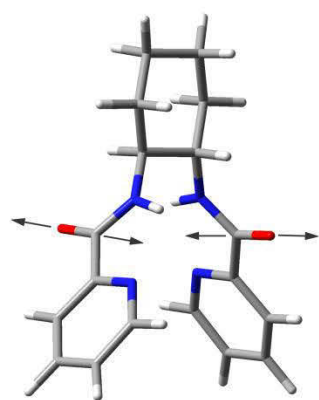


**Table A1.** Vibrational motions of the amide I bands and robust modes analyses

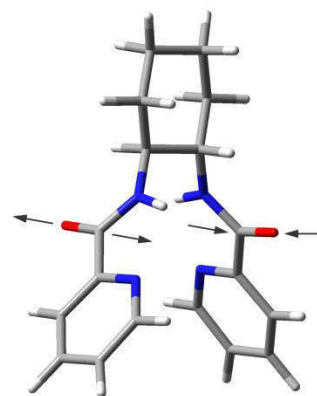
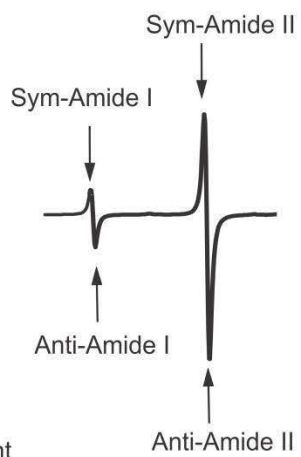
Modes	Freq (cm <sup>-1</sup> )	Rot. Str. (10 <sup>-44</sup> esu <sup>2</sup> cm <sup>2</sup> )	Dip. Str. (10 <sup>-40</sup> esu <sup>2</sup> cm <sup>2</sup> )	R/D  ratio (ppm)	Vib. Assignment
implicit solvation model					
99	1554.03	-1101.81	923.116	119.36	anti-sym. amide II
100	1559.14	923.392	1942.9	47.53	sym. amide II
105	1726.45	-393.537	1652.9	23.81	anti-sym. amide I
106	1729.98	350.6401	63.1195	555.52	sym. amide I
explicit solvation model					
127	1560.38	-968.516	665.484	145.54	anti-sym. amide II
128	1566.87	855.809	1360.19	62.92	sym. amide II
133	1707.54	358.678	44.1198	812.96	sym. amide I
134	1709.66	-468.969	1610.69	29.12	anti-sym. amide I

The concept of robust modes was introduced by Nicu<sup>1</sup> as a mean to judge if a calculated VCD sign is reliable or not. Rotational strength  $R$  is defined as  $R = |\text{EDTM}| * |\text{MDTM}| * \cos \theta$  where  $\theta$  is the angle between electronic (EDTM) and magnetic dipole moment (MDTM). Empirically,  $\theta$  in the range of 60° to 120° are said to be non-robust, while  $\theta$  outside of this range indicates a robust mode. Alternatively, one may also use  $\rho_{\text{Góbi}} = R / D * 100$  introduced by Góbi and Magyarfalvi<sup>1</sup> where a “soft” minimum value of  $\rho_{\text{Góbi}} = 10$  ppm was suggested for a mode to be robust. Both concepts are under much discussion in the VCD community. For further information about this concept, readers are referred to the original papers (<sup>1</sup>Ref. 24 in the main text).

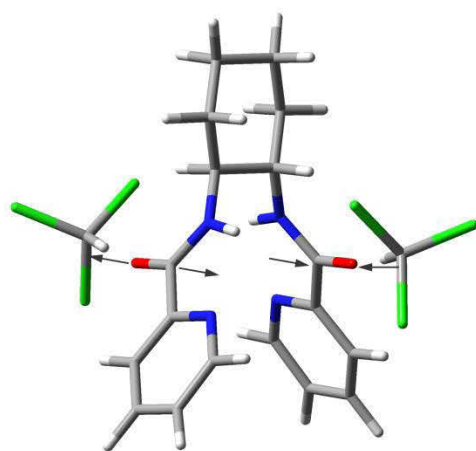
Motions associated with the symmetric and antisymmetric amide I modes are shown below. Their frequency sequences and the associated signs of the bisignate VCD couplets of **3** and the complex of **3** with two CDCl<sub>3</sub> molecules are also provided.



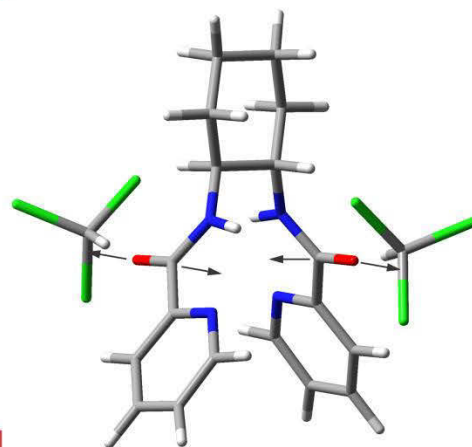
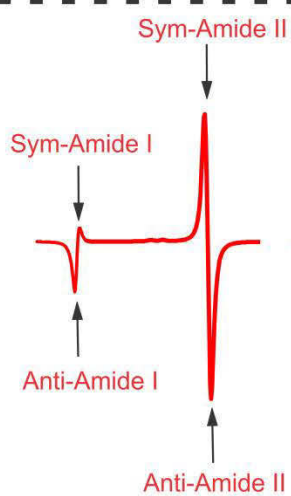
Sym-Amide I vector displacement



Anti-Amide I vector displacement



Anti-Amide I vector displacement



Sym-Amide I vector displacement

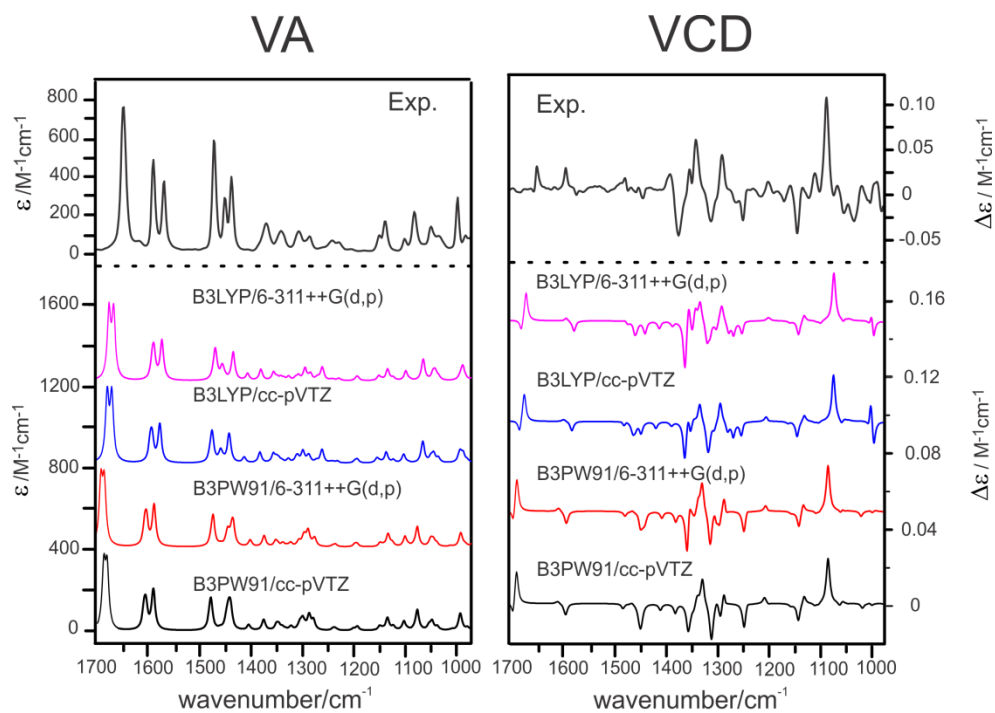


**Figure A5.** Comparison of the experimental VA and VCD spectra with the corresponding spectra of the [Trans-Cis]<sub>equ</sub> conformer of (SS, **1**) calculated with several different combinations of functional and basis sets. Implicit solvation model was applied using PCM of CDCl<sub>3</sub> as solvent.

## Supporting Information

### **Vibrational circular dichroism spectroscopy of two chiral binaphthyl diphosphine ligands and their palladium complexes in solution**

Zahra Dezhahang, Christian Merten, Mohammad Reza Poopari, Yunjie Xu



**B**

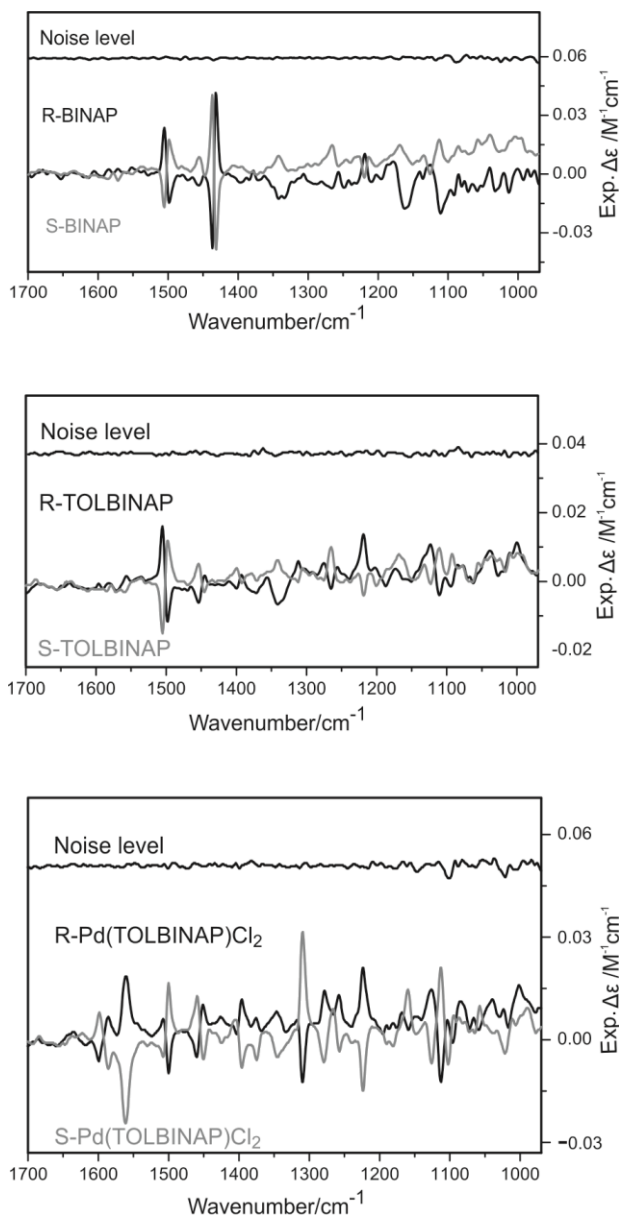


**Figure B1.** The experimental VCD spectra of both R and S enantiomers BINAP, TOLBINAP and Pd(TOLBINAP)Cl<sub>2</sub> in CDCl<sub>3</sub> solution and their related noise levels. In all the VCD spectra shown, the corresponding CDCl<sub>3</sub> spectrum obtained under identical experimental conditions was subtracted off. As one can see, good mirror images have been obtained for all the VCD spectral features measured except a few broad features at the very low wavenumber region. This is likely due to the strong absorption by the solvent starting at about 970 cm<sup>-1</sup>.

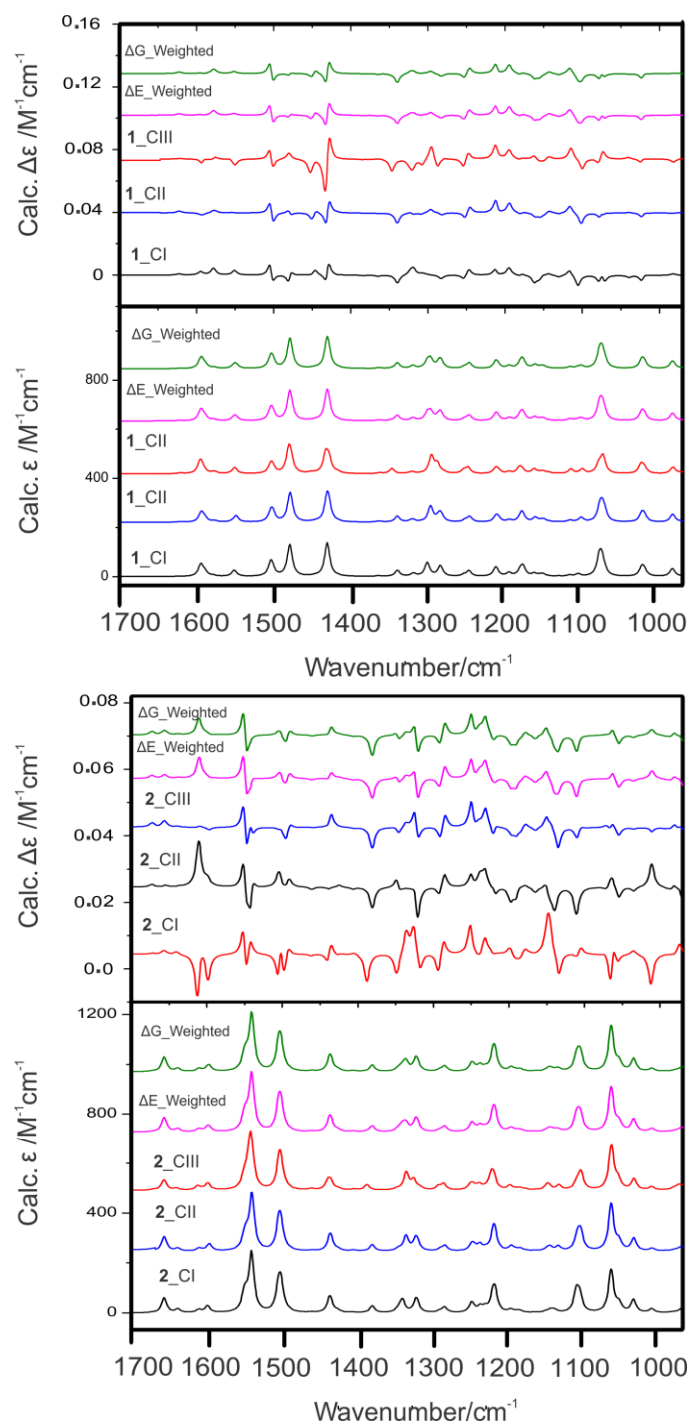


**Figure B2.** The calculated gas phase VA and VCD spectra of the three conformers of BINAP (top) and of the three conformers of TOLBINAP (bottom) and their corresponding population weighted spectra based on the relative energies and the relative free energies at the B3LYP/6-31G(d,p) level.

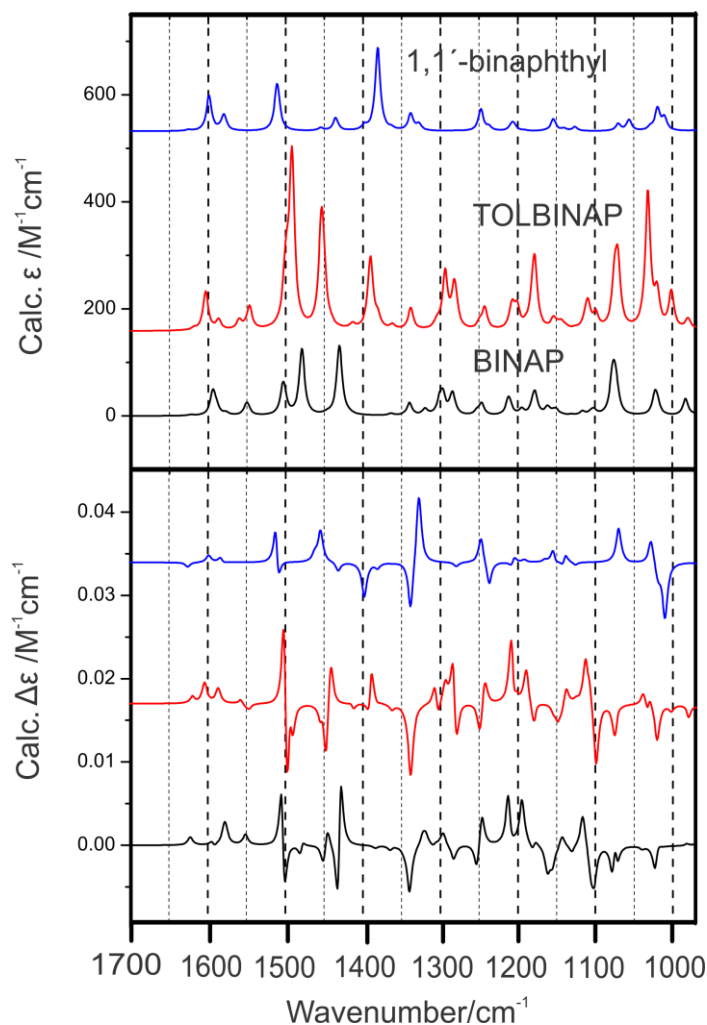


**Figure B3.** Comparison of the calculated gas phased VA and VCD spectra of 1,1'-binaphthyl, BINAP, and TOLBINAP at B3LYP/6-31G(d,p) level. The VA intensity of 1,1'-binaphthyl was amplified by a factor of two for easy comparison. The intense band in the 1430-1460  $\text{cm}^{-1}$  region in BINAP and TOLBINAP corresponds to the C-C stretching and C-H bending vibrational modes of four phenyl rings bonded to phosphorous, which does not show up for 1,1'-binaphthyl. The bands at 1250  $\text{cm}^{-1}$  corresponds to the same vibrational modes in all three systems. The related bisignated VCD feature flip going from 1,1'-binaphthyl to BINAP and TOLBINAP. The intense bands at  $\sim 1500 \text{ cm}^{-1}$  correspond to the C=C stretching vibrational motions of phenyl rings and naphthalene rings.

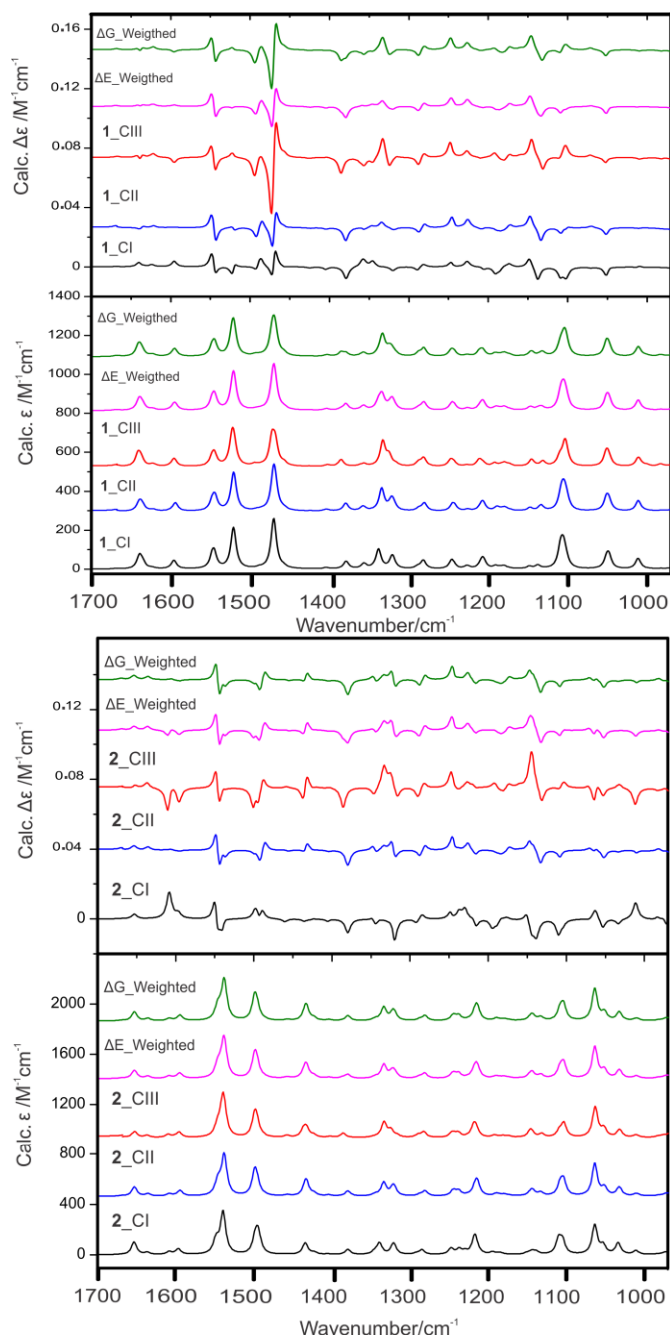


**Figure B4.** The calculated VA and VCD spectra with PCM of chloroform of the three conformers of BINAP (top) and of the three conformers of TOLBINAP (bottom) and their corresponding population weighted spectra based on the relative energies and the relative free energies at the B3LYP/6-31G(d,p) level.



## Supporting Information

**Structural properties and induced helicity of a chiral Pyrrol-2-yl Schiff base ligand and its five transition metal complexes in solution: combined vibrational and electronic CD, and DFT studies**

C

Zahra Dezhahang, Mohammad Reza Poopari, Joseph Cheramy, and Yunjie Xu

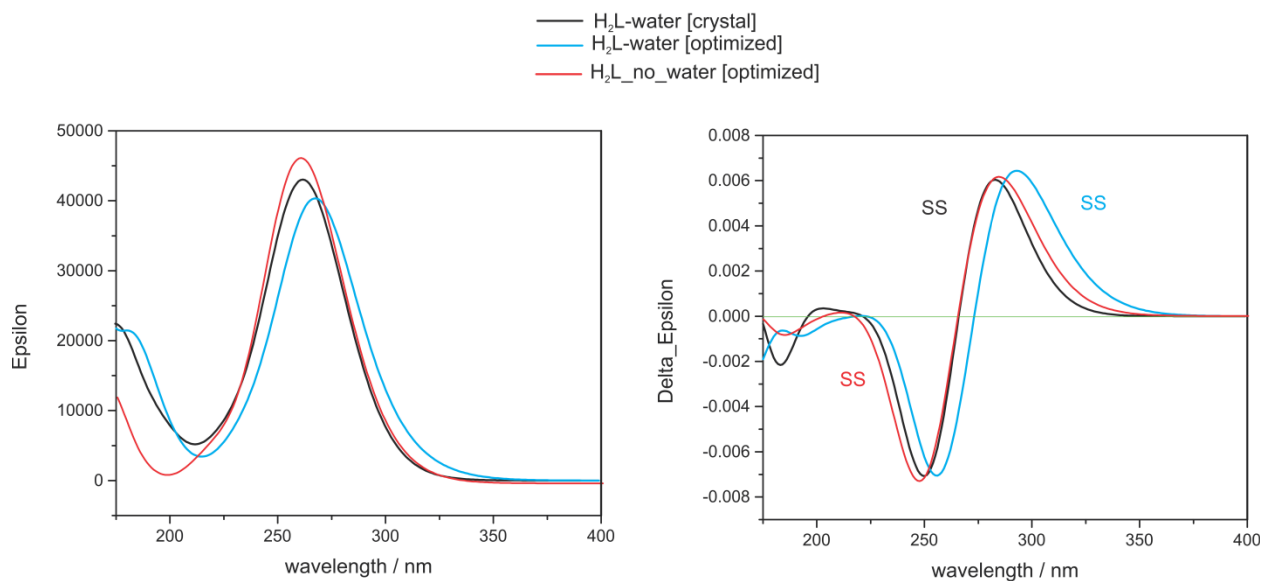


**Figure C1.** The simulated UV (left) and ECD (right) spectra of H<sub>2</sub>L ligand with water, both in crystal and optimized structures, and optimized ligand without water molecule considered.

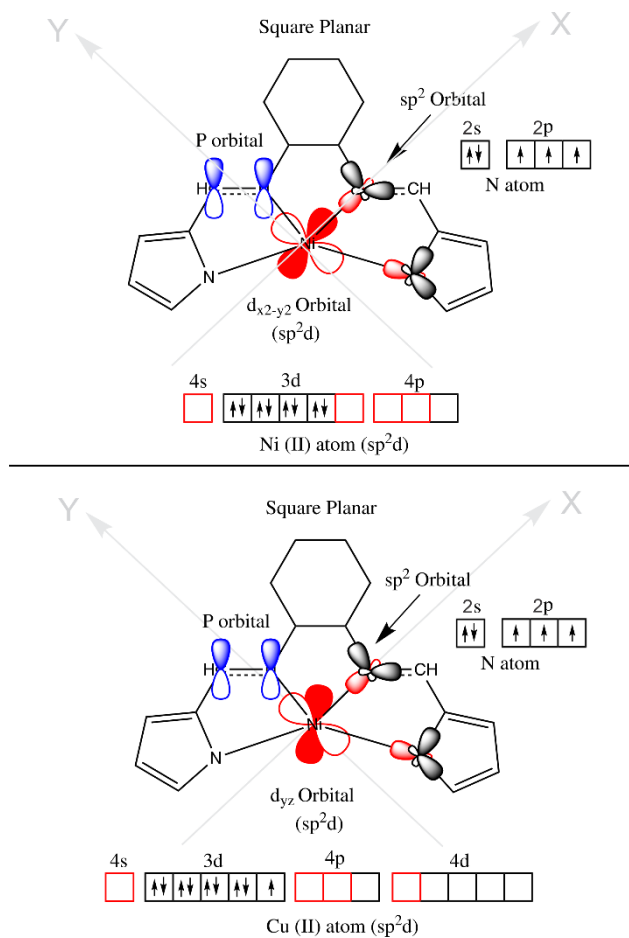


**Figure C2.** Electron configuration and orbital overlapping illustrations of Ni (II) and Cu (II) complexes. The hybridized orbital is used for the  $\sigma$  bond formation (shown in red) while the unhybridized  $p$ -orbital employed for the  $\pi$  bond formation (shown in blue).

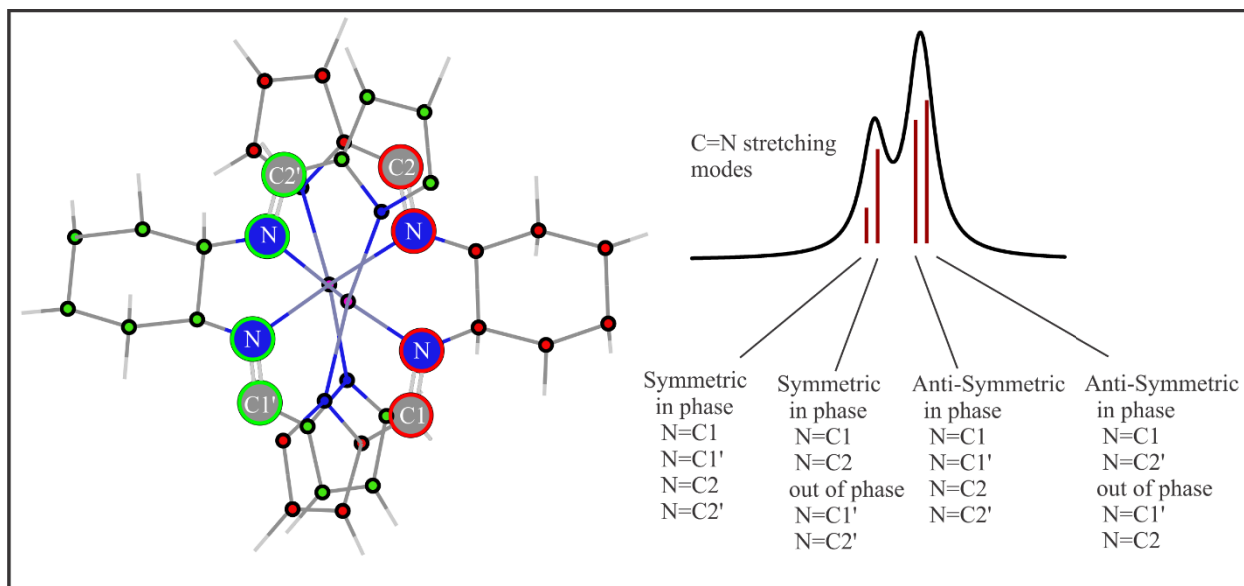


**Figure C3.** Illustration of symmetric and anti-symmetric  $\text{C}=\text{N}$  stretching vibrational modes for  $[\text{M}-\text{Zn}-(R,R)\text{-L}]_2$  complex.

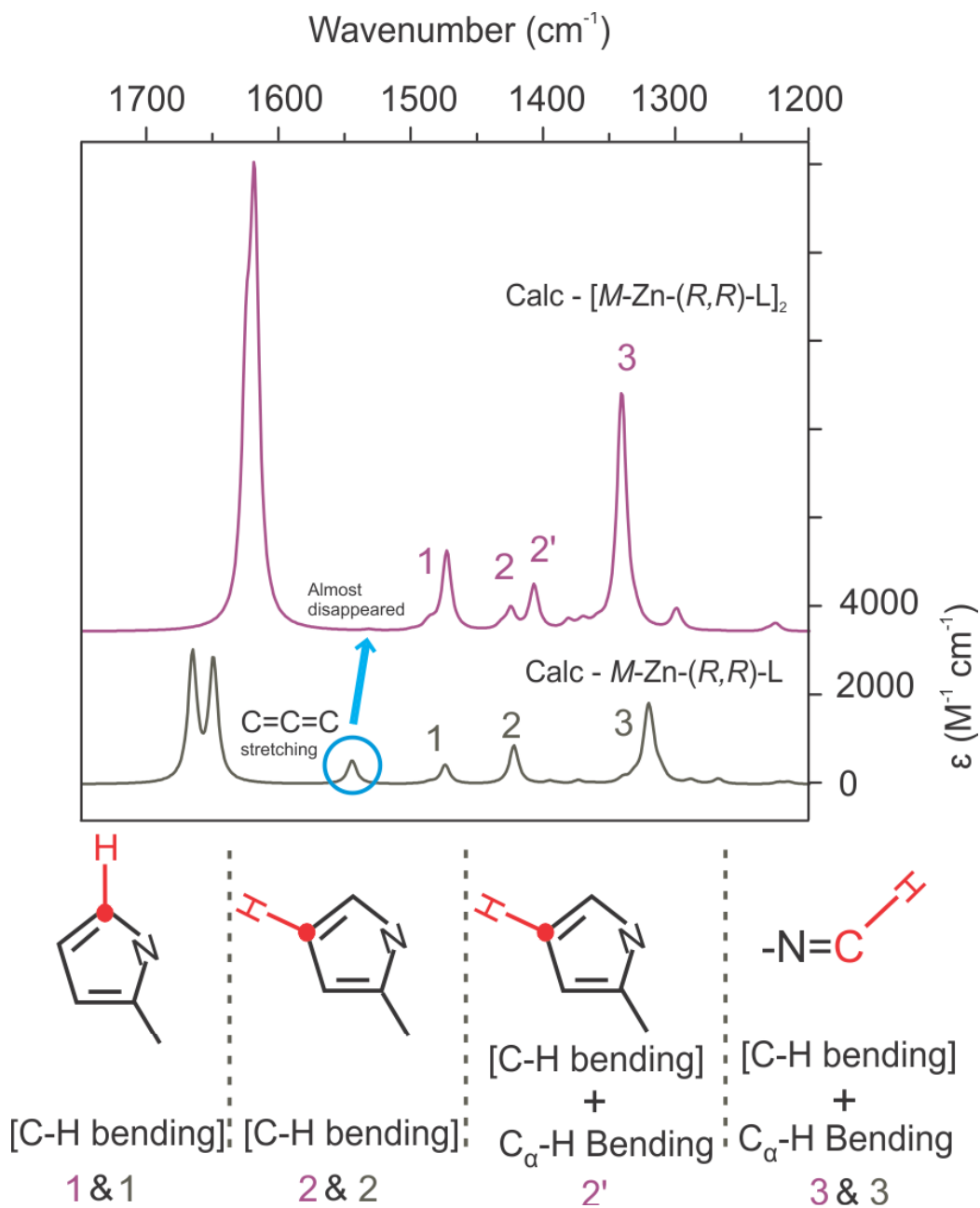


**Figure C4.** Comparison of the theoretical VA spectra of the *mono*- and *di*-nuclear Zn (II) complexes. The main peak assignments are also provided.

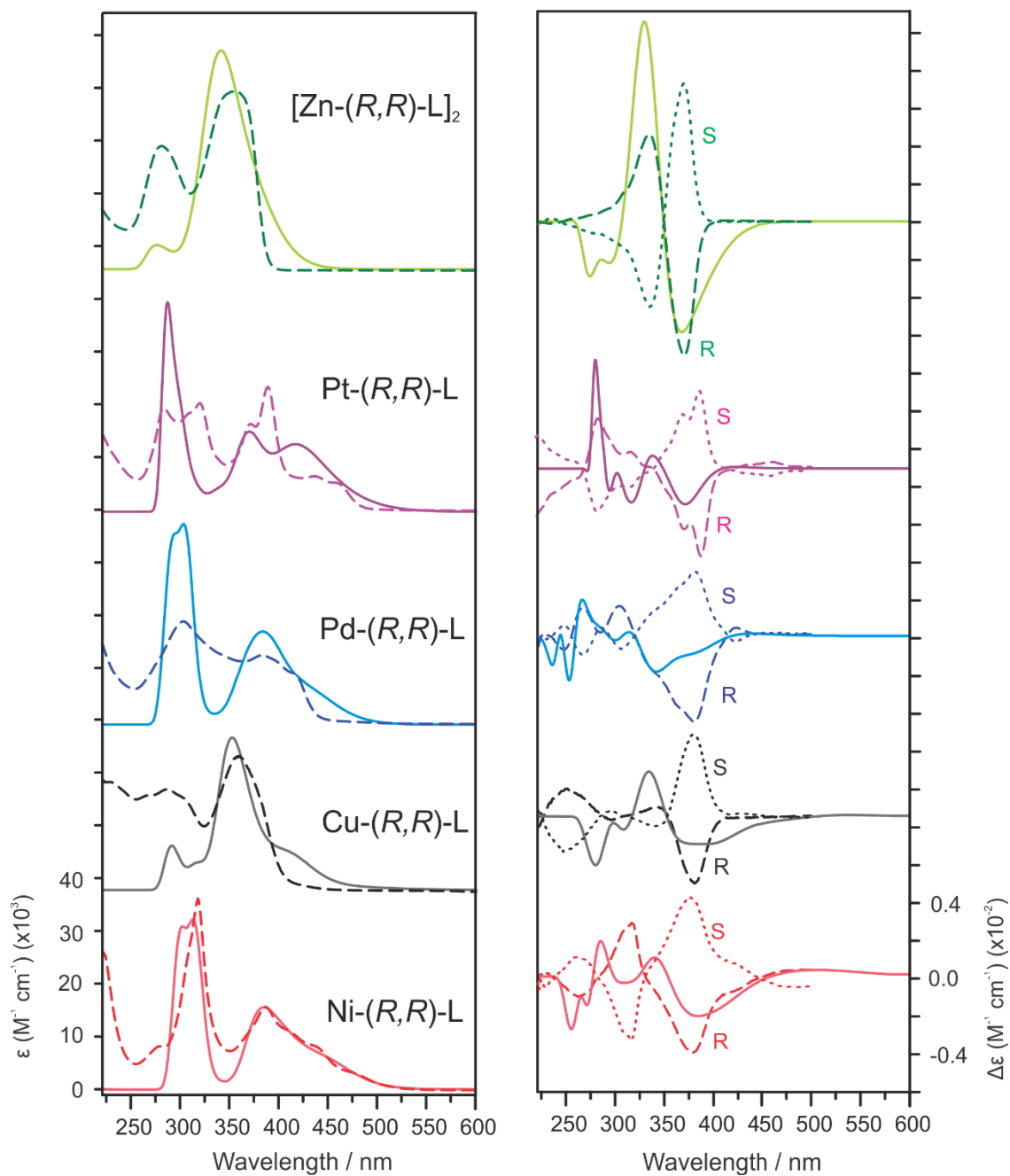


**Figure C5.** Comparison of the experimental and theoretical UV-Vis and ECD spectra of all five metal complexes. The experimental ones are shown in dashed and dotted lines whereas the theoretical spectra are highlighted with solid color.

## Supporting Information

### Diastereomeric preference of a triply axial chiral binaphthyl based molecule: a concentration dependent study by chiroptical spectroscopies

**D**

Zahra Dezhahang, Mohammad Reza Poopari, Eloy Florencio Hernández, Carlos Diaz, Yunjie Xu

#### Contents:

1. Details about the axial chirality at the  $-C=N$  bonds and the *intra* and *extra* labels.
2. Figure S2. Effect of sample concentration on the predominant species of AXF-155 molecule in ECD and VCD experiments.
3. Relative energies (in kcal/mol) of AXF-155 conformers.

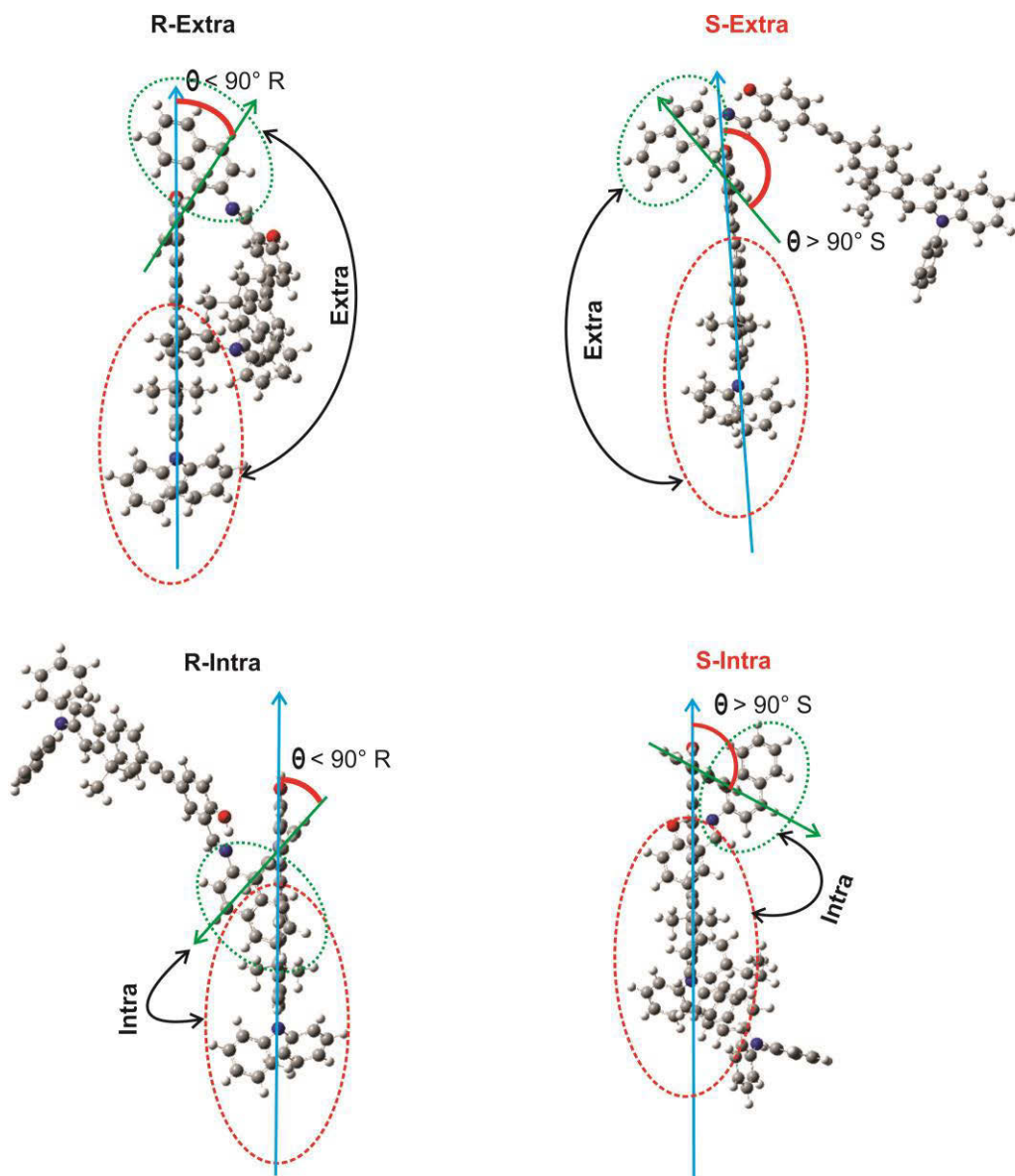


**Figure D1.** Illustrations of naming schemes used for R and S for axial chirality around the —C-N bond and for the *intra* and *extra* labels for the relative position of the bulky group (in red dashed circle) with respect to the binaphthyl half (in green circle) which is not directly connected to it. Place the binaphthyl ring under consideration closer to the viewer and view the chiral axis —C-N end-on. Align the blue arrow from the bulky group to the —O-H group up. Look at  $\theta$  at the right side of the blue line from the blue arrow to the green line. The green arrow is used to aim the identification of *intra* and *extra* labels.



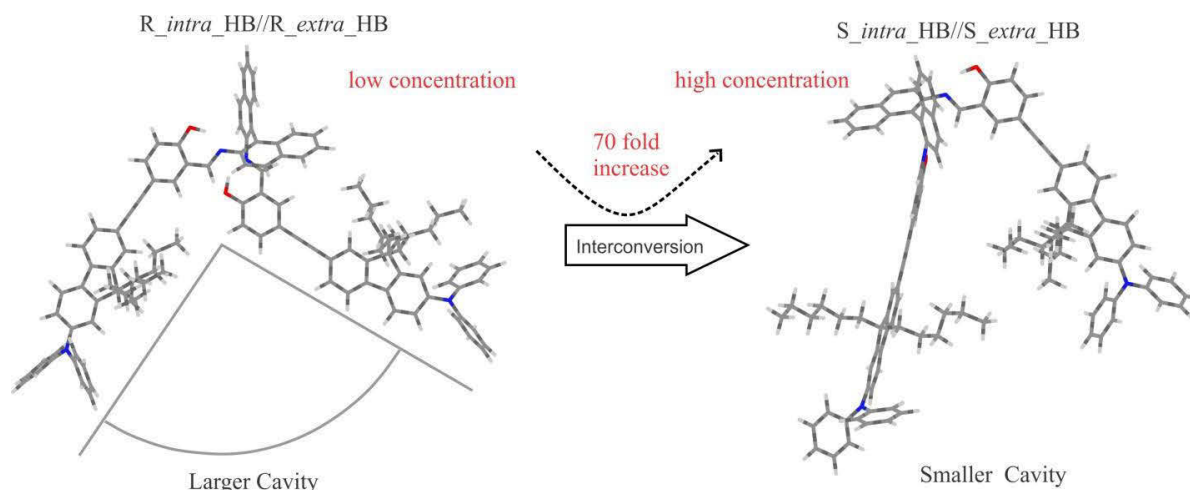


**Figure D2.** Illustration of the different cavity sizes provided by *S*-*intra*-HB//*S*-*extra*-HB (R-SS), and *R*-*intra*-HB//*R*-*extra*-HB for solvent molecules. This may influence their stabilities in highly concentrated and highly diluted solutions.

**Table D1.** Relative energies (in kcal/mol) of AXF-155 conformers using PCM for  $\text{CHCl}_3$

Conformers	6-31G(d)		cc-pVTZ//6-31G(d)	6-31G(d)-D <sup>a</sup>
	$\Delta E^b$	$\Delta G^b$	$\Delta E^b$	$\Delta E^b$
R_intra_HB//R_extra_HB	0.0 <sup>c</sup>	0.0 <sup>c</sup>	0.0 <sup>f</sup>	0.0 <sup>g</sup>
R_extra_HB//R-extra_HB	5.65	5.06	5.40	6.50
R_intra_HB//S_extra_HB	0.28	2.46	0.29	20.50
R_extra_HB//S_extra_HB	0.90	1.29	1.06	0.94
R_extra_HB//S_intra_HB	4.69	7.53	6.47	0.0 <sup>i</sup>
R_intra_HB//S_intra_HB	0.0 <sup>d</sup>	0.0 <sup>d</sup>	0.0 <sup>h</sup>	16.0
S_extra_HB//S_extra_HB	0.0 <sup>e</sup>	0.0 <sup>e</sup>	0.0 <sup>j</sup>	18.66
S_intra_HB//S_extra_HB	3.80	4.77	3.70	0.0 <sup>k</sup>
S_intra_HB//S_intra_HB	5.63	6.93	5.66	15.80

<sup>a</sup> Grimme's D3 dispersion-corrected DFT optimization.

<sup>b</sup>  $\Delta E$  (conformer) =  $E$  (conformer) –  $E$  (most stable one) and  $\Delta G$  values are similarly defined.

<sup>c</sup>  $E = -4699.383299$  H,  $G = -4699.555561$  H.

<sup>d</sup>  $E = -4699.378542$  H,  $G = -4699.553524$  H.

<sup>e</sup>  $E = -4699.381303$  H,  $G = -4699.556087$  H.

<sup>f</sup>  $E = -4702.855238$  H.

<sup>g</sup>  $E = -4701.566950$  H.

<sup>h</sup>  $E = -4702.851107$  H.

<sup>i</sup>  $E = -4701.565878$  H.

<sup>j</sup>  $E = -4702.85403$  H.

<sup>k</sup>  $E = -4701.55732$  H.



**E**

**Contributed journal papers**

# Conformational Distributions of *N*-Acetyl-L-cysteine in Aqueous Solutions: A Combined Implicit and Explicit Solvation Treatment of VA and VCD Spectra\*\*

Mohammad Reza Poopari,<sup>[a]</sup> Zahra Dezhahang,<sup>[a]</sup> Guochun Yang,<sup>[a, b]</sup> and Yunjie Xu<sup>\*[a]</sup>

The conformational distributions of *N*-acetyl-L-cysteine (NALC) in aqueous solutions at several representative pH values are investigated using vibrational absorption (VA), UV/Vis, and vibrational circular dichroism (VCD) spectroscopy, together with DFT and molecular dynamics (MD) simulations. The experimental VA and UV/Vis spectra of NALC in water are obtained under strongly acid, neutral, and strongly basic conditions, as well as the VCD spectrum at pH 7 in D<sub>2</sub>O. Extensive searches are carried out to locate the most stable conformers of the protonated, neutral, deprotonated, and doubly deprotonated NALC species at the B3LYP/6-311++G(d,p) level. The inclusion of the polarizable continuum model (PCM) modifies the geometries and the relative stabilities of the conformers noticeably. The simulated PCM VA spectra show significantly better agreement with the experimental data than the gas-phase ones,

thus allowing assignment of the conformational distributions and dominant species under each experimental condition. To further properly account for the discrepancies noted between the experimental and simulated VCD spectra, PCM and the explicit solvent model are utilized. MD simulations are used to aid the modelling of the NALC-(water)<sub>*N*</sub> clusters. The geometry optimization, harmonic frequency calculations, and VA and VCD intensities are computed for the NALC-(water)<sub>3,4</sub> clusters at the B3LYP/6-311++G(d,p) level without and with the PCM. The inclusion of both explicit and implicit solvation models at the same time provides a decisively better agreement between theory and experiment and therefore conclusive information about the conformational distributions of NALC in water and hydrogen-bonding interactions between NALC and water molecules.

## 1. Introduction

*N*-Acetyl-L-cysteine (NALC; IUPAC: (2*R*)-2-acetamido-3-sulfanylpropanoic acid) is the acetylated form of L-cysteine. In recent years, there has been a significant interest in this molecule because this thio-containing amino acid is a strong antioxidant and is capable of detoxifying free radicals that are implicated in cancer and other diseases.<sup>[1,2]</sup> This pharmaceutical drug is sold as a dietary supplement for its liver protection effects and its ability to boost the glutathione (gamma-L-glutamyl-L-cysteinylglycine) level in cells.<sup>[3]</sup> It is also interesting to note that in recent years, researchers have found that an excessive amount of NALC in the body could potentially cause damage to the heart and lungs.<sup>[4]</sup>

To gain a fundamental understanding of these complex biological processes, detailed knowledge of the conformations of NALC in aqueous solutions under different pH values is essential, since different conformations adopted by NALC in water may influence the NALC-induced structural changes in DNA and consequently the functionality of DNA. Indeed, much attention has been paid to the properties of NALC from both experimental and theoretical sides. This is in part due to the fact that the acetyl side chain can provide other interesting properties related to the C–N amide bond, commonly encountered in peptides. As a result, NALC exhibits a conformational topology that is frequently found in biological systems.<sup>[5,6]</sup> At the same time, the system is small enough to be amenable for high-level ab initio calculations.<sup>[7–10]</sup> Gautier and Bürgi studied the vibrational circular dichroism (VCD) activities of NALC mol-

ecules adsorbed on surfaces of gold nanoparticles.<sup>[11]</sup> More recently, Maes and his colleagues investigated the conformational landscape of NALC by matrix isolation Fourier transform (FT) infrared (IR) spectroscopy in combination with ab initio calculations, in which an extensive search for the neutral NALC conformations was performed.<sup>[12]</sup>

VCD spectroscopy measures the differential absorption of the left versus right circularly polarized IR radiation by a chiral molecule. It has been used extensively to probe absolute configurations and conformations of chiral organic and inorganic molecules in solution.<sup>[13,14]</sup> The magnitude and sign of a VCD feature depend on its rotational strength, that is, the imaginary part of the direct product of the electric transition dipole moment and the associated magnetic dipole moment. For this reason, VCD spectra are highly sensitive to subtle conforma-

[a] M. R. Poopari, Z. Dezhahang, Prof. Dr. G. Yang, Prof. Dr. Y. Xu  
Department of Chemistry  
University of Alberta  
Edmonton, Alberta, T6G 2G2 (Canada)  
E-mail: yunjie.xu@ualberta.ca

[b] Prof. Dr. G. Yang  
Department of Chemistry  
Northeast Normal University  
Changchun 130024, Jilin (P.R. China)

[\*\*] VA = Vibrational Absorption, VCD = Vibrational Circular Dichroism

Supporting information for this article is available on the WWW under <http://dx.doi.org/10.1002/cphc.201200152>.

tional differences and changes, for example, those induced by solvent–solute hydrogen-bonding interactions.<sup>[15–18]</sup> VCD spectroscopy can often discriminate more precisely among conformers than vibrational absorption (VA) spectroscopy, which is also structurally sensitive.

Herein, the detailed conformational distributions of the dominant species of NALC under different pH conditions in aqueous solutions have been investigated by using VA and VCD spectroscopy, together with *ab initio* and molecular dynamics (MD) simulations. In addition, UV/Vis studies have also been used to provide further evidence about the dominant species of NALC under specific conditions. Furthermore, both the implicit polarizable continuum model (PCM) and the explicit solvation model based on the solute–solvent intermolecular hydrogen-bonding interactions have been considered to account for the solvation effects. These models were applied separately and jointly to evaluate their effectiveness. Important conclusions about the conformations of NALC and about NALC–water hydrogen-bonding interactions in aqueous solution have been obtained.

## 2. Results and Discussions

In this section, the VA and UV/Vis spectral evidence for the dominant species under different pH conditions is discussed, followed by the systematic DFT searches for the most stable conformers of all the important species in the gas phase and in solution with the PCM. Subsequently, the potential energy distribution (PED) analyses<sup>[19]</sup> of normal VA modes are described, followed by comparisons of the simulated PCM VA spectra with the experimental data under highly acidic and basic conditions. Finally, the combined PCM and explicit solvent model treatment of the VA and VCD spectra of deprotonated NALC is described, followed by a comparison with the VA and VCD experimental data under pH 7 conditions.

### 2.1. Experimental VA and UV/Vis Spectra of NALC under Different pH Conditions

The measured VA spectra of dissolved NALC in D<sub>2</sub>O at different pH values ranging from 0.65 to 13.0 are summarized in Figure 1. There are significant differences in the VA spectra as the pH value increases. This can be attributed to the presence of different NALC species. For example, dissolving NALC in D<sub>2</sub>O without adding any strong acid or base resulted in a pH value of  $\approx 2.5$ . The dissociation constant of the carboxylic acid moiety in NALC is 3.24.<sup>[20]</sup> Based on the simple relationship,  $\text{pH} = \text{p}K_{\text{a}} + \log \{[A^-]/[\text{HA}]\}$ , one can estimate that 82% of NALC is in the COOH form whereas 18% is in the COO<sup>-</sup> form at pH 2.5. To uncover what species there are at different pH values, we examined the VA carbonyl stretching spectral features in the 1500–1800 cm<sup>-1</sup> region. The carboxylic (C=O) stretch in COOH and the acetyl (C=O) stretch are denoted as  $\nu(\text{CO})_{\text{ca}}$  and  $\nu(\text{CO})_{\text{acr}}$ , respectively. At the two lowest pH values, the two well-resolved peaks at 1718 and 1630 cm<sup>-1</sup> can be unambiguously assigned to  $\nu(\text{CO})_{\text{ca}}$  and  $\nu(\text{CO})_{\text{acr}}$ , the amide I mode, respectively. As the pH increases, the intensity of the

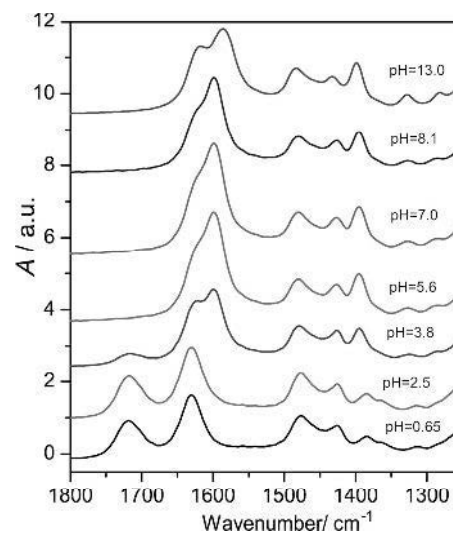


**Figure 1.** Experimental VA spectra of NALC in D<sub>2</sub>O at a series of pH values ranging from 0.65 to 13.0.

carboxylic stretching band decreases and eventually disappears completely when the pH reaches 5.6. In parallel, a new peak at 1599 cm<sup>-1</sup>, which corresponds to the anti-symmetric stretching mode of COO<sup>-</sup>, that is,  $\nu_{\text{as}}(\text{COO}^-)$ , becomes significant at pH 3.8. Related to this, another new band feature at 1395 cm<sup>-1</sup>, which can be tentatively assigned to the COO<sup>-</sup> symmetric stretching mode, that is,  $\nu_{\text{s}}(\text{COO}^-)$ , also becomes obvious at pH 3.8. The  $\nu_{\text{s}}(\text{COO}^-)$  band remains essentially at the same frequency position until the pH reaches  $\approx 13$ . Two strong peaks at 1622 and 1599 cm<sup>-1</sup>, observed at pH 7, correspond to the  $\nu(\text{CO})_{\text{ac}}$  and  $\nu_{\text{as}}(\text{COO}^-)$  mode, respectively. Experimentally, the position of the amide I mode was red-shifted by about 8 cm<sup>-1</sup> from 1630 to 1622 cm<sup>-1</sup> as the pH increased from 0.65 to 7.0, thus indicating that the dominant carrier of the amide I mode has changed. A further shift of about 5 cm<sup>-1</sup> to the red to 1617 cm<sup>-1</sup> was detected for this band when the pH reached 13, again indicating another change in the dominant carrier of the amide I mode.

The detailed VA assignments of the peaks in the lower-wavenumber region are less obvious. These bands are related to the bending, scissoring, wagging, and rocking modes of the CH, CH<sub>2</sub>, CH<sub>3</sub>, NH, OH, and SH groups, as well as the skeleton modes. It is difficult to anticipate how their VA frequencies would alter due to the subtle changes in the charged state, the conformational flexibility, and the water solvent. Their assignments will be discussed in the next section in conjunction with the simulated VA spectra of the most stable conformers.

From the above observation, one can conclude straightforwardly that the carboxylic group exists mostly as COOH at pH values up to  $\approx 2.5$ , whereas the COO<sup>-</sup> form becomes dominant at pH above  $\approx 4$ . These two forms coexist in the pH range of 2.5–4. In what form, that is, the protonated (Pro-), neutral (Neu-), deprotonated (Dep-) or doubly deprotonated (D-Dep-) form, the other part of NALC exists at different pH values is not obvious without the aid of the corresponding spectral simulations. For example, does NALC exist in the protonated form

at pH 0.65? The related questions are whether NALC exist in the zwitterionic form at  $\text{pH} \approx 7$  and if a proton would prefer to attach to the N site rather than the O atom of the acetyl group or the S site in NALC. If one considers that the lone pair of the nitrogen atom in NALC can participate in a resonance structure with the adjacent acetyl C=O group, just as in a regular C–N peptide bond, there is a partial positive charge on the N atom. This makes the N atom a highly unlikely site to accept a proton. It is interesting to point out that in recent years, there have been heated debates about the validity and the accuracy of the description provided by the amide resonance theory.<sup>[21–23]</sup> Addario et al. proposed that in such cases, the most likely protonated site is the oxygen atom of the acetyl group. Such a protonated structure can be stabilized by the formation of a hydrogen-bonded ring where the proton connects the two carbonyl O atoms.<sup>[24]</sup> Empirically, the  $\text{pK}_a$  value of an O-protonated amide is roughly close to zero, while that of the N-protonated amide is about 7.<sup>[25]</sup> If NALC follows this trend closely, one may expect about 20% of the Pro-NALC species at a pH of 0.65, although no specific experimental  $\text{pK}_a$  value is available for the Pro-NALC to our knowledge. These points will be further discussed when comparing the experimental and simulated VA spectral features of different species in the next section.

As the pH reaches 13, another new species appears, which we hypothesized to be D-Dep-NALC with  $\text{COO}^-$  and  $\text{S}^-$ . Since the  $\text{pK}_a$  for the thiol group was reported to be 9.52,<sup>[26]</sup> one can expect that the D-Dep-NALC species becomes increasingly more important than the singly deprotonated species as the pH becomes much higher than 9.52. To obtain the direct spectral signatures related to this change, the UV/Vis spectra of NALC (Figure S1, Supporting Information) were measured under several different pH conditions from strongly acidic to strongly basic. At  $\text{pH} \approx 9.4$ , a new strong shoulder bump in the 220–250 nm region emerges and becomes more prominent as the pH increases. This UV/Vis band had been empirically correlated to a transition of the doubly deprotonated species containing  $\text{S}^-$ .<sup>[27]</sup> We calculated the UV/Vis spectra of the singly deprotonated species containing just  $\text{COO}^-$  and doubly deprotonated species with both  $\text{COO}^-$  and  $\text{S}^-$  (Figure S1, Supporting Information). Indeed, the simulated UV/Vis spectra exhibit the expected difference between the deprotonated and the doubly deprotonated species, consistent with the hypothesis proposed before, thus confirming the dominant existence of  $\text{S}^-$  at pH 13.

Using the semi-empirical program SPARC, which provides  $\text{pK}_a$  estimation for amino acids and peptides,<sup>[28]</sup> a general description of the various species existing at a certain pH value can be predicted. For example, at the highly acidic pH of 0.65, the only species in solution is the neutral form of NALC. As the pH increases to 2.5, this changes to 88% Neu-NALC and 12% Dep-NALC, while the percentage of Dep-NALC increases to 100% as the pH reaches 5.6. At pH values higher than 8.1, the doubly deprotonated form with both  $\text{COO}^-$  and  $\text{S}^-$ , that is, D-Dep-NALC, starts to appear and becomes the dominant species with a 100% population at pH 13.0. The general trend predicted by this program is consistent with the conclusion drawn

from the VA and UV/Vis spectral analyses described above, although the detailed conformational distributions have yet to be derived based on the theoretical spectral simulations to be discussed below. For conciseness, three representative pH conditions of 0.65, 7.0 and 13.0 were selected for discussion, when only a single dominant species is expected in each solution.

## 2.2. Most Stable Conformers of Pro-, Neu-, Dep- and D-Dep-NALC in the Gas Phase and in $\text{D}_2\text{O}$ with the PCM

### 2.2.1. Neu-NALC

The Neu-NALC monomer has seven internal rotational degrees of freedom,<sup>[12]</sup> which makes it a highly flexible molecule. This results in a large number of possible conformations and poses a significant challenge in locating true global minima, that is, the most stable conformers. Conformational searches for Neu-NALC have been reported in a number of previous studies.<sup>[12,29]</sup> We carried out a preliminary systematic search by rotating all these internal rotational degrees of freedom involving heavy atoms by either 60 or 180° sequentially. While the work was in progress, an extensive search for Neu-NALC based on a similar approach was reported.<sup>[12]</sup> The most stable conformers identified are similar to those reported in ref. [12], although a larger basis set has been used in the current study. The geometries of the five most stable ones in the gas phase are depicted in Figure S2 in the Supporting Information, together with their percentage Boltzmann factors at room temperature based on the relative Gibbs free energies. For a highly flexible molecule such as NALC,  $\text{D}_2\text{O}$  solvent may influence the relative stability of its conformers substantially. To account for the water solvent, geometry searches and optimizations were also carried out for Neu-NALC in the PCM of water. The geometries of the five most stable conformers in water with a total Boltzmann percentage population close to 100% are depicted in Figure 2.

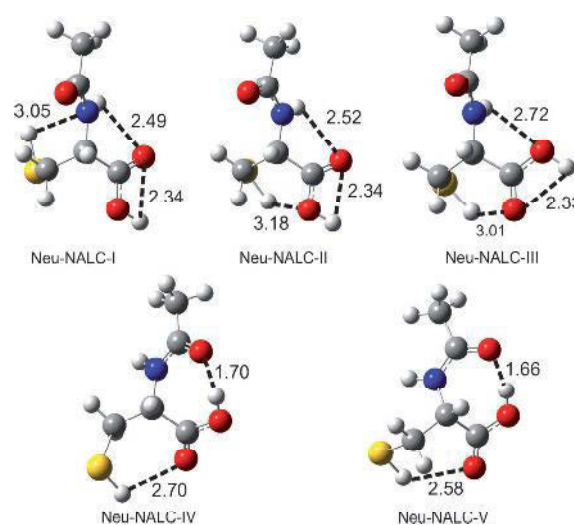


**Figure 2.** Optimized geometries of the five lowest-energy conformers of neutral NALC at the B3LYP/6-311 + +G(d,p) level with the PCM of  $\text{D}_2\text{O}$ . The intramolecular hydrogen-bond lengths and some important van der Waals bond lengths (in Å) are indicated.

The corresponding gas-phase and PCM conformers show very similar features, although the geometries seem to be more compact in the gas phase with generally shorter intramolecular hydrogen-bond lengths than those in the PCM. The three most stable conformers obtained with the PCM all adopt the *cis* configuration of the COOH group, with the most important intramolecular (CO)H...O=C and NH...O=C(OH) bond lengths in the range of 2.3 to  $\approx 2.7$  Å, noticeably longer than the hydrogen-bond length in the gas-phase Neu-NALC structures. The next two most stable conformers adopt the *trans* configuration of the COOH group, with the O and H atoms on opposite sides of the C–O bond, to facilitate the formation of an intramolecular hydrogen bond COH...( $\text{O}=\text{C}$ )<sub>ac</sub>. These most stable conformers all adopt the *trans* amide bond configuration, with the carbonyl O and H atom of amide on opposite sides of the C–N bond, reminiscent of the situation in the vast majority of polypeptides. The corresponding relative total energies  $\Delta E^\circ$  and the relative Gibbs free energies  $\Delta G^\circ$  in the PCM of water are provided in Table 1, together with their Boltzmann percentage population factors at room temperature.

Table 1. Relative total energies $\Delta E^\circ$ [kJ mol <sup>-1</sup> ] and relative Gibbs free energies $\Delta G^\circ$ [kJ mol <sup>-1</sup> ] of the most stable conformers of Neu-, Dep-, and D-Dep-NALC in D <sub>2</sub> O with the PCM solvation model at the B3LYP/6-311++G(d,p) level, and the Boltzmann percentage population factors at room temperature based on $\Delta E^\circ$ and $\Delta G^\circ$ .				
Conformer	$\Delta E^\circ$	$\Delta G^\circ$	pop %, $\Delta E^\circ$	pop %, $\Delta G^\circ$
Neu-NALC				
I	0.00	0.00	50.45	43.20
II	0.61	0.30	39.37	38.29
III	3.97	2.10	10.14	18.50
IV	18.84	23.10	0.03	0.004
V	23.28	27.18	0.004	0.0007
Dep-NALC				
I	0.00	0.00	47.33	43.53
II	0.82	1.35	33.90	25.20
III	3.37	2.17	12.10	18.11
IV	4.82	3.00	6.75	13.14
D-Dep-NALC				
I	0.00	0.00	59.31	69.82
II	0.93	2.07	40.69	30.18

### 2.2.2. Dep-NALC

Based on the discussion in Section 2.1, the main species under neutral pH is Dep-NALC with the COO<sup>-</sup> group. There are four dihedral angles in Dep-NALC which are responsible for the orientations of the heavy atoms (see Figure 3 with atom labeling). To search for the possible conformers of Dep-NALC, a two-dimensional energy map of NALC along the two most important dihedral angles,  $\tau_1$ , that is, dihedral angle S-C1-C2-N and  $\tau_2$ , that is, dihedral angle C1-C2-N-H, calculated at the B3LYP/6-31G(d) level has been generated and is depicted in Figure 3. There are two minima on the 2D energy map where ( $\tau_1, \tau_2$ ) takes on the values of (-9,70) and (230,70). It should be pointed out that the third dihedral angle  $\tau_3$ , which corresponds to the rotation around the amide bond, is typically restricted to values of 180 or 0° based on the amide resonance theory,

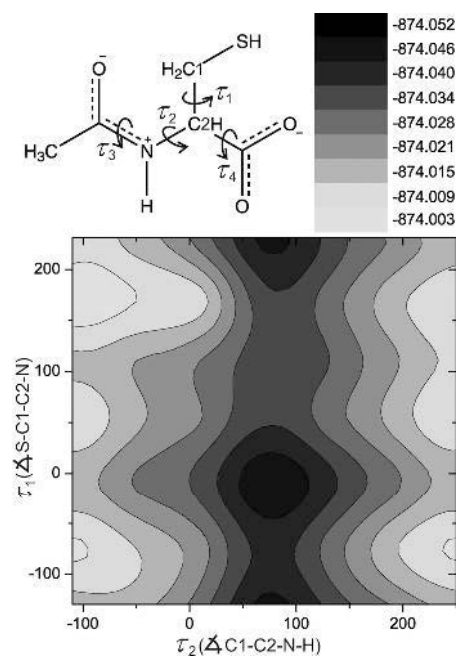


**Figure 3.** Two-dimensional energy plot of Dep-NALC at the B3LYP/6-31G(d) level, scanned along its two most important dihedral angles,  $\tau_1$  and  $\tau_2$ . The definitions of these two dihedral angles and the related angles are also provided. The energy unit is the Hartree. See text for details.

which are related to the *trans* or *cis* peptide bond orientation. In our search, we found that the *trans* configuration is much more stable than the *cis* configuration, consistent with what has been found in the majority of polypeptides. The fourth dihedral angle  $\tau_4$  corresponds to the rotation of the two O atoms of the COO<sup>-</sup> group. This does not generate any new conformers by a 180° rotation. These two angles and the orientation of the hydrogen atom of SH were further optimized to ensure possible intramolecular hydrogen bonds among functional groups, COO<sup>-</sup>, NH, SH, and C=O. The four most stable conformers of Dep-NALC were identified based on the above strategy in the gas phase and also optimized in the PCM. The gas-phase geometries are depicted in Figure S3 in the Supporting Information, together with their respective Boltzmann percentage factors at room temperature based on the relative Gibbs free energies. The corresponding structures obtained in the PCM are provided in Figure 4, with all the important intramolecular distances  $\lesssim 3.2$  Å indicated. As in the case of Neu-NALC, the gas-phase Dep-NALC conformers are more compact than those obtained in the PCM, with in general shorter intramolecular hydrogen-bond lengths. The amide bond in all the conformers adopts the *trans* configuration.

The most important intramolecular hydrogen bond appears to be NH...OCO<sup>-</sup>. While some SH...( $\text{O}=\text{C}$ )<sub>ac</sub> and SH...OCO<sup>-</sup> bond lengths in the gas phase are short enough to be classified as intramolecular hydrogen bonds, these distances are much longer in the associated conformers in the PCM, thus indicating significantly weaker interactions at these sites in the presence of water solvent. As a result, the relative Gibbs free energy ordering also alters slightly upon going from the gas phase to solvation with the PCM. The relative total energies

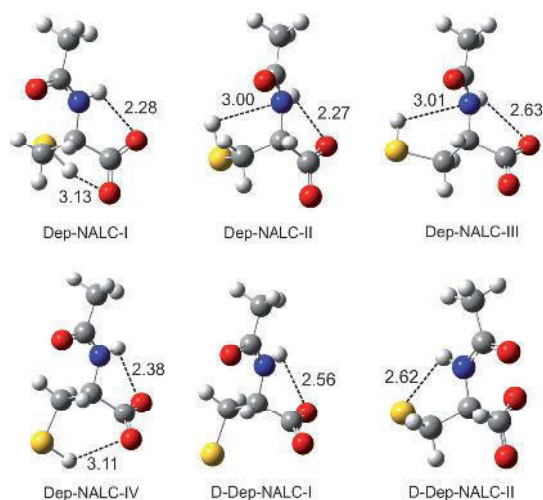


**Figure 4.** Optimized geometries of the four and two lowest-energy conformers of Dep-NALC and D-Dep-NALC, respectively, at the B3LYP/6-311++G(d,p) level with the PCM of D<sub>2</sub>O. The intramolecular hydrogen-bond lengths and some important intramolecular bond lengths (in Å) are indicated.

and relative Gibbs free energies of the four most stable Dep-NALC conformers in the PCM, together with their percentage Boltzmann factors at room temperature, are also provided in Table 1.

### 2.2.3. D-Dep-NALC

A similar conformational search was also carried out for D-Dep-NALC. Here, the NH group has two choices to form intramolecular hydrogen bonds: either with the OCO<sup>-</sup> or S<sup>-</sup> moiety. Although the hydrogen-bonding interaction of the NH group with the carboxylate group tends to be stronger than with S<sup>-</sup>, the energy difference between these two is generally less than 2 kJ mol<sup>-1</sup>. This gives rise to two D-Dep-NALC conformers, whose geometries and relative energies and Gibbs free energies in the PCM are also given in Figure 4 and Table 1, respectively. The associated information for the related conformers in the gas phase is provided in Figure S3 in the Supporting Information.

### 2.2.4. Pro-NALC

Although Pro-NALC has been ruled out as the dominant species under the current experimental conditions, its conformational study is included here for completion. Furthermore, it is of interest to verify if one can use the VA spectral signatures in the fingerprint region to discriminate Pro-NALC from Neu-NALC directly. For the Pro-NALC conformers, as mentioned before, the oxygen atom of the acetyl group was proposed to be the most likely site for protonation.<sup>[24]</sup> Indeed, the Pro-NALC conformer with the CO<sup>+</sup>-H unit, where the proton is attached to the O atom of the acetyl C=O group and forms an intramolecular hydrogen bond to the O atom of the carboxylic C=O group, is found to be  $\approx 13$  kcal mol<sup>-1</sup> more stable than the conformers with the NH<sub>2</sub><sup>+</sup> unit. The structures of the most

stable conformers obtained in the gas phase and with the PCM of water are depicted in Figure S4 in the Supporting Information, together with their percentage Boltzmann population factors at room temperature based on the relative Gibbs free energies. The above finding is consistent with the prediction from the amide resonance theory and with the empirical observations that the most typical protonated site for a peptide bond is at the O site as CO<sup>+</sup>-H. Although the amide oxygen atom is generally considered to be the preferred protonation site in amide, the more exotic N-protonated amides had been reported before in a few rare cases, such as medium-bridged N-protonated lactams.<sup>[30]</sup>

## 2.3. Simulated VA Spectra and VA Assignments of the NALC Conformers

The VA spectra of the four NALC species were simulated for all their most stable conformers obtained in the PCM. PED analyses of the fundamental normal vibrational modes of the most stable conformer of the Neu-, Dep- and D-Dep-NALC species, the relevant species under the experimental conditions of interest, were carried out. Table 2 shows the corresponding VA assignments in the fingerprint region of the Neu-, Dep- and D-Dep-NALC species based on the most stable conformer in the PCM at the B3LYP/6-311++G(d,p) level.

Before discussing the comparison of the simulated spectra with the experimental ones, one question that should be addressed is the extent of the H/D exchange since D<sub>2</sub>O was used as a solvent. In Figure 5c, the simulated VA spectra of Neu-NALC-I, with full to no D substitution at the COOH, NH, and SH functional groups, are provided. The VA band positions typically shift to lower frequencies upon D substitution, although by very different amounts depending on whether the proton directly contributes to the specific vibrational modes or not. The VA simulations of different deuterated isotopologues of Neu-NALC-I show that the H/D exchange at the NH site introduces the most noticeable spectral change in the region of interest, whereas deuteration at the SH and the COOH sites introduces only minor changes in the appearance of the spectrum. Most obviously, the HNC amide II bending mode is red-shifted from 1560 cm<sup>-1</sup> in the non-substituted Neu-NALC-I to 1438 cm<sup>-1</sup> upon D substitution at the NH site. The relative intensity of this band decreases compared to those of the  $\nu(\text{C}=\text{O})_{\text{ca}}$  and  $\nu(\text{C}=\text{O})_{\text{ac}}$  bands. At the same time, both the  $\nu(\text{C}=\text{O})_{\text{ca}}$  and  $\nu(\text{C}=\text{O})_{\text{ac}}$  bands experience a small red shift upon D substitution at the NH site. From the experimental spectrum at pH 0.65 (Figure 5a), one can clearly see that the strong HNC amide II bending mode at 1560 cm<sup>-1</sup>, predicted for the species with no D substitution at the NH site, is not present in the experimental spectrum. In Neu-NALC, the NH site is a less acidic site than the SH and COOH sites. Therefore, if H/D exchange happens at the NH site, one can expect that it happens at the other two sites as well. Consequently, the dominant isotopologue of Neu-NALC-I is fully D substituted at all three functional groups discussed above. Both the gas-phase (see Figure S5, Supporting Information) and the PCM-simulated spectra of different isotopologues of Neu-NALC-I support this conclusion. In all the

**Table 2.** Experimental and the corresponding calculated VA frequencies [ $\text{cm}^{-1}$ ] and VA mode assignments of the most stable conformer of Neu-, Dep-, and D-Dep-NALC at the B3LYP/6-311++G(d,p) level with the PCM.

Exp. freq. <sup>[a]</sup>	Calc. freq. <sup>[b]</sup>	Assignment <sup>[c]</sup>	PED [%]
<b>Neu-NALC</b>			
1718	1752	$\nu(\text{C}=\text{O})_{\text{ca}}$	88
1630	1661	$\nu(\text{C}=\text{O})_{\text{acr}}$ , amide I	80
1476	1488	$\delta(\text{HNC}) + \text{asym CH}_3$ deformation + $\delta(\text{HCC})$	61
1425	1438	$\delta(\text{HNC}) + \delta(\text{HCH})$ /a mixture of $\nu(\text{NC}) + \nu(\text{CC})$ , amide II	39/28
1383	1396	sym $\text{CH}_3$ deformation	82
1362	1372	$\nu(\text{C}-\text{C}) + \nu(\text{N}-\text{C})$	29
1313	1342	$\delta(\text{HCN}) + \delta(\text{HCC}) + \delta(\text{HCS})$	72
<b>Dep-NALC</b>			
1622	1643	$\nu(\text{C}=\text{O})_{\text{acr}}$ , amide I	81
1599	1595	$\nu_{\text{as}}(\text{COO}^-)$	82
1481	1490	asym $\text{CH}_3$ deformation + $\delta(\text{NCO})$	45
1425	1440	$\delta(\text{HNC}) + \text{asym CH}_3$ deformation/ $\nu(\text{NC})$ , amide II	46/30
1395 <sup>[d]</sup>	1395	sym $\text{CH}_3$ deformation	62
	1387	$\nu_3(\text{COO}^-)$	53
1326	1352	$\delta(\text{HCN})$	70
<b>D-Dep-NALC</b>			
1617	1636	$\nu(\text{C}=\text{O})_{\text{acr}}$ , amide I	77
1585	1575	$\nu_{\text{as}}(\text{COO}^-)$	90
1484	1488	asym $\text{CH}_3$ deformation + $\delta(\text{HCC})$	70
1432	1439	$\nu(\text{NC})$ /mixture of $\delta(\text{HNC}) + \delta(\text{NCO}) + \delta(\text{HCH})$ , amide II	38/27
1398 <sup>[d]</sup>	1397	sym $\text{CH}_3$ deformation and a mixture of $\nu_3(\text{COO}^-) + \nu(\text{CC})$	40/33
	1390	sym $\text{CH}_3$ deformation and a mixture of $\nu_3(\text{COO}^-) + \nu(\text{CC})$	48/31
1328	1345	$\tau(\text{HCCO})$	73
1283	1307	$\delta(\text{HCC})$	65

[a] The experimental frequencies are taken from the VA measurements at pH 0.65, 7.0, and 13.0, where Neu-NALC, Dep-NALC or D-Dep-NALC is the only dominant species in each case, respectively. [b] In all VA simulations herein, the fully deuterated species at the COOH, NH, and SH functional groups were used wherever appropriate. See text for detailed discussions. [c]  $\nu$ , stretching,  $\delta$ , bending, and  $\tau$ , torsion. [d] These two bands were not resolved in the experiments. The experimentally observed shoulder at the lower-wavenumber side of this band under neutral pH conditions corresponds to a different Dep-NALC conformer. See Section 2.3 for detailed discussions.

subsequent simulations, the fully deuterated species at these three functional groups have been used whenever applicable.

### 2.3.1. Highly Acidic Conditions

For highly acidic conditions, the observed VA spectrum at pH 0.65 is compared with the population-weighted simulated VA spectra of the Neu-NALC conformers in the gas phase and in the PCM of  $\text{D}_2\text{O}$  in Figure 5. The individual VA spectra of the three most stable conformers are also included. These three conformers account for close to 100% of the total Neu-NALC population based on the Gibbs free energy calculation with the PCM. In general, both the population-weighted PCM and gas-phase spectra show reasonable agreement with the experimental spectrum observed at pH 0.65. The PCM spectrum gives noticeably better overall agreement. For example, the peak frequencies of the two  $\text{C}=\text{O}$  stretching bands obtained with the PCM are much closer to the experimental ones than those predicted in the gas phase.

To verify if it is possible to use VA signatures alone to conclude that Pro-NALC is not the dominant species under the lowest pH conditions measured in this work, the experimental data at pH 0.65 are compared to the simulated VA spectra of

Pro-NALC in the gas phase and with the PCM (see Figure S6, Supporting Information). The two most stable Pro-NALC conformers, with a total population close to 100%, were included in the simulation. In the PCM,  $\nu(\text{C}=\text{O})_{\text{ca}}$  experiences a significant red shift on going from Neu-NALC to Pro-NALC since the proton is hydrogen-bonded to the carboxylate O atom directly, whereas other vibrational modes experience much smaller shifts. As a result, the band gap between the two carbonyl groups in the 1550–1750  $\text{cm}^{-1}$  region becomes much narrower. At the same time, the next strong band in the lower-wavenumber region, corresponding mainly to a mixture of  $\nu(\text{CO})_{\text{ac}}$  and  $\nu(\text{C}-\text{CH}_3)$  stretch, experiences a blue shift, which results in a much narrower band gap between this and the  $\nu(\text{C}=\text{O})_{\text{ca}}$  stretch than in Neu-NALC. Clearly, the predicted Pro-NALC spectral pattern shows a very poor match with the experimental data even with the inclusion of the PCM, in contrast to the comparison with Neu-NALC. One can therefore confidently conclude that Neu-NALC

is the dominant species in  $\text{D}_2\text{O}$  at pH 0.65 whereas Pro-NALC is not.

### 2.3.2. Highly Basic Conditions

For highly basic conditions at pH 13, it was established in Section 2.1 that D-Dep-NALC is the most important species. The experimental VA spectrum at pH 13 is compared with the simulated VA spectra of the two most stable conformers of D-Dep-NALC in  $\text{D}_2\text{O}$  with the polarizable continuum solvation (PCM) solvation model in Figure 6, and with the gas-phase simulations in Figure S7 (Supporting Information). In the population-weighted simulated spectrum with the PCM, the amide I band of D-Dep-NALC shifts to red by about 25  $\text{cm}^{-1}$  (unscaled) compared to that of Neu-NALC, correctly capturing the substantial red shift of 13  $\text{cm}^{-1}$  observed experimentally. A new band, corresponding to  $\nu_{\text{as}}(\text{COO}^-)$  appears at 1585  $\text{cm}^{-1}$  experimentally, compared to a prediction of 1575  $\text{cm}^{-1}$ . The next band, mainly due to the asymmetric deformation of the  $\text{CH}_3$  group, was observed at 1484  $\text{cm}^{-1}$ , blue-shifted by about 8  $\text{cm}^{-1}$  from that observed at 1476  $\text{cm}^{-1}$  with pH 0.65. Again, this blue shift has been correctly predicted with the simulated VA spectra with the PCM. Overall, the PCM-simulated VA spec-



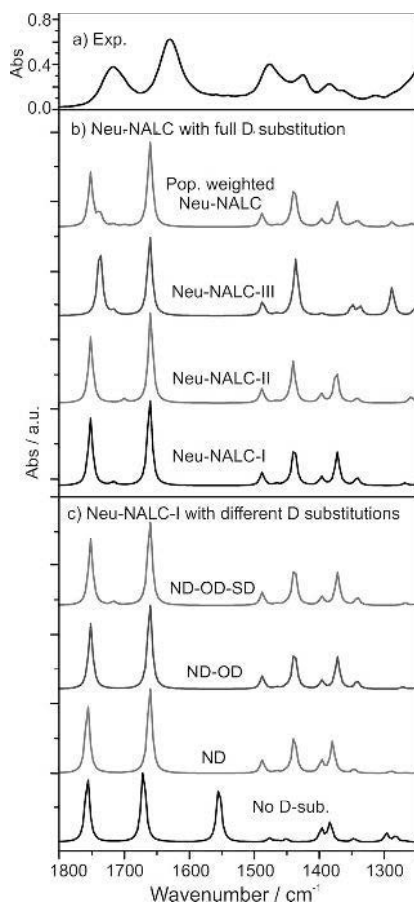


**Figure 5.** Comparisons of a) the experimental VA spectrum of NALC in  $D_2O$  under highly acidic conditions at pH 0.65 with b) the simulated VA spectra of the three most stable Neu-NALC conformers with the PCM of  $D_2O$ , and with their population-weighted VA spectrum based on the relative Gibbs free energies at the B3LYP/6-311++G(d,p) level at room temperature. c) Simulated VA spectra of the different deuterium isotopologues of Neu-NALC-I with the PCM of  $D_2O$  at the B3LYP/6-311++G(d,p) level.

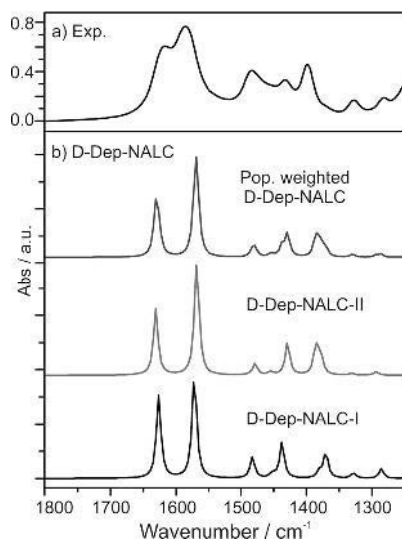


**Figure 6.** Comparisons of the experimental VA spectrum of NALC in  $D_2O$  under the highly basic conditions of pH 13.0 with the simulated VA spectra of the two most stable D-Dep-NALC conformers with the PCM of  $D_2O$ , and with their population-weighted VA spectrum based on the relative Gibbs free energies at the B3LYP/6-311++G(d,p) level at room temperature.

trum shows good agreement with the experimental one. The gas-phase spectrum, on the other hand, shows a much less satisfactory agreement, thereby indicating the importance of taking the effects of water solvent into account in the VA simulation. Based on the good agreement between the PCM simulation and the experimental data, one can conclude that the two most stable conformers of D-Dep-NALC, which favour a close  $NH\cdots OOC$  and  $NH\cdots S^-$  intramolecular interaction, are the most important conformers at pH 13.0.

Overall, the population-weighted simulated VA spectra of the most stable conformers of Neu-NALC and D-Dep-NALC with the PCM demonstrate good agreements with the experimental VA spectra obtained in highly acidic and basic aqueous solutions. In these two cases, it has been shown that the inclusion of the PCM is essential for assigning the dominant species and conformational distributions with good confidence. The parallel comparison for the pH 7 condition will be discussed below. More importantly, the PCM solvation model will be further tested with both VA and VCD experimental data at pH 7 to verify if explicit solvation of water should also be considered.

#### 2.4. A Combined Implicit and Explicit Solvation Treatment of the VA and VCD Spectra Obtained under Neutral Conditions

NALC aqueous solutions under neutral conditions are of special biological interest. In particular, conclusive information about the conformational distributions of the most significant species would be valuable. To firmly reach the correct conclusion and to evaluate the effects of the hydrogen-bonding interactions between NALC and water on the conformational structures and stability of NALC, not only VA but also VCD measurements of NALC in  $D_2O$  at pH 7.0 have been measured. The additional VCD data are highly sensitive to the structural and conformational differences, and thus impose an even more stringent experimental test for comparison with theoretical modelling to reach a final conclusion.

From the analysis of NALC in highly acidic solution, it has been concluded that only the neutral species dominates in such a solution. It is therefore highly unlikely for NALC to exist primarily in the zwitterionic form at neutral pH. Rather, the most likely species should be Dep-NALC. In Figure 7, the experimental VA and VCD spectra are compared to the simulated spectra of the four most stable Dep-NALC conformers and the corresponding population-weighted spectra in the gas phase and in  $D_2O$  using the PCM solvation model. The related results of the Dep-NALC conformers in the gas phase are provided in Figure S8 in the Supporting Information, for comparison. A cursory glance at the spectra predicted with the PCM and in the gas phase suggests that the inclusion of the PCM is essential to reach a good agreement with the experimental VA and VCD data. To facilitate detailed assignments, the experimentally observed VA bands are labelled with the numbers 1 to 6. The simulated VA bands are similarly labelled. Indeed, all major VA peak wavenumbers and intensities were well captured with the PCM simulation, including the experimentally observed

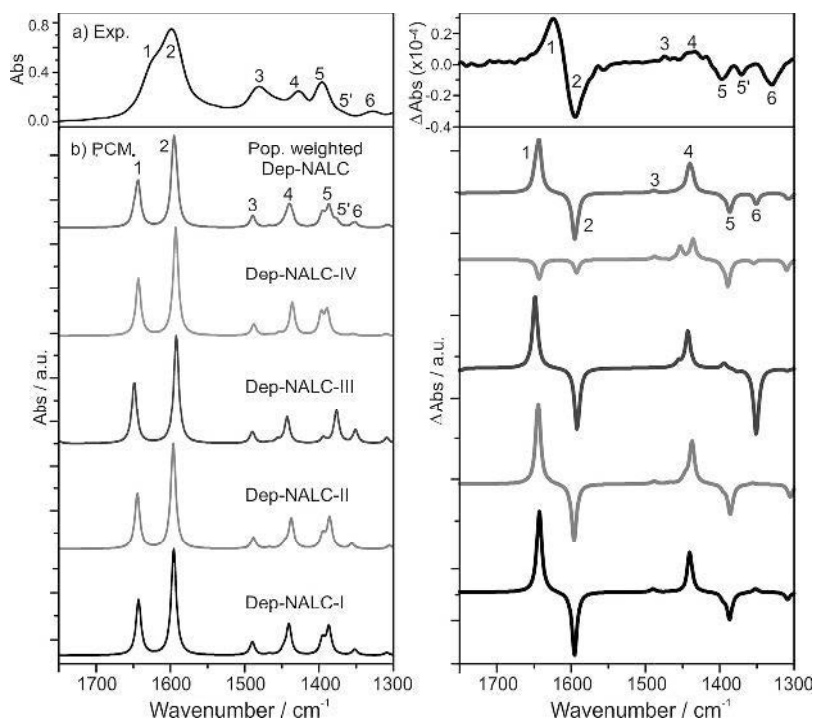


**Figure 7.** Comparisons of the experimental VA and VCD spectra of NALC in D<sub>2</sub>O at neutral pH with the simulated VA and VCD spectra of the four most stable conformers of Dep-NALC with the PCM of D<sub>2</sub>O, and with the corresponding population-weighted spectra based on the relative Gibbs free energies at the B3LYP/6-311++G(d,p) level at room temperature.

shoulder, labelled as 5', near the main VA band 5. The corresponding VCD features are also labelled. While the main VCD features were also well predicted, some details in the 1300–1450 cm<sup>-1</sup> region were not reproduced satisfactorily. The main discrepancy is that the medium-strength VCD band labelled as 5', observed experimentally, was not predicted. A closer examination of the experimental spectra showed that VA band 5 corresponded to VCD band 5, both with the peak wavenumber at 1395 cm<sup>-1</sup>. Similarly, VA band 6 corresponded to VCD band 6, both with the peak wavenumber at 1328 cm<sup>-1</sup>. Therefore, it was speculated that VCD band 5' at 1369 cm<sup>-1</sup> corresponded to the shoulder band 5'. However, this band was not predicted to have a substantial VCD intensity.

At this point, the VCD modes in the fingerprint region were also checked for their robustness. The concept of robust modes was first introduced by Nicu and Baerends<sup>[31]</sup> to evaluate the sensitivity of VCD patterns to the functionals and basis sets used in the DFT simulations of VCD spectra and to assist fast, reliable, absolute configuration assignments. As mentioned before, the VCD intensity and sign are determined by the imaginary value of the dot product of the electric and magnetic transition dipole moments. For a particular VA mode whose  $\theta$ , the angle between the electric and magnetic transition dipole vectors, is close to 90°, the sign of the VCD band can be altered if  $\theta$  crosses 90°. As a result, the authors suggested classifying those VCD modes with  $\theta$  from 60 to 120° as non-robust. Góbi and Magyarfalvi<sup>[32]</sup> proposed a new alternative measure of robustness using the ratio,  $\mathcal{R}$ , of dipole and rotational strengths. They further suggested to use 10 ppm of

this ratio as a “soft” robust mode criterion and that one should give an extra amount of scrutiny to those VCD bands with this ratio below 10 ppm. The advantages of this new alternative criterion had been discussed in detail in ref. [32]. The rotational and dipole strengths of the VCD modes in the fingerprint region of interest of the most stable conformer of Dep-NALC in the PCM and those solvated with four water molecules in the PCM are listed in Table S1 in the Supporting Information, together with the associated ratios. In general, all the VCD modes in this region in the PCM with high enough rotational strength to be observed experimentally can be considered robust or nearly robust.<sup>[32]</sup> It is our experience that the soft 10 ppm criterion can be further pushed to a lower limit. This and further similar examinations of other conformers, however, do not

provide a satisfactory answer to the missing VCD band.

It was then hypothesized that such discrepancies could be due to the hydrogen-bonding interactions between water and NALC. Such interactions had been showed to produce chirality transfer VCD features of water solvent before.<sup>[15–18]</sup> These interactions have therefore been considered below in our effort to systematically evaluate the effects of both explicit and implicit solvation with water on the respective VA and VCD spectroscopy.

#### 2.4.1. Estimation of the Coordination Number of the First Solvation Shell by MD Simulations

For a highly flexible molecule such as NALC in the gas phase, the intramolecular hydrogen-bonding interaction is an important factor which influences the relative stability of conformers. Upon solvation of NALC in water, on the other hand, the intermolecular hydrogen-bonding interaction between NALC and D<sub>2</sub>O can compete with the intramolecular hydrogen-bonding interaction, and therefore modify the relative stability of conformers and change their structures. To account for the NALC–water hydrogen-bonding interaction, a family of Dep-NALC–(water)<sub>*N*</sub> clusters with *N* the number of water molecules were constructed. To estimate the coordination number of the first water solvation shell, that is, the number of water molecules that are directly hydrogen-bonded to NALC, an analysis of the atom–atom radial distribution functions (RDFs) generated from the MD simulations was carried out. The details of the MD simulations are described in the Experimental and Theoretical De-

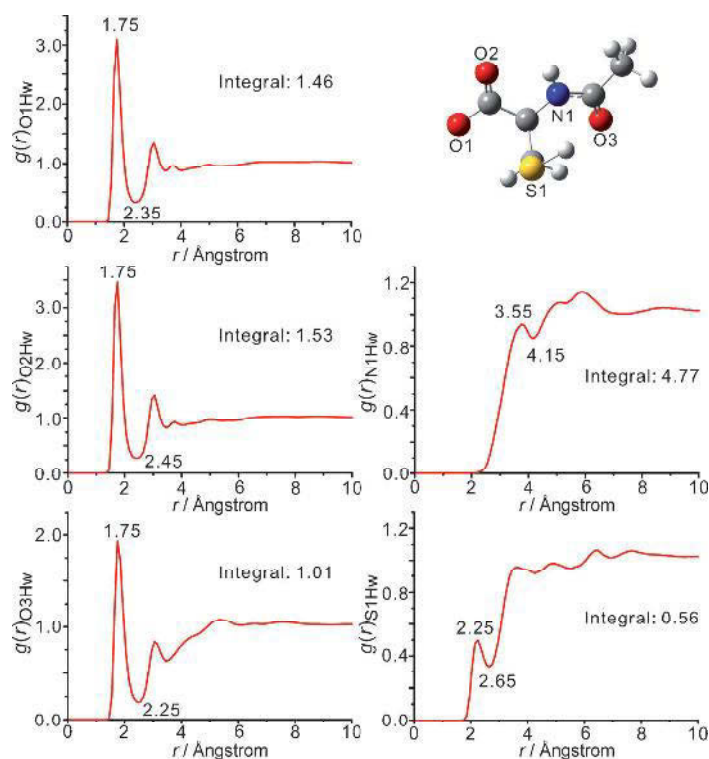


**Figure 8.** RDFs obtained from the MD simulation of NALC in water. The atom labelling for NALC is given in the upper right corner. Hw is the hydrogen atom of water.

tails section. Five relevant RDFs, together with the atom labelling used, are depicted in Figure 8. An RDF,  $g(r)$ , describes the density of a certain particle at a distance  $r$  from an arbitrary central atom. For example,  $g(r)_{O1HW}$ ,  $g(r)_{O2HW}$  and  $g(r)_{O3HW}$  in Figure 8 show the density of the hydrogen atom of water around the two carboxylic oxygen atoms O1 and O2 and the acetyl oxygen atom O3, respectively. Each of them reaches its first maximum at 1.75 Å with a well-defined sharp peak, thus indicating clearly the hydrogen-bonding nature of the intermolecular interaction. Integration of this first peak out to the minimum in the aforementioned  $g(r)_{O1HW}$ ,  $g(r)_{O2HW}$  and  $g(r)_{O3HW}$  gives a water coordination number of 1.5, 1.5, and 1.0, respectively. On the other hand,  $g(r)_{N1HW}$  shows a relatively broad peak at 3.55 Å, which indicates that there is no N1...HW hydrogen bond, although it is still possible to have an N1H...OW hydrogen bond.  $g(r)_{S1HW}$  shows the first maximum at 2.25 Å, which indicates a possible S1...HW hydrogen bond with a water coordination number of 0.56. Thus, the coordination number of the first water shell is about 4.

#### 2.4.2. Explicit and Implicit Solvation of Dep-NALC

Based on the RDF analysis and the MD snapshots, the three most stable gas-phase Dep-NALC conformers with a combined Boltzmann percentage population factor of above 90% were explicitly solvated with three and four water molecules. For the Dep-NALC-(water)<sub>3</sub> clusters, that is, Dep-NALC-3W, two water molecules are hydrogen-bonded to the carboxylic

oxygen atoms to form a five-membered heavy-atom hydrogen-bonded ring, while another water is inserted into the existing SH...O<sub>ac</sub> ring to form the so-called insertion complex. Such insertion complexes with cooperative hydrogen-bonded rings have been investigated recently and were found experimentally to be the most favourable geometries for this type of water-solvated cluster.<sup>[33,34]</sup> For the Dep-NALC-4W clusters, the fourth water molecule is placed at the N1H site to form an N1H...OW hydrogen bond. Altogether, six low-energy conformers have been located.

To account for the existence of the bulk water environment, we further solvated the Dep-NALC-3,4W clusters with the PCM of bulk water. The optimized geometries obtained with the PCM are summarized in Figure 9, together with their respective percentage Boltzmann population factors at room temperature based on the relative Gibbs free energies. The important intermolecular hydrogen and van der Waals bond lengths are also indicated in Figure 9. The corresponding structures of Dep-NALC-3,4W clusters in the gas phase are depicted in Figure S9 in the Supporting Information. Interestingly, the explicit solva-

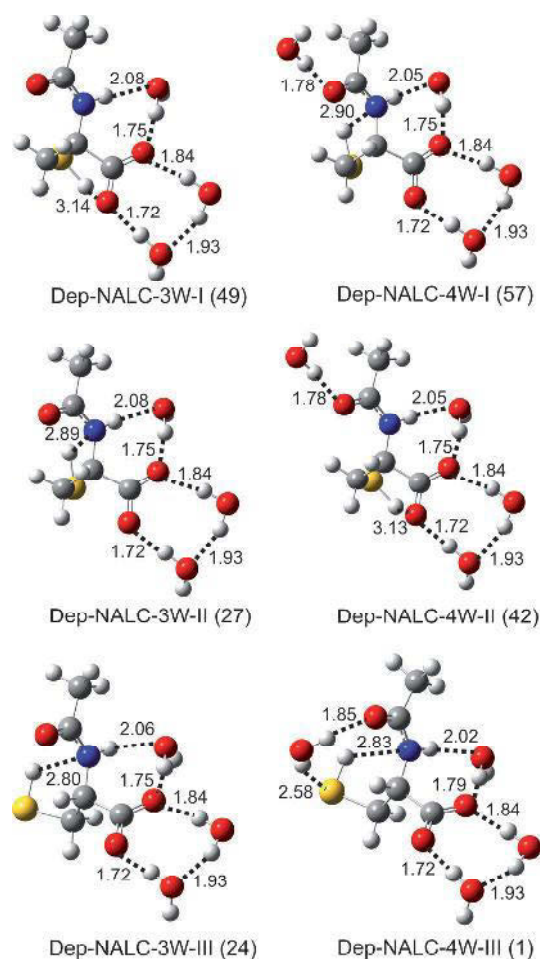


**Figure 9.** Optimized geometries of the six most stable conformers of the Dep-NALC-(water)<sub>3,4</sub> clusters at the B3LYP/6-311++G(d,p) level with the PCM. The numbers in parentheses are the percentage Boltzmann population factors based on the relative Gibbs free energies at 298 K. The intramolecular hydrogen-bond lengths and some important van der Waals bond lengths (in Å) are indicated.

tion of Dep-NALC with three or four water molecules has a very similar effect on the conformational stability and structures as the inclusion of the PCM bulk water. For example, the SH...N or SH...O bond lengths increase on going from the gas phase to the explicit solvation model. A similar observation was made upon going from the gas phase to the PCM solvation model. The further inclusion of the PCM for the explicitly solvated Dep-NALC-3,4W clusters introduced some additional changes, especially in their VA and VCD spectra, as discussed below.

The simulated VA and VCD spectra of the Dep-NALC-4W clusters in the gas phase and with the PCM to account for water solvent are shown in Figure 10, together with the experimental VA and VCD data at pH 7.0. For comparison, the related spectra of the Dep-NALC-3W clusters in the gas phase and with the PCM are provided in Figure S10 in the Supporting Information. Explicit solvation of Dep-NALC with three or four

water molecules introduced in general a moderate red shift of the  $\nu_{\text{as}}(\text{COO}^-)$  and  $\nu(\text{C=O})_{\text{ac}}$  and a small blue shift for the bands in the 1400–1500  $\text{cm}^{-1}$  region. The directions of shifts experienced were the same when either explicit or implicit solvation of Dep-NALC was incorporated into the simulations, but the extent of the red shift was much larger with the PCM. The further implicit PCM solvation of the Dep-NALC-3,4W clusters brought the predicted peak frequencies into much better agreement with the experimental ones. All seven observed bands labelled in the experimental VA spectrum correlate very well with the ones in the simulated spectrum when the implicit and explicit solvation were incorporated together (Figure 10a). With regard to the VCD spectral features, it is also interesting to note that the explicit solvation model has changed the major VCD features in a similar way to the implicit solvation model discussed previously for Dep-NALC. For example, the positive–negative bisignated VCD feature at the  $\nu(\text{COO}^-)_{\text{as}}$

and  $\nu(\text{C=O})_{\text{ac}}$  bands has been predicted for the three conformers of interest with explicit solvation as with the PCM solvation model. The further PCM solvation of the Dep-NALC-3,4W clusters brought some additional changes to the VCD features, most noticeably in the 1300–1500  $\text{cm}^{-1}$  region. For all three solvated conformers, the VCD band 3 has now been predicted to be positive, albeit with a small intensity, compared to the negative sign predicted with explicit solvation only. Although we do acknowledge that the experimentally observed intensity for the VCD band 3 is quite weak, only slightly above noise level, it is nevertheless encouraging that both the sign and magnitude of this VCD band have been correctly reproduced with this combined solvation model. More importantly, the previously missing VCD band 5' is now visible, although the relative intensity of VCD bands 5' and 6 is still out of accord with experiment if one applies the population factors based on the DFT relative free energies for these solvated water clusters. A more detailed examination of the simulated VA and VCD spectra of the conformers revealed that although the VA spectra for all conformers are very similar in this region, the VCD features are somewhat dif-

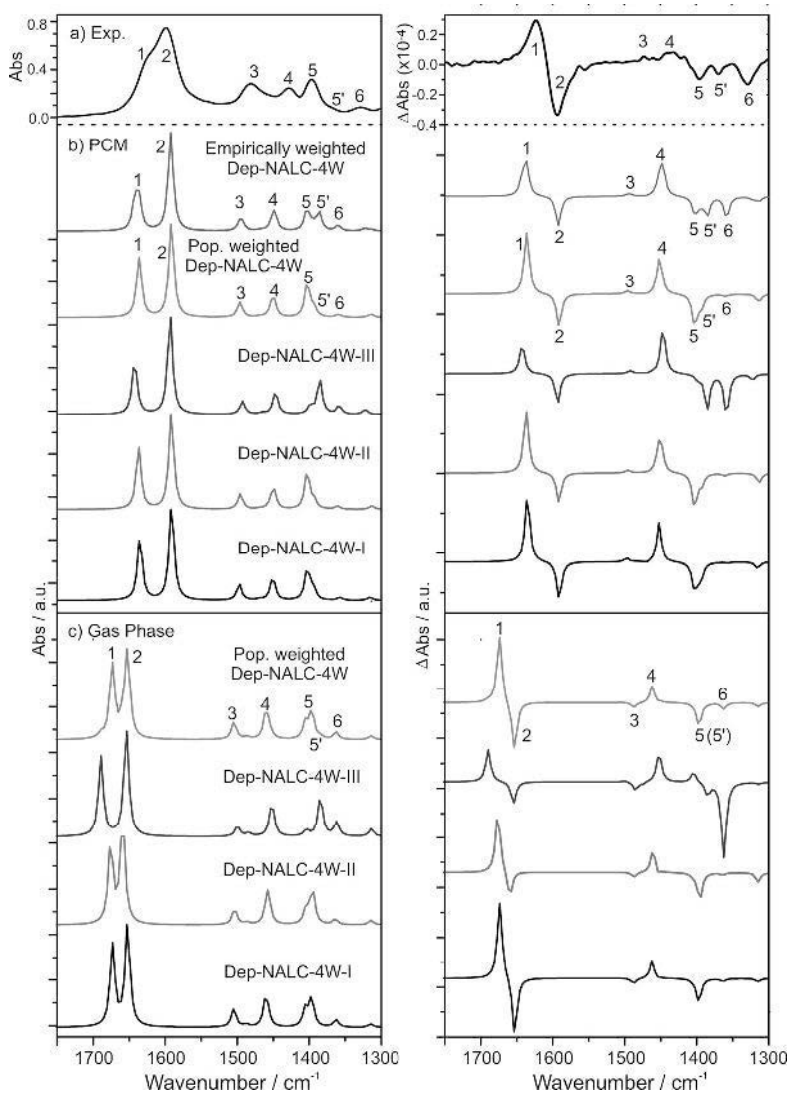


**Figure 10.** Comparisons of a) the experimental VA and VCD spectra of NALC in  $\text{D}_2\text{O}$  under neutral pH conditions with b) the corresponding spectra of the most stable Dep-NALC-4W conformers with the PCM of  $\text{D}_2\text{O}$  and c) in the gas phase at the B3LYP/6-311 + + G(d,p) level. The DFT and empirically population-weighted spectra are also provided.

ferent. For example, Dep-NALC-4W-III conformer shows much more intense negative VCD bands at the positions of bands 5' and 6, in accord with the experimental observation. It is plausible that this conformer actually contributes more than the Boltzmann factor predicted by the DFT relative Gibbs free energies. New VA and VCD spectra generated with an empirical population ratio of 25:25:50% for these conformers are also provided in Figure 10. This empirical factor was chosen to best reproduce the experimental spectral features. One rationale behind this is that the DFT spectral features have been generally regarded as quite reliable, whereas the DFT relative Gibbs free energies for hydrogen-bonded clusters are typically only reliable to a few kcal mol<sup>-1</sup>. It is satisfying that the empirically weighted VA and VCD spectra have captured all the VA and the more subtle VCD details discussed above. This demonstrates that both explicit and implicit solvation with water play important roles in interpreting VA and, in particular, VCD measurements in aqueous solution. The inclusion of both solvation models can significantly improve the agreement with the experimental data and provide a more accurate and detailed description of the conformational distributions in aqueous solution.

### 3. Conclusions

The conformations of NALC, the acetylated form of cysteine, under different pH conditions have been investigated using VA and VCD spectroscopy, complemented with *ab initio* calculations and MD simulations. It has been shown that the inclusion of the polarizable continuum bulk water solvation model is essential to obtain correct VA assignments and conformational distributions of Neu-, Dep- and D-Dep-NALC in aqueous solutions. It has been further established that hydrogen-bonding interactions between NALC and water molecules play an important role in the appearance of the VA and VCD spectra. The results presented indicate that the inclusion of both explicit water solvation and implicit solvation with the PCM is crucial to capture all the VCD features in addition to the VA features observed, and thus provide accurate information about conformational distributions of NALC in water.

### Experimental and Theoretical Details

**FTIR VA and VCD Measurements:** NALC was purchased from Aldrich and used without further purification. All solutions were prepared in deuterium oxide (D<sub>2</sub>O; 99.99% D, Aldrich) to avoid strong absorption due to the H<sub>2</sub>O bending band at  $\approx 1640$  cm<sup>-1</sup>, which interferes with the amide I band of NALC. VA and VCD spectra were measured by using an FTIR spectrometer Vertex 70 with a PMA50 module (Bruker). To obtain a good VCD spectrum, the concentration and path length were optimized to ensure that the VA absorption coefficients for the bands of interest were between 0.2 and 0.8. A low-pass filter with a cutting wavelength at  $\approx 1800$  cm<sup>-1</sup> was used. All reported data were obtained using a BaF<sub>2</sub> sample cell (International Crystal Laboratories) with an optimized path length of 0.015 mm and concentration of 1.4 M. A 0.015 mm PTFE spacer (International Crystal Laboratories) was used for this purpose without calibration. NALC solutions with pH values ranging from 0.65 to

13.0 were prepared by adding a small amount of 6 M DCl or 6 M NaOH dropwise. For the pH 7 solution, the raw VCD spectrum was measured with a total collection time of 6 h (3 × 2 h) and a resolution of 4 cm<sup>-1</sup>. The final VCD spectrum was obtained by subtracting the solvent spectrum obtained under identical conditions since the opposite enantiomer of NALC is not available commercially.<sup>[13]</sup>

**UV/Vis Measurements:** UV/Vis spectra of 0.0014 M NALC in aqueous solution at several different pH values ranging from 3.0 to -12.3 were collected on a Hewlett Packard 8453 UV/Vis spectrophotometer using a PTFE cell with a 1 cm path length.

**DFT Calculations:** Conformational investigations, geometry optimizations, and calculations of harmonic vibrational frequencies and VA and VCD intensities of the species of interest were carried out using the Gaussian 03<sup>[35]</sup> and Gaussian 09<sup>[36]</sup> programs. The combination B3LYP/6-31G was used initially to locate the possible lowest-energy conformers of the Pro-, Neu-, Dep-, and D-Dep-NALC monomers. The hybrid functional B3LYP<sup>[37,38]</sup> was chosen because it has been extensively used in describing strong hydrogen-bonded complexes<sup>[39-41]</sup> and because of its well-documented reliability in predicting VCD intensities.<sup>[42-45]</sup> To account for solvation, both the integral equation formalism (IEF) implicit PCM solvation model and the explicit solvation model based on the hydrogen-bonded clusters of Dep-NALC-(water)<sub>N</sub> were employed. The dielectric constant of D<sub>2</sub>O,  $\epsilon = 78.3553$ , was used in the PCM. The significant aspects of the PCM solvation model had been reviewed in detail previously.<sup>[46]</sup> The number of water molecules hydrogen-bonded to Dep-NALC was estimated from the analysis of the RDFs obtained from the MD simulations described below. In addition, the solvated Dep-NALC-(D<sub>2</sub>O)<sub>N</sub> was placed inside a PCM solvation model to account simultaneously for the explicit hydrogen-bonding interactions between Dep-NALC and water molecules and the effects of bulk water. For the final calculations, B3LYP/6-311++G(d,p) was used for geometry optimizations and subsequent calculations of harmonic vibrational frequencies and VA and VCD intensities of all four species without and with the PCM, as well as for the much larger Dep-NALC-(H<sub>2</sub>O)<sub>N</sub> clusters without and with the PCM. For the simulation of VA and VCD spectra, a Lorentzian line shape with a half width at half maximum of 4 cm<sup>-1</sup> was used.

**Molecular Dynamics Simulations:** All MD simulations were performed using the Sander module in the AMBER 9<sup>[47]</sup> suite of programs. The xLeap graphical interface module was used to build the starting configuration of NALC. The AMBER ff99 force field based on molecular mechanics was used. The NALC molecule was solvated in a rectangular periodic box with the pre-equilibrium TIP3P<sup>[48]</sup> water molecules with a cut-off of 10.0 Å. The initial configuration was relaxed in two sequential runs: first, 500 steps of steepest descent algorithm were applied to remove any bad contacts, followed by another 500 steps of conjugate gradient algorithm. The final configuration obtained was then used as the starting point for a 600 ps heating and equilibrating MD simulation under NVT conditions. The system was first heated from 0 to 300 K in 200 ps and was then equilibrated at 300 K in 400 ps to ensure equilibrium was reached completely. A 6 ns production MD simulation was then performed under NPT conditions ( $T = 300$  K,  $P = 1$  atm) with a time step of 2 fs.

### Acknowledgements

*This research was funded by the University of Alberta, the Natural Sciences and Engineering Research Council of Canada, Petro-Canada, and the Canada Research Chairs Program. We gratefully*

acknowledge access to the computing facilities provided by the Academic Information and Communication Technology group at the University of Alberta.

**Keywords:** amino acids · conformation analysis · density functional calculations · molecular dynamics · vibrational spectroscopy

- [1] S. De Flora, R. Balansky, C. Bennicelli, A. Camoirano, F. D'Agostini, A. Iz-zotti, C. F. Cesarone in *Drugs, Diet and Disease: Mechanistic Approaches to Cancer, Vol. 1* (Eds.: C. Ioannides, D. F. V. Lewis), Harwood, New York, **1995**, pp. 151–203.
- [2] D. C. Malins, K. E. Hellström, K. M. Anderson, P. M. Johnson, M. A. Vinson, *Proc. Natl. Acad. Sci. USA* **2002**, *99*, 5937–5941.
- [3] M. Berk, D. L. Copolov, O. Dean, K. Lu, S. Jeavons, I. Schapkaitz, M. Anderson-Hunt, A. L. Bush, *Biol. Psychiatry* **2008**, *64*, 468–475.
- [4] L. A. Palmer, A. Doctor, P. Chhabra, M. L. Sheram, V. E. Laubach, M. Z. Karlinsey, M. S. Forbes, T. Macdonald, B. Gaston, *J. Clin. Invest.* **2007**, *117*, 2592–2601.
- [5] G. Albrecht, R. B. Corey, *J. Am. Chem. Soc.* **1939**, *61*, 1087–1103.
- [6] F. R. Tortonda, J. L. Pascual-Ahuir, E. Silla, I. Tunonon, F. J. Ramirez, *J. Chem. Phys.* **1998**, *109*, 592–602.
- [7] S. Gronert, R. A. J. O'Hair, *J. Am. Chem. Soc.* **1995**, *117*, 2071–2081.
- [8] E. Tajkhorshid, K. J. Jalkanen, S. Suhai, *J. Phys. Chem. B* **1998**, *102*, 5899–5913.
- [9] C. F. Correia, P. O. Balaj, D. Scuderi, P. Maitre, G. Ohanessian, *J. Am. Chem. Soc.* **2008**, *130*, 3359–3370.
- [10] Z. Ji, R. Santamaria, I. L. Garzón, *J. Phys. Chem. A* **2010**, *114*, 3591–3601.
- [11] C. Gautier, T. Bürgi, *Chem. Commun.* **2005**, 5393–5395.
- [12] B. Boeckx, R. Ramaekers, G. Maes, *J. Mol. Spectrosc.* **2010**, *261*, 73–81.
- [13] "Vibrational Circular Dichroism Spectroscopy of Chiral Molecules": G. Yang, Y. Xu, in *Top. Curr. Chem.: Electronic and Magnetic Properties of Chiral Molecules and Supramolecular Architectures, Vol. 298* (Eds.: R. Naaman, D. N. Beratan, D. H. Waldeck), Springer, Berlin, **2011**, pp. 189–236.
- [14] a) T. B. Freedman, X. Cao, D. A. Young, L. A. Nafie, *J. Phys. Chem. A* **2002**, *106*, 3560–3565; b) T. B. Freedman, X. Cao, L. A. Nafie, A. Solladié-Cavallo, L. Jierry, L. Bouerat, *Chirality* **2004**, *16*, 467–474.
- [15] M. Losada, H. Tran, Y. Xu, *J. Chem. Phys.* **2008**, *128*, 014508.
- [16] M. Losada, P. Nguyen, Y. Xu, *J. Phys. Chem. A* **2008**, *112*, 5621–5627.
- [17] G. Yang, Y. Xu, *J. Chem. Phys.* **2009**, *130*, 164506.
- [18] M. Losada, Y. Xu, *Phys. Chem. Chem. Phys.* **2007**, *9*, 3127–3135.
- [19] M. H. Jamroz, *Vibrational Energy Distribution Analysis VEDA 4*, Warsaw, **2004–2010**.
- [20] *Remington's Pharmaceutical Sciences, 16th ed.* (Ed.: A. Osol), Mack Publishing Co., Easton, **1980**, p. 805.
- [21] K. B. Wiberg, C. M. Breneman, *J. Am. Chem. Soc.* **1992**, *114*, 831–840.
- [22] J. I. Mujika, J. M. Matxain, L. A. Eriksson, X. Lopez, *Chem. Eur. J.* **2006**, *12*, 7215–7224.
- [23] C. R. Kemnitz, M. J. Loewen, *J. Am. Chem. Soc.* **2007**, *129*, 2521–2528.
- [24] V. Addario, Y. Guo, I. K. Chu, Y. Ling, G. Ruggerio, C. F. Rodriguez, A. C. Hopkinson, K. W. M. Siu, *Int. J. Mass Spectrom.* **2002**, *219*, 101–114.
- [25] A. J. Williams, *J. Am. Chem. Soc.* **1976**, *98*, 5645–5651.
- [26] M. Friedman, J. F. Cavins, J. S. Wall, *J. Am. Chem. Soc.* **1965**, *87*, 3672–3682.
- [27] G. E. Clement, T. P. Hartz, *J. Chem. Educ.* **1971**, *48*, 395–397.
- [28] "Estimation of Chemical Reactivity Parameters and Physical Properties of Organic Molecules Using SPARC": L. A. Carreira, S. Hilal, S. W. Karickhoff, *Theoretical and Computational Chemistry, Quantitative Treatment of Solute/Solvent Interactions* (Eds.: P. Politzer, J. S. Murray), Elsevier, Amsterdam, **1994**.
- [29] a) M. A. Zamora, H. A. Baldoni, J. A. Bombasaro, M. L. Mak, A. Perczel, O. Farkas, R. D. Enriz, *J. Mol. Struct. THEOCHEM* **2001**, *540*, 271–283; b) J. A. Bombasaro, M. A. Zamora, H. A. Baldoni, R. D. Enriz, *J. Phys. Chem. A* **2005**, *109*, 874–884.
- [30] M. Szostak, L. Yao, V. W. Day, D. R. Powell, J. Aubé, *J. Am. Chem. Soc.* **2010**, *132*, 8836–8837.
- [31] V. P. Nicu, E. J. Baerends, *Phys. Chem. Chem. Phys.* **2009**, *11*, 6107–6118.
- [32] S. Góbi, G. Magyarfalvi, *Phys. Chem. Chem. Phys.* **2011**, *13*, 16130–16133.
- [33] Z. Su, Y. Xu, *Angew. Chem.* **2007**, *119*, 6275–6278; *Angew. Chem. Int. Ed.* **2007**, *46*, 6163–6166.
- [34] Z. Kisiel, E. Białkowska-Jaworska, D. P. Zaleski, J. L. Neill, A. L. Steber, B. H. Pate, *International Symposium on Molecular Spectroscopy, 66th Meeting, June 20–24, 2011*, <http://molspect.chemistry.ohio-state.edu/symposium/>, abstract #WH10.
- [35] Gaussian 03 (Revision E.01), M. J. Frisch, G. W. Trucks, H. B. Schlegel, G. E. Scuseria, M. A. Robb, J. R. Cheeseman, J. A. Montgomery, Jr., T. Vreven, K. N. Kudin, J. C. Burant, J. M. Millam, S. S. Iyengar, J. Tomasi, V. Barone, B. Mennucci, M. Cossi, G. Scalmani, N. Rega, G. A. Petersson, H. Nakatsuji, M. Hada, M. Ehara, K. Toyota, R. Fukuda, J. Hasegawa, M. Ishida, T. Nakajima, Y. Honda, O. Kitao, H. Nakai, M. Klene, X. Li, J. E. Knox, H. P. Hratchian, J. B. Cross, V. Bakken, C. Adamo, J. Jaramillo, R. Gomperts, R. E. Stratmann, O. Yazyev, A. J. Austin, R. Cammi, C. Pomelli, J. W. Ochterski, P. Y. Ayala, K. Morokuma, G. A. Voth, P. Salvador, J. J. Dannenberg, V. G. Zakrzewski, S. Dapprich, A. D. Daniels, M. C. Strain, O. Farkas, D. K. Malick, A. D. Rabuck, K. Raghavachari, J. B. Foresman, J. V. Ortiz, Q. Cui, A. G. Baboul, S. Clifford, J. Cioslowski, B. B. Stefanov, G. Liu, A. Liashenko, P. Piskorz, I. Komaromi, R. L. Martin, D. J. Fox, T. Keith, M. A. Al-Laham, C. Y. Peng, A. Nanayakkara, M. Challacombe, P. M. W. Gill, B. Johnson, W. Chen, M. W. Wong, C. Gonzalez, J. A. Pople, Gaussian, Inc., Wallingford, CT, **2004**.
- [36] Gaussian 09 (Revision B.01), M. J. Frisch, G. W. Trucks, H. B. Schlegel, G. E. Scuseria, M. A. Robb, J. R. Cheeseman, G. Scalmani, V. Barone, B. Mennucci, G. A. Petersson, H. Nakatsuji, M. Caricato, X. Li, H. P. Hratchian, A. I. Izmaylov, J. Bloino, G. Zheng, J. L. Sonnenberg, M. Hada, M. Ehara, K. Toyota, R. Fukuda, J. Hasegawa, M. Ishida, T. Nakajima, Y. Honda, O. Kitao, H. Nakai, T. Vreven, J. A. Montgomery, Jr., J. E. Peralta, F. Ogliaro, M. Bearpark, J. J. Heyd, E. Brothers, K. N. Kudin, V. N. Staroverov, R. Kobayashi, J. Normand, K. Raghavachari, A. Rendell, J. C. Burant, S. S. Iyengar, J. Tomasi, M. Cossi, N. Rega, J. M. Millam, M. Klene, J. E. Knox, J. B. Cross, V. Bakken, C. Adamo, J. Jaramillo, R. Gomperts, R. E. Stratmann, O. Yazyev, A. J. Austin, R. Cammi, C. Pomelli, J. W. Ochterski, R. L. Martin, K. Morokuma, V. G. Zakrzewski, G. A. Voth, P. Salvador, J. J. Dannenberg, S. Dapprich, A. D. Daniels, Ö. Farkas, J. B. Foresman, J. V. Ortiz, J. Cioslowski, D. J. Fox, Gaussian, Inc., Wallingford CT, **2009**.
- [37] A. D. Becke, *J. Chem. Phys.* **1993**, *98*, 5648–5652.
- [38] C. T. Lee, W. T. Yang, R. G. Parr, *Phys. Rev. B* **1988**, *37*, 785–789.
- [39] A. K. Chandra, S. Parveen, T. Zeegers-Huyskens, *J. Phys. Chem. A* **2007**, *111*, 8884–8891.
- [40] J. N. Woodford, *J. Phys. Chem. A* **2007**, *111*, 8519–8530.
- [41] P. I. Dem'yanov, R. M. Gschwind, *Organometallics* **2006**, *25*, 5709–5723.
- [42] P. J. Stephens, F. J. Devlin, C. F. Chabalowski, M. J. Frisch, *J. Phys. Chem.* **1994**, *98*, 11623–11627.
- [43] T. Kuppens, W. Herrebout, B. van der Veken, P. Bultinck, *J. Phys. Chem. A* **2006**, *110*, 10191–10200.
- [44] L. Ducasse, F. Castet, A. Fritsch, I. Huc, T. Buffeteau, *J. Phys. Chem. A* **2007**, *111*, 5092–5098.
- [45] T. Brotin, D. Cavagnat, J.-P. Dutasta, T. Buffeteau, *J. Am. Chem. Soc.* **2006**, *128*, 5533–5540.
- [46] J. Tomasi, B. Mennucci, R. Cammi, *Chem. Rev.* **2005**, *105*, 2999–3093.
- [47] D. A. Case, T. A. Darden, T. E. Cheatham, C. L. Simmerling, J. Wang, R. E. Duke, R. Luo, K. M. Merz, D. A. Pearlman, M. Crowley, R. C. Walker, W. Zhang, B. Wang, S. Hayik, A. Roitberg, G. Seabra, K. F. Wong, F. Paesani, X. Wu, S. Brozell, V. Tsui, H. Gohlke, L. Yang, C. Tan, J. Mongan, V. Hornak, G. Cui, P. Beroza, D. H. Mathews, C. Schafmeister, W. S. Ross, P. A. Kollman, AMBER 9, University of California, San Francisco, CA, **2006**.
- [48] W. L. Jorgensen, C. Jenson, *J. Comput. Chem.* **1998**, *19*, 1179.

Received: February 21, 2012

Published online on April 27, 2012

## Vibrational absorption and vibrational circular dichroism spectra of leucine in water under different pH conditions: Hydrogen-bonding interactions with water

Mohammad Reza Poopari, Peiyan Zhu, Zahra Dezhahang, and Yunjie Xu

Citation: *J. Chem. Phys.* **137**, 194308 (2012); doi: 10.1063/1.4767401

View online: <http://dx.doi.org/10.1063/1.4767401>

View Table of Contents: <http://jcp.aip.org/resource/1/JCPSA6/v137/i19>

Published by the American Institute of Physics.

### Additional information on J. Chem. Phys.

Journal Homepage: <http://jcp.aip.org/>

Journal Information: [http://jcp.aip.org/about/about\\_the\\_journal](http://jcp.aip.org/about/about_the_journal)

Top downloads: [http://jcp.aip.org/features/most\\_downloaded](http://jcp.aip.org/features/most_downloaded)

Information for Authors: <http://jcp.aip.org/authors>

## ADVERTISEMENT

### Instruments for advanced science

#### Gas Analysis



- dynamic measurement of reaction gas streams
- catalysis and thermal analysis
- molecular beam studies
- dissolved species probes
- fermentation, environmental and ecological studies

#### Surface Science



- UHV TPD
- SIMS
- end point detection in ion beam etch
- elemental imaging - surface mapping

#### Plasma Diagnostics



- plasma source characterization
- sputter and desorption process reaction kinetic studies
- analysis of neutral and radical species

#### Vacuum Analysis



- partial pressure measurement and control of process gases
- reactive sputter process control
- vacuum diagnostics
- vacuum coating process monitoring

contact Hiden Analytical for further details

**HIDEN**  
ANALYTICAL

[info@hideninc.com](mailto:info@hideninc.com)  
[www.HidenAnalytical.com](http://www.HidenAnalytical.com)

CLICK to view our product catalogue 

# Vibrational absorption and vibrational circular dichroism spectra of leucine in water under different pH conditions: Hydrogen-bonding interactions with water

Mohammad Reza Poopari, Peiyan Zhu, Zahra Dezhahang, and Yunjie Xu<sup>a)</sup>

*Department of Chemistry, University of Alberta, Edmonton, Alberta T6G 2G2, Canada*

(Received 13 September 2012; accepted 29 October 2012; published online 21 November 2012)

Vibrational absorption (VA) and vibrational circular dichroism (VCD) spectroscopy have been used to study leucine, a flexible branched-chain amino acid, in aqueous solution. The VA spectra in the range of 1800–1250  $\text{cm}^{-1}$  of leucine in  $\text{D}_2\text{O}$  under three representative pHs from strongly acidic (pH = 1), near neutral (pH = 6), to strongly basic (pH = 13), have been measured. The related VCD spectrum has been obtained under near neutral condition. Searches have been carried out to identify the most stable conformers of the Zwitterionic, protonated, and deprotonated forms of leucine in water. The geometry optimization, harmonic frequency calculations, and VA and VCD intensities have been computed at the B3LYP/6-311++G(d,p) level with the implicit polarizable continuum solvation model. While the observed VA spectra under three pHs can be well interpreted with the inclusion of the implicit solvation model, both implicit and explicit solvation models have been found to be crucial for the adequate interpretation of the complex VCD features observed. Molecular dynamics simulations and radial distribution functions have been used to aid the modeling of the leucine-(water)<sub>N</sub> clusters. It has been recognized that the insertion of a water molecule between the  $\text{COO}^-$  and  $\text{NH}_3^+$  functional groups in the explicit solvated clusters is critical to reproduce the VCD signatures observed. Furthermore, the inclusion of the implicit bulk water environment has been found to be essential to lock water molecules, which are directly hydrogen bonded to leucine, into the positions expected in solution. The application of the explicit and implicit solvation models simultaneously allows new insights into the hydrogen bonding network surrounding leucine in aqueous solution and the role of the surrounding bulk water in stabilizing such hydrogen-bonding network. © 2012 American Institute of Physics. [<http://dx.doi.org/10.1063/1.4767401>]

## I. INTRODUCTION

Leucine is one of the essential amino acids which cannot be synthesized by animals or humans. On the other hand, it can be produced in plants or microorganisms from pyruvic acid.<sup>1</sup> Human body obtains the necessary amount of leucine by digesting it as part of proteins in human diet. Leucine is the only amino acid capable of stimulation of muscle protein synthesis<sup>2</sup> and is found to play an important role in slowing down the rate of degradation of muscle tissues by increasing the synthesis of muscle proteins.<sup>3</sup> Because of its biological importance and its relative small number of electrons which makes it amenable to high-level quantum chemistry calculations, leucine has attracted considerable interest from both experimentalists and theorists. Conformations of neutral leucine in the gas phase were investigated by jet-cooled rotational spectroscopy.<sup>4</sup> An extensive exploration of the conformational space was performed to characterize all possible gas phase structures of canonical leucine using the density functional theory (DFT) method<sup>5,6</sup> where the proton affinity and the gas phase basicity were also determined. It has been established that amino acids tend to stay in the neutral form in the gas phase,<sup>7–9</sup> whereas under physiological con-

ditions with nearly neutral pH in aqueous solution, they prefer the Zwitterionic form. Indeed, theoretical calculations indicated that zwitterions of leucine are not stable in the gas phase.<sup>10</sup> In a recent report, Rai *et al.* used DFT together with the polarizable continuous model (PCM) to study the conformations of the Zwitterionic and the canonical forms of leucine in solution.<sup>10</sup> Vibrational and dielectric properties of leucine, as well as a group of other amino acids, were studied using the DFT method implemented within the plane wave pseudopotential framework.<sup>11</sup> Ji and Shen reported a sum frequency vibrational spectroscopic study of leucine molecules at the air-water interface from solutions with different concentrations and pH values.<sup>12</sup>

In the current study, experimental vibrational absorption (VA) and vibrational circular dichroism (VCD) measurements have been utilized, in combination with molecular dynamics (MD) and DFT calculations, to investigate the dominant species and conformational distributions of leucine in aqueous solution under three representative pHs, i.e., strongly acidic (pH = 1), near neutral (pH = 6), and strongly basic (pH = 13). Experimental and theoretical VCD spectroscopic studies of some amino acids were reported before.<sup>13</sup> VCD spectroscopy, which measures the differential absorption of the left versus right circularly polarized light by a chiral molecule, is highly sensitive to subtle conformational changes and to intermolecular interactions of chiral solutes with water.<sup>14–18</sup>

<sup>a)</sup> Author to whom correspondence should be addressed. Electronic mail: [yunjie.xu@ualberta.ca](mailto:yunjie.xu@ualberta.ca). Tel.: 1-780-492-1244. Fax: 1-780-492-8231.



The most stable conformers of the Zwitterionic, protonated and deprotonated leucine in water have been identified. Both implicit and explicit solvation models have been considered to account for the solvent effects. While the VA spectra of leucine under three pH conditions can be adequately interpreted using the implicit PCM, the complex and delicate VCD features require detailed analyses of the hydrogen bonding interactions between leucine and water molecules. The radial distribution function (RDF) analysis has been performed to aid the constructions of the explicit solvation model, i.e., the leucine-(water)<sub>N</sub> clusters. Some very interesting different behaviors have been observed between the leucine-(water)<sub>N</sub> clusters in the gas phase and with the PCM of water. These observations have been discussed in terms of the role that the bulk water environment plays in stabilizing or destabilizing the hydrogen bonding interactions between water molecules and leucine. Further discussions about the importance of the choice of the leucine-(water)<sub>N</sub> clusters used and their initial conformations have also been presented. It has been found that inclusion of implicit solvation model, i.e., PCM, together with the explicit solvation model is crucial to capture the experimentally observed spectral features.

## II. EXPERIMENTAL AND COMPUTATIONAL DETAILS

### A. VA and VCD measurements

L-, D-, and racemic-leucine (98%, 99%, and 99% purity, respectively) were purchased from Sigma Aldrich and used without further purification. All samples were prepared by dissolving leucine in D<sub>2</sub>O solvent (purity 99.9%) in order to access the finger print region from 1800 to 1250 cm<sup>-1</sup>. To record the VA and VCD spectra, a Fourier transform infrared spectrometer (Vertex 70, Bruker) with a VCD optical bench (PMA 50) is used. A sample cell which consists of a pair of BaF<sub>2</sub> windows and a Teflon spacer between them was used. Leucine is considered a hydrophobic amino acid because of its branched aliphatic side-chain, i.e., isobutyl group, (CH<sub>3</sub>)<sub>2</sub>CH. As a result, its solubility in water is strongly reduced. This low solubility makes it challenging to perform VCD measurements of leucine in water. To minimize solvent interference and to optimize the experimental condition for VCD measurements, a concentration of 0.15 M with a path length of 50 μm were used. The VA spectra were measured at three representative pHs, i.e., pH = 1, pH = 6, and pH = 13 corresponding to the strongly acidic, near neutral, and strongly basic condition, respectively. The acidic and basic conditions were obtained by adding concentrated DCl and NaOD dropwise to reach the desired pHs. The VCD intensities under the strongly acidic and basic conditions were found to be very weak. Consequently, reliable VCD measurements could not be obtained for these conditions. Therefore, only VCD spectrum obtained under neutral condition is reported. The raw VCD spectrum was measured with a total collection time of 4 h (4 × 1 h) and a resolution of 4 cm<sup>-1</sup>. Although the racemic leucine is also available commercially, its solubility in water is much lower than the enantiopure samples and was, therefore, not used for the VCD measurements. The final VCD spectra were obtained by subtracting the solvent measurements under identical conditions. The D- and L-leucine

VCD spectra show good mirror image quality. For simplicity, we use L-leucine throughout the paper.

### B. DFT calculations

GAUSSIAN09 suite of programs has been used to perform all geometry optimizations, potential energy surface scan, harmonic frequency calculations, and the VA and VCD intensities predictions.<sup>19</sup> The Becke, three-parameter, Lee-Yang-Parr (B3LYP), combined with a triple zeta basis set with the addition of two polarization and diffuse functions, i.e., 6-311++G (d,p), have been used for all the geometry searches and optimizations of the most stable conformers of the protonated, deprotonated, and Zwitterionic forms of leucine and the Zwitterionic leucine-(water)<sub>N</sub> clusters. For leucine in D<sub>2</sub>O, there is D/H exchange and all the hydrogen atoms in the OH and NH groups of leucine were replaced by D in the calculations. The integral equation formalism version of PCM<sup>20</sup> using the universal force field radii was applied in order to account for the effects of solvent water molecules implicitly. For this purpose, the dielectric constant of water, 78.3553, was used. A Lorentzian line shape with a half-width at half-height of 4 cm<sup>-1</sup> was used for the simulations of VA and VCD spectra. No scaling factor was applied to the harmonic frequencies.

### C. MD simulations

MD simulations were performed for leucine in water using PMEMD module built in the AMBER 11 suite packages.<sup>21</sup> The goal was to locate the most likely hydrogen bonding sites between leucine and water and to estimate the number of water molecules directly hydrogen bonded to leucine. To build up the initial configuration for MD simulations, the xLeap graphical interface was utilized. The AMBER ff99 force field based on molecular mechanics was used. A leucine molecule was solvated with 620 pre-equilibrated TIP3P water molecules in a rectangular periodic box with a cut-off of 10 Å. Initial minimization was performed in two sequential steps. First, to remove any bad contacts, 1000 steps of the steepest descent algorithm were used and then 1000 steps of the conjugate gradient algorithm were applied. Second, a 600 ps heating and equilibrating MD simulation was performed under NVT conditions for the configuration obtained from the minimization process. In this step, the system was first heated from 0 to 300 K in 200 ps and then was equilibrated at 300 K for 400 ps to ensure that the equilibrium was reached. Finally, a 5 ns MD production was carried out under NPT condition at 300 K and with a time step of 2 fs. To estimate the number of water molecules directly hydrogen bonded to leucine, the related RDFs have been calculated based on the MD results and analyzed.

## III. RESULTS AND DISCUSSIONS

### A. Experimental and simulated VA spectra under three pH conditions

It was recognized in our initial conformational searches in the gas phase and with the PCM of water that the amine

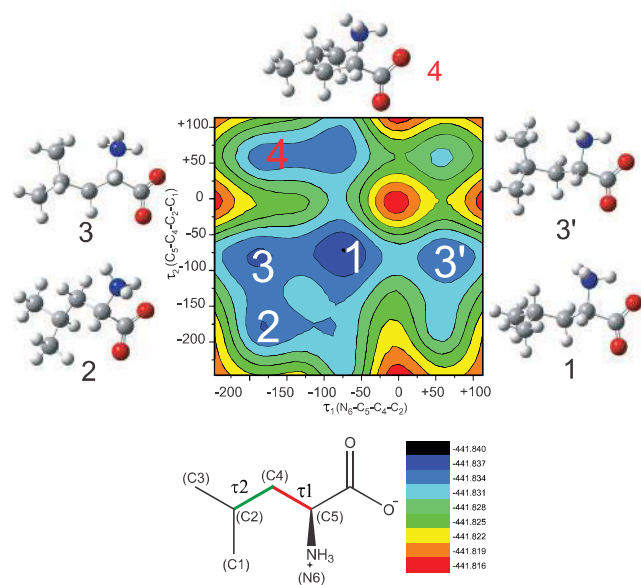


FIG. 1. Two-dimensional PES plot of the Zwitterionic form of leucine at the B3LYP/6-311++G(d,p) level, scanned along its two dihedral angles,  $\tau_1$  and  $\tau_2$  (in degree). The atom labelling of leucine and the two C–C bonds associated with these two dihedral angles are shown at the bottom. The energy unit is in hartree. Several low energy minima are indicated, together with the corresponding conformations.

group tends to make intramolecular hydrogen bonding interactions with its adjacent  $\text{COO}^-$  or  $\text{COOH}$  group, making this part molecule almost rigid. Two dihedral angles, namely,  $\tau_1$  ( $\text{N}_6\text{-C}_5\text{-C}_4\text{-C}_2$ ) and  $\tau_2$  ( $\text{C}_5\text{-C}_4\text{-C}_2\text{-C}_1$ ) (see Figure 1 for atom labelling), corresponding to the rotations around the two C–C bonds, are the most effective dihedral angles in generating new conformations. It was also recognized that the inclusion of the implicit water solvent could have substantial effects on the resulting conformations of flexible chiral molecules. Therefore, it is desirable to include the PCM of water in the initial geometry searches. A potential energy surface (PES) scan along these two dihedral angles was carried out at the B3LYP/6-311++G(d,p) level with the PCM of water for the Zwitterionic form of leucine. In the previous theoretical studies of leucine, conformational searches had been carried out for the neutral species in the gas phase<sup>4–6</sup> and for the Zwitterionic species at a lower level with B3LYP/6-311G(d).<sup>10</sup> The resulting PES is shown in Figure 1. Several minima were found and those which are potentially important at room temperature are indicated in the figure.

Final geometry optimizations at the B3LYP/6-311++G(d,p) level with the PCM of water were carried out for the minima identified in the PES scan. The harmonic frequency calculations at the same level of theory were then performed to verify whether the optimized geometries are true minima or not. No imaginary frequency was detected for all the stable structures identified. As it turned out, the conformer at 3' changed into the same one at 3 (see Figure 1) during the optimization process. The conformer at 4 has negligible contribution at room temperature and is not considered in the later calculations. Similar searches were performed for the protonated and deprotonated species. Figure 2 summarizes the three most stable structures of the Zwitterionic, protonated,

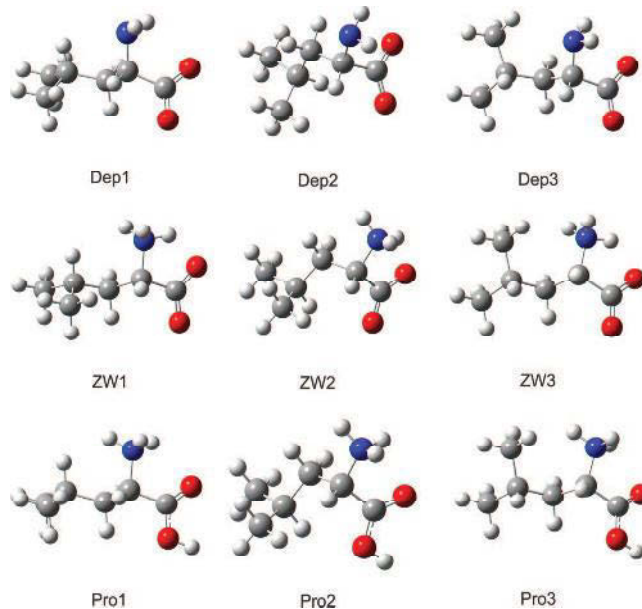


FIG. 2. Three most stable structures of the deprotonated (top), Zwitterionic (middle), and protonated (bottom) forms of leucine obtained at the B3LYP/6-311++G(d,p) level with the PCM of water.

and deprotonated forms of leucine obtained. Table I lists the relative zero-point corrected energies and Gibbs free energies of the three most stable conformers of the three species obtained at the B3LYP/6-311++G(d,p) level with the PCM of water. The Boltzmann percentage population factors at 298 K of the three most stable conformers in each category are also listed.

In Figure 3, the experimental VA spectra in  $\text{D}_2\text{O}$  obtained at the three aforementioned pHs are compared with the population weighted VA spectra of the deprotonated, Zwitterionic, and protonated forms of leucine. The VA spectra at these three pHs are noticeably different, characteristic of the existence of different dominant species under each pH. One main difference is the band positions of the carbonyl stretches of the carboxylic groups. Such difference is nicely captured by the calculated VA spectra of the three leucine species. Under the strongly acidic condition where the protonated form of leucine is expected to be the main species, the  $\text{C}=\text{O}$  stretch

TABLE I. The relative zero-point energy corrected total energies and Gibbs free energies of the three most stable conformers of the Zwitterionic, deprotonated, and protonated forms of leucine at the B3LYP/6-311++G(d,p) level with the PCM of water, together with their percentage Boltzmann population factors at 298 K.

Conformers	$\Delta E$ (kJ/mol)	Pop%– $\Delta E$	$\Delta G$ (kJ/mol)	Pop%– $\Delta G$
ZW1	0	80.4	0	88.5
ZW2	5.82	7.7	6.45	6.5
ZW3	5.67	8.1	8.08	3.4
DEP1	0	74.1	0	90.7
DEP2	2.82	23.8	6.14	7.6
DEP3	8.82	2.1	9.93	1.7
PRO1	0	76.1	0	83.9
PRO2	3.42	19.1	4.50	13.8
PRO3	6.82	4.9	8.98	2.2

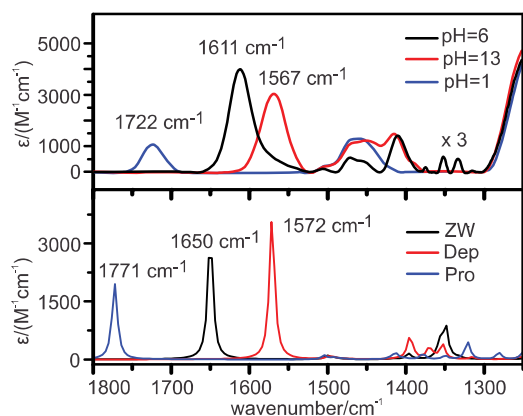


FIG. 3. Comparison of the experimental VA spectra of leucine under three representative pH conditions with the simulated VA spectra of the most stable conformer of the deprotonated, Zwitterionic, and protonated forms of leucine at 298 K.

appears at the highest wavenumber,  $1723\text{ cm}^{-1}$ . This observation is consistent with the fact that this C=O stretch is from the COOH group. In the near neutral solution, a  $112\text{ cm}^{-1}$  redshift from the acidic solution is observed for the C=O stretch. This is because the Zwitterionic form of leucine becomes dominant and the corresponding asymmetric carboxylate stretch emerges at  $1611\text{ cm}^{-1}$ . Lastly, another  $43\text{ cm}^{-1}$  redshift is seen when the pH value reaches  $\sim 13$ , i.e., under strongly basic condition. This additional redshift is due to the changes in the intramolecular hydrogen bonding interactions, going from  $\text{COO}^-\cdots\text{H}_3\text{N}^+$  in the Zwitterionic form of leucine to  $\text{COO}^-\cdots\text{H}_2\text{N}$  in the deprotonated form. We also further checked if one could discriminate the neutral and Zwitterionic species of leucine by using the VA data alone. The simulated VA spectra of the two most stable Zwitterionic and neutral leucine conformers, i.e., ZW1, ZW2, Neu1, and Neu2, respectively, are provided in Figure 4, together with the experimental VA spectrum under near neutral condition. At this pH, the most intense experimental peak appears at  $1611\text{ cm}^{-1}$ , corresponding well to the simulated peaks of ZW1 at  $1648\text{ cm}^{-1}$  and ZW2 at about  $1650\text{ cm}^{-1}$ , whereas

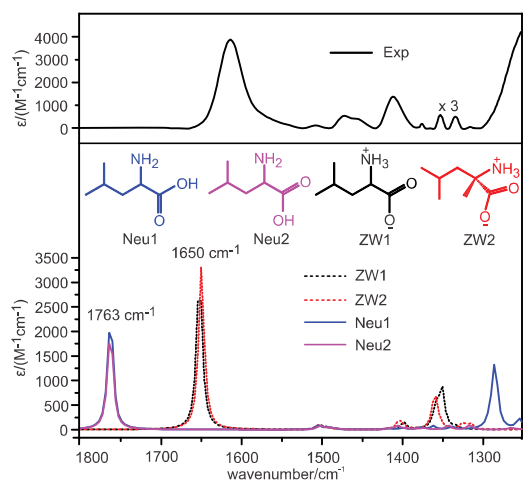


FIG. 4. Comparison of the VA spectra of the two most stable conformers of the Zwitterionic and neutral forms of leucine and the experimental VA spectrum under near neutral condition.

the associated peaks of Neu1 and Neu2 emerge at a much higher wavenumber of  $1763\text{ cm}^{-1}$ . Clearly, the dominant species of leucine under near neutral pH condition is in the Zwitterionic form. Overall, the VA pattern is highly structural sensitive and can be used to tell apart different dominant species in this case by focusing on the carbonyl stretch region. Detailed assignments for the lower frequency region are less obvious because of severe peak-overlapping, although the general patterns predicted for ZW1 and ZW2 are roughly consistent with the experimental data. It appears that the VA data can be well interpreted without the detailed consideration of the explicit hydrogen bonding interactions between leucine and water molecules. The situation is, however, different with the VCD measurements (see Sec. III B).

## B. Explicit and implicit solvent effects in the VCD spectrum under neutral condition

Although the VA spectra can be satisfactorily interpreted by modeling leucine with the PCM of water, the VCD spectrum obtained under neutral condition, on the other hand, could not be well interpreted without considering the explicit hydrogen bonding interactions of leucine with water molecules. This can be seen by comparing the experimental data with the simulated VA and VCD spectra of ZW1 and ZW2 in the gas phase and with the PCM of water (Figure S1 of the supplementary material<sup>22</sup>). To systematically investigate such effects, we started with the construction of leucine-(water)<sub>N</sub> clusters based on the MD calculations performed. RDF measures the probability of finding an atom at certain distance from a center atom of interest over the whole simulation time. The analysis of such RDFs can help to identify the number of water molecules directly hydrogen bonded to leucine. Figure 5 shows the RDF calculations carried out for the Zwitterionic form of leucine. Each RDF reaches its first

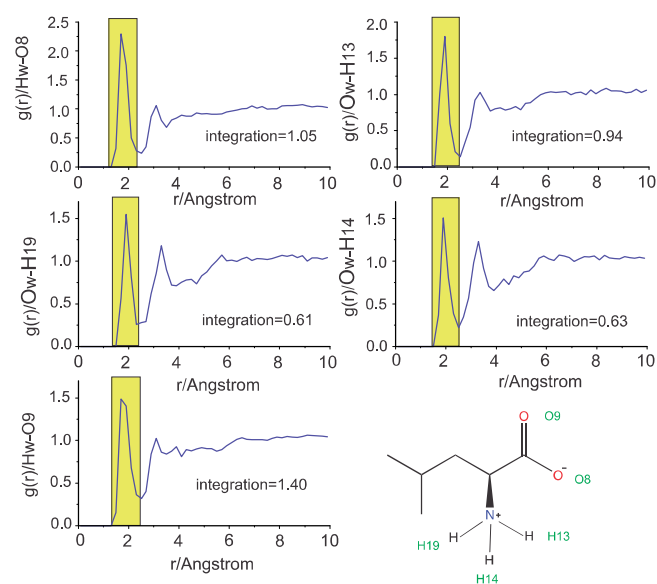


FIG. 5. RDFs obtained from the MD simulations of the Zwitterionic form of leucine in water. The atom labelling of leucine used in the graphs is presented at the bottom. H<sub>W</sub> and O<sub>W</sub> refer to the hydrogen and oxygen atom of water molecules, respectively.

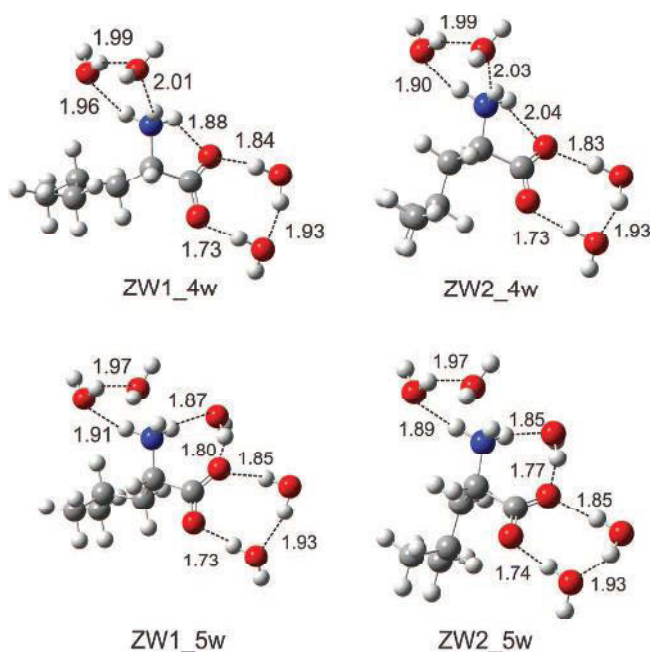


FIG. 6. Optimized geometries of the most stable conformers of the Zwitterionic leucine-(water)<sub>4,5</sub> clusters at the B3LYP/6-311++G(d,p) level with the PCM of water. The important hydrogen bonding lengths (in Å) are also indicated.

maximum at  $\sim 1.75$  Å with a well-defined sharp peak, indicating the hydrogen bonding nature of the interactions. Integration of this first peak out to the minimum provides the water coordination numbers which are also included in the figure. For example, the integrals for the RDFs centered at the two oxygen atoms of the carboxylate group are roughly 1 in each case, suggesting that the  $\text{COO}^-$  are explicitly solvated by about two water molecules on average. The corresponding integration values for the three H atoms of  $\text{NH}_3^+$  are between 0.6 and 1, indicating the existence of about one water molecule per binding site. Altogether, about four to five water molecules are directly hydrogen bonded to leucine on average. Based on the MD snapshots and chemical intuition, two different hydrogen bonding configurations were proposed. Both with two water molecules hydrogen bonded

to  $\text{COO}^-$ . At the amine site, one configuration involves two water molecules hydrogen bonded to the two amine hydrogen atoms, while the third amine hydrogen atom is intramolecular hydrogen bonded to  $\text{COO}^-$ . The other one has the third amine hydrogen atom also involved in intermolecular hydrogen bonding with water. The above considerations lead to the leucine-(water)<sub>4</sub> and leucine-(water)<sub>5</sub> clusters. Since the first two most stable Zwitterionic leucine monomeric conformers carry more than 95% of the total population, we used only these two dominant Zwitterionic leucine conformers to build the leucine-(water)<sub>N</sub> clusters. The explicit hydrogen bonded solvated water clusters based on these two leucine conformers with 4 or 5 water molecules are ZW1\_4w, ZW2\_4w, ZW1\_5w, and ZW2\_5w (see Figure 6). These structures are also optimized at the B3LYP/6-311++G(d,p) level with the PCM of water. The optimized geometries are summarized in Figure 6. The Cartesian coordinates of the relevant species at the PCM/B3LYP/6-311++G(d,p) level are provided in Table S1–S3 of the supplementary material.<sup>22</sup>

It is worthwhile to point out some interesting observations about these water solvated clusters during their geometry optimizations in the gas phase and with the PCM of water. We observed, for example, that in the optimization of ZW1\_4w, the structure converged more quickly with the inclusion of the PCM of water than in the gas phase, using the same initial geometry. The optimization step number is 33 and 77 for with the PCM of water and in the gas phase, respectively. This observation is illustrated in Figure 7. In the gas phase, the system experienced a good number of large oscillations before finally converged. This is because the water molecules can move freely and attempt to maximize the possible hydrogen bonding interactions primarily among themselves and also with leucine. The inclusion of the PCM of water provides a dielectric medium which also restricts the movement of the water molecules involved and directs them to best solvate the solute molecule. It, therefore, prevents severe alternations in the hydrogen bonding arrangements, resulting in smoother and faster geometry optimizations of such solvated clusters in solution. It is also worth mentioning that the total job cpu time for the PCM calculation was almost one third of that for the gas phase calculation. It was noted

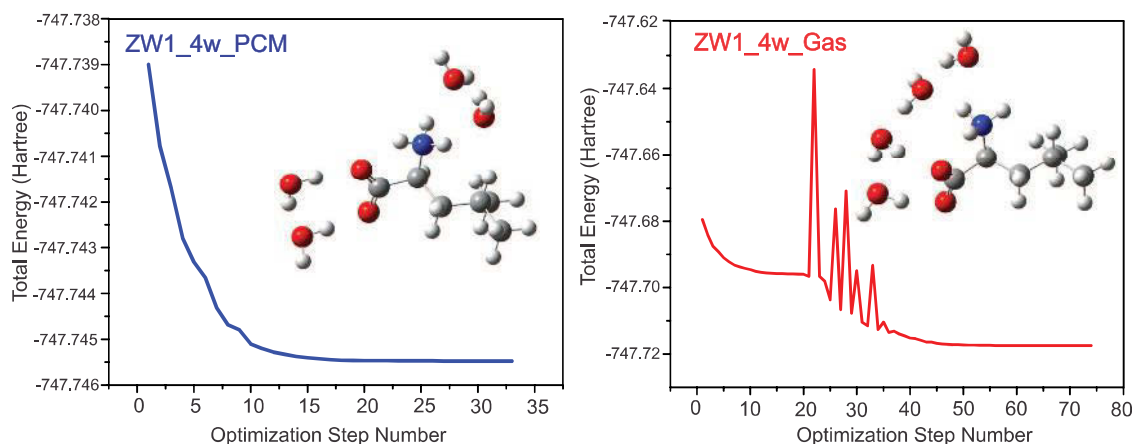


FIG. 7. Comparison of the optimization step numbers of ZW1\_4w at the B3LYP/6-311++G(d,p) level with the PCM of water (left) and in the gas phase (right).

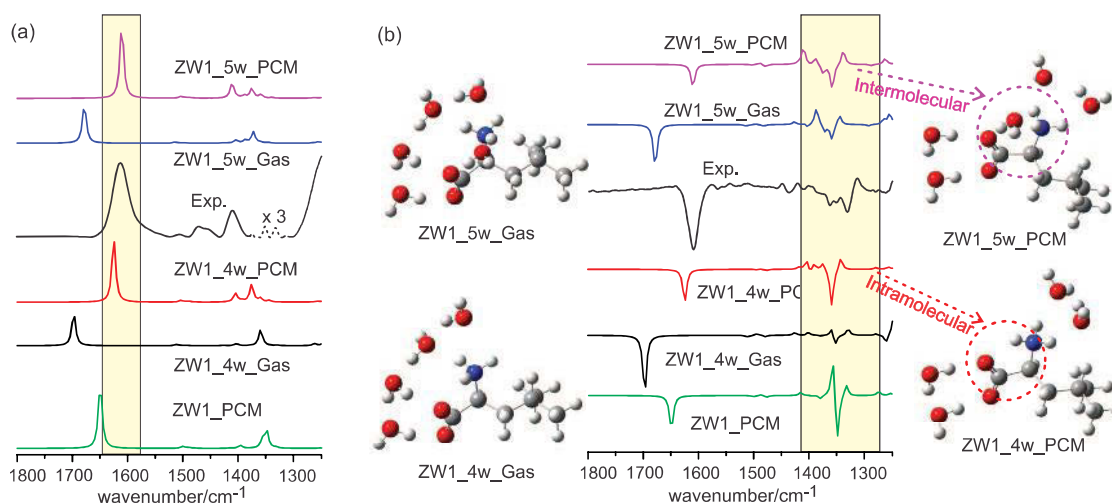


FIG. 8. Comparison of the VA (a) and VCD (b) spectra of ZW1\_4w and ZW1\_5w in the gas phase and with the PCM of water with the corresponding experimental data under near neutral condition.

by ourselves and in some previous publications<sup>23</sup> that the inclusion of the PCM of water may sometimes tear apart the intermolecular hydrogen bonding interactions between chiral solute and water molecules proposed in the initial solvated water clusters. In retrospect, those initial geometries proposed were most likely based largely on maximizing the possible hydrogen bonds among water molecules and with solute, i.e., to stabilize the small solvated clusters without the bulk solvent environment. It is, therefore, not too surprising that such proposed clusters may not be favored in solution. The present initial structures, on the other hand, were proposed based on the MD snapshots when bulk solvent had been included. These discussions highlight the importance of choosing the suitable initial geometries of the solvated water clusters. The main point is that the faster optimization we observed with PCM is due to the fact that the initial geometry of the leucine-(water)<sub>N</sub> cluster based on the MD snapshots is much closer to the true explicitly solvated cluster in water than that based on the lowest energy gas phase solvated cluster. Overall, the explicit solvation arrangement between solute and water molecules in solution is more faithfully captured when the bulk solvent environment is taken into account than in the gas phase.

The calculated VA and VCD spectra of the ZW1\_4w and ZW1\_5w clusters in the gas phase and with the PCM of water are compared with the related experimental data in Figure 8. The calculated VA and VCD spectra of ZW1 with the PCM of water are also included in Figure 8, while ZW1 by itself is unstable in the gas phase. It is clear that ZW1 with the PCM of water provides poor agreement with the experimental spectra, especially the VCD spectral features. Since the ZW2\_4w and ZW2\_5w clusters carry only about 6% of the total population, to simplify the following discussions, we focus only on the ZW1-(water)<sub>4,5</sub> clusters. The corresponding VA and VCD spectra of ZW2-(water)<sub>4,5</sub> clusters in the gas phase and with the PCM of water are given in Figure S2 of the supplementary material.<sup>22</sup> The robust mode calculations for ZW1-(water)<sub>5</sub> are summarized in Table S4 of the supplementary material.<sup>22</sup> As can be seen from Table S4, most of the strong to medium VCD features in the observed MI-VCD spectrum

are robust, except the COO<sup>-</sup> band at 1611 cm<sup>-1</sup>. From the VA spectral comparison in Figure 8(a), the carboxylic vibrational mode positions predicted with PCM, highlighted in the figure, are in better agreement with the experiment than the gas phase ones. In fact, the gas phase predictions for both 4w and 5w water solvated clusters are blueshifted by more than 50 cm<sup>-1</sup>. It also appears that the relative intensities of the most prominent observed VA bands in the 1500–1350 cm<sup>-1</sup> region are better presented with the inclusions of both the explicit and implicit water solvation models than with the implicit model alone. For the VCD spectral comparison, the delicate and complex signatures observed in the 1500–1300 cm<sup>-1</sup> region in the highlighted part of Figure 8(b) is best captured by the +/+/-/-/+ VCD bands of ZW1\_5w with the PCM of water. It was recognized through closer examination that the insertion of a water molecule between the COO<sup>-</sup> and the NH<sub>3</sub><sup>+</sup> groups, which is locked into the position by the inclusion of the PCM of water, is important to reproduce such complex VCD features. Without such an insertion, such as in ZW1\_4w, the complex VCD signatures could not be reproduced. The usage of the PCM of water, as discussed before, is an essential and economic means to adequately account for the bulk water environment. To achieve similar results with explicit water molecules, it would require additional layers of water molecules in order to provide a faithful representation of the continuous solvent environment. Such modeling is computationally much more expensive.

#### IV. CONCLUSIONS

VA and VCD spectra of leucine in water under three representative pHs have been evaluated. The measured VA spectra clearly show the existence of different species under strongly acidic, nearly neutral, and strongly basic. Such differences have been well interpreted with the calculated VA spectra of the protonated, Zwitterionic, and deprotonated leucine conformers with the PCM of water. The complex and delicate VCD spectral signatures obtained for leucine in water

under near neutral condition, on the other hand, require the consideration of both explicit and implicit solvation models. It was found that the insertion of a water molecule between the  $\text{COO}^-$  and  $\text{NH}_3^+$  functional groups is critical to reproduce the complex VCD signatures observed. Furthermore, the inclusion of the PCM of water is essential to lock water molecules which are directly hydrogen bonded to leucine into the positions expected in solution. Some interesting behaviors of the explicit solvated water clusters were observed during their geometry optimizations with and without PCM. Such behaviors have been discussed in terms of the effects of bulk water environment and the initial geometries proposed. To faithfully account for the solvent effects of leucine in water, the inclusion of the implicit solvent model combined with the explicit water solvated clusters has been found to be critical.

## ACKNOWLEDGMENTS

This research was funded by the University of Alberta, the Natural Sciences and Engineering Research Council of Canada. We thank Dr. G. Yang for discussions at the early stage of this project. We also gratefully acknowledge access to the computing facilities provided by the Academic Information and Communication Technology group at the University of Alberta and by the Western Canada Research Grid (Westgrid). Y.X. holds a Tier I Canada Research Chair in Chirality and Chirality Recognition.

<sup>1</sup>D. L. Nelson and M. M. Cox, *Lehninger Principles of Biochemistry*, 3rd Ed. (Worth Publishing, New York, 2000).

<sup>2</sup>M. R. Etzel, "Manufacture and use of dairy protein fractions," *J. Nutr.* **134**(4), 996S (2004).

<sup>3</sup>L. Combaret, D. Dardevet, I. Rieu, M. Pouch, D. Béchet, D. Taillandier, J. Grizard, and D. Attaix, *J. Physiol.* **569**, 489 (2005).

<sup>4</sup>E. J. Cocinero, A. Lesarri, J. Grabow, J. C. Lopez, and J. L. Alonso, *ChemPhysChem* **8**, 599 (2007).

<sup>5</sup>A. K. Rai, C. Song, and Z. Lin, *Spectrochim. Acta, Part A* **73**(5), 865 (2009).

<sup>6</sup>S. Dokmaïrijan, V. S. Lee, and P. Nimmanpipug, *J. Mol. Struct.: THEOCHEM* **953**, 28 (2010).

<sup>7</sup>M. J. Locke and R. T. McIver, Jr., *J. Am. Chem. Soc.* **105**, 4226 (1983).

<sup>8</sup>P. D. Godfrey and R. D. Brown, *J. Am. Chem. Soc.* **117**, 2019 (1995).

<sup>9</sup>M. Chen, Z. Huang, and Z. Lin, *J. Mol. Struct.* **719**, 153 (2005).

<sup>10</sup>A. K. Rai, X. Xu, Z. Lin, and D. K. Rai, *Vib. Spectrosc.* **56**, 74 (2011).

<sup>11</sup>P. R. Tulip and S. J. Clark, *J. Chem. Phys.* **121**, 5201 (2004).

<sup>12</sup>N. Ji and Y.-R. Shen, *J. Chem. Phys.* **120**, 7107 (2004).

<sup>13</sup>Z. Ji, R. Santamaria, and I. L. Garzon, *J. Phys. Chem. A* **114**, 3591 (2010); P. Zhang and P. L. Polavarapu, *Appl. Spectrosc.* **60**, 378 (2006); E. Tajkhorshid, K. J. Jalkanen, and S. Suhai, *J. Phys. Chem. B* **102**, 5899 (1998).

<sup>14</sup>M. Losada and Y. Xu, *Phys. Chem. Chem. Phys.* **9**, 3127 (2007).

<sup>15</sup>M. Losada, H. Tran, and Y. Xu, *J. Chem. Phys.* **128**, 014508/1-11 (2008); M. Losada, P. Nguyen, and Y. Xu, *J. Phys. Chem. A* **112**, 5621 (2008).

<sup>16</sup>G. Yang and Y. Xu, "Vibrational circular dichroism spectroscopy of chiral molecules," in *Electronic and Magnetic Properties of Chiral Molecules and Supramolecular Architectures*, edited by R. Naaman, D. N. Beratan, D. H. Waldeck (Springer-Verlag, Berlin, 2011) [*Top. Curr. Chem.* **298**, 189–236 (2011)]; G. Yang and Y. Xu, *J. Chem. Phys.* **130**, 164506 (2009).

<sup>17</sup>J. Sadlej, J. C. Dobrowolski, and J. E. Rode, *Chem. Soc. Rev.* **39**, 1478 (2010).

<sup>18</sup>P. Zhu, G. Yang, M. R. Poopari, Z. Bie, and Y. Xu, *ChemPhysChem* **13**, 1272 (2012); M. R. Poopari, Z. Dezhahang, G. Yang, and Y. Xu, *ibid.* **13**, 2310 (2012).

<sup>19</sup>M. J. Frisch, G. W. Trucks, H. B. Schlegel *et al.*, GAUSSIAN 09, Revision B.01, Gaussian, Inc., Wallingford, CT, 2009.

<sup>20</sup>J. Tomasi, B. Mennucci, and R. Cammi, *Chem. Rev.* **105**, 2999 (2005).

<sup>21</sup>D. A. Case, T. A. Darden, T. E. Cheatham III, C. L. Simmerling, J. Wang, R. E. Duke, R. Luo, R. C. Walker, W. Zhang, K. M. Merz, B. Roberts, B. Wang, S. Hayik, A. Roitberg, G. Seabra, I. Kolossváry, K. F. Wong, F. Paesani, J. Vanicek, J. Liu, X. Wu, S. R. Brozell, T. Steinbrecher, H. Gohlke, Q. Cai, X. Ye, J. Wang, M.-J. Hsieh, G. Cui, D. R. Roe, D. H. Mathews, M. G. Seetin, C. Sagui, V. Babin, T. Luchko, S. Gusarov, A. Kovalenko, and P. A. Kollman, AMBER 11, University of California, San Francisco, 2010.

<sup>22</sup>See supplementary material at <http://dx.doi.org/10.1063/1.4767401> for VA and VCD spectra of some leucine and leucine-(water)<sub>N</sub> conformers in the gas phase and with the PCM of water.

<sup>23</sup>V. W. Jürgensen and K. Jalkanen, *Phys. Biol.* **3**, S63 (2006).

# A comparative VCD study of methyl mandelate in methanol, dimethyl sulfoxide, and chloroform: explicit and implicit solvation models†

Cite this: *Phys. Chem. Chem. Phys.*, 2013, **15**, 1655

Mohammad Reza Poopari, Zahra Dezhahang and Yunjie Xu\*

Vibrational absorption (VA) and vibrational circular dichroism (VCD) spectra of methyl mandelate, a prototype chiral molecule, in a series of organic solvents, namely methanol (MeOH- $d_4$ ), dimethyl sulfoxide (DMSO- $d_6$ ), and chloroform (CDCl<sub>3</sub>), have been measured in the finger print region from 1800 to 1150  $\text{cm}^{-1}$ . Implicit solvation models in the form of polarizable continuum model and explicit solvation models have been employed independently and simultaneously. The goal is to evaluate their efficiencies in dealing with solvent effects in each solution and to establish a general strategy to adequately account for effects of solvents. Molecular dynamics (MD) simulation and radial distribution function analysis have been performed to aid the construction of the explicit solvation models. Initial geometry searches have been carried out at the B3LYP/6-31G(d) level for the methyl mandelate monomer and its explicit 1 : 1 and 1 : 2 solute–solvent hydrogen-bonded complexes. B3LYP/cc-pVTZ has been used for all the final geometry optimizations, the vibrational frequency, VA and VCD intensity, and optical rotation dispersion (ORD) calculations. The results show that inclusion of solvent explicitly and implicitly at the same time has significant impacts on the appearance of the VA and VCD spectra, and is crucial for reliable spectral assignments when solvents are capable of hydrogen-bonding interactions with solutes. When no strong solvent–solute hydrogen-bonding interactions in the case of chloroform are expected, the gas phase monomer model is adequate for spectral interpretation, while inclusion of implicit solvation improves the frequency agreement with experiment. ORD spectra of methyl mandelate in the aforementioned solvents at different concentrations under 5 excitation wavelengths have also been measured. The comparison between the calculated and the experimental ORD spectra supports the conclusions drawn from the VA and VCD investigations.

Received 5th August 2012,  
Accepted 29th November 2012

DOI: 10.1039/c2cp42722b

[www.rsc.org/pccp](http://www.rsc.org/pccp)

## Introduction

Chiroptical spectroscopy, such as vibrational circular dichroism (VCD) spectroscopy, in combination with density functional theory (DFT) calculations, has emerged in recent years as a powerful new tool to probe absolute configurations and conformations of chiral molecules in solution.<sup>1,2</sup> To achieve a reliable interpretation, it is often necessary to consider effects of solvents since solvents can have significant and non-intuitive effects on the corresponding chiroptical measurements.<sup>3–5</sup> For example, the VCD features of peptides and natural products may vary considerably depending on the solvent properties.<sup>6–8</sup> It has been demonstrated experimentally that the water bending vibrational mode can gain markedly

VCD intensity in chiral aqueous solutions<sup>9–13</sup> and such chirality transfer VCD signatures are highly sensitive to the hydrogen-bonding network consisting of the chiral solute and the surrounding water molecules.<sup>14,15</sup> For example, chirality transfer effects and effects of solvent in general in the VCD spectra of methyl lactate, a simple chiral  $\alpha$ -hydroxyester, in water<sup>9</sup> and in methanol,<sup>16</sup> have been investigated.

Methyl mandelate (MM), methyl 2-hydroxy-2-phenylacetate (IUPAC), is a relatively small chiral  $\alpha$ -hydroxyester with multifunctional groups, including a phenyl ring. It was chosen as the model chiral molecule for investigation of solvent effects because it has a few interesting features. First, it has three electronegative atoms and a hydroxyl hydrogen atom, thus offering a range of intermolecular hydrogen-bonding options with suitable solvent molecules in solution. Second, as an  $\alpha$ -hydroxyester, it has an intramolecular OH $\cdots$ O=C hydrogen bond, providing the opportunity to examine the competition between intra- and intermolecular hydrogen bonding interactions. Third, the presence of a phenyl

Department of Chemistry, University of Alberta, Edmonton, Alberta, Canada T6G 2G2.  
E-mail: [yunjie.xu@ualberta.ca](mailto:yunjie.xu@ualberta.ca); Fax: +1-780-492-8231; Tel: +1-780-492-1244

† Electronic supplementary information (ESI) available. See DOI: 10.1039/c2cp42722b

ring with delocalized electrons may give rise to different chemistry compared to methyl lactate and influence the closeness and orientation of solvent molecules that are hydrogen-bonded to MM. Indeed, the solubility of MM in aqueous solution is much lower than methyl lactate because of the replacement of its methyl group by a bulky and more polarizable phenyl group. On the other hand, MM is highly soluble in organic solvents such as methanol, dimethyl sulfoxide (DMSO), and chloroform. While vibrational absorption (VA) spectra of MM in carbon tetrachloride were investigated before,<sup>17</sup> its VCD spectra in the CH and OH stretching regions were also reported previously.<sup>18</sup> Kuppens *et al.* used MM as an example to showcase VCD spectroscopy as a powerful tool to determine absolute configurations of chiral molecules in solution.<sup>19</sup> Le Barbu-Debus *et al.* probed chiral recognition between MM and methyl glycolate and between MM and methyl lactate in the gas phase by means of IR/UV double-resonance spectroscopy.<sup>20</sup> More recently, Albrecht *et al.* studied the self-aggregation pattern of MM and unravelled the influence of relative chirality of the aggregating monomers by means of several spectroscopic techniques, such as matrix-Fourier transform infrared (FTIR) and jet-FTIR spectroscopy.<sup>21</sup> Finally, MM and its associated free mandelic acid are also of practical importance in the field of enantioselective chemistry for their usage in separation of racemates.<sup>22</sup>

In the current study, VA and VCD spectra of MM in a series of organic solvents, namely methanol, dimethyl sulfoxide, and chloroform have been measured to unveil the effects of MM-solvent interactions. The main focus is on how different degrees of hydrogen-bonding capability of solvents influence the outcome of VCD measurements and on developing a strategy to model the solvent effects adequately in all cases. Molecular dynamics (MD) simulation and the corresponding radial distribution functions (RDFs) have been utilized to examine how the MM molecules behave in methanol solution. To properly account for solvation effects, both the implicit polarizable continuum model (PCM) and the explicit solvation model have been considered separately and jointly. As pointed out by Polavarapu and co-workers, a combination of different chiroptical techniques usually give rise to more reliable interpretations of chiroptical measurements.<sup>23</sup> This is because different chiroptical techniques, such as VCD spectroscopy and optical rotation dispersion (ORD) spectroscopy, are all sensitive to environmental perturbations but with various degrees of sensitivity to specific chemical and physical properties. We have therefore further carried out experimental ORD measurements and theoretical modeling to verify if the conclusions reached with the VA and VCD investigations are also supported by the ORD studies.

## Experimental and theoretical details

### FTIR VA and VCD measurements

(*S*)-(+)-MM (99%), (*R*)-(–)-MM (99%), and the racemic MM were purchased from Alfa Aesar and used without further purification. Three different solvents, *i.e.* MeOH-*d*<sub>4</sub>, DMSO-*d*<sub>6</sub>, and CDCl<sub>3</sub>, all fully-deuterated, were purchased from Sigma Aldrich and used for the VA and VCD measurements. The corresponding spectra

of MM in carbon tetrachloride which have been reported before<sup>19</sup> were re-measured to provide comparison with those obtained in the other three solvents. The experimental VA and VCD spectra were obtained using an FTIR spectrometer (Vertex 70, Bruker) equipped with a VCD module (PMA50, Bruker) at room temperature.<sup>9</sup> To obtain reproducible and good quality VCD spectra, the concentration and path length were optimized to ensure that the VA absorbance for most VA bands in the frequency region of interest is between 0.2 and 0.8. Since the absorption strength of the carbonyl stretching band is about a factor of two or more larger than the other vibrational bands, separated VCD measurements were carried out for the region above and below 1650 cm<sup>-1</sup>. The upper frequency region was measured using a 0.1 mm PTFE spacer (International Crystal Laboratory) and at a concentration of 0.30 M. The region below 1650 cm<sup>-1</sup> was measured with twice the concentration and the same path length. All VCD spectra were measured with a total duration time of 3 h (3 × 1 h), or about ~13 000 scans, and with a resolution of 4 cm<sup>-1</sup>, except in the case of methanol where we used 6 × 0.5 h. For baseline correction, the final VCD spectra were obtained by subtracting the corresponding spectra of racemic MM in the respective solvents measured under identical conditions. We use the *R*-enantiomer for MM throughout this paper. VCD spectra of the *R*- and *S*-MM in the three solvents are provided in Fig. S1(a) (ESI†) to demonstrate the quality of the measurements.

### ORD measurements

Solutions with 0.06, 0.30, and 0.60 M of MM in non-deuterated methanol and chloroform, and 0.06, 0.30, 0.60, and 1.20 M of MM in non-deuterated dimethyl sulfoxide were prepared. The ORD data were collected at a series of wavelengths at 589 nm of sodium D line, and at 578, 546, 436, and 365 nm of a mercury lamp, by means of a Perkin-Elmer 240 polarimeter.

### DFT calculations

The Gaussian 03<sup>24</sup> and 09<sup>25</sup> program packages were used for all the geometry optimizations, harmonic frequency calculations, and the calculations of the VA and VCD intensities at the B3LYP/cc-pVTZ level. The same level of theory was used in ref. 19 for MM. For the calculations of ORD spectra, time-dependent (TD) DFT at the B3LYP/cc-pVTZ level of theory was utilized. A Lorentzian line shape with a half-width at half-height (HWHH) of 4 cm<sup>-1</sup> was used for simulations of VA and VCD spectra. For MM in methanol (MeOH-*d*<sub>4</sub>), there is D/H exchange and the hydroxyl hydrogen atom of MM is replaced by D in all the calculations. In the other two solvents, no D/H exchanges are expected. The integral equation formalism (IEF) version of PCM<sup>26</sup> using universal force field (UFF) radii was applied in order to account for the effects of solvent molecules implicitly. For this purpose, the dielectric constants of 32.61, 46.82, and 4.71 were used for methanol, dimethyl sulfoxide, and chloroform, respectively. For the ORD calculations, excitation wavelengths,  $\lambda$ , at 589, 578, 546, 436, and 365 nm were used. No scaling factor was applied for the comparisons of the simulated results with the experimental ones.



## MD simulation

The Amber 11 suite of programs<sup>27</sup> was utilized to perform MD calculations of MM in a specific solvent using the PMEMD module. The goal here was to locate the sites for strong hydrogen-bonding interactions between the solute and solvent molecules and to estimate the number of solvent molecules which are directly hydrogen-bonded to MM. The AMBER ff99 force field based on molecular mechanics approximation was used. A rectangular periodic box with 888 pre-equilibrated methanol molecules with a cut-off of 16.0 Å was used to solvate the MM molecule. A four-step MD simulation was carried out in this study. First, the system was minimized using 1000 steps of a steepest descent algorithm, followed by 1000 steps of a conjugate gradient algorithm. Then, a 200 ps heating from 0 K to 300 K under the NVT ensemble was conducted. After that the whole system was equilibrated for a duration of 400 ps at 300 K. Lastly, a 5 ns production MD was done under NPT conditions. RDFs were calculated to estimate the number of solvent molecules directly hydrogen-bonded to MM within the first shell of solvation.

## Results and discussions

### Comments on the experimental VA and VCD spectra in different solvents

Fig. 1 shows the comparison of the experimental VA and VCD spectra of MM in MeOH-*d*<sub>4</sub>, DMSO-*d*<sub>6</sub>, and CDCl<sub>3</sub> in the region of 1800–1150 cm<sup>-1</sup>. Despite an overall similarity among the three VA spectra and among the three VCD spectra, there are noticeable differences in the VCD spectra among these three solvents. At the highest wavenumber region, *i.e.* the carbonyl stretching region, while MM in CDCl<sub>3</sub> shows a more or less symmetric peak, the corresponding band in DMSO has a noticeable shoulder and the main peak is blue shifted by ~13 cm<sup>-1</sup> from that in CDCl<sub>3</sub>, whereas the band in methanol is substantially broadened and is also blue shifted compared to that in CDCl<sub>3</sub>. In the middle section of 1700–1350 cm<sup>-1</sup>, the VA spectra of all three look similar, whereas the VCD features are somewhat different. The most noticeable difference is the negative VCD band at ~1392 cm<sup>-1</sup> in CDCl<sub>3</sub> which is missing in the other two solvents. In the lowest wavenumber region of 1350–1150 cm<sup>-1</sup>, vibrational bands show severe overlapping and the resulting VA and VCD spectra

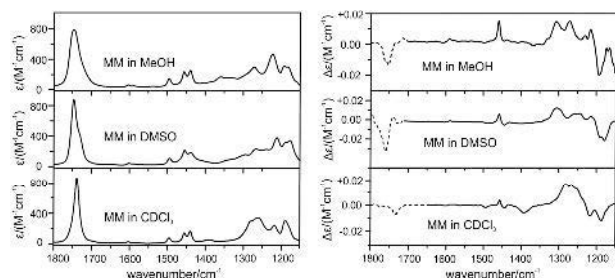


**Fig. 1** Experimental VA (left) and VCD (right) spectra of MM in three different organic solvents. The VCD carbonyl stretching sections marked with dotted lines were measured with half of the concentration used for the rest of the spectra to avoid saturation (see Experimental section for details).

appear quite different among the three solvents. For example, the VCD features show the  $+/-/-$  pattern in the chloroform solution, which turn into the  $+/+/-$  sequence in DMSO and  $+/+ +/-$  in methanol. Compared to the VA spectra, the differences among the three solvents are generally more distinctive in the VCD spectra since VCD signatures are often considerably more sensitive than VA patterns to the conformational distribution and the solvent environments. For completion, the corresponding VA and VCD spectra of MM in CCl<sub>4</sub> are also compared with the corresponding spectra in CDCl<sub>3</sub> in Fig. S1(b) (ESI<sup>†</sup>). The spectra obtained in CCl<sub>4</sub> are essentially the same as those published previously.<sup>19</sup> It is also noted that the VA and VCD spectra of MM in CDCl<sub>3</sub> and in CCl<sub>4</sub> look essentially identical, suggesting that the dominant species in these two solvents are the same.

### Different approaches to simulate VA and VCD spectra of MM in solution

Several approaches have been undertaken in order to adequately account for the experimental features observed, to gain insights into the solute–solvent interactions, and to establish some general rules in dealing with solvents with different degrees of hydrogen-bonding capability. The first step is to establish the lowest energy conformers of MM and simulate its gas phase VA and VCD spectra. This is described in the next subsection. Second, to account for the different VA and VCD spectral features observed, one needs to systematically investigate and compare the effects of these three very different solvents. For example, they have very different dielectric constants, with  $\epsilon = 32.613$ , 46.826, and 4.7113, for methanol, dimethyl sulfoxide, and chloroform, respectively. Their ability to make hydrogen-bonds with MM also varies. Methanol solvent is considered as a polar protic solvent and has an acidic proton capable of hydrogen-bonding interaction. Chloroform is a nearly non-polar solvent with three electron-withdrawing atoms attached to a carbon atom, thus its hydrogen atom is more acidic compared to those of methane. Lastly, dimethyl sulfoxide is a polar aprotic solvent with no acidic hydrogen atoms capable of hydrogen-bonding interaction. Rather, it acts as a hydrogen-bond acceptor agent. Since the approaches used for the solvents capable or not capable of hydrogen-bonding interactions will be different, the simulated VA and VCD spectra of MM in methanol and in DMSO are discussed in Strongly solute–solvent hydrogen-bonded systems section, whereas those of MM in chloroform are in Systems with no strong solute–solvent hydrogen-bonds section.

### Search for the lowest energy conformers of MM

The MM molecule has a number of rotatable single bonds which can bring about new conformations. Two dihedral angles, namely  $\tau_1$  (C<sub>4</sub>–C<sub>12</sub>–O<sub>16</sub>–H<sub>17</sub>) and  $\tau_2$  (C<sub>4</sub>–C<sub>12</sub>–C<sub>14</sub>–O<sub>15</sub>), corresponding to rotation around the C<sub>12</sub>–O<sub>16</sub> and C<sub>12</sub>–C<sub>14</sub> bonds (see Fig. 2 for atom labelling) are the most effective dihedral angles in generating new conformations. A potential energy surface (PES) scan along these two dihedral angles was carried out at the B3LYP/6-31G(d) level. The level of theory was chosen because it offers a good combination of accuracy and computational efficiency.

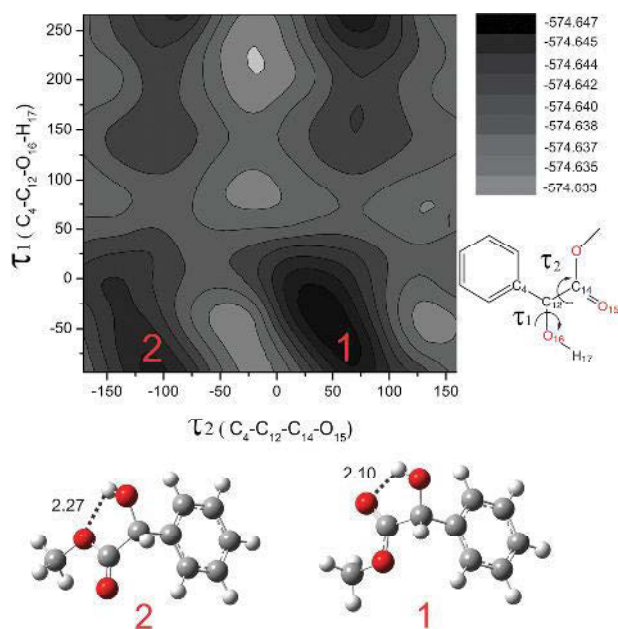


**Fig. 2** Two-dimensional PES plot of MM at the B3LYP/6-31G(d) level, scanned along its two dihedral angles,  $\tau_1$  and  $\tau_2$  (in degrees). The atom labelling of MM and the motions associated with these two dihedral angles are provided at the side bar. See the text for the detailed definitions of these two dihedral angles. The energy unit is in Hartree. The optimized geometries of the two most stable MM conformers are shown at the bottom. The hydrogen-bonding distances (in Å) are also indicated.

The two-dimensional plot of the PES scan along those two aforementioned dihedral angles is depicted in Fig. 2. As one can see, the deepest minimum detected is related to the most stable structure of MM with  $\tau_1 = -64.2^\circ$  and  $\tau_2 = 69.2^\circ$  where the hydroxyl hydrogen atom points at the O atom of the carbonyl group to form an intramolecular hydrogen-bonded ring. Based on the PES plot, there is a second minimum at  $\tau_1 = -64.2^\circ$  and  $\tau_2 = -110.7^\circ$  where the intramolecular hydrogen-bond acceptor is the ester O atom rather than the carbonyl O atom in the most stable structure. These two structures were optimized at the B3LYP/cc-pVTZ level and the resulting geometries are also included in Fig. 2. We also performed a transition state calculation to estimate the conversion barrier between these two minima at the B3LYP/cc-pVTZ level of theory. The result is provided in Fig. S2 (ESI<sup>†</sup>). The relative free energy difference between these two conformers is about  $2.4 \text{ kcal mol}^{-1}$  and the conversion barrier is  $\sim 8.1 \text{ kcal mol}^{-1}$  from the most stable conformer to the second most stable one. Consequently, the most stable conformer is the only conformer which contributes significantly at room temperature and is therefore the only one considered in the following treatments of solvent effects.

### Strongly solute–solvent hydrogen-bonded systems

**Methanol.** The simulated VA and VCD spectra of the MM monomer in the gas phase and with the PCM model using methanol as solvent are shown in Fig. 3. The simulated gas phase VA and VCD spectra are very different from the experimental ones, making it not possible to assign the spectra accordingly.

The inclusion of the bulk methanol with PCM has improved the agreement between theory and experiment noticeably. In particular, the relative intensities of the VA bands in the  $1350\text{--}1150 \text{ cm}^{-1}$  region are in better agreement with the experimental one, so are the VCD features in the same region. However, there are still considerable differences which make the assignments somewhat ambiguous. For example, the relative intensities of the VCD features in the  $1350\text{--}1150 \text{ cm}^{-1}$  region are still not in accord with the experiment. While only one relatively weak negative VCD band at the lowest wavenumber end was predicted with the implicit methanol solvation model, one strong negative VCD band was detected experimentally. The bandwidth of the carbonyl stretch is substantially broaden compared to that in  $\text{CDCl}_3$  or  $\text{CCl}_4$ , suggesting hydrogen-bonding interactions with methanol. Therefore, explicit solvation of MM by methanol was considered in the following.

To facilitate the construction of the MM–methanol complexes, RDF calculations were performed for MM in methanol. The RDFs of MM in methanol are provided in Fig. S3 (ESI<sup>†</sup>). Each RDF represents the probability of finding an atom of methanol molecules at a distance ( $r$ ) from a center atom of MM. For example,  $g(r)_{\text{O1Hm}}$  shows the probability of finding the hydrogen atom of methanol molecules at a distance  $r$  from the carbonyl oxygen atom of MM. Om and Hm refer to the O and H atoms of methanol. The particular RDF has a well defined sharp first maximum at  $\sim 1.89 \text{ \AA}$ , indicating hydrogen-bonding nature of

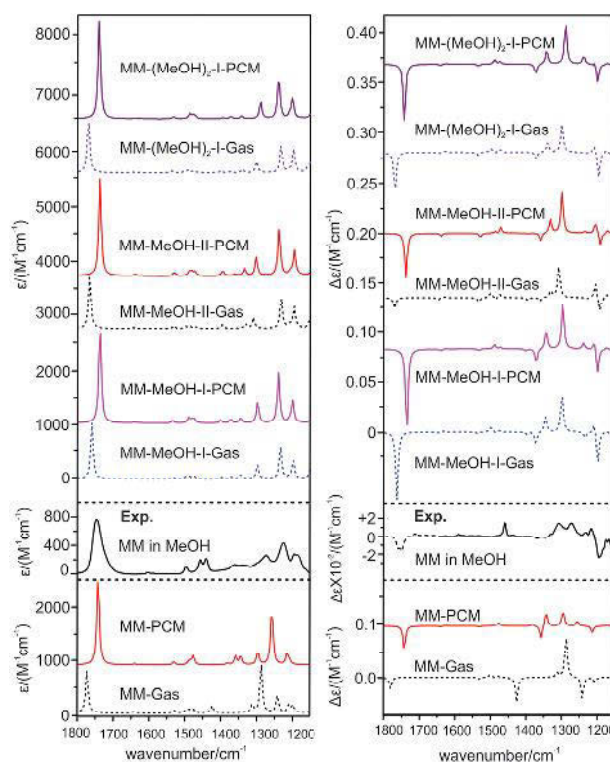


**Fig. 3** Comparisons of the experimental VA (left) and VCD (right) spectra of MM in MeOH (middle) with the corresponding spectra of the MM monomer in the gas phase and with PCM (bottom) and of the two most stable 1 : 1 MM–MeOH conformers and the most dominant 1 : 2 MM–(MeOH)<sub>2</sub> conformer in the gas phase and with PCM (top) calculated at the B3LYP/cc-pVTZ level.

the interaction. The integration to the first minimum provides a number of 1.57 which implies that on average, about one or two methanol molecules are directly hydrogen-bonded to MM at this site. On the other hand, the RDF corresponding to the intermolecular interaction between the ester O atom of MM with the H atom of methanol shows no well defined peaks. This indicates no strong hydrogen-bonding interaction with methanol at this site of MM on average.

Based on the RDF results, MM is most likely hydrogen-bonding to methanol through  $O_2H_1 \cdots O_m$  and  $C=O_1 \cdots H_m$  interactions. The integrated values to the first minimum suggest that on average there can be one or two methanol molecules directly hydrogen-bonded to MM. Therefore, several explicit 1 : 1 and 1 : 2 MM–methanol complexes were proposed accordingly. The first one is where one methanol molecule is inserted into the existing intramolecular hydrogen-bonding ring and is hydrogen-bonded, respectively, to  $O_1$  and  $H_1$  as a proton donor and acceptor. This results in two 1 : 1, *i.e.* MM–MeOH-I and MM–MeOH-II, where the methyl group of methanol and the phenyl ring of MM are at the opposite or the same side of the intermolecular hydrogen-bonded ring, respectively. Such insertion conformers<sup>9,11,28</sup> are much more stable than the addition conformers where the methanol molecule is associated through intermolecular hydrogen-bonding with the O atom of the carbonyl or the hydroxyl group, without breaking the existing intramolecular hydrogen-bond of MM. The more subtle preference for MM–MeOH-I *versus* II is due to the repulsion between the phenyl ring and the methyl group. MM–MeOH-I is considerably more favourable than II since its phenyl group is further away from the methyl group of methanol.

We also evaluated the 1 : 2 MM–(MeOH)<sub>2</sub> complexes. The second methanol molecule can be inserted into the existing intermolecular hydrogen-bonded ring of the 1 : 1 insertion conformers to form a larger concerted hydrogen-bonded ring, resulting in an insertion complex. Or it can be hydrogen-bonded to the oxygen atom of the carbonyl or the hydroxyl group, leaving the existing intermolecular hydrogen-bonded ring in the 1 : 1 complex intact. It was shown in a number of previous studies<sup>9,16</sup> that the so-called insertion complexes of the type MM–(MeOH)<sub>2</sub>-I and II are substantially more stable than the purely association or mixed insertion and association complexes such as MM–(MeOH)<sub>2</sub>-III and IV. The association of the hydrogen atom of methanol with the lone pair of the ester O atom was found to be much less favorable compared to the  $O_2H_1 \cdots O_m$  and  $C=O_1 \cdots H_m$  interactions, consistent with the RDF results reported here, showing no well defined sharp peaks, thus no hydrogen-bonding interaction at the ester O site.

It was shown in a few previous studies that the addition of even just one more solvent molecule may significantly influence the preferred binding sites at the solute molecules<sup>30,31</sup> and also alter the appearance of the VCD spectrum.<sup>9,12,16,32</sup> On the other hand, to build up several explicit solvation layers of the methanol molecules surrounding a MM molecule would be prohibitory expensive computationally. To this end, we have taken the approach to apply the continuum solvation model, *i.e.* PCM,

around the explicitly solvated 1 : 1 and 1 : 2 MM–methanol complexes to account for the effects of surrounding bulk methanol molecules. Such a combined explicit and implicit solvation approach was used recently to account for the solvation effects of an amino acid in aqueous solution.<sup>33</sup> It would be of considerable interest to verify if this approach is generally applicable for the cases when strong solute–solvent hydrogen-bonding interactions are expected.

The equilibrium geometries obtained for the 1 : 1 and 1 : 2 complexes were re-optimized with the PCM model using methanol as solvent. The final optimized geometries of the dominant 1 : 1 and 1 : 2 conformers with the PCM model using methanol as solvent are given in Fig. 4, together with the important hydrogen-bonding distances. The corresponding gas phase structures are provided in Fig. S4 (ESI†). Only relatively small changes in geometries were observed with the inclusion of PCM. It seems that the addition of bulk methanol by PCM in general strengthens the strongest intermolecular hydrogen-bond in the complex, and weakens the other intermolecular hydrogen-bonding interactions slightly. These are evidenced by the shortening or lengthening of the respective hydrogen-bond lengths in Fig. 4 and Fig. S4 (ESI†). The relative free energies of the most stable 1 : 1 and 1 : 2 MM–methanol conformers in the gas phase and with PCM are summarized in Table 1, together with their Boltzmann population factors at room temperature. The numbers I, II, and *etc.* in the names indicate the most stable, the second most stable, and *etc.* conformers of each class of the complexes, respectively. It is noted that the relative stability ordering of these conformers does not alter with the addition of PCM.

The simulated VA and VCD spectra of the dominant 1 : 1 and 1 : 2 MM–methanol conformers in the gas phase and with

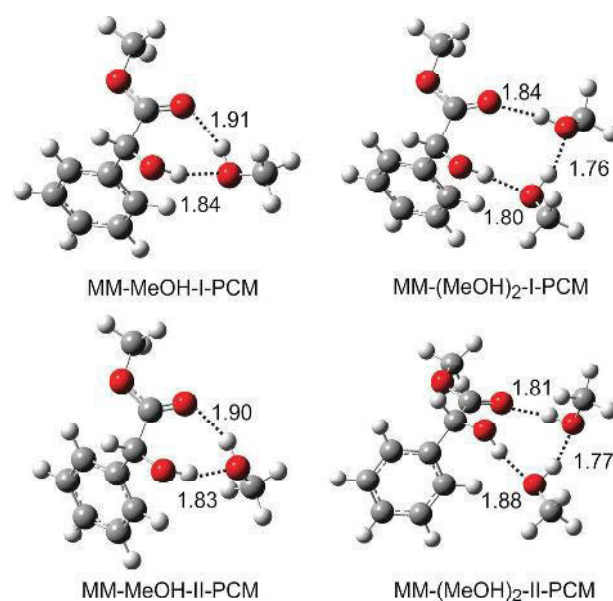


**Fig. 4** Optimized geometries of the most stable conformers of the 1 : 1 MM–MeOH and 1 : 2 MM–(MeOH)<sub>2</sub> complexes at the B3LYP/cc-pVTZ level with the PCM model using methanol as solvent. The intermolecular hydrogen-bond lengths (in Å) are indicated.

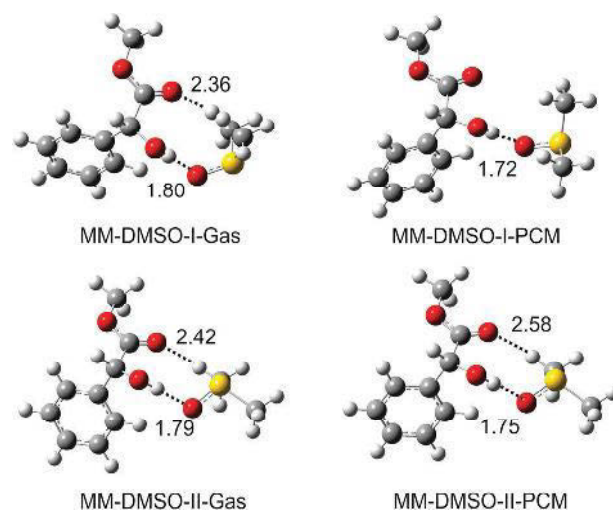
**Table 1** The relative free energies of the most stable 1 : 1 and some 1 : 2 MM–solvent complexes

Solvent	Complexes	$\Delta G^a$ (kcal mol <sup>-1</sup> )	Pop <sup>a</sup> (%)
Methanol	MM–MeOH-I	0.00 (0.00)	80.4 (75.6)
	MM–MeOH-II	0.84 (0.67)	19.6 (24.4)
	MM–(MeOH) <sub>2</sub> -I	0.00 (0.00) <sup>b</sup>	70.40 (93.4) <sup>b</sup>
	MM–(MeOH) <sub>2</sub> -II	0.73 (1.57)	20.44 (6.5)
DMSO	MM–(MeOH) <sub>2</sub> -III	1.34	7.28
	MM–DMSO-I	0.00 (0.00)	99.0 (94.7)
	MM–DMSO-II	2.70 (1.64)	1.0 (5.9)
CDCl <sub>3</sub>	MM–CDCl <sub>3</sub> -I	0.00	94.3
	MM–CDCl <sub>3</sub> -II	1.72	5.1
	MM–CDCl <sub>3</sub> -III	2.99	0.6

<sup>a</sup> The gas phase values obtained at the DFT/B3LYP/cc-pVTZ level. The corresponding values with the PCM of the respective solvents are in parentheses. <sup>b</sup> Only the two most stable 1 : 2 conformers were calculated with the PCM model using methanol as solvent.

the PCM model using methanol as solvent are also depicted in Fig. 3, together with the experimental VA and VCD spectra of MM in methanol. For completion, the corresponding VA and VCD spectra of the minor 1 : 2 conformers, which contribute in total less than 7%, are given in Fig. S5 (ESI<sup>†</sup>) together with the most important ones for comparison. From Fig. 3, one can see that the VA spectrum of the dominant MM–MeOH-I conformer (~80%) with PCM shows better agreement in terms of relative VA band intensities in the 1350–1150 cm<sup>-1</sup> region with experiment. More importantly, the VCD features of MM–MeOH-I with PCM in the same region agree much better with the experimental ones than the implicit solvation model alone. Not only their signs and their amplitudes, but also their frequency positions are better predicted. The importance of the further inclusion of the PCM model with the explicit solvation model can be appreciated by comparison between MM–MeOH-I in the gas phase and with PCM. First, the predicted band frequencies moved closer to their experimental values with PCM. Second, the negative VCD band of MM–MeOH-I at ~1234 cm<sup>-1</sup> changed its sign with the inclusion of PCM and is now in agreement with the experiment. It is interesting to note that the VA and VCD spectra of the 1 : 2 MM–(MeOH)<sub>2</sub>-I conformer with PCM which has over 93% population at room temperature are essentially the same as those of MM–MeOH-I with PCM. Overall, the combined explicit and implicit solvation model provides satisfactory interpretation of the observed VA and VCD spectra of MM in methanol and gives better performance than either model alone.

**Dimethyl sulfoxide.** Compared to methanol, dimethyl sulfoxide does not have any acidic hydrogen atom and consequently the solute–solvent hydrogen-bonding interaction occurs only when the oxygen atom of a dimethyl sulfoxide molecule is placed in close proximity to the hydrogen atom of the hydroxyl group of MM. For this reason, only the 1 : 1 MM–DMSO complex was considered for the explicit solvation of MM in dimethyl sulfoxide. Two lowest energy conformers, MM–DMSO-I and II were identified. These two conformers are related to whether the phenyl ring and the methyl group of DMSO are at the opposite or the same side of the intermolecular hydrogen-bonded ring, as shown in Fig. 5. MM–DMSO-I where the methyl group points further away from the phenyl ring of MM is much more stable

**Fig. 5** Optimized geometries of the two most stable 1 : 1 conformers of MM–DMSO at the B3LYP/cc-pVTZ level in the gas phase and PCM. The important intermolecular distances less than 3.0 Å are indicated.

than MM–DMSO-II where the distance between these two groups is closer. In the gas phase, a secondary hydrogen-bond between the hydrogen atom of the methyl group of DMSO and the O atom of the carbonyl group of MM is noted for both conformers, evidenced by their 2.36 Å and 2.42 Å intermolecular bond lengths in Fig. 5. These two conformers were re-optimized with the PCM model using DMSO as solvent and the corresponding geometries are also provided in Fig. 5. It is interesting to note that the bulk DMSO seems to strengthen the primary hydrogen-bond, and on the other hand, weaken the secondary hydrogen-bonding interaction. While the primary hydrogen-bond (S=O···H) length is shortened by about 0.08 to 0.04 Å in these two conformers, the secondary hydrogen-bond length lengthens significantly from 2.36 to 3.72 Å in MM–DMSO-I and from 2.42 to 2.58 Å in MM–DMSO-II when the PCM of DMSO was applied. Similar phenomena but to a lesser degree have also been observed for the methanol case when the PCM of solvent was applied to the explicit solvation models. Nevertheless, MM–DMSO-I remains the dominant one in solution. The relative free energies and the Boltzmann factors at room temperature of these two conformers in the gas phase and with PCM of DMSO at the B3LYP/cc-pVTZ level of theory are summarized in Table 1.

In Fig. 6, the simulated VA and VCD spectra of the MM monomer and the 1 : 1 MM–DMSO complex in the gas phase and with PCM are compared with the experimental spectra obtained in DMSO. Both the VA and VCD spectra of the MM monomer in the gas phase and with PCM show noticeable disagreement in the 1350–1150 cm<sup>-1</sup> region with the respective experimental data. From Fig. 6, it is obvious that neither the gas phase nor the PCM model of the MM monomer alone can bring out all the main experimental features observed. In particular, the VA intensity pattern of the bands in the 1350–1150 cm<sup>-1</sup> region is clearly in disagreement with the experimental spectrum. At the same time, the experimental VCD signatures in the same region show the +/+/- pattern from higher to lower frequencies

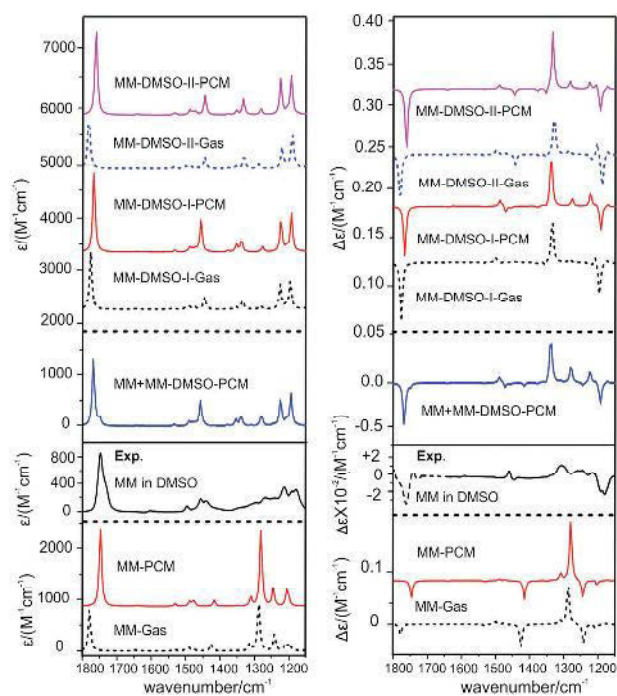


**Fig. 6** Comparisons of the experimental VA and VCD spectra of MM in DMSO (middle) with the corresponding simulated spectra of the gas phase and PCM of the MM monomer (bottom) and of the two most stable 1 : 1 MM–DMSO complexes in the gas phase and with PCM (top) calculated at the B3LYP/cc-pVTZ level. The empirically population weighted VA and VCD spectra of MM itself and the MM–DMSO complex at room temperature are also presented for comparison with the experimental data (see the text for details).

and this pattern was not at all predicted with the gas phase and the PCM of MM models. The strong negative VCD feature predicted with MM in the gas phase and with PCM at about  $1424\text{ cm}^{-1}$  is obviously absent in the corresponding experimental VCD spectrum. The explicit solvation model, *i.e.* MM–DMSO-I and II in the gas phase, on the other hand, generated considerable pattern changes in both the simulated VA and VCD spectra. It is also noted that MM–DMSO-I and II show quite similar overall VA and VCD patterns, although the former one carries  $\sim 99\%$  of population at room temperature based on the relative free energies calculated. Clearly, the experimental VA intensity pattern of the bands in the low wavenumber region is now much better captured with the explicit solvation model. Even more importantly, the experimental  $+/+/-$  VCD pattern in the same low wavenumber region is now reproduced. Furthermore, the strong negative VCD band at  $\sim 1420\text{ cm}^{-1}$  which is absent in the experiment is also no longer visible in the calculation. Finally, the experimental  $+/-$  bisignate VCD feature at  $\sim 1460\text{ cm}^{-1}$  is correctly predicted with the explicit solvated MM–DMSO-I. The inclusion of the implicit bulk DMSO molecules surrounding the explicit solvated DMSO has brought the predicted frequencies closer to the experimental ones and modified the relative intensity of a few VA and VCD bands to better agreement with the experiment, but generated no drastic pattern changes.

With the much better overall agreement between experimental and theoretical VA and VCD spectra provided by the

combined implicit and explicit solvation model, it was possible to examine some finer spectral details. For example, the C=O stretching band shows a shoulder at the lower frequency side. The corresponding VCD spectrum also has a second weak, negative VCD feature at the lower frequency side of the main C=O band. A possible explanation is that these are due to the co-existence of a small amount of the MM monomer which are not hydrogen-bonded to DMSO in solution. Indeed, both the shoulder of the VA band and the small additional VCD feature in the C=O stretch region can be well explained by the simulated VA and VCD spectra of the MM monomer with the PCM model using DMSO as solvent. The second strongest VA feature predicted at  $\sim 1283\text{ cm}^{-1}$  for the MM monomer is visible in the same region in the observed experimental spectrum. The related strongest VCD feature of the MM monomer is also visible as a slightly split peak in the same region. These comparisons are highlighted in Fig. 6 with the inclusion of the empirically population weighted VA and VCD spectra of MM (10%) and MM–DMSO (90%) (see “popW-MM + MM–DMSO-PCM” in Fig. 6). We also noted that the carbonyl stretching frequency of MM–DMSO was predicted to be blue-shifted by about  $13\text{ cm}^{-1}$  from the MM monomer, in good agreement with the experimental shift of  $13\text{ cm}^{-1}$  observed. This experimental shift is estimated using the main C=O band in DMSO and that in  $\text{CDCl}_3$  (*vide infra*) since it is difficult to get the exact band frequency of the shoulder accurately. For completion, we also include the simulated VA and VCD of the second MM conformer and MM dimer in DMSO in Fig. S6 (ESI<sup>†</sup>). One can clearly see that neither of them contributes noticeably to the observed spectra.

Overall, it is satisfying that the combined implicit and explicit solvation model reproduced all the main VA and VCD spectral features in the experimental ones in methanol and in DMSO. One important point is that it is essential to consider the hydrogen-bonding interactions between methanol and MM and between DMSO and MM using the explicit solvation model in order to interpret the VA and VCD experimental data reliably. Although the further inclusion of PCM of bulk DMSO has improved the agreement only slightly in the DMSO case, the effects of bulk solvent molecules in the case of methanol are more severe. It is therefore advisable to include both models simultaneously in treating solvents that are capable of intermolecular hydrogen-bonding interactions with solutes.

### Systems with no strong solute–solvent hydrogen-bonds

**Chloroform.** The chloroform solvent can be categorized as a non-polar solvent with no acidic proton capable of hydrogen-bonding interaction. It is very different from methanol and DMSO discussed above. Therefore, one may expect that it is enough to account for the solvent effects using just the implicit solvent model. On the other hand, chloroform has three withdrawing chlorine atoms attached to a carbon atom to pull off the electron density from the hydrogen atom, making it accessible for the  $\text{CH}\cdots\text{O}$  type secondly hydrogen-bonding interaction. The MM molecule has three oxygen atoms which may be involved in such interaction with the chloroform molecule.

For completion, we also construct the 1 : 1 MM-CDCl<sub>3</sub> and 1 : 2 MM-(CDCl<sub>3</sub>)<sub>2</sub> complexes to examine the VA and VCD features of these somewhat weakly bound systems. For the 1 : 1 complex, the deuterium and chlorine atoms of CDCl<sub>3</sub> can be inserted into the existing intramolecular hydrogen-bonded ring of MM or the hydrogen atom can be attached to the carbonyl or the ester O atom while leaving the intramolecular hydrogen-bonded ring of MM intact. The association of the hydrogen atom of CDCl<sub>3</sub> with the carbonyl O atom while maintaining the intramolecular hydrogen-bonded ring of MM did not result in a stable conformer. The association at the hydroxyl O atom resulted in the most stable conformer, while the association at the ester O atom produced the least stable conformer. This is of no surprise since the ester O atom is a highly unlikely site for hydrogen-bonding based on our RDF analysis. It is interesting to see that the insertion type conformer is only the second most stable conformer in this case, in contrast to the previous findings with methanol and DMSO. This is because the CH...O type secondly hydrogen-bonding interaction is weaker than the existing intramolecular OH...O=C bond. Consequently, in the competition of intra- and intermolecular interactions, the former wins. Fig. 7 shows the optimized geometries of these explicitly solvated complexes in the gas phase. The relative free energies of these 1 : 1 complexes at room temperature at the B3LYP/cc-pVTZ level are also summarized in Table 1. Similar searching strategies were applied to construct the 1 : 2 MM-(CDCl<sub>3</sub>)<sub>2</sub> complexes as well. The associated results of the 1 : 2 conformers are summarized in Fig. S7 (ESI†).

The simulated VA and VCD spectra of the MM monomer in the gas phase and with PCM are compared with the experimental data in Fig. 8, together with the respective spectra of the 1 : 1 explicit solvated MM conformers. The corresponding comparison for the 1 : 2 explicit solvated MM complex is provided in Fig. S8 (ESI†). In contrast to the cases of methanol and DMSO, it is already possible to interpret the observed VA and VCD spectra based on just the gas phase spectra of the MM monomer. The main VA spectral features, for example, the overall relative VA band intensities and wavenumber positions, were largely reproduced with the gas phase MM. So were all the main VCD features, such as the negative C=O band, all the weak bands in the 1520–1420 cm<sup>-1</sup> region, the medium strength VCD band at 1392 cm<sup>-1</sup> which is missing in the methanol and DMSO experimental spectra, and the +/+/-/- pattern in the 1350–1150 cm<sup>-1</sup> region. The inclusion of the PCM again brought about a better frequency agreement

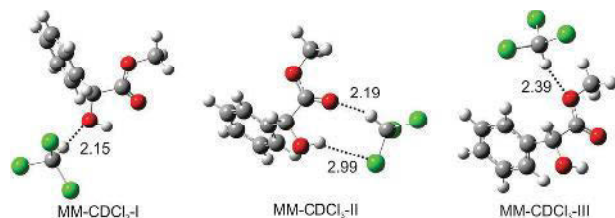


Fig. 7 Optimized geometries of the three most stable conformers of the 1 : 1 MM-CDCl<sub>3</sub> complex at the B3LYP/cc-pVTZ level in the gas phase. The intermolecular interaction bond lengths (in Å) are indicated.

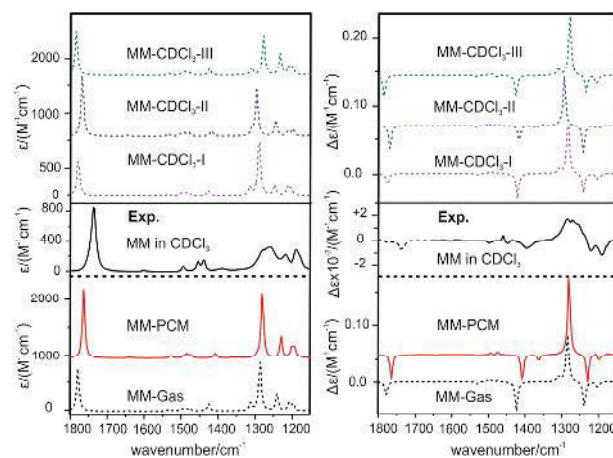


Fig. 8 Comparisons of the experimental VA and VCD spectra of MM in CDCl<sub>3</sub> (middle) with the corresponding simulated spectra of the gas phase and PCM of the MM monomer (bottom) and of the three most stable 1 : 1 MM-(CDCl<sub>3</sub>) complexes in the gas phase (top) calculated at the B3LYP/cc-pVTZ level.

with the experimental data, but did not alter either the VA or VCD features substantially. Please note that the two +/+ bands move closer together with PCM and are not as well resolved in the simulation as in the experiment. It appears that for CDCl<sub>3</sub>, the implicit solvation model or even just the gas phase monomer model are accurate enough to interpret the experimental features. Having said that, we were also interested to see how the explicit solvation model alters the appearance of the VA and VCD spectra. It is interesting to see that all the 1 : 1 MM-CDCl<sub>3</sub> conformers show general similar VA and VCD features. The most dominant one, with about 94% population, exhibits VA and VCD spectral features which are essentially identical to those of the MM monomer. It appears that the weak explicit intermolecular interaction between MM and CDCl<sub>3</sub> does not alter the VA and VCD spectra of MM noticeably. Although one does not expect a substantial amount of the 1 : 2 explicit solvated MM-(CDCl<sub>3</sub>)<sub>2</sub> in solution at room temperature, we nevertheless compare their simulated VA and VCD spectra in Fig. S8 (ESI†) with the experimental data. Again, the overall main features are similar to those obtained with just MM, supporting the above statement. In a recent VCD study of some very different molecular systems, *i.e.* chiral binaphthyl diphosphine ligands and their palladium complexes, it was found that: similar to the present case, the addition of the solvent PCM had not changed the conformational distribution; but unlike the current case, the addition of the PCM of solvent has noticeable effects on the appearance of VCD spectra.<sup>34</sup> It is therefore advisable to include PCM of solvents in VCD simulations. In the case of MM in CCl<sub>4</sub>, one can expect that the observed VA and VCD spectra to be explained by those of the MM monomer. This is indeed the case since the spectra obtained in CCl<sub>4</sub> are essentially the same as those in CDCl<sub>3</sub>.

### Experimental and simulated ORD comparison

Fig. 9 shows the experimental specific ORD curves of MM measured in methanol, chloroform, and dimethyl sulfoxide at a series of concentrations over five excitation wavelengths using

sodium D line and mercury lamps. The specific ORD measurements are generally concentration independent in the concentration range from 0.06 M to 1.2 M, meaning that the specific optical rotation value at a certain wavelength in a specific solvent does not change noticeably with respect to concentration. This observation suggests that generally the nature of solute–solvent interactions is kept more or less the same from the very dilute solution to the more concentrated one. The observation may also suggest that there is no drastic change in the dominant MM conformer in the three different organic solvents employed here. Both statements are supported by the vibrational studies discussed above. The theoretical ORD values of MM in methanol, chloroform, and DMSO at the five experimental excitation wavelengths have been calculated by using TDDFT at the B3LYP/cc-pVTZ level. All the proposed solvation models have been used in the calculations. For conciseness, the calculated ORD results of the most relevant species derived from the VA and VCD studies are summarized in Fig. 9 for comparison with the experimental one, while the complete set of ORD theoretical results of methanol are collected in Fig. S9 (ESI<sup>†</sup>).

It is recognized that the TDDFT method utilized for ORD calculations has certain deficiency in obtaining the key excitation energy and the related rotational strength adequately.<sup>35</sup> For example, the ORD values calculated by the B3LYP method tend to be too large in magnitude because the key excitation energy is usually underestimated and the related rotational strength overestimated.<sup>31,36</sup> Indeed, the ORD values calculated for the MM monomer in the gas phase and with PCM are much larger negative numbers than the corresponding measurements, for example in CDCl<sub>3</sub>. Although the accuracy of the current *ab initio* calculations of ORD values may not allow a meaningful quantitative comparison with the experimental ones, one can nevertheless check if the general trends observed can be reproduced theoretically and if consistent conclusions

can be reached with the dominant species derived from the VA and VCD studies discussed above.

From Fig. 9, one can see that the ORD values predicted for the MM monomer with and without PCM are more or less the same, and similar observation can be made for the 1 : 1 MM–DMSO complex. For this reason, we omitted the plots of the 1 : 1 MM–MeOH and MM–CDCl<sub>3</sub> complexes with PCM to avoid overcrowding in Fig. 9. At first glance, one may wonder if the 1 : 1 MM–CDCl<sub>3</sub>-I conformer, which has ~94% of the 1 : 1 cluster population at room temperature, provides better agreement with the experimental data since smaller specific ORD values were predicted for it at the wavelengths measured. However, in order to compare the specific ORD values of the 1 : 1 complex with the experimental data one needs to multiply the theoretical values by a scaling factor equivalent to the mass ratio of the 1 : 1 complex with respect to the MM monomer or about 1.8. This is because the experimental specific ORD values were determined using the concentration of MM itself in g mol<sup>-1</sup>, whereas the calculated specific ORD values of the 1 : 1 complex were computed with respect to the complex. This resulted in even larger negative ORD values than the MM monomer, thus indirectly supporting the conclusion reached with the vibrational studies that in CDCl<sub>3</sub>, the dominant species is the MM monomer. In the cases of methanol and DMSO, the experimental ORD values are noticeably smaller than those in CDCl<sub>3</sub>. On the other hand, the theoretical ORD values of MM itself in the three solvents were predicted to be quite similar. These observations indirectly suggest that the dominant species in these two solutions are different from that in CDCl<sub>3</sub>. Indeed, the most abundant 1 : 1 MM–DMSO conformer (~99%) exhibits much smaller ORD values with a correction factor of 1.5 implemented. Similarly, the population weighted 1 : 1 MM–MeOH complexes provide smaller negative ORD values with a correction factor of 1.2 than the MM itself. Overall, the ORD investigations presented support the conclusions drawn from

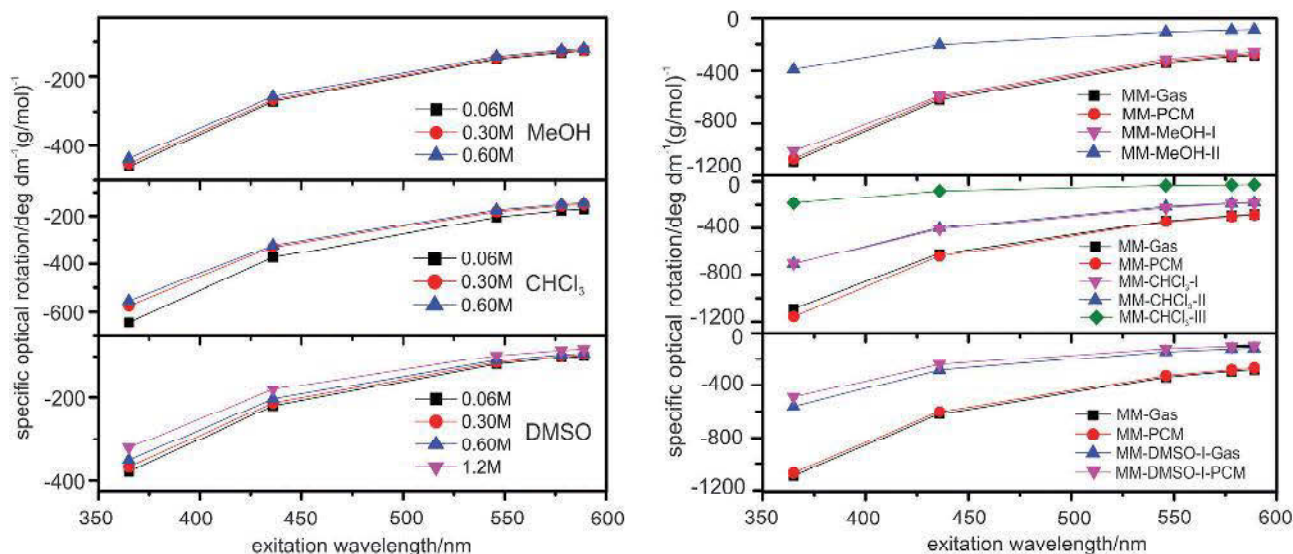


Fig. 9 Comparison of the experimental and calculated specific ORD values of MM in methanol, CHCl<sub>3</sub>, and DMSO solvents.

the VA and VCD studies despite the less desirable accuracy of the current ORD calculations.

## Conclusions

VA and VCD spectra of MM in three different organic solvents, namely, methanol, dimethyl sulfoxide, and chloroform have been measured and compared. The experimentally observed differences among these three solvents highlight the conformational sensitivity of VA and in particular VCD spectroscopy and the severity of the effects of solvents. By applying DFT and MD simulations, a general approach of using the combined explicit and implicit solvation model has been developed to account for the observed differences in both VA and VCD spectra among these three solvents. It was found that in the case of strongly hydrogen-bonding systems, such as MM in methanol and in DMSO, the application of the explicit solvent model is highly recommended. The first shell of solvation can be achieved by hydrogen-bonding interaction between solvent and solute at the important sites suggested by MD simulations. The further inclusion of the implicit solvation model is beneficial and can rectify some persistent mismatches when the explicit solvation model alone is applied. For the non-strongly hydrogen-bonding systems, such as MM in chloroform and in CCl<sub>4</sub>, the gas phase MM monomer or the MM monomer with PCM are sufficient to simulate the VA and VCD spectra for comparison against experiment. It is nevertheless advisable to include the PCM of solvents since more drastic changes in VCD spectra with the inclusion of PCM have been reported before.<sup>34</sup> Finally, the related ORD experiments and simulations also support the conclusions reached with the vibrational studies.

## Acknowledgements

This research was funded by the University of Alberta and the Natural Sciences and Engineering Research Council of Canada. We thank the anonymous referees for their constructive comments and suggestions. We also gratefully acknowledge access to the computing facilities provided by the Academic Information and Communication Technology group at the University of Alberta and by the Western Canada Research Grid (Westgrid). YX holds a senior Canada Research Chair in Chirality and Chirality Recognition.

## Notes and references

- 1 L. A. Nafie, *Vibrational Optical Activity: Principles and Applications*, John Wiley & Sons, Ltd., Chichester, 2011.
- 2 Y. He, B. Wang, R. K. Dukor and L. A. Nafie, *Appl. Spectrosc.*, 2011, **65**, 699–723.
- 3 E. L. Eliel, S. H. Wilen and M. P. Doyle, *Basic Organic Stereochemistry*, Wiley-Interscience, New York, 2001.
- 4 S. M. Wilson, K. B. Wiberg, J. R. Cheeseman, M. J. Frisch and P. H. Vaccaro, *J. Phys. Chem. A*, 2005, **109**, 11752–11764.
- 5 P. L. Polavarapu, *Chirality*, 2012, **24**, 909–920.
- 6 T. A. Keiderling, *Curr. Opin. Chem. Biol.*, 2002, **6**, 682–688.
- 7 K. J. Jalkanen, R. M. Nieminen, M. Knapp-Mohammady and S. Suhai, *Int. J. Quantum Chem.*, 2003, **92**, 239–259.
- 8 E. Debie, P. Bultinck, W. Herrebout and B. van der Veken, *Phys. Chem. Chem. Phys.*, 2008, **10**, 3498–3508.
- 9 M. Losada and Y. Xu, *Phys. Chem. Chem. Phys.*, 2007, **9**, 3127–3135.
- 10 J. C. Dobrowolski, J. E. Rode and J. Sadlej, *Practical aspect of Computational Chemistry I*, 2011, ch. 15, pp. 451–478.
- 11 M. Losada, H. Tran and Y. Xu, *J. Chem. Phys.*, 2008, **128**, 014508.
- 12 M. Losada, P. Nguyen and Y. Xu, *J. Phys. Chem. A*, 2008, **112**, 5621–5627.
- 13 G. Yang and Y. Xu, *J. Chem. Phys.*, 2009, **130**, 164506–164515.
- 14 J. Sadlej, J. C. Dobrowolski, J. E. Rode and M. H. Jamróz, *Phys. Chem. Chem. Phys.*, 2006, **8**, 101–113; J. Sadlej, J. C. Dobrowolski and J. E. Rode, *Chem. Soc. Rev.*, 2010, **39**, 1478–1488.
- 15 G. Yang and Y. Xu, *Vibrational Circular Dichroism Spectroscopy of Chiral Molecules*, in *Top. Curr. Chem., Volume: Electronic, Magnetic Properties of Chiral Molecules and Supramolecular Architectures*, ed. R. Naaman and D. N. Beratan and D. H. Waldeck, Springer-Verlag, Berlin Heidelberg, 2011, vol. 298, pp. 189–236.
- 16 Y. Liu, G. Yang, M. Losada and Y. Xu, *J. Chem. Phys.*, 2010, **132**, 234513–234524.
- 17 R. J. Piffath and S. Sass, *Appl. Spectrosc.*, 1972, **26**, 92–95.
- 18 D. M. P. Gigante, F. Long, L. A. Bodack, J. M. Evans, J. Kallmerten, L. A. Nafie and T. B. Freedman, *J. Phys. Chem. A*, 1999, **103**, 1523–1537.
- 19 T. Kuppens, P. Bultinck and W. Langenaeker, *Drug Discovery Today: Technol.*, 2004, **1**, 269–275.
- 20 K. Le Barbu-Debus, M. Broquier, A. Mahjoub and A. Zehnacker-Rentien, *J. Phys. Chem. A*, 2008, **112**, 9731–9741.
- 21 M. Albrecht, A. Borba, K. Le Barbu-Debus, B. Dittrich, R. Fausto, S. Grimme, A. Mahjoub, M. Nedić, U. Schmitt, L. Schrader, M. A. Suhm, A. Zehnacker-Rentien and J. Zischang, *New J. Chem.*, 2010, **34**, 1266–1288.
- 22 G. D. Yadav, A. D. Sajgure and S. B. Dhoot, *J. Chem. Technol. Biotechnol.*, 2008, **83**, 1145–1153.
- 23 P. Polavarapu, *Chirality*, 2008, **20**, 664–672.
- 24 M. J. Frisch, G. W. Trucks, H. B. Schlegel, G. E. Scuseria, M. A. Robb, J. R. Cheeseman, J. A. Montgomery Jr, T. Vreven, K. N. Kudin, J. C. Burant, J. M. Millam, S. S. Iyengar, J. Tomasi, V. Barone, B. Mennucci, M. Cossi, G. Scalmani, N. Rega, G. A. Petersson, H. Nakatsuji, M. Hada, M. Ehara, K. Toyota, R. Fukuda, J. Hasegawa, M. Ishida, T. Nakajima, Y. Honda, O. Kitao, H. Nakai, M. Klene, X. Li, J. E. Knox, H. P. Hratchian, J. B. Cross, V. Bakken, C. Adamo, J. Jaramillo, R. Gomperts, R. E. Stratmann, O. Yazyev, A. J. Austin, R. Cammi, C. Pomelli, J. W. Ochterski, P. Y. Ayala, K. Morokuma, G. A. Voth, P. Salvador, J. J. Dannenberg, V. G. Zakrzewski, S. Dapprich, A. D. Daniels, M. C. Strain, O. Farkas, D. K. Malick, A. D. Rabuck, K. Raghavachari, J. B. Foresman, J. V. Ortiz, Q. Cui, A. G. Baboul, S. Clifford, J. Cioslowski, B. B. Stefanov, G. Liu, A. Liashenko, P. Piskorz,



- I. Komaromi, R. L. Martin, D. J. Fox, T. Keith, M. A. Al-Laham, C. Y. Peng, A. Nanayakkara, M. Challacombe, P. M. W. Gill, B. Johnson, W. Chen, M. W. Wong, C. Gonzalez and J. A. Pople, *Gaussian 03, Revision E.01*, Gaussian, Inc., Wallingford, CT, 2004.
- 25 M. J. Frisch, G. W. Trucks, H. B. Schlegel, G. E. Scuseria, M. A. Robb, J. R. Cheeseman, G. Scalmani, V. Barone, B. Mennucci, G. A. Petersson, H. Nakatsuji, M. Caricato, X. Li, H. P. Hratchian, A. F. Izmaylov, J. Bloino, G. Zheng, J. L. Sonnenberg, M. Hada, M. Ehara, K. Toyota, R. Fukuda, J. Hasegawa, M. Ishida, T. Nakajima, Y. Honda, O. Kitao, H. Nakai, T. Vreven, J. A. Montgomery Jr, J. E. Peralta, F. Ogliaro, M. Bearpark, J. J. Heyd, E. Brothers, K. N. Kudin, V. N. Staroverov, R. Kobayashi, J. Normand, K. Raghavachari, A. Rendell, J. C. Burant, S. S. Iyengar, J. Tomasi, M. Cossi, N. Rega, J. M. Millam, M. Klene, J. E. Knox, J. B. Cross, V. Bakken, C. Adamo, J. Jaramillo, R. Gomperts, R. E. Stratmann, O. Yazyev, A. J. Austin, R. Cammi, C. Pomelli, J. W. Ochterski, R. L. Martin, K. Morokuma, V. G. Zakrzewski, G. A. Voth, P. Salvador, J. J. Dannenberg, S. Dapprich, A. D. Daniels, Ö. Farkas, J. B. Foresman, J. V. Ortiz, J. Cioslowski and D. J. Fox, *Gaussian 09, Revision B.01*, Gaussian, Inc., Wallingford CT, 2009.
- 26 J. Tomasi, B. Mennucci and R. Cammi, *Chem. Rev.*, 2005, **105**, 2999–3093.
- 27 D. A. Case, T. A. Darden, T. E. Cheatham III, C. L. Simmerling, J. Wang, R. E. Duke, R. Luo, R. C. Walker, W. Zhang, K. M. Merz, B. P. Roberts, B. Wang, S. Hayik, A. Roitberg, G. Seabra, I. Kolossváry, K. F. Wong, F. Paesani, J. Vanicek, J. Liu, X. Wu, S. R. Brozell, T. Steinbrecher, H. Gohlke, Q. Cai, X. Ye, J. Wang, M.-J. Hsieh, G. Cui, D. R. Roe, D. H. Mathews, M. G. Seetin, C. Sagui, V. Babin, T. Luchko, S. Gusarov, A. Kovalenko and P. A. Kollman, *AMBER 11*, University of California, San Francisco, 2010.
- 28 N. Borho, M. A. Suhm, K. Le Barbu-Debus and A. Zehnacker, *Phys. Chem. Chem. Phys.*, 2006, **8**, 4449–4460.
- 29 N. Seurre, K. Le Barbu-Debus, F. Lahmani, A. Zehnacker, N. Borho and M. A. Suhm, *Phys. Chem. Chem. Phys.*, 2006, **8**, 1007–1016.
- 30 Z. Su, Q. Wen and Y. Xu, *J. Am. Chem. Soc.*, 2006, **128**, 6755–6760.
- 31 Z. Su and Y. Xu, *Angew. Chem., Int. Ed.*, 2007, **119**, 6275–6278 (*Angew. Chem., Int. Ed.*, 2007, **46**, 6163–6166).
- 32 P. Zhu, G. Yang, M. R. Poopari, Z. Bie and Y. Xu, *ChemPhysChem*, 2012, **13**, 1272–1281.
- 33 M. R. Poopari, Z. Dezhahang, G. Yang and Y. Xu, *ChemPhysChem*, 2012, **13**, 2310–2321; M. R. Poopari, P. Zhu, Z. Dezhahang and Y. Xu, *J. Chem. Phys.*, 2012, **137**, 194308.
- 34 Z. Dezhahang, C. Merten, M. R. Poopari and Y. Xu, *Dalton Trans.*, 2012, **41**, 10817–10824.
- 35 T. D. Crawford, in *Comprehensive Chiroptical Spectroscopy: Methodologies and Theoretical Simulations*, ed. N. Berova, P. L. Polavarapu, K. Nakanishi and R. W. Woody, John Wiley & Sons, Inc, 1st edn, 2012, vol. 1, ch. 23, pp. 675–697.
- 36 J. Autschbach, S. Patchkovskii, T. Ziegler, S. J. A. van Gisbergen and E. J. Baerends, *J. Chem. Phys.*, 2002, **117**, 581–592.



Contents lists available at ScienceDirect

# Spectrochimica Acta Part A: Molecular and Biomolecular Spectroscopy

journal homepage: [www.elsevier.com/locate/saa](http://www.elsevier.com/locate/saa)

## Identifying dominant conformations of N-acetyl-L-cysteine methyl ester and N-acetyl-L-cysteine in water: VCD signatures of the amide I and the C=O stretching bands



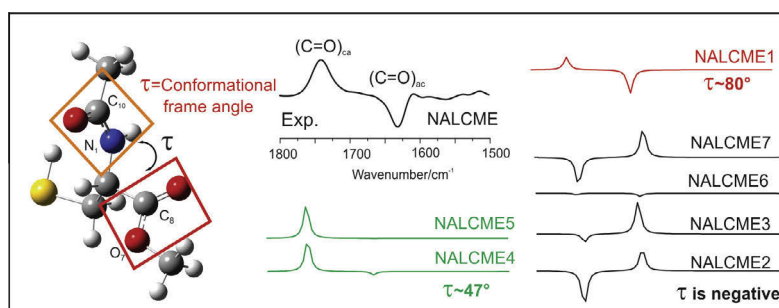
Mohammad Reza Poopari, Zahra Dezhahang, Yunjie Xu\*

Department of Chemistry, University of Alberta, Edmonton, Alberta T6G 2G2, Canada

### HIGHLIGHTS

- VCD signatures of two amino acid derivatives are obtained.
- Sign inversion of the amide I VCD band among different species is explained.
- An empirical structural–spectral relationship is established.
- The VCD markers proposed show high sensitivity to conformational variations.
- Solvent influence on conformational geometries and stability is emphasized.

### GRAPHICAL ABSTRACT



### ARTICLE INFO

Article history:  
Available online 7 September 2013

Keywords:  
Solvent effects  
Hydrogen-bonding  
Conformational preference  
N-acetyl-L-cysteine  
Vibrational circular dichroism  
Amide I and C=O stretching band

### ABSTRACT

Infrared (IR) and vibrational circular dichroism (VCD) spectra of N-Acetyl-L-Cysteine Methyl Ester (NALCME) and N-Acetyl-L-Cysteine (NALC) in D<sub>2</sub>O under different pHs were measured. We focus on the VCD signatures of the amide I and the C=O stretching spectral signatures of the neutral NALCME and NALC species and the related ones of the deprotonated NALC species in the region of 1800–1500 cm<sup>-1</sup>. A sign inversion is observed for the amide I VCD band going from the neutral NALCME and NALC to the deprotonated NALC species. Density functional theory (DFT) calculations were carried out to search for the possible conformations of these three species and to simulate their IR and VCD spectra at the B3LYP/aug-cc-pVTZ level in the gas phase and with the polarization continuum model of water solvent. The most stable conformations found for neutral NALCME and NALC exhibit drastically difference VCD patterns, whereas those of deprotonated NALC show similar patterns. We establish an empirical structural–spectral relationship where the aforementioned VCD signatures can be used as spectral markers to identify dominant conformations of these two amino acid derivatives under different pHs. It is recognized that the dominant conformers identified using the VCD spectral markers differ from those based on the relative DFT energies for neutral NALCME and NALC. The influence of solvent on both the conformational geometries and their relative stabilities is discussed. The aforementioned discrepancy can be attributed to the explicit solute–solvent hydrogen-bonding interactions which are not accounted for in the calculations. The empirical structural–spectral relationship identified can potentially be applied to large, related amino acids and polypeptides in water.

© 2013 Elsevier B.V. All rights reserved.

\* Corresponding author. Tel.: +1 780 492 1244; fax: +1 780 492 8231.  
E-mail address: [yunjie.Xu@ualberta.ca](mailto:yunjie.Xu@ualberta.ca) (Y. Xu).

## Introduction

Infrared (IR) spectroscopy and the related vibrational circular dichroism (VCD) spectroscopy [1,2] have been used to provide information about conformational distributions of amino acids [3,4] and polypeptides, as well as secondary structures of proteins [5] in film or in solution. VCD spectroscopy measures the differential absorbance of the left versus the right circularly polarized lights accompanying a vibrational transition. As a result, VCD spectroscopy exhibits unique sensitivity to chirality and is also highly sensitive to structural deformations due to environmental perturbations in comparison to regular IR spectroscopy [6,7]. To extract the rich structural information encoded in the VCD spectral patterns measured, one needs to carry out extensive density functional theory (DFT) calculations in order to identify the possible conformations of the targeted systems and to simulate their VCD spectra. This approach has been utilized successfully in a significant number of studies reported [1,2,8–10]. In highly polar solvents such as water, however, less satisfactory agreements between the experimental and theoretical simulated spectra result because the solvent effects can be drastic [11,12]. For example, the inclusion of bulk solvent using models such as the polarizable continuum model (PCM) is critical in some cases [12]. Yet in some other cases, the VCD features observed can only be reproduced by further considering explicit hydrogen-bonding interactions between chiral solute and water molecules [4,13–16]. Since it may be too expensive to include explicit water molecules in the simulations of larger biomolecules in aqueous solution, it is of significant interest to investigate in details why the PCM approaches are able to adequately interpret the observed IR and VCD spectra at one time and not at another. It is well known that the final simulated spectral features rely on both the spectral signatures of individual conformers and their Boltzmann population contributions. We therefore focus our attention on evaluating these two factors for two model chiral molecular systems, namely N-Acetyl-L-Cysteine Methyl Ester (NALCME) and N-Acetyl-L-Cysteine (NALC) in water under different pHs. Both NALCME and NALC are used for example, as mucolytic agents to reduce the viscosity of mucus secretions, while NALC is also used in the management of paracetamol overdose [17,18].

These two model systems are chosen for two main reasons. First, standard amino acids and their derivatives are chemically highly versatile molecules with a wide range of applications in pharmacy, biology, and chemistry. Their specific functions in water depend strongly on the pH of the solution and the particular conformations they adopt under such conditions. It is therefore highly desirable to obtain information about their dominant conformations in water under different pH conditions. Second, NALCME has fewer hydrogen-bonding sites compared to NALC. In comparison to NALC, its ability to form intramolecular hydrogen-bonds and intermolecular hydrogen-bonds with water molecules is significantly reduced. This allows one to evaluate how methyl substitution of the carboxylic group influences the dominant conformations in aqueous solution and how the related IR and VCD spectral features change. Although the VCD spectrum of NALC under neutral pH = 7 was reported previously [15], we include the VCD spectra of NALC under acidic conditions of pH = 2.5 and 3.1 in this study since the dominant species are different under the neutral and acidic conditions. In particular, we focus on the amide I band and the C=O stretching bands associated with the –COOH and –COOMe (Me = –CH<sub>3</sub>) groups in the region of 1800–1500 cm<sup>-1</sup> which have strong IR and VCD intensities. We examine the dominant conformations predicted and how their geometries and relative stabilities change from the gas phase calculations to those with the PCM of water solvent. We aim to establish empirical structural–spectral relationships which one may utilize

to extract conformational structural information for larger and related chiral molecular systems.

## Experimental and theoretical details

### Experimental IR and VCD measurements

NALC (99% purity), NALCME (90%, purity) and D<sub>2</sub>O (99.9%, purity) were obtained from Aldrich and were used without further purification. D<sub>2</sub>O was used as solvent for all the IR and VCD measurements reported. The experimental IR and VCD spectra were recorded using a Fourier transform IR spectrometer (VERTEX 70, Bruker) equipped with a VCD module (PMA50, Bruker) at room temperature [13]. The spectral range of 1800–1500 cm<sup>-1</sup> was selected for the current study where the solvent does not show any strong interference. In order to obtain VCD spectra with good quality, the concentration and path-length were optimized so that the experimental absorption coefficients are in the range of 0.2–0.8 for the relevant IR bands. Solutions with a concentration of ~0.6 M and a path-length of 0.05 mm were used. All VCD spectra were obtained with a resolution of 4 cm<sup>-1</sup> and with a total measurement time of 3 h (3 × 1 h), roughly ~4300 scans per hour. Upon dissolving of NALC sample in water, a solution with a pH value of ~2.5 is obtained. The NALC solutions with higher pH values were prepared by adding a small amount of 6 M NaOD dropwise. Upon dissolving of NALCME sample in water, a solution with a pH value of ~6.6 is made. Please note that the pH values reported are the direct read out values in a D<sub>2</sub>O solution using a H<sub>2</sub>O-calibrated pH-meter. Please see Ref. [19] for the detailed differences between pH and pD. The final reported VCD spectra were baseline corrected using the solvent spectra obtained under the same condition.

### Theoretical

The Gaussian 09 [20] suite of programs was used in all the geometry optimization calculations, potential energy surface scans, and harmonic vibrational frequencies calculations, as well as the IR and VCD intensities predictions. DFT [21] calculations were performed with the Becke, three-parameter, Lee–Yang–Parr (B3LYP) [22–24] hybrid functional and the augmented correlation-consistent triple zeta basis sets with added diffuse functions, i.e. aug-cc-pVTZ [25] for all conformational searches and spectral simulations. A Lorentzian line shape with a half-width at half-height (HWHH) of 4 cm<sup>-1</sup> was used for the simulations of IR and VCD spectra. The integral equation formalism of polarization continuum model (IEF-PCM) [26] using the universal force field (UFF) radii was used to account for the effects of solvent molecules implicitly. A dielectric constant of 78.3553 was used for D<sub>2</sub>O. It was established previously [15] that the H/D exchange happens at the three possible hydrogen-bonding sites, namely the –COOH, –SH and –NH sites, under the current experimental conditions. Consequently, in all the spectral simulation performed in this study, all these possible sites are fully D substituted whenever it is appropriate. Please note that we use *R*-enantiomers throughout this study.

## Results and discussions

### The experimental IR and VCD spectra

Fig. 1 shows the experimental IR and VCD spectra of NALCME at pH = 6.6 and NALC at pH = 7, 3.1, and 2.5. Comparing to NALC, NALCME has no acidic proton and the dominant species is expected to be the same in the pH range from 2.5 to 7.0. Therefore, only one pH result is reported here. Different spectral features are noted for

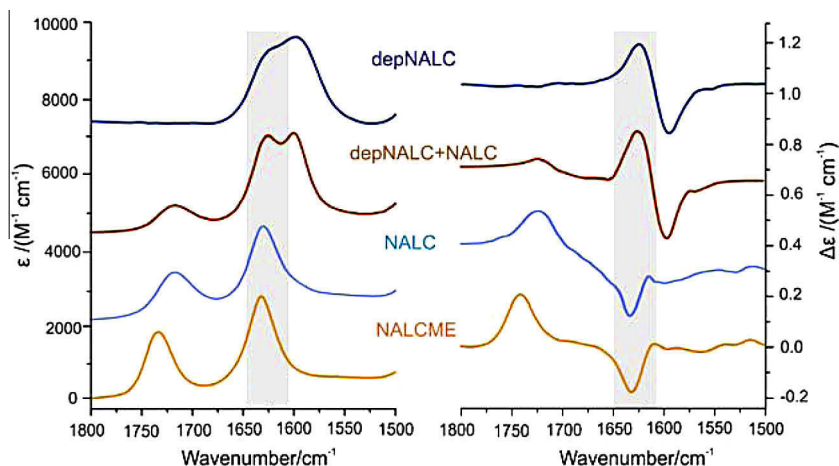


**Fig. 1.** Experimental IR (left) and VCD (right) spectra of NALC in water at pH = 7, 3.1, 2.5 and of NALCME in water at pH = 6.6, from the top to the bottom, respectively. The dominant species under each pH are also indicated.

NALC under different pHs. It is known from the previous study that the carboxylic group exists essentially as  $-\text{COOH}$  at a pH value of 2.5, and as  $\text{COO}^-$  at pH = 7.0, whereas both species coexist at pH = 3.1 [15]. While IR spectra at pH values ranging from 0.65 to 13 and VCD spectrum at pH = 7.0 of NALC were reported in Ref. [15], the VCD spectra of NALC at pH = 2.5 and 3.1 are reported here for the first time. At pH = 2.5, two IR bands are observed for NALC at  $\sim 1720$  and  $\sim 1630$   $\text{cm}^{-1}$ . These correspond to the  $\text{C}=\text{O}$  stretch of the  $-\text{COOH}$  group, i.e.  $\nu(\text{C}=\text{O})_{\text{ca}}$  where ‘ca’ stands for carboxylic acid’, and the amide I mode, i.e.  $\nu(\text{C}=\text{O})_{\text{ac}}$  where ‘ac’ stands for acetyl. At pH = 3.1 and 7, a new band corresponding to the asymmetric stretch of  $-\text{COO}^-$ , i.e.  $\nu_{\text{as}}(\text{COO}^-)$ , appears at  $1599$   $\text{cm}^{-1}$ . For NALCME, two IR bands are observed, corresponding to the  $\text{C}=\text{O}$  stretch of the  $-\text{COOME}$  group, i.e.  $\nu(\text{C}=\text{O})_{\text{ester}}$ , and the amide I band,  $\nu(\text{C}=\text{O})_{\text{ac}}$ , from high to low wavenumber. In the case of NALCME, the amide I band occurs at essentially the same wavenumber position as the NALC molecule, whereas  $\nu(\text{C}=\text{O})_{\text{ester}}$  emerges at  $\sim 1735$   $\text{cm}^{-1}$  which is blue shifted by  $\sim 15$   $\text{cm}^{-1}$  compared to  $\nu(\text{C}=\text{O})_{\text{ca}}$  of NALC. The experimental VA and VCD spectra extended down to  $1300$   $\text{cm}^{-1}$  are provided in Fig. S1, Supporting Information.

Another interesting observation highlighted in Fig. 1 is the sign reversal of the VCD amide I mode. For neutral NALC and NALCME, this band exhibits a negative VCD sign, whereas for the deprotonated NALC species, i.e. depNALC, the sign of this VCD band changes to positive. In addition, the VCD signs of the  $\nu(\text{C}=\text{O})_{\text{ca}}$  of neutral NALC and of  $\nu(\text{C}=\text{O})_{\text{ester}}$  of NALCME remain positive.

In the following, we use theoretical modeling to explain these observations. In particular, we focus on the comparison of the experimental and theoretical VCD patterns of the most stable conformers of the NALCME, NALC, and depNALC species predicted. Our goals are to establish useful empirical structural-spectral relationships and to explore a suitable approach to interpret the experimental VCD spectra in water adequately and efficiently.

#### Conformational searches

The conformational search of depNALC is discussed first since NALC and NALCME also contain similar molecular fragments. A preliminary two-dimensional energy plot of depNALC at the B3LYP/6-31G(d) level in the gas phase, scanned along two of its most important rotational angles about the  $\text{C}3-\text{C}5$  and  $\text{C}3-\text{N}1$  bonds (see Fig. 2 for atom labeling), was reported previously [15]. It was recognized that the lone electron pairs of the N atom is involved in a resonance structure with the adjacent  $-\text{C}=\text{O}$

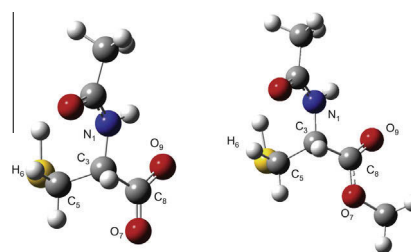


**Fig. 2.** Atom labeling for the depNALC (left) and NALCME (right) molecules.

group, and the  $-\text{NH}$  group forms an intramolecular hydrogen-bond with the  $-\text{COO}^-$  group. As a result, this part of molecule is fairly rigid. Therefore, the main conformational freedom involves the rotation of the  $-\text{SH}$  group about the  $\text{C}3-\text{C}5$  bond. We further carried out the potential energy scan along this angle at the B3LYP/aug-cc-pVTZ level in the gas phase and with the PCM of water solvent. The scanned results obtained in the gas phase and with PCM are provided in Fig. S2, Supporting Information. Altogether, five most stable conformers of depNALC with the PCM of water solvent were optimized and proved to be true minima with no negative frequencies. Their geometries with the PCM of water solvent are provided in Fig. 3, while the corresponding gas phase geometries are given in Fig. S3, Supporting Information. To facilitate easy differentiation of the conformers, all intramolecular hydrogen-bond lengths or van der Waals bond lengths less than  $3$  Å are indicated in the related figures. Their relative energies and the associated Boltzmann population factors at room temperature of these five conformers are summarized in Table 1. We note that the most stable conformers identified are similar to those obtained with the 6-311++G(d,p) basis set [15], although with a somewhat different stability order.

For the next species, i.e. neutral NALC, its conformational landscape had been studied extensively before both in the gas phase and with the PCM of water solvent [15–28]. Therefore, only the six most stable NALC conformers re-optimized at the B3LYP/aug-cc-pVTZ are reported here. Their geometries with the PCM of water solvent are shown in Fig. 3, while the corresponding gas phase geometries are depicted in Fig. S4, Supporting Information. Their relative energies and the associated Boltzmann population factors at room temperature are provided in Table 1.

For NALCME, because of the methyl substitution at the carboxylic site of NALC, its ability to form hydrogen-bonds is reduced and

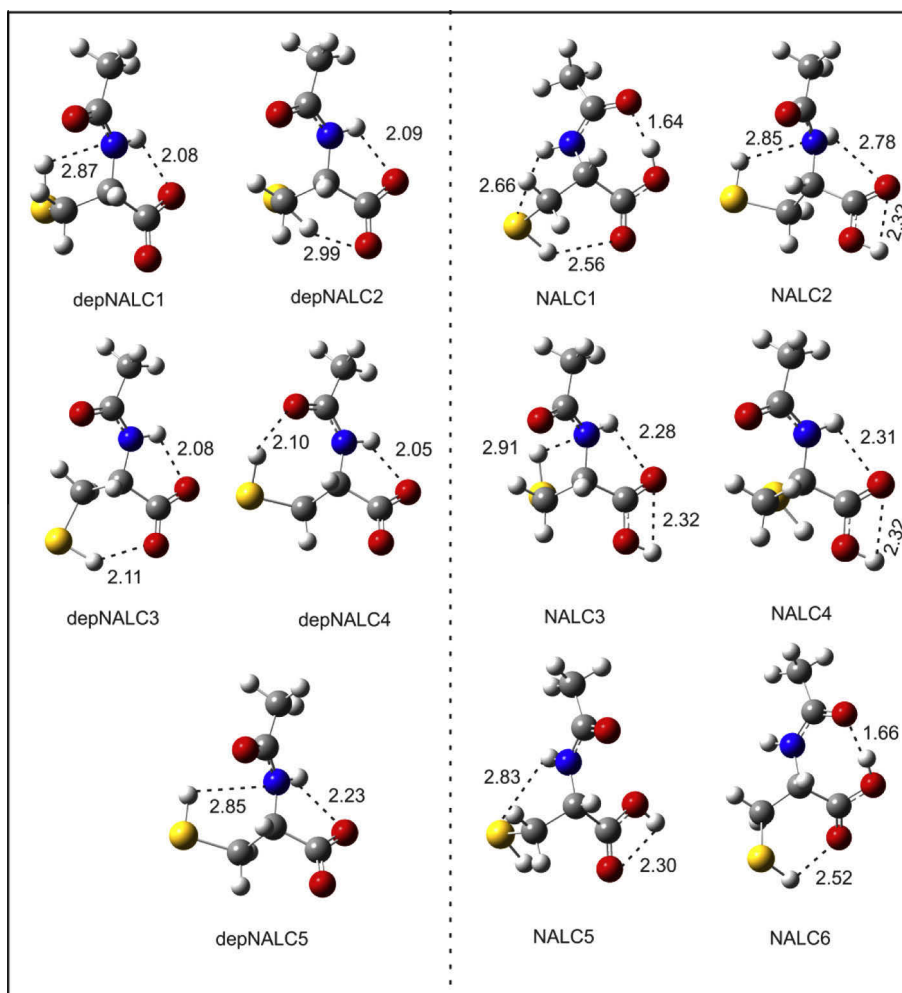


**Fig. 3.** Geometries of the most stable conformers of depNALC and the neutral NALC at the PCM/B3LYP/aug-cc-pVTZ level. All relevant intramolecular bonds with a bond length less than 3 Å are indicated.

the conformational landscape for NALCME is less-complicated compared to that of neutral NALC. In fact, methyl esterification was used before as a method to eliminate or minimize the inter- and intramolecular hydrogen-bonding interactions in the related chiral systems, such as 2-(2-chlorophenoxy) propanoic acid and 2-(3-chlorophenoxy) propanoic acid, in order to identify their absolute configurations [27]. Building on the results obtained for neutral NALC [15,28], potential energy scans along the two dihedral angles namely,  $O_9-C_8-C_3-N_1$  and  $H_6-C_5-C_3-N_1$  (see Fig. 2 for atom labeling) were performed. Such scans allow the  $-CH_2SH$  group to make an intramolecular hydrogen-bond with either the  $-NH$  or the  $-COOMe$  group. Furthermore, such hydrogen-bonding interaction can happen either with the carbonyl or the ester oxygen atom of the  $-COOMe$  group. Overall, seven most stable conformers were identified. The optimized geometries of these seven conformer at the PCM/B3LYP/aug-cc-pVTZ level are shown in Fig. 4, while the corresponding gas phase geometries are summarized in Fig. S5, Supporting Information. Their relative energies and the related Boltzmann population factors at room temperature obtained with the PCM of water solvent and in the gas phase are also summarized in Table 1.

The energy spread is relatively small among these conformers. For example, NALCME1 and NALCME3 differ only in one main aspect:  $-NH$  points to the ester oxygen atom in NALCME3 instead of the carboxylate oxygen atom as in NALCME1. It is known from both the solution [13,15] and the gas phase [29,30] experimental

studies that the  $-NH \cdots O_{ester}$  or  $-OH \cdots O_{ester}$  interactions contribute less to the stabilization energy compared to the  $-NH \cdots O=C$  or  $-OH \cdots O=C$  interactions. Indeed, the intramolecular hydrogen-bonding distance of  $-NH \cdots O=C$  in NALCME1 is 2.26 Å, whereas that distance of  $-NH \cdots O_{ester}$  in NALCME3 is 2.78 Å.

#### *Changes in the conformational geometries and their relative stability ordering in the gas phase and with the PCM of water solvent*

To appreciate the effects of bulk solvent, it is interesting to highlight some changes in the geometries and the relative stability of the most stable conformers from the gas phase and to the presence of an implicit solvent. For consistency, the following discussions are based on the relative free energies at room temperature (see Table 1). Comments about the differences in the  $\Delta G$ - and  $\Delta E$ -based stability orderings are provided at the end of the section.

The most stable conformer of depNALC in the gas phase exhibits an  $-NH \cdots OCO^-$  intramolecular hydrogen-bond, and at the same time the H atom of the  $-SH$  group points toward the oxygen atom of  $OCO^-$  (see Fig. S3). The corresponding PCM conformer has a similar geometrical arrangement with the same intramolecular hydrogen-bonds. The exception is that the intramolecular hydrogen-bond lengths become noticeably longer: from about 1.8 Å in the gas phase to about 2.1 Å with the PCM of water solvent. The two aforementioned cyclic hydrogen-bond formations deliver significant stability to the particular structure in the gas phase. While

**Table 1**

Values of the relative free energy  $\Delta G$  (in kcal/mol) in the gas phase and with PCM, and the relative zero-point-corrected energy  $\Delta E$  (kcal/mol) with PCM, as well as the corresponding Boltzmann population percentage factors at room temperature of the most stable conformers of depNALC, neutral NALC and NALCME at the B3LYP/aug-cc-pVTZ level.

Conformers	PCM		Gas phase		PCM	
	$\Delta G$ [rank] <sup>a</sup>	pop% $\Delta G$	$\Delta G$ [rank] <sup>b</sup>	pop% - $\Delta G$	$\Delta E$ [rank] <sup>c</sup>	pop% - $\Delta E$
<i>Deprotonated NALC</i>						
depNALC1	0.00 [1]	39.68	0.42 [2]	29.97	0.01 [2]	37.72
depNALC2	0.04 [2]	36.54	1.95 [4]	2.29	0.00 [1]	38.49
depNALC3	0.60 [3]	14.34	0.00 [1]	61.48	0.50 [3]	16.33
depNALC4	1.05 [4]	6.74	1.35 [3]	6.25	1.21 [4]	4.92
depNALC5	1.59 [5]	2.70	N/A <sup>d</sup>		1.61 [5]	2.53
<i>Neutral-NALC</i>						
NALC1	0.00 [1]	25.82	0.22 [3]	20.15	0.00 [1]	70.50
NALC2	0.08 [2]	22.45	0.65 [5]	9.70	2.10 [5]	2.03
NALC3	0.16 [3]	5.90	0.00 [1]	29.05	1.47 [3]	19.42
NALC4	0.34 [4]	14.49	0.06 [2]	26.33	1.83 [4]	3.21
NALC5	0.48 [5]	11.35	0.43 [4]	13.95	2.33 [6]	1.37
NALC6	0.82 [6]	6.74	2.11 [6]	0.82	0.84 [2]	17.00
<i>Methyl ester-NALC</i>						
NALCME1	0.00 [1]	21.53	2.24 [6]	0.97	0.61 [3]	13.92
NALCME2	0.05 [2]	19.70	0.71 [3]	2.80	0.88 [4]	8.95
NALCME3	0.09 [3]	18.37	2.81 [7]	0.37	1.19 [6]	5.21
NALCME4	0.23 [4]	14.52	0.00 [1]	42.44	0.00 [1]	39.43
NALCME5	0.32 [5]	12.50	0.21 [2]	29.80	0.35 [2]	21.64
NALCME6	0.56 [6]	8.36	0.80 [4]	10.90	1.23 [7]	4.91
NALCME7	0.86 [7]	5.04	1.63 [5]	2.73	1.12 [5]	5.93

<sup>a</sup> Relative stability based on  $\Delta G$  obtained with the PCM of water.

<sup>b</sup> Relative stability based on  $\Delta G$  obtained in the gas phase.

<sup>c</sup> Relative stability based on the zero-point-energy corrected  $\Delta E$  obtained with the PCM of water solvent.

<sup>d</sup> This optimized structure in the gas phase turns to depNALC4 (see Fig. S3).

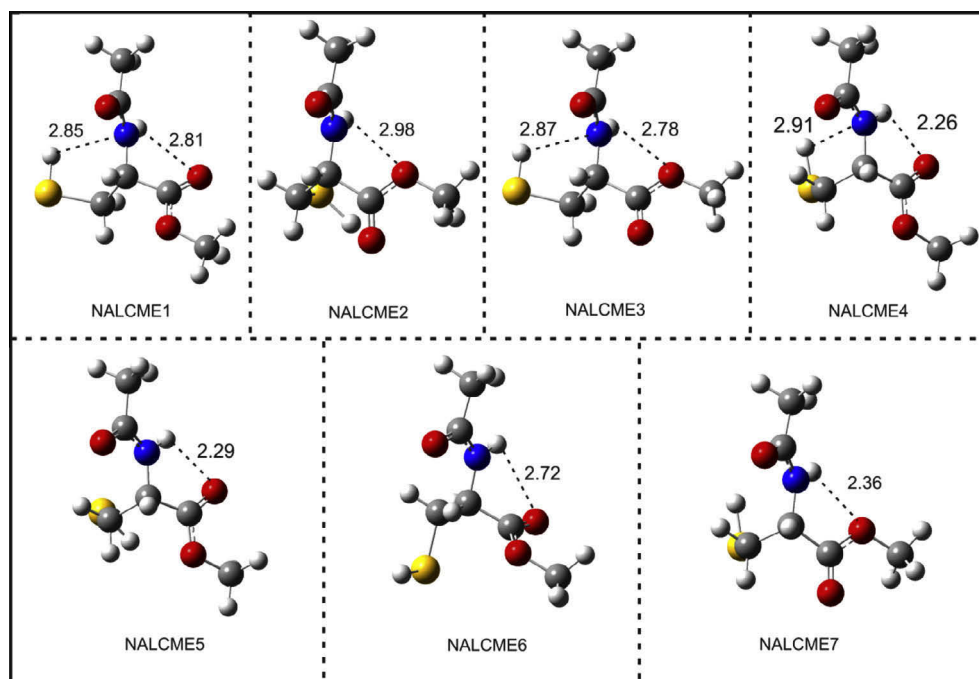


**Fig. 4.** Geometries of the seven most stable conformers of NALCME at the PCM/B3LYP/aug-cc-pVTZ level. All relevant intramolecular bonds with a bond length less than 3 Å are indicated.

this most stable conformer of depNALC in the gas phase carries about 60% of the total population, its corresponding structure optimized with the PCM of water solvent contributes only about 14%. In general, the intramolecular hydrogen-bond or van der Waals bond lengths associated with the  $-\text{SH}$  group are in the range of 2.10–2.99 Å in the conformers obtained with the PCM of water, while their values vary from 1.88 to 2.88 Å in the gas phase. As a result of these geometric changes, the relative stability ordering

of the depNALC conformers also changes going from the gas phase to the PCM of water solvent.

For the NALC species, a number of dihedral angles are important in generating the low energy conformations. This flexibility brings about a more complex conformational landscape. It is interesting to note that all six conformers identified in the gas phase have the one-to-one corresponding PCM conformers. Similarly, for the NALCME, the inclusion of the implicit solvent model tends to alter

some dihedral angles for those involved in the intramolecular hydrogen-bonds, such as the  $\text{-NH}$  and  $\text{-SH}$  groups. While the first five conformers with PCM contribute about 10–26% each to the total population, i.e. contribute fairly evenly, this trend is not seen with those in the gas phase where two main conformers contribute over 70% to the total population.

Overall, the bulk solvent environment plays two important roles here, namely to modify both the relative stability ordering of the conformers and their geometries. Generally speaking, the gas phase structures are more compact than those obtained with the PCM of water solvent. This is not surprising since without the interference of water solvent, the solute molecule is free to optimize the possible intramolecular hydrogen-bonds, resulting in more compact geometries.

The relative stability orderings based on  $\Delta G$  and on  $\Delta E$  are more or less the same for the depNALC species, with the first two most stable conformers having essential the same stability. For NALC, although the most stable conformer is strongly favored with about 70% of the total population based on  $\Delta E$ , the contributions of the five lowest energy conformers are fairly evenly distributed based on  $\Delta G$ . Related observation can also be made for NALCME. Overall, stability orderings based on the  $\Delta G$  and  $\Delta E$  values differ slightly for depNALC, and more drastically for NALC and NALCME, as can be seen from Table 1. Since the amount of order or disorder is directly associated with the entropy term which makes the two terms,  $\Delta G$  and  $\Delta E$ , different, one can expect different stability ordering based on these two terms. In fact, a strong temperature dependence of the  $\Delta G$  values for different conformers in other systems had been clearly demonstrated in a number of previous studies [31]. Consequently, it is not surprising that the stability ordering of the conformers based on  $\Delta G$  can differ noticeably from that based on  $\Delta E$ . For the solution measurements considered here, it is logical to use  $\Delta G$  rather than  $\Delta E$  for population weighed spectral simulations.

#### Comparison of the experimental and simulated IR and VCD spectra

##### NALCME

The experimental IR and VCD spectra of NALCME are compared with the corresponding spectra of individual conformer in Fig. 5 to

facilitate detailed comparison. It is noted that the peak frequencies of the  $\nu(\text{C=O})_{\text{ester}}$  stretch mode for all seven conformers show only a small spread, i.e. from  $1755\text{ cm}^{-1}$  to  $1740\text{ cm}^{-1}$ . For the amide I bands, this spread is even smaller, i.e. from  $\sim 1675\text{ cm}^{-1}$  to  $1666\text{ cm}^{-1}$ . Therefore, based on the comparison of the calculated and observed IR spectral features, one cannot tell apart of these possible conformers. The VCD spectral features, on the other hand, differ drastically for the different conformers of NALCME. While NALCME1 shows a positive–negative couplet in accord with the experimental observation, NALCME2, NALCME3, and NALCME7 all show a negative–positive couplet, in contrary to the experiment. Furthermore, NALCME4 and NALCME5 have both very low or diminishing amide I VCD intensity, whereas two negatives VCD bands with low intensities are predicted for NALCME6.

It is clear from Fig. 5 that the population weighted VCD spectrum based on the  $\Delta G$ -Boltzmann factors in Table 1 would be in poor agreement with the experiment. While the room temperature Boltzmann factors suggest similar amount of NALCME1, 2, and 3 in solution, the spectral signatures observed indicate that NALCME1 should dominate over NALCME2 and 3 in order to obtain the experimental observed features. One may argue that the DFT energies predicted are off. There are, however, a substantial body of literature, where such predictions serve their purposes well [2,32,33]. In general, it appears that the relative free energy predictions tend to deviate more when water is the solvent and the targeted chiral molecules have multiple hydrogen-bonding sites. It is therefore desirable to probe this phenomenon further by examining the related systems which have stronger hydrogen-bonding capability. In the following sections, we look at the cases of depNALC and neutral NALC.

##### depNALC

The dominant species of NALC in water at pH = 7.0 is depNALC. The corresponding experimental IR and VCD spectra were reported before and both implicit and explicit solvation models at the B3LYP/6-311++G (d,p) level were utilized to interpret the experimental data [15]. For completion, the comparison of the experimental and simulated IR and VCD spectra with the new basis set, aug-cc-pVTZ, is presented in Fig. 6. It is interesting to note that

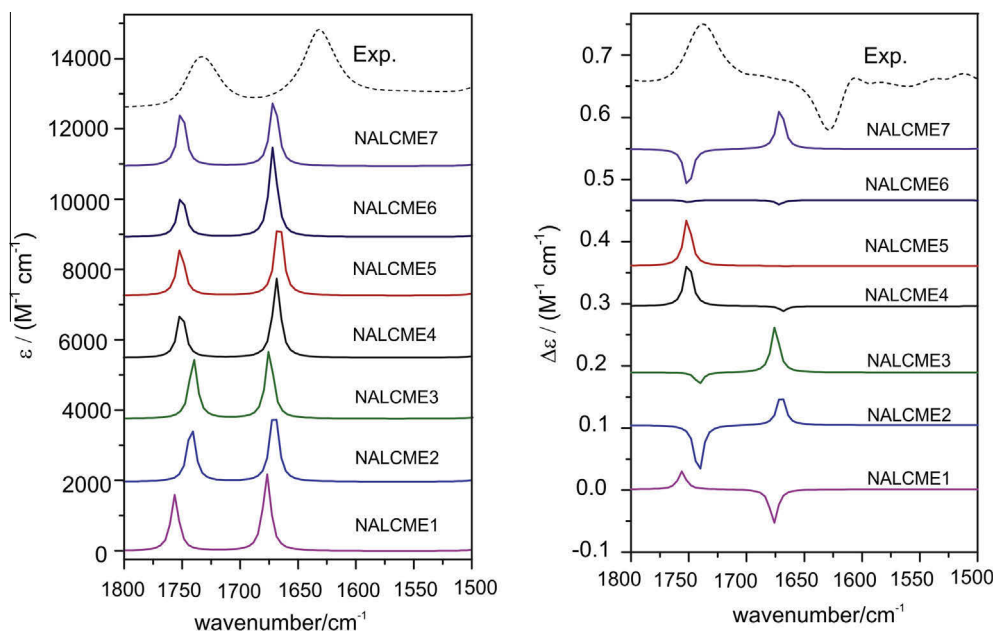
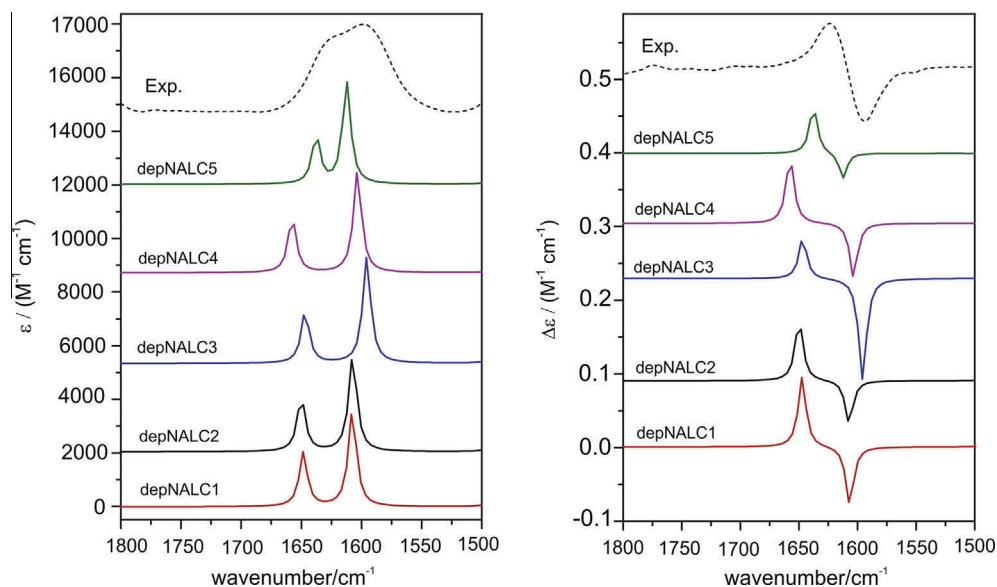


Fig. 5. Comparison of the experimental IR (left) and VCD (right) spectra of NALCME with the related theoretical spectra of the seven conformers of NALCME at the PCM/B3LYP/aug-cc-pVTZ level.



**Fig. 6.** Comparison of the experimental IR (left) and VCD (right) spectra of depNALC with the related theoretical spectra of the five conformers of depNALC at the PCM/B3LYP/ aug-cc-pVTZ level.

all five most stable conformers exhibit two closely spacing IR bands, corresponding to the amide I and  $\nu_{as}(\text{COO}^-)$  bands, from high to low wavenumber. They also all show a positive–negative VCD couplet. The spacing between the amide I and the carboxylate bands differ slightly among conformers. This spacing depends mainly on the relative orientation of the  $-\text{SH}$  group with respect to the rest of the molecule where it can make an intramolecular hydrogen-bond with either  $-\text{NH}$ ,  $-(\text{O}=\text{C})_{ac}$  or  $-\text{COO}^-$ . Since both experimental IR and VCD bands appear quite broad in the spectra, it is likely that all these conformers contribute to the observed spectra. In the previous study, it was found that the significant hydrogen-bonding interactions with water molecules influence mostly the VCD features in the  $1500\text{--}1300\text{ cm}^{-1}$  region [15]. Nevertheless, the most stable conformers identified with the joint implicit and explicit solvent approach [15] are consistent with those predicted with the PCM model. On the other hand, since all the conformers show very similar IR and VCD patterns, it is not possible to discriminate one against another. This is in contrast to the case of NALCME.

#### Neutral NALC

In Fig. 7, the experimental IR and VCD spectra of NALC in water at  $\text{pH} \approx 2.5$  are compared with the simulated spectra of the six most stable conformers of the neutral NALC which is the dominant species at such a low pH value. While the  $\nu(\text{C}=\text{O})_{ca}$  bands are predicted to have very similar peak wavenumbers for all six conformers, the amide I bands spread widely. In particular, the  $\nu(\text{C}=\text{O})_{ac}$  bands of NALC1 and NALC6 are red shifted by  $\sim 65\text{ cm}^{-1}$  compared to NALC2. This is because in these two conformers, the  $-(\text{OH})_{ca}$  group points toward the  $-(\text{C}=\text{O})_{ac}$  group to make an intramolecular hydrogen-bond, whereas the  $-(\text{C}=\text{O})_{ac}$  groups in the other conformers are free. Since the experimental  $\nu(\text{C}=\text{O})_{ac}$  band of NALC appears at essentially the same peak position as for NALCME, and NALCME does not have the  $-(\text{OH})_{ca}$  group to form such an intramolecular hydrogen-bond, we conclude that NALC1 and NALC6 do not contribute significantly in solution. At the same time, their corresponding  $\nu(\text{C}=\text{O})_{ac}$  VCD signals are positive, in contrary to the sign of the corresponding experimental VCD band at  $\sim 1630\text{ cm}^{-1}$ . A closer examination reveals that this strongest experimental IR band has a tail at the lower frequency side. Correspondingly, there

is a small positive VCD bump at  $\sim 1615\text{ cm}^{-1}$ . These observations suggest that there may be a small amount of NALC1 in solution.

The other four conformers have very similar IR patterns and one cannot tell them apart based on the IR spectral features observed. On the other hand, the VCD features predicted for these four conformers are quite different. NALC5 shows the VCD couplet with the opposite sign of the experiment. While the  $\nu(\text{C}=\text{O})_{ca}$  bands of NALC3 and NALC4 have the same positive sign as the experiment, their VCD bands at the amide I band have diminishing intensity, in contrast to the experiment. The only remaining conformer, namely NALC2, shows consistent VCD signatures as the experiment. We therefore conclude that overall, NALC2 contributes dominantly to the observed spectra, while some small contributions from other conformers may also be present as discussed above.

As can be seen from Table 1, the first three conformers of NALC were predicted to have very similar stability, whereas the experimental data clearly suggest that only one of them, i.e. NALC2, is the dominant conformer. This conclusion echoes the result obtained with NALCME: it is possible to utilize the rich VCD spectral patterns to identify the dominant conformers even though the calculated abundance of these conformers may not support the same conclusion. The latter point will be further discussed in ‘The solute-water hydrogen-bonding interactions and DFT conformational stabilities’.

#### The conformational structure markers

It is known that the sign and the intensity of a VCD band are associated with its rotational strength  $R$ .  $R$  can be expressed as the imaginary part of the dot product of the electric and magnetic transition dipole moment vectors, i.e.  $R = |\boldsymbol{\mu}| \cdot |\boldsymbol{m}| \cos \theta$ , [1] where  $|\boldsymbol{\mu}|$  and  $|\boldsymbol{m}|$  are the magnitudes of the electric and magnetic transition dipole moment vectors, respectively, and  $\theta$  is the angle between these two vectors. Clearly, the sign of a particular VCD band is determined by the angle  $\theta$ . On the other hand, such  $\theta$  values do not provide one with the intuitive structural information. We therefore set out to seek a more direct, empirical correlation between the observed VCD signatures and the corresponding conformational structures. The four atoms involved in the amide bonds are essentially in one plane due to the resonance structure of the



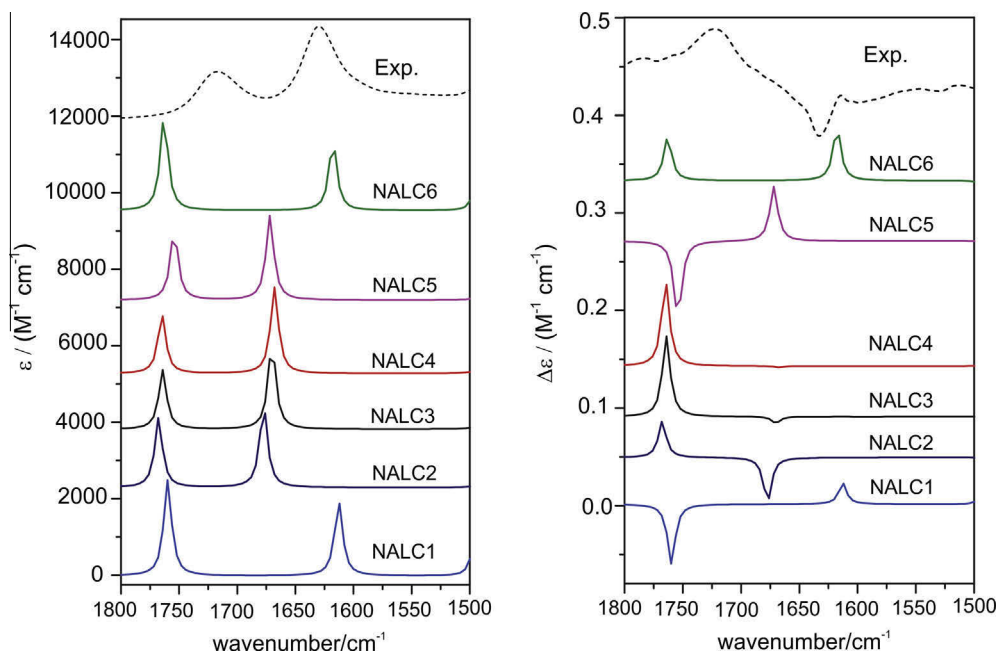


Fig. 7. Experimental IR (left) and VCD (right) spectra of NALC at pH = 2.5 where the dominant species is the neutral form of NALC. The corresponding simulated spectra of the six most stable NALC conformers at the PCM/B3LYP/aug-cc-pVTZ level are also presented.

with the  $\text{—NH}$  group with the adjacent  $\text{—C=O}$  group. Here, we define a *conformational frame angle*,  $\tau$ , which is the dihedral angle between this amide plane and the  $\text{—COO}$  plane. This angle characterizes the most important conformational arrangement of the three targeted species, except the orientation of the  $\text{—SH}$  group. For depNALC,  $\tau$  can in principle take on values ranging from  $\text{—}90^\circ$  to  $+90^\circ$  where “+” means clockwise rotation viewing from the amide plane to the  $\text{—COO}$  plane and “ $\text{—}$ ” the opposite. For neutral NALC and NALCME, this range expands to  $\text{—}180^\circ$  to  $+180^\circ$  since there are either an H atom or a methyl group attached to the  $\text{—COO}$  group, respectively. The values of this conformational frame angle for all conformers studied here are summarized in Fig. 8. The  $\tau$  values are color coded. Red indicates that the conformer with this specific  $\tau$  value has both VCD signatures in agreement with the experiment. Black means that one or both VCD signature bands show opposite signs to those observed or both bands have diminishing intensities. Green indicates that while the  $\text{C=O}$  stretching band shows consistent sign as the experiment, the amide I band has very weak or diminishing intensity.

As one can see, all five conformers of depNALC have a positive  $\tau$  value ranging from about  $32^\circ$  to  $51^\circ$ . All them show the positive amide I VCD bands and the negative  $\nu_{\text{as}}(\text{COO}^-)$  VCD bands, in accordance with the experimental observed spectral features. For the neutral NALC conformers, those with the *negative*  $\tau$  values all show the *opposite* amide I VCD sign compared to the experiment, whereas NALC2 with a positive  $\tau$  value of about  $80^\circ$  has both of its amide I and carboxylic bands agree well with the experiment. NALC3 and 4 have the  $\tau$  values of about  $47^\circ$  and both have very weak VCD amide I band. The same parallel observation can be made for NALCME conformers as for the NALC conformers. In particular, the dominant conformers identified for NALC and NALCME in water, i.e. NALC2 and NALCME1, have essentially the same conformational frame angle of about  $80^\circ$ . Of course,  $\tau$  does not have a simple one-to-one relationship to  $\theta$ s. Nevertheless, as shown here, the VCD signatures observed for the amide I band and the  $\text{C=O}$  stretching bands can be used as markers to identify such conformational preference in water.

For depNALC, the conformational frame as defined above is fairly rigid. It is not surprising that all five conformers show very

much the same VCD signatures in the  $1800\text{--}1500\text{ cm}^{-1}$  region. Furthermore, it appears that these two VCD bands are not sensitive to the relative orientation of the  $\text{—SH}$  group in the molecule since this is precisely how the five conformers are generated. On the other hand, one may expect different VCD signatures for the  $\text{—SH}$  stretching band. Indeed, the simulated VCD features of the  $\text{—SH}$  mode for these five conformers are very different (see Fig. S6, Supporting Information). Unfortunately, this mode is too weak to be measured experimentally.

#### The solute-water hydrogen-bonding interactions and DFT conformational stabilities

It is recognized in the current study that the dominant conformers identified are not necessarily those predicted theoretically. Although DFT population factors have been used successfully in many cases, their applications with highly polar solvents tend to be less successful. One can hypothesize that the explicit solute-water hydrogen-bonding interactions may alter the relative stability of individual conformers significantly. Indeed, clear evidences of such explicit hydrogen-bonding interactions between chiral solute and water molecules in aqueous solution were demonstrated previously using chirality transfer spectral features [13,14,34] and other characteristic changes in the VCD spectra [4,15]. For a number of small model chiral molecular systems, it has been possible to probe the chiral solute-water interaction in solution directly. Using both the implicit and explicit solvation models, the experimental VCD features observed can be accounted for in detail. For large chiral molecular systems with multiple relevant conformers, on the other hand, it may be too expensive or not feasible to utilize the explicit solvation methodology. The approach of using the IR and VCD spectral signatures simulated with the PCM model of water solvent as markers to extract information about chirality and dominant conformations is a viable alternative, as demonstrated in the current study.

It is also noted that some detailed IR spectral features could not be explained satisfactorily based on the PCM of water solvent. For example, the  $15\text{ cm}^{-1}$  blue shift of  $\nu(\text{C=O})_{\text{ester}}$  of NALCME compared to  $\nu(\text{C=O})_{\text{ca}}$  of neutral NALC was not correctly predicted. It

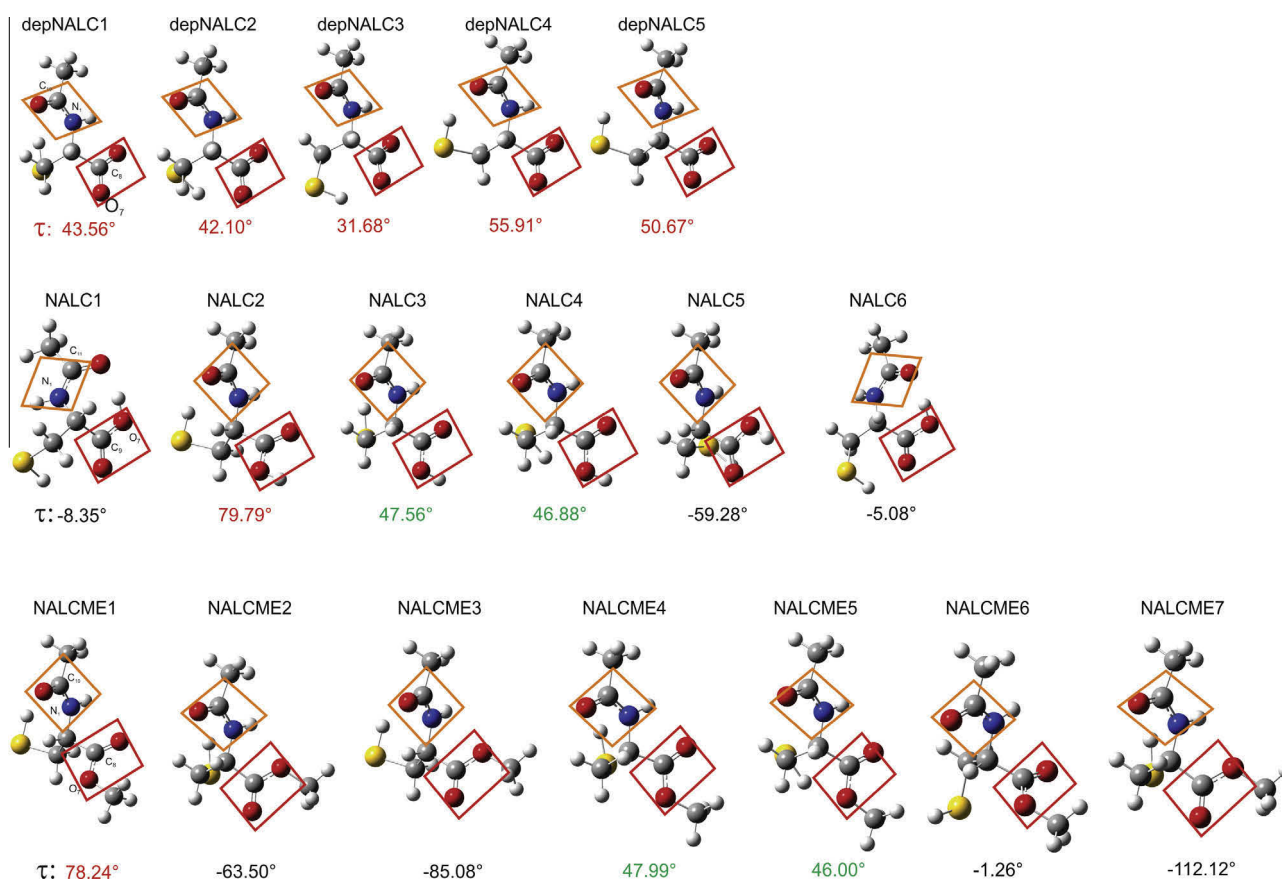


Fig. 8. Conformational frame angle  $\tau$  (in degree) for all the conformers reported in Table 1. The  $\tau$  values are color coded. See text for the detailed discussions.

is acknowledged that such a small vibrational shift is in general challenging to reproduce with harmonic vibrational calculations. In addition, the PCM approach does not capture the explicit hydrogen-bonding interactions between NALCME and water and between NALC and water. A plausible reason for such a blue shift is that the neutral form of NALC can engage more extensively in the hydrogen-bonding interactions between water and the  $-\text{COOH}$  group, causing  $\nu(\text{C}=\text{O})_{\text{ca}}$  to red-shifted more significantly compared to that of NALCME.

## Conclusions

IR and VCD spectral signatures of the amide I and  $\text{C}=\text{O}$  stretching bands of NALCME and NALC were measured in water under different pHs. With the extensive conformational calculations and the detailed analyses of the resulting spectral features and structural parameters, we establish a clear relationship between the observed VCD spectral signatures and the preferred conformations. The sign inversion observed for the amide I VCD band going from neutral NALCME and NALC to depNALC is explained satisfactorily based on the changes in the corresponding conformational frame angles in these species. In addition, the geometric changes going from the gas phase to the PCM of water solvent were investigated to highlight the effects of a dielectric bulk environment.

It is noted that drastically different VCD spectral signatures were predicted in the above spectral window for different conformers of neutral NALC and NALCME. This advantage allows one to confidently identify the particular conformations favored in solution, regardless of their DFT stability ordering. The present study shows that the relative free energies predicted may not reflect the actual situation in solution as demonstrated in the cases of neutral NALCME and NALC. Such deviations are rationalized in

terms of the interferences from the explicit hydrogen-bonding interactions between chiral solute and water molecules. Based on the current study, it is recommended to include the PCM of water solvent in the studies of amino acids and the related chiral molecules since it is relatively inexpensive and can capture some of the main conformational changes in the presence of a dielectric solution environment.

## Acknowledgements

This research was funded by the University of Alberta and the Natural Sciences and Engineering Research Council of Canada. We gratefully acknowledge access to the computing facilities provided by the Shared Hierarchical Academic Research Computing Network (Sharcnet). YX holds a senior Canada Research Chair in Chirality and Chirality Recognition.

## Appendix A. Supplementary material

Supplementary data associated with this article can be found, in the online version, at <http://dx.doi.org/10.1016/j.saa.2013.08.118>.

## References

- [1] L.A. Nafie, *Vibrational Optical Activity: Principles and Applications*, John Wiley & Sons, Chichester, UK, 2011.
- [2] P.J. Stephens, F.J. Devlin, J.-J. Pan, *Chirality* 20 (2006) 643–663; T.B. Freedman, X. Cao, R.K. Dukor, L.A. Nafie, *Chirality* 15 (2003) 743–758.
- [3] P. Zhang, P.L. Polavarapu, *Appl. Spectrosc.* 60 (2006) 378–385; W.M. Zuk, T.B. Freedman, L.A. Nafie, *J. Phys. Chem.* 93 (1989) 1771–1779.
- [4] M.R. Poopari, P. Zhu, Z. Dezhahang, Y. Xu, *J. Chem. Phys.* 137 (2012). 194308/1–7; P. Zhu, G. Yang, M.R. Poopari, Z. Bie, Y. Xu, *ChemPhysChem* 13 (2012) 1272–1281.

- [5] T.A. Keiderling, *Curr. Opin. Chem. Biol.* 6 (2002) 682–688; T.A. Keiderling, J. Kubelka, J. Hilario, *Vibrational circular dichroism of biopolymers. Summary of methods and applications*, in: M. Braiman, V. Gregoriou (Eds.), *Vibrational spectroscopy of polymers and biological systems*, Taylor & Francis; CRC Press., Atlanta; Boca Raton, FL, 2006, pp. 253–324.
- [6] G. Yang, Y. Xu, *Vibrational circular dichroism spectroscopy of chiral molecules*, in: R. Naaman, D.N. Beratan, D.H. Waldeck (Eds.), *Top. Curr. Chem.: Electronic and Magnetic Properties of Chiral Molecules and Supramolecular Architectures*, vol. 298, Springer, Berlin, 2011, pp. 189–236.
- [7] E. Debie, P. Bultinck, W. Herrebout, B. van der Veken, *Phys. Chem. Chem. Phys.* 10 (2008) 3498–3508; V.P. Nicu, E. Debie, W. Herrebout, B. Van der Veken, P. Bultinck, E.J. Baerends, *Chirality* 21 (2009) E287–E297.
- [8] C. Gautier, T. Burgi, *Chem. Commun.* 43 (2005) 5393–5395.
- [9] P.L. Polavarapu, N. Jeirath, S. Walia, *J. Phys. Chem. A* 113 (2009) 5423–5431; G. Yang, J. Li, Y. Liu, T.L. Lowary, Y. Xu, *Org. Biomol. Chem.* 8 (2010) 3777–3783; G. Yang, Y. Xu, J. Hou, H. Zhang, Y. Zhao, *Dalton Trans.* 39 (2010) 6953–6959; G. Yang, Y. Xu, J. Hou, H. Zhang, Y. Zhao, *Chem. Eur. J.* 16 (2010) 2518–2527; G. Yang, H. Tran, E. Fan, W. Shi, T.L. Lowary, Y. Xu, *Chirality* 22 (2010) 734–743.
- [10] C. Merten, K. Hiller, Y. Xu, *Phys. Chem. Chem. Phys.* 14 (2012) 12884–12891; Z. Dezhahang, C. Merten, M.R. Poopari, Y. Xu, *Dalton Trans.* 41 (2012) 10817–10824.
- [11] V.P. Nicu, E.J. Baerends, P.L. Polavarapu, *J. Phys. Chem. A* 116 (2012) 8366–8373.
- [12] M.R. Poopari, Z. Dezhahang, Y. Xu, *Phys. Chem. Chem. Phys.* 15 (2013) 1655–1665.
- [13] J. Sadlej, J.C. Dobrowolski, J.E. Rode, *Chem. Soc. Rev.* 39 (2010) 1478–1488.
- [14] M. Losada, P. Nguyen, Y. Xu, *J. Phys. Chem. A* 112 (2008) 5621–5627; M. Losada, Y. Xu, *Phys. Chem. Chem. Phys.* 9 (2007) 3127–3135.
- [15] M.R. Poopari, Z. Dezhahang, G. Yang, Y. Xu, *ChemPhysChem* 13 (2012) 2310–2311.
- [16] J. Šebek, B. Gyurcsik, J. Šebestík, Z. Kejík, L. Bednářová, P. Bour, *J. Phys. Chem. A* 111 (2007) 2750–2760; V.W. Jürgensen, K. Jalkanen, *Phys. Biol.* 3 (2006) S63–S79.
- [17] L. Borgström, B. Kågedal, O. Paulsen, *Eur. J. Clinical Pharm.* 31 (1986) 217–222.
- [18] M.Z. Kanter, *Am. J. Health-System Pharm.* 63 (2006) 1821–1827.
- [19] A. Krężel, W. Bal, *J. Inorg. Biochem.* 98 (2004) 161–166.
- [20] Gaussian 09, Revision B.01, M.J. Frisch, G.W. Trucks, H.B. Schlegel, G.E. Scuseria, M.A. Robb, J.R. Cheeseman, G. Scalmani, V. Barone, B. Mennucci, G.A. Petersson, H. Nakatsuji, M. Caricato, X. Li, H.P. Hratchian, A.F. Izmaylov, J. Bloino, G. Zheng, J.L. Sonnenberg, M. Hada, M. Ehara, K. Toyota, R. Fukuda, J. Hasegawa, M. Ishida, T. Nakajima, Y. Honda, O. Kitao, H. Nakai, T. Vreven, J.A. Montgomery, Jr., J.E. Peralta, F. Ogliaro, M. Bearpark, J.J. Heyd, E. Brothers, K.N. Kudin, V.N. Staroverov, R. Kobayashi, J. Normand, K. Raghavachari, A. Rendell, J.C. Burant, S.S. Iyengar, J. Tomasi, M. Cossi, N. Rega, J.M. Millam, M. Klene, J.E. Knox, J.B. Cross, V. Bakken, C. Adamo, J. Jaramillo, R. Gomperts, R.E. Stratmann, O. Yazyev, A.J. Austin, R. Cammi, C. Pomelli, J.W. Ochterski, R.L. Martin, K. Morokuma, V.G. Zakrzewski, G.A. Voth, P. Salvador, J.J. Dannenberg, S. Dapprich, A.D. Daniels, Ö. Farkas, J.B. Foresman, J.V. Ortiz, J. Cioslowski, D.J. Fox, Gaussian, Inc., Wallingford CT, 2009.
- [21] J.K. Labanowski, J.W. Andzelm (Eds.), *Density Functional Methods in Chemistry*, Springer-Verlag, New York, 1991.
- [22] K. Kim, K.D. Jordan, *J. Phys. Chem.* 98 (1994) 10089–10094.
- [23] P.J. Stephens, F.J. Devlin, C.F. Chabalowski, M.J. Frisch, *J. Phys. Chem.* 98 (1994) 11623–11627.
- [24] C.T. Lee, W.T. Yang, R.G. Parr, *Phys. Rev. B* 37 (1988) 785–789.
- [25] D.E. Woon, T.H. Dunning Jr., *J. Chem. Phys.* 98 (1993) 1358–1371.
- [26] J. Tomasi, B. Mennucci, R. Cammi, *Chem. Rev.* 105 (2005) 2999–3093.
- [27] J. He, P.L. Polavarapu, *Spectrochim. Acta Part A* 61 (2005) 1327–1334.
- [28] B. Boeckx, R. Ramaekers, G. Maes, *J. Mol. Spectrosc.* 261 (2010) 73–81.
- [29] N. Borho, M.A. Suhm, K. Le Barbu-Debusch, A. Zehnacker, *Phys. Chem. Chem. Phys.* 8 (2006) 4449–4460.
- [30] N. Borho, Y. Xu, *Phys. Chem. Chem. Phys.* 9 (2007) 1324–1328; P. Ottaviani, B. Velino, W. Caminati, *Chem. Phys. Lett.* 428 (2006) 236–240.
- [31] See for example D.J. Miller, J.M. Lisy, *J. Am. Chem. Soc.* 130 (2008) 15393–15404.
- [32] Z. Dezhahang, C. Merten, M.R. Poopari, Y. Xu, *Dalton Trans.* 41 (2012) 10817–10824.
- [33] M.A. Muñoz, O. Muñoz, P. Joseph-Nathan, *Chirality* 22 (2010) 234–241.
- [34] G. Yang, Y. Xu, *J. Chem. Phys.* 130 (2009). 164506/1–9; Y. Liu, G. Yang, M. Losada, Y. Xu, *J. Chem. Phys.* 132 (2010). 234513/1–11.

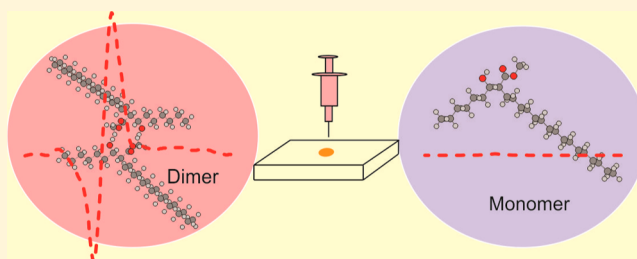
# Absolute Configuration and Conformation of Two Fráter–Seebach Alkylation Reaction Products by Film VCD and ECD Spectroscopic Analyses

Mohammad Reza Poopari, Zahra Dezhahang, Ke Shen, Lei Wang, Todd L. Lowary, and Yunjie Xu\*

Department of Chemistry, University of Alberta, 11227 Saskatchewan Drive, Edmonton, Alberta T6G 2G2, Canada

**S** Supporting Information

**ABSTRACT:** Two chiroptical spectroscopic techniques, namely, electronic and vibrational circular dichroism (ECD and VCD), as well as NMR spectroscopy have been utilized to determine the absolute configurations and geometries of two Fráter–Seebach alkylation reaction products with long hydrocarbon chains. The experimental studies have been complemented with density functional theory calculations. Strong characteristic bisignate VCD signatures in the carbonyl stretching region have been observed for both compounds in film state. Truncated models, i.e., without the long CH<sub>2</sub> chains, have been utilized to examine different hydrogen-bonding topologies between two monomeric moieties and to simulate the corresponding IR and VCD spectra of the dimers. In addition, the exciton coupling model has also been applied to the —C=O groups of the two monomeric moieties, which can be coupled through intermolecular hydrogen-bonding. On the basis of these simplified approaches, the absolute configurations of the compounds have been unambiguously assigned using VCD and ECD spectroscopy. Spectral simulations in the IR and UV–vis regions have also been carried out with the full dimers to validate the fitness of the truncated model. The study shows that the combination of the film VCD and ECD techniques is a relatively straightforward method to determine the absolute configurations of such synthetic compounds.



## INTRODUCTION

The Fráter–Seebach alkylation<sup>1,2</sup> reaction is an efficient means for the diastereoselective introduction of  $\alpha$ -substituents to chiral  $\beta$ -hydroxy esters using superbases such as lithium diisopropylamide (LDA) or lithium bis(trimethylsilyl)amide (LHMDS). In such reactions, both hydrocarbon groups, which are connected to the two stereogenic carbon centers of the  $\beta$ -hydroxy ester product (Figure 1), can be engineered as

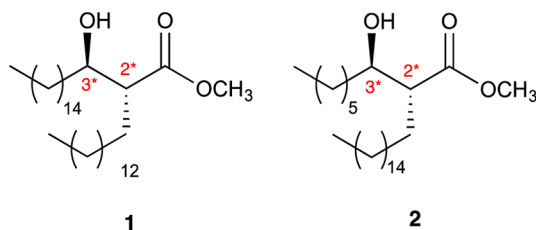


**Figure 1.** Chemical structure of 1 and 2. The stereogenic centers are indicated with \*.

needed.<sup>3</sup> In the current study, two chiral  $\beta$ -hydroxy esters with different lengths of  $\alpha$ -hydrocarbon chain substituents (1 and 2, Figure 1) have been synthesized by using the Fráter–Seebach alkylation reaction. Each product contains two stereogenic carbon centers where one is connected to an —OH group and the other one to an ester (—CO<sub>2</sub>Me) group. In addition, a long

hydrocarbon chain is attached to each stereogenic carbon center. The synthesis of 1 was reported before,<sup>4,5</sup> whereas that of 2 is reported here for the first time.

These compounds are synthetic analogs of mycolic acids, lipids that are found in the cell wall of a number of actinomycete bacteria.<sup>6</sup> In particular, they are important constituents of cell wall arabinogalactan in the human pathogens *Mycobacterium tuberculosis* and *Mycobacterium leprae*, the causative agents of tuberculosis and leprosy, respectively.<sup>7</sup> The two compounds have been synthesized for use in the preparation of a library of glycolipids that will be used to probe the host immune response that occurs upon infection by mycobacteria.

One of the most important properties for further biological and other applications is the absolute configuration of the products. The three-dimensional spatial arrangement of a chiral molecular system can be determined by using different spectroscopic tools such as NMR spectroscopy, X-ray crystallography, electronic circular dichroism (ECD) spectroscopy, and vibrational CD (VCD) spectroscopy. Each method has its own pros and cons and also level of confidence in the absolute configuration assignment. While X-ray crystallography has been used extensively for this purpose, it is often tedious if not impossible to obtain the necessary single crystals for many

**Received:** October 24, 2014

**Published:** December 1, 2014

synthetic products. VCD spectroscopy has been utilized successfully in recent years to determine absolute configurations and characterize chiroptical properties of synthetic compounds<sup>8</sup> and natural products.<sup>9</sup> In this study, we have applied both VCD and ECD spectroscopies, complemented with density functional theory (DFT) calculations, to determine the absolute configuration (AC) of these products and to characterize the associated hydrogen (H)-bonding interactions under film conditions. We have further discussed the benefits of using two complementary chiroptical spectroscopic tools to enhance the level of confidence in the AC assignments.<sup>10</sup> For comparison, the absolute configuration of the stereogenic carbinol carbon, i.e., 3\* in Figure 1, has also been established by using an approach similar to the Mosher ester method<sup>11</sup> and complemented with the DFT calculations of NMR chemical shifts.

The VCD and ECD measurements have been carried out by using a cast film in the current study. There are a number of advantages associated with the cast film technique. One is that the resulting spectra have no contribution from the solvent molecules and no interference from the solvent molecules through H-bonding interactions or other intermolecular interactions. The latter greatly simplifies the necessary theoretical modeling for spectral interpretation. The other point is that the film measurements generally require less amount of sample compared to the solution measurements.<sup>12</sup> For example, Polavarapu and co-workers found that for *L*-phenylalanine and *L*-tryptophan, which have low solubility in water, the cast film technique is the method of choice.<sup>13</sup> Not only strong water interference could be eliminated to uncover amide I bands,<sup>14</sup> but also the signal-to-noise ratio of film-VCD spectra was enhanced noticeably compared to that obtained in solution.<sup>15</sup> More recently, the reversal of helical chirality of fibrils in dried film under different pH conditions was studied by Nafie and co-workers using VCD spectroscopy.<sup>16</sup> One known drawback of the cast film VCD technique is the possible formation of microcrystalline assemblies during film preparation, thus preventing artifact-free VCD spectra to be obtained. This, however, depends on specific solute and solvent properties and can be avoided by choosing an appropriate solvent or using the matrix-assisted film-VCD technique reported previously.<sup>17</sup> Experimental aspects of solid state VCD measurements were reviewed by Abbate and co-workers.<sup>18</sup> Furthermore, procedures for verifying if the system is free of such artifacts and for correcting such artifacts were reported before<sup>19</sup> and have utilized in the current study.

## RESULTS AND DISCUSSION

**1. Experimental IR and VCD Spectra in Film and in Solution.** Figure 2 shows the experimental IR spectra of **1** in film and in CDCl<sub>3</sub> solvent. Clearly, the main IR features are similar in film and in solution, except the noticeable baseline elevation and band overlapping in the region below 1450 cm<sup>-1</sup> in the solution measurement due to solvent interference. The film IR spectrum also shows two closely spaced bands at ~1720 cm<sup>-1</sup> separated by ~12 cm<sup>-1</sup>, while the corresponding feature in solution shows only one broad band at roughly the same position. The raw solution IR spectrum and the corresponding solvent IR spectrum are provided in Figure S1, Supporting Information. The corresponding VCD spectrum in solution, on the other hand, shows a poor signal-to-noise ratio, possibly a result of intermolecular interactions with CDCl<sub>3</sub>.<sup>20</sup> Because of the limited amount of the synthetic sample, no further testing

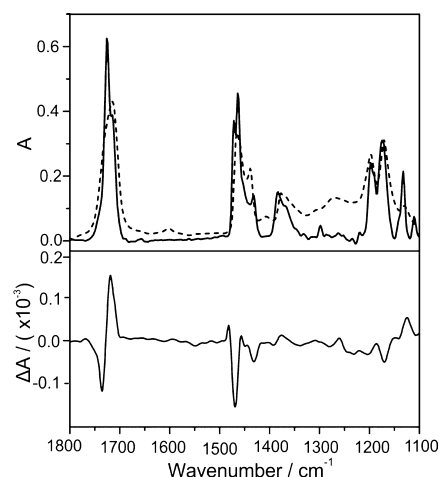


**Figure 2.** Experimental IR spectra of **1** in film (solid) and in CDCl<sub>3</sub> solution (dashed). The corresponding experimental VCD spectrum in film is shown at the bottom.

with other solvents was carried out. Rather, we focus on the experimental data obtained with the film method.

The observation of the two closely spaced IR bands in the C=O stretching region in film may indicate the formation of a dimer. This is because the monomer of **1** features essentially only one type of intramolecular H-bond with the hydroxyl H atom pointing to the carbonyl O atom (Section 3). Furthermore, differences in the orientation of the hydrocarbon chains typically result in much smaller separation in the carbonyl region than that observed (Section 3). The clear evidence for the formation of a dimer comes from the greatly enhanced +/− bisignated VCD couplet in the same region, going from low to high wavenumber. Such noticeably enhanced VCD signatures are common for two strongly coupled C=O oscillators.<sup>21–23</sup> On the other hand, one would generally expect low VCD intensity in the carbonyl stretching region if the two oscillators are not coupled, for example, from conformers due to different hydrocarbon chain orientations (see Section 3).

**2. NMR Spectroscopic and DFT Determination of Chirality at the Carbinol C Atom.** There are two stereogenic centers in these two products: one is at the carbinol C atom whose chirality was set by an enantioselective reduction of a ketone using a chiral catalyst and the other during the alkylation reaction (see Experimental Section). In this section, we utilized an approach analogous to the Mosher ester analysis<sup>11</sup> for the determination of the absolute configuration of the stereogenic carbinol carbon atom. Since  $\alpha$ -methoxy- $\alpha$ -trifluoromethylphenylacetic acid (MTPA-OH), also known as Mosher's acid, is rather expensive, we chose a cheaper chiral acid, i.e., (*S*)-(+)-*O*-acetylmandelic acid, as our NMR shift agent. Briefly, **3**, the product of the above enantioselective reduction of a ketone and a precursor for **1**, was reacted with (*S*)-(+)-*O*-acetylmandelic acid, as shown in Scheme 1. Since **3** was produced with 93% ee, we expected to obtain two diastereomeric esters with (2*R*,5*S*) and (2*S*,5*S*) absolute configurations. The resulting ester <sup>1</sup>H NMR spectroscopic experiments show two well resolved peaks at 3.64 and 3.37 ppm with the latter having much less intensity, arising from the methyl group of the methyl ester. Generally speaking, because of the different orientation of the phenyl group in these two diastereomeric esters shown in Figure 3, one may speculate that

**Scheme 1. Production of a Mosher Ester Analogue for the NMR Spectroscopic Determination of the Absolute Configuration at the Carbinol C of 3**

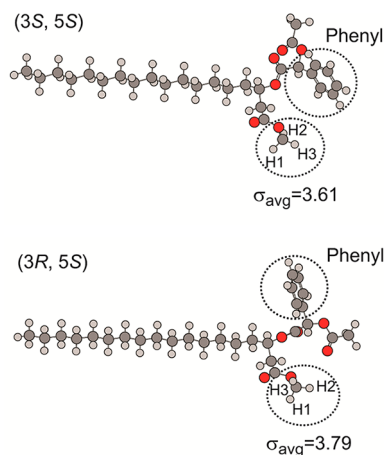
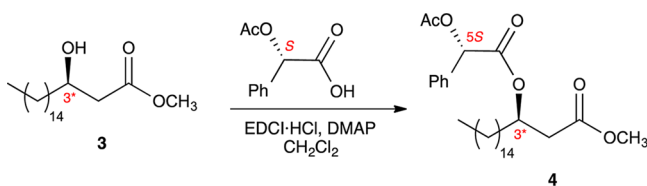


**Figure 3.** Optimized geometries of the two diastereomeric esters (3*S*,5*S*) and (3*R*,5*S*) and the corresponding NMR shifts of the methyl protons predicted at the 6-311++G(d,p)//6-31+G(d) level. The first and second chiral labels refer to the chirality of the carbinol carbon and the acid used, respectively. Note that in (3*S*,5*S*), the methyl protons are better shielded by the aromatic group than in (3*R*,5*S*), as highlighted with dotted lines.

the methyl protons in the (2*S*,5*S*) ester are more shielded and therefore move upfield in its NMR spectrum. To validate this assumption, the corresponding DFT calculations at the 6-311++G(d,p)//6-31+G(d) was carried out. The ( $\delta_{RS} - \delta_{SS}$ ) NMR shift value was predicted to be +0.18 ppm, in good agreement with the experimental +0.27 nm. In calculating these NMR shifts, we have adopted the linear scaling model reported by Rablen et al.<sup>24</sup> From this combined experimental and theoretical approach, we deduced that the chirality at the carbinol C of the 1 and 2 is *R* for the major product.

**3. Absolute Configuration of 1 and 2 from Chiroptical Spectroscopy with Simplified Models. Truncated Models.**

For both 1 and 2, the –OH and –CO<sub>2</sub>Me groups can in principle adopt two H-bonding topologies, i.e., –OH⋯O=C or –OH⋯OMe intramolecular H-bonds. It is well documented that the –OH⋯O=C H-bonding topology is strongly preferred.<sup>25,26</sup> The more subtle conformations related to the long hydrocarbon chains will be addressed in Section 4.

In order to determine the absolute configurations of the 1 and 2 from chiroptical measurements in film, we need to consider the H-bonded dimers alluded to in Section 1. First, the experimental IR and VCD spectra of both 1 and 2 with different alkyl chains show somewhat similar features in the fingerprint region (vide infra). Second, the most prominent VCD features observed are in the carbonyl stretching region, whereas the vibrational modes of the alkyl chains in the fingerprint region are generally below 1500 cm<sup>-1</sup>. We therefore decided to first utilize the truncated models where the long alkyl chains are replaced with the methyl groups to reduce computational cost. Such simplified approach was reported before for complex systems with a long hydrocarbon chain or formed H-bonded dimers.<sup>27</sup>

Two intermolecular H-bonding models are proposed in Figure 4. In Model\_I, the two O=C groups act as the proton acceptors and the –OH groups as the H-donors. In Model\_II,

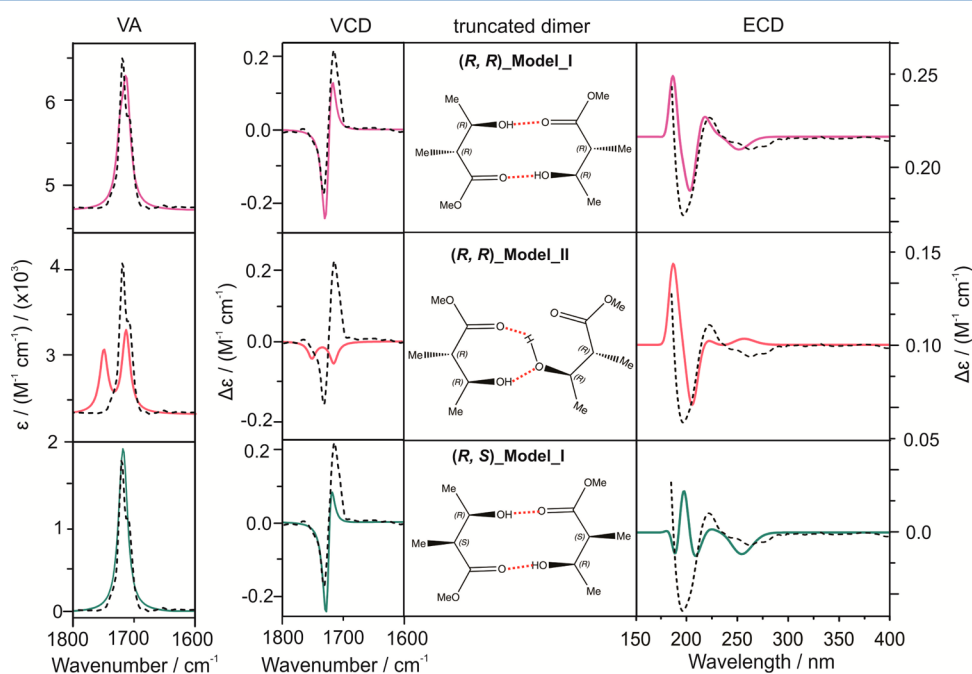


**Figure 4.** Calculated VA and VCD spectra (left) in the carbonyl stretching region and ECD spectra (right) of the truncated dimers. The truncated models used are provided in the middle. For clarity, only experimental VA and VCD data (dotted line) of 1 and ECD data of 2 are shown for comparison. The vertical units are those of the calculated ones.

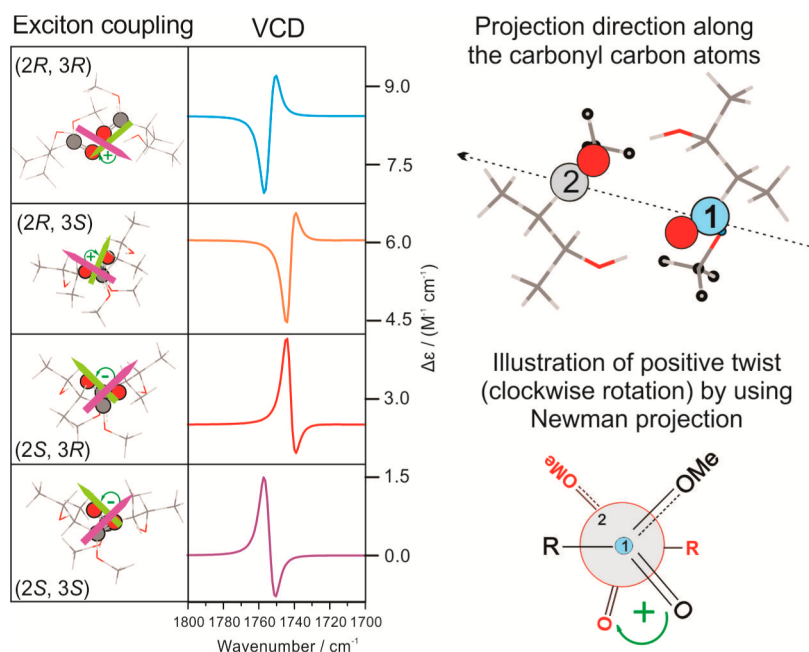


**Figure 5.** Illustration of the exciton coupling phenomenon of the two chromophoric carbonyl moieties in Model\_I.

one hydroxyl group is inserted into the existing intramolecular H-bond of the other molecule and acts both as the H-donor and acceptor. The simulated IR and VCD spectra of Model\_I and II of the truncated (2*R*,3*R*) and (2*S*,3*R*) products in the 1800 to 1700  $\text{cm}^{-1}$  region. The corresponding results of (2*S*,3*S*) and (2*R*,3*S*) are not shown since (2*S*,3*S*) and (2*R*,3*S*) give the same IR and the mirror-imaged VCD spectra as (2*R*,3*R*) and (2*S*,3*R*), respectively. In Model\_I where the two  $\text{—C=O}$  groups are involved in the intermolecular H-bonded ring, the calculated VCD features exhibit greatly enhanced intensity with the  $+/-$  bisignate couplet from low to high wavenumber for both (*R,R*) and (*R,S*) isomers. For Model\_II, since one  $\text{—C=O}$  group is not involved in the intermolecular H-bonding interaction, its IR band appears blue-shifted relative to the one which is involved in the intermolecular H-bond. The said IR band is also blue-shifted with respect to the IR bands of the two  $\text{—C=O}$  groups in Model\_I, which are both involved in the H-bonds. Furthermore, in Model\_II, the two  $\text{—C=O}$  groups are not coupled oscillators. Their motions clearly appear to be independent of each other in GaussView.<sup>28</sup> As a result, the VCD features in this region change from the intense  $+/-$  bisignate pattern in Model\_I to two weak negative bands, which are well separated in wavenumber in Model\_II.

It is interesting to note that both the (2*R*,3*R*) and (2*S*,3*R*) isomers in Model\_I generate similar VCD features in the carbonyl stretching region. This is somewhat unexpected since the carbinol C is further away from the  $\text{—C=O}$  group than the second chiral C atom which is directly connected to the  $\text{—CO}_2\text{Me}$  group. One may intuitively expect that the chirality of C connected to the ester group would have a greater influence on the VCD features at the carbonyl stretching region than the carbinol chirality. In this case, such a “common-sense” prediction has not worked. A closer examination of the related diastereomeric structures reveal that the carbonyl groups in the (2*S*,3*R*) isomer need to twist differently compared to those in the (2*R*,3*R*) isomer in order to form the intermolecular H-bonds. Indeed, researchers in the chiroptical field have become increasingly aware of the effects of conformational or structural

twists on chiroptical spectral features, in addition to the permanent chirality of the system.<sup>29,30</sup> In this particular case one can picture a structural arrangement that generates a positive twist for the two coupled  $\text{—C=O}$  groups using the exciton coupling model discussed below. Clearly, Model\_I with the (2*R*,3*R*) and (2*S*,3*R*) isomers are both consistent with the experimental VCD data, while the carbonyl VCD features of Model\_II deviate noticeably from the experiment. Therefore, the VCD study indicates that chirality at the carbinol C atom is *R*, consistent with the NMR spectroscopic result. However, one cannot tell if the compound is of (2*R*,3*R*) or (2*S*,3*R*) with only the experimental carbonyl VCD features.

To complement the VCD study, we have also carried out ECD spectral simulations of the two aforementioned models and the related diastereomers. The resulting calculated ECD spectra are also summarized in Figure 4. Experimentally, ECD spectra of both 1 and 2 consist of a broad and shallow negative, a positive, and a strong negative band, going from long to short wavelengths. For simplicity, only the ECD spectrum of 2 is shown in Figure 4, while that of 1 is provided in the next section. As one can see, the experimental ECD data are again well-captured by Model\_I with the (2*R*,3*R*) isomer. Furthermore, the simulated ECD features of Model\_I with the (2*S*,3*R*) isomer are considerably different than those of the (2*R*,3*R*) isomer. Therefore, ECD spectral features also allow one to identify the chirality at both stereogenic carbons. The combined ECD and VCD approach is desirable. The VCD features provide a clear indication of the formation of the H-bonded dimer and the preferred H-bonding model utilized, thus greatly reducing the amount of structural search needed, while the ECD features provide a clear discrimination among the diastereomers proposed. Therefore, the combined ECD and VCD spectroscopic approach enables one to determine the chirality of the stereogenic centers of these two synthetic compounds independently of the NMR spectroscopic data.

**Exciton Coupling Model.** The exciton coupling model has been used broadly and successfully to interpret ECD spectral features since its development by Harada and Nakanishi.<sup>31</sup> One

attractive feature is that it is easy to use, with little computational demand. More recently, Monde et al. explored the application of this method for interpreting VCD spectral features.<sup>32</sup> The  $\text{—C=O}$  stretching modes are well-suited for the VCD exciton coupling approach because they are well-localized and often well separated from other modes, and their related electric transition moments are essentially parallel to the  $\text{C=O}$  bond. We have therefore tested the validity of such a simple and useful approach on these two synthetic compounds here.

Both **1** and **2** show a bisignate VCD signal at  $\sim 1720\text{ cm}^{-1}$ . Such spectral features imply the presence of two electric transition moments, which can interact through space, thus causing the split-type bisignate VCD signals. The absorbing chromophores can either be identical or not. More importantly, they do not necessarily need to exist in the same molecule to start with. Rather, in the current case, dimerization through intermolecular H-bonding interaction is enough to bring the two chromophores close enough to couple and to cause the bisignate VCD signatures.<sup>33</sup> If the two chromophoric sites are oriented in a positive twist with respect to each other, i.e., clockwise rotation, looking down from the closest electric transition moment to the one further away, it produces  $+/-$  couplet signals from low to high wavenumber (see Figure 5). The opposite coupling features are generated if the two transition moments are in a negative twist arrangement, i.e., counterclockwise rotation. As can be seen in Figure 5, the two  $\text{—C=O}$  bonds are in a positive twist in Model\_I with the (2*R*,3*R*) monomers and therefore capture the experimental signatures correctly, while the two are in a negative twist with the (2*S*,3*S*) monomers. Furthermore, the dimer with the (2*S*,3*R*) monomers also provides a positive twist, consistent with the truncated models discussed before.

While the exciton VCD method works well for the two  $\text{—C=O}$  bonds in Model\_I where both are involved in the same intermolecular H-bonded ring, its application to the two  $\text{—C=O}$  bonds in Model\_II is less obvious. Although geometrically these two  $\text{—C=O}$  chromophores are in a negative twist in Model\_II with the (*R,R*) isomer (see Figure S2, Supporting Information), the corresponding VCD signatures in the  $\text{—C=O}$  stretching region emerge as two weak negative bands rather than an intense bisignate couplet. It appears that these two chromospheres do not have any strong coupling with each other. This was already alluded to in the discussion of the truncated Model\_II (Figure 5). In Model\_II, the stretching motions of the two  $\text{—C=O}$  groups show essentially no synchronization at all, i.e., no symmetric and antisymmetric characters. Rather, they are independent of each other and therefore exciton coupling does not apply here.

**4. Spectral Simulations with Full 1 and 2 Monomers and Dimers.** The simplified models such as the truncated model and exciton coupling method work well to provide the absolute configuration assignments from the experimental spectra. However, we thought it important to extend the calculations to include full geometries of both monomers and dimers of **1** and **2** to test the validity of the truncated model and to examine what additional information can be extracted from the experimental data. For the monomer of **1**, our preliminary molecular mechanics simulation shows a large number of conformers with bends at different positions of the long hydrocarbon chains. The most stable conformers sampled are provided in Figure S3, Supporting Information, together with their corresponding IR and VCD spectra. There is only

one dominant conformer that has the  $\text{—OH}\cdots\text{O(=C)}$  H-bond and all  $\text{CH}_2$  groups in the *trans* arrangement, i.e., both alkyl groups extended. The latter finding is consistent with previous experimental and theoretical studies, which showed that the all *trans* conformation is by far the dominant one for the shorter chains such as those considered here.<sup>34</sup>

For the full dimer geometry, we utilized the dominant all *trans* monomeric conformer and the intermolecular H-bonding topology of Model\_I. Dimers containing bended hydrocarbon chains are much less stable than that with all *trans* hydrocarbon chains. So are those with Model\_II binding topology. Therefore, these much less stable conformers are not considered further here. The dominant monomeric and dimeric geometries are summarized in Figure 6 for both **1** and **2**. We

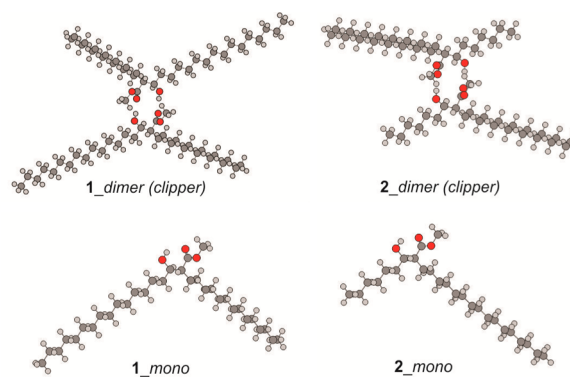
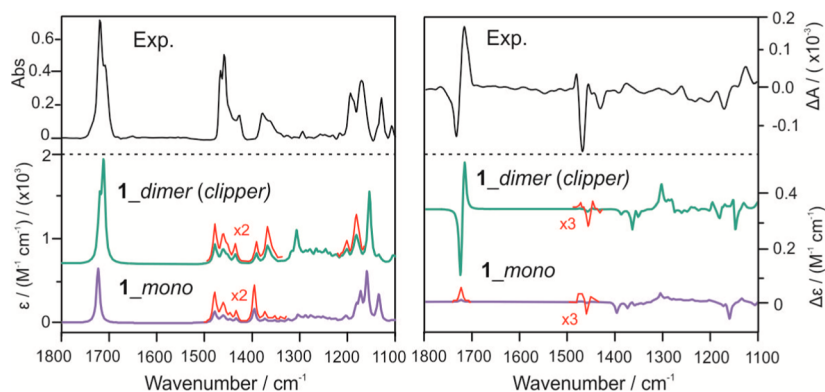


Figure 6. Dominant monomeric and dimeric structures of **1** and **2**.

have also tested the inclusion of dispersion correction in our calculation. This resulted in a geometry in which the hydrocarbon chains are bunched together rather than extended (see Figure S4, Supporting Information). This is likely due to an overcorrection of the dispersion interaction.<sup>35</sup> The resulting IR and VCD spectra of the dimer of **1** (*bunched*) are compared with the corresponding experimental data in Figure S5, Supporting Information. The agreement achieved with the dispersion correction is somewhat worse compared to the standard DFT calculation, and we therefore left out the dispersion correction in the remainder of the paper.

Figure 7 shows the comparison of the experimental and theoretical VA and VCD spectra of the monomer and dimer of **1**. As can be seen, the simulated IR spectrum of the **1\_dimer (clipper)** captures essentially all the important IR bands observed in this region, although the relative intensities of some IR bands are not reproduced precisely. For example, the triplet IR bands observed in the  $1500\text{—}1400\text{ cm}^{-1}$  region were observed with higher relative intensity than predicted. The agreement between the simulated IR spectrum of the **1** monomer and the experimental data is considerably worse. For the corresponding VCD spectra, the prominent  $+/-$  couplet from low to high wavenumber observed in the carbonyl stretching region is well reproduced by the dimer, but not at all by the monomer. This is consistent with the truncated model and exciton coupling model presented above. The  $+/-/+$  triplet features observed experimentally in the  $1500\text{—}1400\text{ cm}^{-1}$  region are also reproduced theoretically, although the predicted intensity is lower than the experimental one, as in the case of the corresponding IR bands. Making detailed assignments in the low wavenumber region is challenging because the vibrational modes associated with the hydrocarbon chains





**Figure 7.** Comparison of the experimental IR (left) and VCD (right) spectra with the corresponding simulated spectra of the dominant monomer and dimer of **1** at the B3LYP/cc-pVTZ level of theory.

such as scissoring, wagging, twisting motions of  $\text{CH}_2$  groups, bending motions of  $-\text{CH}_3$  groups (both terminal methyl of the hydrocarbon chains and the  $-\text{CO}_2\text{Me}$  groups), and bending modes of  $-\text{C}_\alpha\text{H}$  and  $-\text{OH}$  groups overlap severely. Overall, **1\_dimer (clipper)** provides satisfactory agreement with the experiment, while its monomer does not.

For the sake of completeness, simulations of the UV–vis and ECD spectra of both monomer and dimer of **1** were carried out. Figure 8 shows the comparison of the experimental and

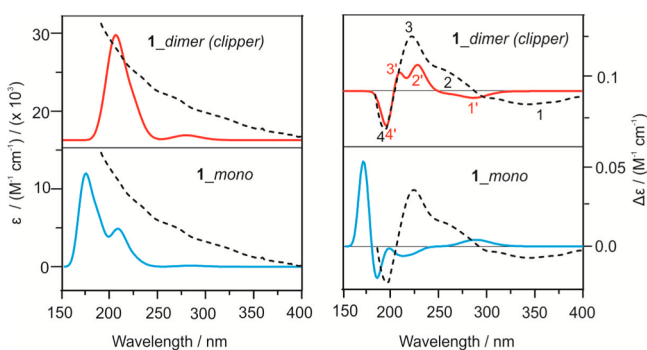


**Figure 8.** Experimental (dotted-line) UV–vis (left) and ECD (right) spectra are compared with the corresponding simulated (color solid-line) spectra of the dominant monomer and dimer of **1** at the B3LYP/6-31G(d,p) level of theory. The vertical units used are for the calculated ones. The experimental and the corresponding calculated ECD features of the dimer are marked with Arabic numbers 1–4 and 1'–4', respectively.

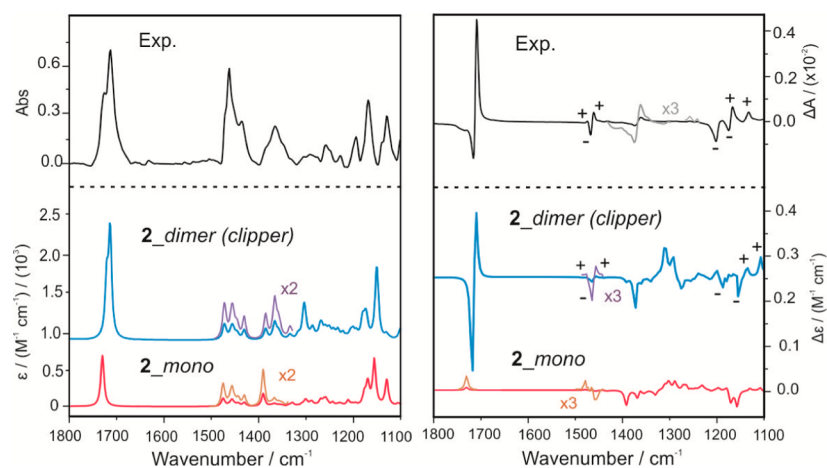
theoretical ECD spectra of the monomer and dimer of **1**, as well as the corresponding UV–vis spectra. In the calculated spectra, the monomer exhibits two bands centered at  $\sim 170$  and  $205$  nm, while the dimer shows an intense broad UV–vis peak at  $\sim 210$  nm and a low-intensity one at  $\sim 275$  nm, which are bathochromic shifted from those of the monomer due to intermolecular H-bonding interactions. The experimental UV–vis spectrum consists of a very broad band. As a result, one cannot differentiate between the monomer or dimer preference using the UV–vis spectrum. The experimental ECD spectrum consists of several Cotton bands with the  $-/+ / + / -$  trend from long to short wavelengths. These unique spectral features are well reproduced by the simulated ECD spectrum of the dimer. To guide the eye, the experimental bands are labeled with numbers 1 to 4, while the corresponding calculated bands are

labeled with 1' to 4'. It is also clear that the monomer does not reproduce the experimental ECD data.

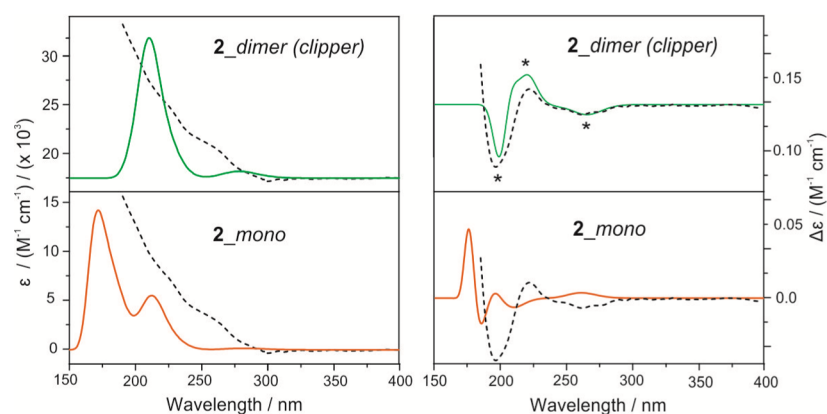
The same calculation procedure has also been repeated for the monomer and dimer of **2**. Figure 9 shows the comparison of the experimental and theoretical VA and VCD spectra of **2**. The positions of almost all the observed IR bands are well reproduced by the simulated IR spectrum of the dimer of **2**, including the two closely spaced bands in the carbonyl stretching region. The intensity of some IR bands are not as well captured as their positions. For example, the triplet at the  $1500\text{--}1400$   $\text{cm}^{-1}$  region was predicted to be less intense than observed, similar to the case of **1**. As can be seen from Figure 9, the corresponding observed VCD spectral features can be satisfactorily assigned based on the predicted VCD spectrum of the dimer of **2**. Not only the intense bisignate carbonyl VCD stretching bands due to the dimer are correctly captured, but also most of the VCD features in the lower wavenumber region. For example, the  $+ / - / +$  VCD features mentioned above are well reproduced by using the dimer but not by the monomer of **2**. Also, the  $+ / + / - / -$  features from low to high  $\text{cm}^{-1}$  in the  $1125\text{--}1100$   $\text{cm}^{-1}$  region are consistent with the dimeric structure of **2**.

Figure 10 compares the experimental UV–vis and ECD spectra with the corresponding simulated spectra of the monomer and dimer of **2**. As one can see, the simulated UV–vis and ECD spectra of the **2** dimeric *clipper* structure agree well with the corresponding experimental ones. For example, the  $- / + / -$  ECD features from long to short wavelength are well reproduced by the calculation. Overall, the dimeric *clipper* structure fulfills the experimental observation, allowing one to assign confidently the absolute configuration and dimeric *clipper* structure to the sample. The better agreement for **2** compared to **1** may perhaps be due to the fact that **2** contains one noticeably shorter hydrocarbon chain and thus less severe overlaps in the low wavenumber region.

Finally, we compared the simulated spectra using the full dimer geometries for these two compounds with the truncated Model\_I. The experimental UV–vis spectra observed for both **1** and **2** are very broad, with no noticeable difference. The main experimental ECD features observed are also quite similar for both compounds, although the two positive ECD bands are better resolved for **1** than **2**. The simulated UV–vis and ECD spectra also appear similar for the **1\_dimer (clipper)** versus the **2\_dimer (clipper)**. Furthermore, it is satisfying to note that the ECD simulations also capture the subtle differences in the



**Figure 9.** Comparison of the experimental IR (top) and VCD (bottom) spectra with the corresponding simulated spectra of the dominant monomer and dimer of **2** at the B3LYP/cc-pVTZ level of theory.



**Figure 10.** Experimental (dotted-line) and theoretical (colored solid-line) UV (left) and ECD (right) spectral comparison of the monomer and dimer structures of **2** at the B3LYP/6-31G(d,p) level of theory.

experimental ECD features of the **1** and **2** samples due to the length of the hydrocarbon side chains, although the length generally does not affect the electronic transitions and the corresponding ECD features significantly. This is essentially the reason for the success of the simplified truncated model. Since the IR and VCD spectra have a much narrower bandwidth and contain some vibrational modes directly related to the hydrocarbon chains in the fingerprint region, we compared the simulated IR and VCD spectra of **1\_dimer (clipper)** and **2\_dimer (clipper)** with those of the truncated Model\_I in Figure S6, Supporting Information. In this fingerprint region, the IR spectra of all three systems look very much the same, while there are some obvious differences for the corresponding VCD spectra in the region below  $1500\text{ cm}^{-1}$ . In particular, Model\_I exhibits much different VCD features in the region below  $1400\text{ cm}^{-1}$  from those of **1\_dimer (clipper)** and **2\_dimer (clipper)**. This potentially means that some details about the hydrocarbon chains may be extracted from the VCD features in this region. Unfortunately, because of the severe overlapping of the bands in this region, it is currently very challenging to capture the VCD features *exactly* right in order to extract detailed structural information related to the hydrocarbon chains.

## CONCLUSIONS

We have applied ECD and VCD spectroscopy, together with DFT calculations, to determine the absolute configurations and geometries of two Fráter–Seebach alkylation reaction products with long hydrocarbon chains to be (*2R,3R*) with extended all *trans* hydrocarbon chains. The strongly enhanced carbonyl stretching VCD features indicate that the compounds in the film state exist predominantly as H-bonded dimers. Two simplified models, i.e., the truncated model and the exciton coupling model, have also been utilized and tested against the calculations performed for the full dimers. It appears that these simplified models are sufficient to allow extraction of chirality information on the systems and to identify the main H-bonding interaction. We have also carried out an NMR spectroscopic study, complemented with DFT calculations, to determine the chirality of the carbinol carbon. Consistent results have been obtained with NMR spectroscopy and chiroptical spectroscopy. Overall, the study shows that the combination of the film VCD and ECD techniques is a relatively straightforward method to determine the absolute configurations of such synthetic compounds in film.

## EXPERIMENTAL SECTION

**IR and VCD Measurements.** Compounds **1** and **2** were dissolved either in chloroform or acetone and a few drops of the resulting solution were placed on an  $\text{CaF}_2$  window and let to dry at room

temperature. IR and VCD spectra were recorded using a Fourier transform IR spectrometer equipped with a VCD module. The concentration and film thickness were optimized so that the absorption coefficients of the IR bands of interest are in the range of 0.2–0.9. The spectral ranges of 1800–1100  $\text{cm}^{-1}$  were selected for the purpose of this paper. All IR and VCD spectra were obtained with a resolution of 4  $\text{cm}^{-1}$  and with a total measurement time of 3 h (3  $\times$  1 h). The final reported VCD spectra were baseline corrected using the background spectra subtraction. A sample holder which can be rotated freely from 0° to 360° was constructed. The cast film  $\text{CaF}_2$  window was mounted on the rotatable holder. The VCD spectra were found to be essentially the same with angles at 0°, 45° and 90°, confirming that the samples have no noticeable anisotropy.

**UV–Vis and ECD Measurements.** The UV–vis spectra of the samples in film were collected using a Spectrophotometer. The thickness of the cast film was optimized to have the UV–vis absorbance in the range of 0.2–0.9. Thereafter, the ECD spectra were collected using a circular dichroism spectrometer. The final ECD spectra were background-corrected.

**Theoretical Modeling.** The Gaussian 09<sup>36</sup> suite of programs has been used for all geometry optimization and harmonic vibrational frequencies calculations, as well as the IR and VCD intensities predictions. DFT<sup>37</sup> calculations were performed with the Becke, three-parameter, Lee–Yang–Parr (B3LYP)<sup>38</sup> hybrid functional and the augmented correlation-consistent triple- $\zeta$  basis sets, i.e., cc-pVTZ,<sup>39</sup> for final conformational calculations and spectral simulations. A factor of 0.98 was used for the frequency scaling. A Lorentzian line shape with a half-width at half-height (HWHH) of 4  $\text{cm}^{-1}$  was used for the simulations of IR and VCD spectra.

UV–vis and ECD spectral simulations were carried out using the time dependent-DFT (TD-DFT) approach and the 6-31G(d,p) basis set. The basis set employed offers a good compromise between accuracy and computational expense. We have added an extra polarization p-function to the double- $\zeta$  6-31G(d) basis set which is considered to be the minimal basis set recommended for optical spectral simulations.<sup>40</sup> UV–vis and ECD calculations for **1** were also done with 6-31+G(d) for comparison (see Figure S7, Supporting Information). The UV–vis spectra have been simulated with the first 100 electronic excited states. A Gaussian line shape with a half-width at half-height (HWHH) of 0.33 eV was used for the simulations of UV–vis and ECD spectra.

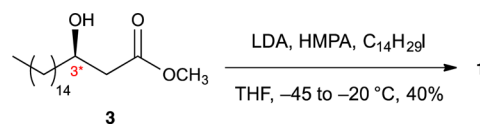
For the initial conformational search of **1** and **2**, we have employed the Spartan program.<sup>41</sup> About 1000 conformers were predicted by using either the universal force field (UFF) molecular mechanics (MM) or semiempirical AM1 method<sup>42</sup> and the “conformer distribution” option implemented in the Spartan program. About 100 most stable conformers were kept for further analyses and similar conformers were identified with the MM and AM1 methods. Four conformers were deemed relevant at room temperature with their relative energy within  $\sim 20$  kJ/mol. These most stable conformers were reoptimized with the DFT approach described above and only one dominant structure was identified. See the Results and Discussion section for more information.

**Synthesis. General Methods.** All reagents were purchased from commercial sources and were used without further purification unless noted. All reactions were carried out under a positive pressure of argon or nitrogen at room temperature unless specified and were monitored by TLC on silica gel 60-F<sub>254</sub> (0.25 mm). Visualization of the reaction components was achieved using UV fluorescence (254 nm) and/or by charring with acidified anisaldehyde solution in ethanol. Organic solvents were evaporated under reduced pressure and the products were purified by column chromatography on silica gel (230–400 mesh). Optical rotations were measured in a microcell (10 cm, 1 mL) at ambient temperature and are in units of degree·mL/(g·dm). <sup>1</sup>H NMR spectra were recorded at 500 MHz and chemical shifts are referenced to residual  $\text{CHCl}_3$  (7.26 ppm,  $\text{CDCl}_3$ ). <sup>13</sup>C NMR spectra were recorded at 125 MHz and chemical shifts are referenced to  $\text{CDCl}_3$  (77.0 ppm). Reported splitting patterns are abbreviated as s = singlet, d = doublet, t = triplet, m = multiplet, br = broad, app =

apparent. ESI-TOF/MS spectra were recorded on samples suspended in THF or  $\text{CH}_3\text{OH}$  and added NaCl.

**(2*R*,3*R*)-Methyl-3-hydroxy-2-tetradecyloctadecanoate (1).**<sup>4</sup> A solution of lithium diisopropylamine (8 mL) prepared from *n*-BuLi (2.5 M hexane solution, 2.64 mL, 6.6 mmol) and diisopropylamine (0.93 mL, 6.6 mmol) was cooled to  $-78$  °C, and the  $\beta$ -hydroxy ester **3**<sup>4</sup> (0.691 g, 2.2 mmol) was added as a solution in THF (2 mL). After 1 h at  $-45$  °C, 1-iodododecane (1.43 g, 4.4 mmol) and HMPA (0.76 mL, 4.4 mmol) were added via a syringe. The mixture was stirred at  $-45$  °C for 3 h then warmed slowly to  $-20$  °C overnight. The mixture was treated with saturated  $\text{NH}_4\text{Cl}$  and extracted with ether. The ether layer was washed with brine, dried over  $\text{MgSO}_4$  and concentrated. The crude product was purified by column chromatography (hexane–EtOAc, 10:1) to give **1** (0.44 g, 40%) as a white solid (Scheme 2):  $R_f$  =

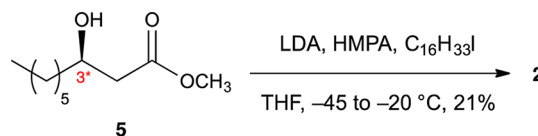
### Scheme 2. Synthetic Route for 1



0.67 (hexane–EtOAc, 4:1);  $[\alpha]_D +4.8$  ( $c$  0.7,  $\text{CHCl}_3$ ); <sup>1</sup>H NMR (500 MHz;  $\text{CDCl}_3$ )  $\delta$  3.71 (s, 3H), 3.68–3.62 (m, 1H), 2.43 (dt, 1H,  $J$  = 9.1, 5.3 Hz), 2.39 (d, 1H,  $J$  = 8.3 Hz), 1.73–1.25 (m, 54H), 0.88 (t, 6H,  $J$  = 7.0 Hz); <sup>13</sup>C NMR (125 MHz;  $\text{CDCl}_3$ )  $\delta$  176.2, 72.3, 51.4, 51.0, 35.7, 31.9, 29.68, 29.67, 29.65, 29.61, 29.58, 29.56, 29.55, 29.53, 29.49, 29.41, 29.35, 27.4, 25.7, 22.7, 14.1; HR ESIMS  $m/z$  [ $\text{M} + \text{Na}$ ]<sup>+</sup> Calcd for  $\text{C}_{33}\text{H}_{66}\text{O}_3\text{Na}$  533.4903, found 533.4904.

**(*R*)-Methyl-2-((*R*)-1-hydroxyheptyl)octadecanoate (2).** A solution of lithium diisopropylamine (5 mL) prepared from *n*-BuLi (1.6 M hexane solution, 2.5 mL, 4 mmol) and diisopropylamine (0.56 mL, 4 mmol) was cooled to  $-78$  °C, and the  $\beta$ -hydroxy ester **5**<sup>5</sup> (0.37 g, 2 mmol, mixture of stereoisomers 50% ee) was added as a solution in THF (2 mL). After 1 h at  $-45$  °C, 1-iodododecane (1.76 g, 2.5 mmol) and HMPA (0.52 mL, 1.5 mmol) were added via a syringe. The mixture was stirred at  $-45$  °C for 5 h then warmed slowly to  $-20$  °C overnight. The mixture was treated with saturated  $\text{NH}_4\text{Cl}$  and extracted with ether. The ether layer was washed with brine, dried over  $\text{MgSO}_4$  and concentrated. The crude product was purified by column chromatography (hexane–EtOAc, 10:1) to give **2** (0.173 g, 21%, 50% ee) as a white solid (Scheme 3):  $R_f$  = 0.69 (hexane–EtOAc, 4:1);  $[\alpha]_D$

### Scheme 3. Synthetic Route for 2



+4.3 ( $c$  0.6,  $\text{CHCl}_3$ ); <sup>1</sup>H NMR (500 MHz;  $\text{CDCl}_3$ )  $\delta$  3.73 (s, 3H), 3.70–3.65 (m, 1H), 2.46 (dt, 1H,  $J$  = 9.2, 5.3 Hz), 2.42 (d, 1H,  $J$  = 8.3 Hz), 1.75–1.27 (m, 40H), 0.90 (t, 6H,  $J$  = 6.9 Hz); <sup>13</sup>C NMR (125 MHz;  $\text{CDCl}_3$ )  $\delta$  176.2, 72.3, 51.5, 51.0, 35.7, 31.94, 31.78, 29.71, 29.70, 29.67, 29.66, 29.64, 29.58, 29.51, 29.44, 29.37, 29.22, 27.4, 25.7, 22.70, 22.61, 14.13, 14.08; HR ESIMS  $m/z$  [ $\text{M} + \text{Na}$ ]<sup>+</sup> Calcd for  $\text{C}_{26}\text{H}_{52}\text{O}_3\text{Na}$  435.3797, found 435.3809.

**(*S*)-(+)-*O*-Acetylmandelic ester 4.** To a stirred solution of  $\beta$ -hydroxy ester **3**<sup>4</sup> (62.9 mg, 0.2 mmol) and (*S*)-(+)-*O*-acetylmandelic acid (58.3 mg, 0.3 mmol) in  $\text{CH}_2\text{Cl}_2$  (4 mL) was added EDCI-HCl (76.7 mg, 0.4 mmol) at 0 °C and the mixture was stirred for 1 min. Subsequently, DMAP (2.4 mg, 0.02 mmol) was added, and the mixture was stirred for an additional 30 min at the same temperature. The resulting mixture was diluted with  $\text{CH}_2\text{Cl}_2$  (6 mL), and was washed with brine. The organic layer was dried over anhydrous  $\text{Na}_2\text{SO}_4$  and concentrated. Then the resulting crude product was purified by column chromatography (hexane–EtOAc, 8:1) to give the **4** (93.1 mg, 17.8 mmol, 95%) as a white solid:  $R_f$  = 0.4 (hexane–

EtOAc, 4:1);  $^1\text{H}$  NMR (400 MHz;  $\text{CDCl}_3$ )  $\delta$  7.46–7.44 (m, 2H), 7.39–7.35 (m, 3H), 5.86 (s, 3H), 5.25–5.22 (m, 1H), 3.63 (s, 1H), 2.64 (dd, 1H,  $J = 15.6, 7.6$  Hz), 2.52 (dd, 1H,  $J = 15.6, 5.6$  Hz), 2.17 (s, 1H), 1.50–1.44 (m, 2H), 1.26–0.95 (m, 26H), 0.88 (t, 3H,  $J = 7.0$ );  $^{13}\text{C}$  NMR (100 MHz;  $\text{CDCl}_3$ )  $\delta$  170.0, 169.7, 167.8, 133.5, 128.8, 128.3, 127.2, 74.2, 71.5, 51.4, 38.7, 33.4, 31.5, 29.3, 29.2, 29.0, 28.9, 28.7, 24.1, 22.3, 20.2, 13.7; HR ESIMS  $m/z$  [ $\text{M} + \text{Na}$ ] $^+$  Calcd for  $\text{C}_{29}\text{H}_{46}\text{O}_6\text{Na}$ : 513.3187, found 513.3177.

## ■ ASSOCIATED CONTENT

### ■ Supporting Information

Raw IR spectra of **1** and  $\text{CDCl}_3$  solvent; Exciton coupling of (*R,R*)\_Model\_II; Conformers of **1** and their IR and VCD spectra; The structure of **1\_dimer** (*bunched*) and its IR and VCD spectra; IR and VCD spectra of full **1** and **2\_dimer** and of the truncated Model\_I.  $^1\text{H}$  and  $^{13}\text{C}$  NMR spectra of **1**, **2** and **4**. This material is available free of charge via the Internet at <http://pubs.acs.org>.

## ■ AUTHOR INFORMATION

### Corresponding Author

\*E-mail: [yunjie.xu@ualberta.ca](mailto:yunjie.xu@ualberta.ca).

### Notes

The authors declare no competing financial interest.

## ■ ACKNOWLEDGMENTS

This research was funded by the University of Alberta, the Natural Sciences and Engineering Research Council of Canada and the Alberta Glycomics Centre. We also gratefully acknowledge access to the computing facilities provided by the Academic Information and Communication Technology group at the University of Alberta and by the Western Canada Research Grid (Westgrid). Y.X. holds a senior Canada Research Chair in Chirality and Chirality Recognition.

## ■ REFERENCES

- Fráter, G. *Helv. Chim. Acta* **1979**, *62*, 2825–2828.
- (a) Fráter, G.; Müller, U.; Günther, W. *Tetrahedron* **1984**, *40*, 1269–1277. (b) Seebach, D.; Wasmuth, D. *Helv. Chim. Acta* **1980**, *63*, 197–200.
- Khan, A. A.; Chee, S. H.; Stocker, B. L.; Timmer, M. S. M. *Eur. J. Org. Chem.* **2012**, 995–1002.
- Ratovelomanana-Vidal, V.; Girard, C.; Touati, R.; Tranchier, J. P.; Hassine, B. B.; Genêt, J. P. *Adv. Synth. Catal.* **2003**, *345*, 261–274.
- Nishizawa, M.; Yamamoto, H.; Imagawa, H.; Barbier-Chassefière, V.; Petit, E.; Azuma, I.; Papy-Garcia, D. *J. Org. Chem.* **2007**, *72*, 1627–1633.
- Barry, C. E.; Lee, R. E.; Mdluli, K.; Sampson, A. E.; Schroeder, B. G.; Slayden, R. A.; Yuan, Y. *Prog. Lipid Res.* **1998**, *37*, 143–179.
- Kaur, D.; Guerin, M. E.; Skovierova, H.; Brennan, P. J.; Jackson, M. *Adv. Appl. Microbiol.* **2009**, *69*, 23–78.
- (a) Brotin, T.; Vanthuyne, N.; Cavagnat, D.; Ducasse, L.; Buffeteau, T. *J. Org. Chem.* **2014**, *79*, 6028–6036. (b) Cherblanc, F. L.; Lo, Y.-P.; Herrebout, W. A.; Bultinck, P.; Rzepa, H. S.; Fuchter, M. J. *J. Org. Chem.* **2013**, *78*, 11646–11655. (c) Yang, G.; Li, J.; Liu, Y.; Lowary, T. L.; Xu, Y. *Org. Biomol. Chem.* **2010**, *8*, 3777–3783.
- (a) Torres-Valencia, J. M.; Chávez-Ríos, O. E.; Cerda-García-Rojas, C. M.; Burgueño-Tapia, E.; Joseph-Nathan, P. *J. Nat. Prod.* **2008**, *71*, 1956–1960. (b) Muñoz, M. A.; Chamy, C.; Bucio, M. A.; Hernández-Barragán, A.; Joseph-Nathan, P. *Tetrahedron Lett.* **2014**, *55*, 4274–4277.
- (10) (a) Polavarapu, P. L. *Chirality* **2008**, *20*, 664–672. (b) Polavarapu, P. L. *Chirality* **2012**, *24*, 909–920.
- (11) (a) Hoye, T. R.; Jeffrey, C. S.; Shao, F. *Protocols* **2007**, *10*, 2451–2458. (b) Seco, J. M.; Quiñoá, E.; Riguera, R. *Chem. Rev.* **2004**, *104*, 17–117. (c) Dale, J. A.; Mosher, H. S. *J. Am. Chem. Soc.* **1973**, *95*, 512–519.
- Petrovic, A. G.; Bose, P. K.; Polavarapu, P. L. *Carbohydr. Res.* **2004**, *339*, 2713–2720.
- Zhang, P.; Polavarapu, P. L. *Appl. Spectrosc.* **2006**, *60*, 378–385.
- Shanmugam, G.; Polavarapu, P. L. *J. Am. Chem. Soc.* **2004**, *126*, 10292–10295.
- (15) (a) Shanmugam, G.; Polavarapu, P. L. *Biophys. J.* **2004**, *87*, 622–630. (b) Shanmugam, G.; Polavarapu, P. L.; Gopinath, D.; Jayakumar, R. *Biopolym.: Pept. Sci.* **2005**, *80*, 636–642. (c) Shanmugam, G.; Polavarapu, P. L. *Biophys. Chem.* **2004**, *111*, 73–77.
- Kurouski, D.; Lombardi, R. A.; Dukor, R. K.; Lednev, I. K.; Nafie, L. A. *Chem. Commun.* **2010**, *46*, 7154–7156.
- (17) (a) Petrovic, A. G.; Polavarapu, P. L. *J. Phys. Chem. B* **2005**, *109*, 23698–23705. (b) Shanmugam, G.; Polavarapu, P. L. *Appl. Spectrosc.* **2005**, *59*, 673–681.
- Castiglioni, E.; Biscarini, P.; Abbate, S. *Chirality* **2009**, *21*, E28–E36.
- (19) (a) Merten, C.; Kowalik, T.; Hartwig, A. *Appl. Spectrosc.* **2008**, *62*, 901–905. (b) Buffeteau, T.; Laguné-Labarthe, F.; Sourisseau, C. *Appl. Spectrosc.* **2005**, *59*, 732–745.
- (20) (a) Dezhahang, Z.; Poopari, M. R.; Xu, Y. *Chem.—Asian J.* **2013**, *8*, 1205–1212. (b) Debie, E.; Jaspers, L.; Bultinck, P.; Herrebout, W.; Van Der Veken, B. *Chem. Phys. Lett.* **2008**, *450*, 426–430.
- (21) Losada, M.; Tran, H.; Xu, Y. *J. Chem. Phys.* **2008**, *128*, 014508/1–11.
- Yang, G.; Xu, Y. *Phys. Chem. Chem. Phys.* **2008**, *10*, 6787–6795.
- Gobi, S.; Vass, E.; Magyarfalvi, G.; Tarczay, G. *Phys. Chem. Chem. Phys.* **2011**, *13*, 13972–13984.
- Rablen, P. R.; Pearlman, S. A.; Finkbiner, J. *J. Phys. Chem. A* **1999**, *103*, 7357–7363.
- Poopari, M. R.; Dezhahang, Z.; Xu, Y. *Phys. Chem. Chem. Phys.* **2013**, *15*, 1655–1665.
- (26) (a) Thomas, J.; Sukhorukov, O.; Jäger, W.; Xu, Y. *Angew. Chem., Int. Ed.* **2014**, *53*, 1156–1159. (b) Thomas, J.; Sukhorukov, O.; Jäger, W.; Xu, Y. *Angew. Chem., Int. Ed.* **2013**, *52*, 4402–4405.
- (27) (a) Muñoz, M. A.; Areche, C.; Roviro, J.; San-Martín, A.; Joseph-Nathan, P. *Heterocycles* **2010**, *81*, 625–635. Cichewicz, R. H.; Clifford, L. J.; Lassen, P. R.; Cao, X.; Freedman, T. B.; Nafie, L. A.; Deschamps, J. D.; Kenyon, V. A.; Flanary, J. R.; Holman, T. R.; Crews, P. *Bioorg. Med. Chem.* **2005**, *13*, S600–S612.
- Dennington, R.; Keith, T.; Millam, J. *GaussView*, Version 5; Semichem Inc.: Shawnee Mission, KS, 2009.
- (29) (a) Frelek, J.; Butkiewicz, A.; Gorecki, M.; Wojcieszczyk, R. K.; Luboradzki, R.; Kwit, M.; Rodee, M. F.; Szczepiek, W. *J. RSC Adv.* **2014**, *4*, 43977–43993. (b) Bouchet, A.; Brotin, T.; Linares, M.; Ågren, H.; Cavagnat, D.; Buffeteau, T. *J. Org. Chem.* **2011**, *76*, 1372–1383.
- (30) (a) Dezhahang, D.; Poopari, M. R.; Hernández, F. E.; Diaz, C.; Xu, Y. *Phys. Chem. Chem. Phys.* **2014**, *16*, 12959–12967. (b) Losada, M.; Xu, Y. *Phys. Chem. Chem. Phys.* **2007**, *9*, 3127–3135.
- Harada, N.; Nakanishi, K. *Circular Dichroic Spectroscopy Exciton Coupling in Organic Stereochemistry*; University Science Books: Mill Valley, CA, 1983.
- Taniguchi, T.; Monde, K. *J. Am. Chem. Soc.* **2012**, *134*, 3695–3698.
- (33) Berova, N.; Nakanishi, K.; *Circular Dichroism: Principles and Applications*, 2nd ed.; Berova, N., Nakanishi, K., Woody, R. W., Eds.; Wiley-VCH: New York, 2000; p 337.
- (34) (a) Williams, S. D.; Johnson, T. J.; Sharpe, S. W.; Yavelak, V.; Oates, R. P.; Brauer, C. S. *J. Quant. Spectrosc. Radiat. Transfer* **2013**, *129*, 298–307. (b) Luttschwager, N. O. B.; Wassermann, T. N.; Mata, R. A.; Suhm, M. A. *Angew. Chem., Int. Ed.* **2012**, *52*, 463–466. (c) Wexler, A. S. *Spectrochim. Acta* **1965**, *21*, 1725–1742.
- Roy, D.; Marianski, M.; Maitra, N. T.; Dannenberg, J. J. *J. Chem. Phys.* **2012**, *137*, 134109/1–12.
- (36) Frisch, M. J.; Trucks, G. W.; Schlegel, H. B.; Scuseria, G. E.; Robb, M. A.; Cheeseman, J. R.; Scalmani, G.; Barone, V.; Mennucci, B.; Petersson, G. A.; Nakatsuji, H.; Caricato, M.; Li, X.; Hratchian, H.

P.; Izmaylov, A. F.; Bloino, J.; Zheng, G.; Sonnenberg, J. L.; Hada, M.; Ehara, M.; Toyota, K.; Fukuda, R.; Hasegawa, J.; Ishida, M.; Nakajima, T.; Honda, Y.; Kitao, O.; Nakai, H.; Vreven, T.; Montgomery, J. A., Jr.; Peralta, J. E.; Ogliaro, F.; Bearpark, M.; Heyd, J. J.; Brothers, E.; Kudin, K. N.; Staroverov, V. N.; Kobayashi, R.; Normand, J.; Raghavachari, K.; Rendell, A.; Burant, J. C.; Iyengar, S. S.; Tomasi, J.; Cossi, M.; Rega, N.; Millam, N. J.; Klene, M.; Knox, J. E.; Cross, J. B.; Bakken, V.; Adamo, C.; Jaramillo, J.; Gomperts, R.; Stratmann, R. E.; Yazyev, O.; Austin, A. J.; Cammi, R.; Pomelli, C.; Ochterski, J. W.; Martin, R. L.; Morokuma, K.; Zakrzewski, V. G.; Voth, G. A.; Salvador, P.; Dannenberg, J. J.; Dapprich, S.; Daniels, A. D.; Farkas, Ö.; Foresman, J. B.; Ortiz, J. V.; Cioslowski, J.; Fox, D. J. *Gaussian 09*, Revision C.01; Gaussian, Inc.: Wallingford, CT, 2009.

(37) Kohn, W.; Sham, L. J. *Phys. Rev.* **1965**, *140*, A1133–A38.

(38) (a) Becke, A. D. *J. Chem. Phys.* **1993**, *98*, 5648–5652. (b) Lee, C. T.; Yang, W. T.; Parr, R. G. *Phys. Rev. B: Condens. Matter Mater. Phys.* **1988**, *37*, 785–789.

(39) Kendall, R. A.; Dunning, T. H., Jr.; Harrison, R. J. *J. Chem. Phys.* **1992**, *96*, 6796–6806.

(40) Nafie, L. A. *Vibrational Optical Activity: Principles and Applications*; John Wiley & Sons Ltd.: New York, 2011.

(41) SPARTAN '08; Wavefunction, Inc.: Irvine, CA, 2008; [www.wavefun.com/products/spartan.html](http://www.wavefun.com/products/spartan.html).

(42) Dewar, M. J. S.; Zoebisch, E. G.; Healy, E. F. *J. Am. Chem. Soc.* **1985**, *107*, 3902–3909.